UNIVERSITÀ DEGLI STUDI DI PADOVA
CENTRO RICERCHE FUSIONE

UNIVERSITEIT GENT
FACULTEIT INGENIEURSWETENSCHAPPEN EN ARCHITECTUUR

Joint Ph.D. programme for Fusion Science and Engineering

Functional and manufacturing optimization of the beam source for the Neutral Beam Injector of DTT

Supervisor (UniPD):

Doct. Eng. Agostinetti Piero
(Consorzio RFX)

Supervisor (UGent):

Prof. Kristel Crombé

Ph.D. Candidate:

Veronese Fabio

Mat. 1227387

February 16th, 2023
35th cycle

Contents

Riassunto

Il Divertor Test Tokamak (DTT) sarà un nuovo centro sperimentale, previsto di essere costruito in Italia tra pochi anni, e parte di un piano di ricerca più grande programmato dall'EFDA nel 2012, che ha immaginato una Mappa in 8 passi verso la generazione di potenza elettrica da un Demonstration Fusion Power Plant (DEMO) entro il 2050. Questa struttura in particolare mira a coprire con esperienza sul campo una lacuna sulla conoscenza dei Plasma Facing Components durante il complesso processo di estrapolazione da macchine sperimentali ad esperimenti a piena potenza come ITER o futuri reattori di tipo DEMO, non colmabile semplicemente con sufficienti simulazioni numeriche. I suoi obiettivi principali sono:

- Sviluppo di Plasma Facing Components (PFCs) in grado di sopportare flussi di potenza molto grandi ($\approx 5 \div 10\,\mathrm{MW\ m^{-2}}$);
- Selezione della geometria di divertore e dell'espansione di flusso magnetico per ridurre il flusso normale sul target, per esempio ridistribuendo il calore su una superficie più larga;
- Rimozione dell'energia di plasma prima che raggiunga il target tramite radiazioni da impurità aumentando la densità di plasma di confine e iniettando impurità nella regione di SOL, per ridurre la frazione di potenza riscaldante che si deposita sul divertore, almeno fino ad un livello compatibile con la tecnologia dei materiali;
- Riciclo ed aumento della densità con abbassamento della temperatura vicino ai punti di contatto, con conseguente "distacco" (la temperatura scende al di sotto quella richiesta per la ionizzazione; perciò la particelle si neutralizzano e non c'è flusso diretto di plasma o potenza sui bersagli del divertore).

Questo DTT tokamak dovrà possedere una certa flessibilità nelle condizioni di lavoro per studiare, testare e proporre una soluzione da poter usare poi ovunque necessario; di conseguenza, deve essere in grado di realizzare esperimenti in scala integrando il maggior numero possibile degli aspetti propri delle potenze in gioco e scarico particelle (simili a DEMO). Per ottenere questo obiettivo ambizioso, è stata stimata la necessità di riscaldamenti ausiliari da iniettori di neutri (NBI) nell'ordine di circa 10 MW di potenza; a tal fine, un singolo iniettore è stato proposto, con una corrente

estratta totale di circa 40 A di D^- usando un sistema di accelerazione elettrostatica di 510 keV. Questi sistemi, seppur semplici nel concetto di usare griglie cariche per accelerare particelle, presentano un grande numero di complessità, non linearità e problemi critici che richiedono simulazioni accurate in ogni aspetto fisico che le interessa:

- Dinamica del fascio di particelle cariche
- Elettromagnetismo
- Reazioni di tipo fisico (elastiche, scambio carica, ecc., collisioni)
- Scambio di calore (da impatto di particelle)
- Meccanica dei solidi (deformazioni dovute alla variazione di temperatura)

Ognuno di questi aspetti contribuisce all'altro ad un certo livello, da cui l'importanza di una simulazione accurata. In questo momento, basandosi sui bisogni specifici di ogni simulazione, vari codici sono stati usati:

- Per analisi più delicate di tipo *single-beamlet*, la comprovata combinazione dei codici non commerciali SLACCAD e EAMCC3D.
- Per analisi più complesse con interazioni *multi-beamlet*, tracciamento di particelle nell'intero NBI e simulazione di vuoto, il codice commerciale agli elementi finiti (FEM) multifisico COMSOL®.
- Per automatizzazione e *post-processing* di dati, il software ingegneristico commerciale MATLAB®.

Questo lavoro di tesi si focalizza sul soddisfare alcuni vari criteri di progetto per DTT NBI, simili a quelli di ITER o di lavori pre-concettuali per DEMO. I criteri qui considerati riguardano aspetti di ottica e trasmissione del fascio, seguendo scelte fatte in passato dal team di DTT ed altri ricercatori perlopiù in termini di geometria di griglia, materiali, potenza estratta, densità del gas di sottofondo, e simili. Per portare a termine il lavoro, è stato sviluppato un insieme di codici, capace di stimare ogni aspetto desiderato dell'NBI basandosi su condizioni al contorno prestabilite; varie migliorie e nuovi concetti sono stati proposti e validati tramite simulazione.
I capitoli successivi sono dedicati a lavori paralleli svolti durante il periodo di dottorato, nel dettaglio su DEMO NBI ed il Beam Driven Plasma Neutralizer, il quale è stato l'argomento principale della visita presso il laboratorio di IPP Garching (Capitolo 5), e sull'esperimento SPIDER presso il Consorzio RFX (Capitolo 6). Queste esperienze sono state cruciali per sviluppare abilità ed acquisire conoscenze necessarie per migliorare il lavoro su DTT NBI.

Summary

The Divertor Test Tokamak (DTT) will be a new experimental facility expected to be built in Italy in the near future, and part of a greater research plan envisioned by EFDA in 2012, that devised a Roadmap in 8 steps towards the generation of electrical power by a Demonstration Fusion Power Plant (DEMO) by 2050. This one in particular aims to cover with on-field experience the gap in Plasma Facing Components knowledge during the complex extrapolation process from proof-of-principle devices to actual full-power experiments like ITER and future DEMO-like reactors, that cannot simply be filled with numerical simulations. Its main objectives are:

- Development of Plasma Facing Components (PFCs) able to withstand very large power fluxes ($\approx 5 \div 10\,\mathrm{MW\ m^{-2}}$);
- Selection of the divertor geometry and of the magnetic flux expansion to reduce the normal heat flux on the target, i.e. by distributing the heat over a larger surface;
- Removal of plasma energy before it reaches the target via impurity radiation by increasing edge plasma density and injecting impurities in the SOL region, as to decrease the fraction of the heating power that impinges on the divertor, up to a level compatible with the materials technology;
- Recycling and increase of density lowering the temperature close to the target, with consequent detachment (the temperature drops below that required for ionization; therefore, the particles are neutralized and there is no direct plasma flux or power to the divertor targets).

This DTT tokamak will need to be flexible enough in its working conditions to study, test and propose a solution then to be used directly where needed; consequently, it must be able to realize scaled experiments integrating most of the possible aspects of the DEMO power and particle exhaust. In order to obtain this ambitious objective, auxiliary heating from Neutral Beam Injection has been estimated in the order of 10 MW of power; to that end, a single injector has been proposed, with an extracted total current of about 40 A of D^- using a 510 keV electrostatic acceleration system. These systems, albeit simple in the concept of using grids to accelerate particles,

present a manifold of complications, non-linearities and critical issues that call for accurate simulation in each physical aspect that is encompassed within:

- Charged particle beam dynamics
- Electromagnetism
- Physical reactions (elastic, charge-exchange, etc. collisions)
- Heat transfer (from particle impact)
- Solid mechanics (deformations due to temperature variation)

Each one of these aspects contributes to another to some degree, hence the importance of accurate evaluation. At this moment, based on the specific need of each simulation, a number of codes have been used:

- For more delicate single-beamlet analysis, the field-tested combination of the SLACCAD and EAMCC3D non-commercial codes.
- For more complex multi-beamlet interaction analysis, full-NBI particle tracing and vacuum simulation, the commercial Finite Element Method (FEM) multi-physics simulation code COMSOL®.
- For automatization and data post-processing, the commercial engineering software MATLAB®.

This thesis work focuses first on satisfying various unmet project criteria for DTT NBI, similar to those in ITER and in pre-conceptual works for DEMO. Said criteria considered here regard aspects of beam optics and total beam transmission, following the choices made previously by the DTT team and other researchers mostly on term of grid geometry, materials, extracted power, gas background density, and such. To do this, a suite of codes has been developed, able to estimate each desired aspect of the NBI based on established boundary conditions; various improvements and novel concepts have been proposed and validated through simulation.
The following chapters are dedicated to parallel works done during the Ph.D. period, namely on DEMO NBI and the Beam Driven Plasma Neutralizer, which was the main scope of the visit at the IPP Garching research centre (Chapter 5), and on the SPIDER experiment at Consorzio RFX (Chapter 6). These experiences have been crucial in developing skills and acquiring the know-how needed to improve the work on DTT NBI.

Scientific contributions produced during the Ph.D.

1. F. Veronese, P. Agostinetti, A. Murari and A. Pepato, *"Performance Optimization of the Electrostatic Accelerator for DTT Neutral Beam Injector"* in IEEE Transactions on Plasma Science, 2022, DOI: 10.1109/TPS.2022.3169433. In occasion of the SOFE 2021 conference.

2. F. Veronese, P. Agostinetti, C. Hopf, G. Starnella, *"Functional Optimization for a Beam Driven Plasma Neutralizer in DEMO Neutral Beam Injector"*, under review at Fusion Engineering and Design. In occasion of the SOFT 2022 conference.

3. F. Veronese, P. Agostinetti, G. Calabrò, F. Crisanti, P. Fanelli, R. Lombroni, and A. Murari, *"Comparison among possible design solutions for the Stray Field Shielding System of the DTT Neutral Beam Injector"*, to be submitted at Journal of Instrumentation. In occasion of the NIBS 2022 conference.

Chapter 1

Fusion energy

SUMMARY - Fusion energy is a important topic in our day and age, and is often hailed as one of the possible main way of production of renewable electrical energy in humanity near future. This chapter deals with a general overlook on the principles behind magnetically confined thermonuclear fusion, as well as details on key experiments as ITER.

1.1 Introduction

Never like at this point and age in the history of humanity, there has been such a need for power: the power to shape mountains with bores, travel to space, operate a pump, go to work in an electric train after turning off the electric heater back at home, charging the latest battery-eating phone; as humans grow, the demand for energy naturally grows with them. To satisfy it though we are disposed to destroy the very planet that host the small lives that we seek to improve, waging both literal and economical wars against anything that does not goes our way. This is the basis of the great "energy problem", that the scientific community set to resolve before long, and with one of the possibilities being to inquire further into the use of fusion power plants as a definitive solution to the issue.

In these next paragraphs a little summary of the expected pros and cons will be listed, trying to point out the reasons for this choice and the know-how that will have to be developed to bring to fruition what could be mankind greatest accomplishment of this century, a future controlled thermonuclear fusion power plant; secondly referring explicitly to one of the greatest international projects regarding techno-scientific progress in said context: the ITER (International Thermonuclear Experimental Reactor) project.

This Ph.D. thesis is the result of three very fruitful years at Consorzio RFX, one of the most important contributors to the worldwide scientific effort on fusion and

home to the MITICA and SPIDER experiments, as well as to the greatest RFP tokamak in the world, the soon to be assembled RFX-mod2.

1.2 Energy outlook

As of today, electrical power production still greatly relies on generation by traditional thermal plants burning fossil fuels such as coal, natural gas, oil and petroleum distillates, releasing in the atmosphere large amounts of carbon dioxide, nitrous and sulphurous oxides, extremely dangerous to the environment if not recaptured (e.g. coal combustion generates anhydrides that by reacting with water are the main responsible of the *acid rain* phenomenon). A number of other more politics-centered problematics ride on how energy is generated and distributed, such as delicate geopolitical equilibria or the dependence from foreign and unstable regions for fuel supply: Europe is learning this lesson the hard way in this historical period, in the Russo-Ukrainian conflict, with almost 40% of its gas supply [1] being jeopardized during winter.
Moreover, these conventional energy sources are not inexhaustible: various estimations project that, at the current rate of production and use, reserves are expected to last up to 139 years for coal, 49 for natural gas and 54 for oil [1]. Even supposing to have reserves for another 200 years, the problem would be just slightly postponed onto the next generations, rushing them to find a solution in our stead. This without even considering that the global energy request is constantly increasing by the year.

"Alternatives" are plenty to the fossil fuels for power production: fission plants, hydroelectric, photovoltaic, eolic, geothermic, and a lot more; nevertheless, there is an important distinction to be made between alternative and integrative energy sources: very often people talking about alternative energy sources include all the aforementioned. That, is a mistake: as a matter of fact, the only real alternative in the list is the nuclear fission plant, the others being mere integratives. The distinction is as simple as significant: alternative sources are potentially up to the challenge of satisfying the global need of energy, while the others are not, by sheer difference in TWh production. A reliable alternative could then be fission power plants: theoretically, building enough of these high-tech reactors (especially latest-gen versions) to cover the needs of the entire planet would be possible. Some countries are already producing enough (and more) than their internal energy request by main fission power plants use, but there are many a reason (since their first appearance) as to why governments are looking for other solutions:

1. Fission plants need radioactive "fuels" such as ^{238}U, ^{239}Pu, ^{233}U, with elevate contamination hazard, not easily obtainable and not equally distributed along the world.

2. These plants produce as by-products radioactive elements such as ^{141}Ba and

^{137}Cs, the second being very dangerous because soluble in water. Moreover, the problem of radioactive waste disposal remains, again with high contamination hazard and logistic problems: as an example, the ^{239}Pu has a halving time of 24200 years and needs a storage time of about 300000 years.

3. Recent incidents (the constant danger of attack on the Zaporizhzhia power plant) or more historic ones (Chernobyl) showed to the world how problematic these plants can be in case of faults, natural disasters or human mistakes or wars.

4. The problem of the finite availability of ^{235}U still stands.

As a focus on the last point made, a several-hundred years' worth of ^{235}U has been esteemed [1] to be available in nature, and as a plus last-gen plants can use ^{233}U and ^{239}Pu, which are in an even larger availability. However, the other three points are reason enough to make this power source a constant threat. If dividing nuclei has a lot of issues, it is advisable to try to start from the bottom, by fusing light nuclei together: what happens every day in the Sun.

1.3 Nuclear fusion

The fundamental concept of nuclear fusion is to collide two (or more) light nuclei overcoming their barrier potential, obtaining a new nucleus with a total mass that is lower than the sum of the starting nuclei. This mass difference is transformed into energy flowing out of the system in the form of radiation or particle kinetic energy, as expected by the well-known Einstein's equation $E = \Delta mc^2$. This happens because, for nuclei with mass number $A < 56$, the binding energy defined as:

$$B = (N_{m_n} + Z_{m_z} - m(N, Z))\, c^2 \tag{1.1}$$

where N is the number of neutrons and Z the number of protons, increases with the number of nucleons. This energy manifests through fast neutral particles, that heat the container they are in. It is then possible to convert such energy through more conventional means in electric energy to power up transmission, distribution lines and utencies.
From a physical point of view, the phenomenon is very well established and simply verified by observing what happens every day in the Sun and in the other stars in the Universe; from a technological point of view though the circumstances of obtaining fusion are obviously way more complex. While "our" fusion relies on particle collisions in a controlled environment, this is quite different from what usually happens in stars, where the so-called *proton-proton chain* reaction is catalysed by the immense gravity causing quantum tunnelling of atoms to easily overcome the potential barrier. The principal nuclear reactions that are being contemplated as solutions in a future

thermonuclear reactor involve some of the lightest particles in the universe, namely Deuterium (D), Tritium (T) (both hydrogen isotopes) and ^{3}He. These are [2]:

$$\begin{aligned} \mathrm{D} + \mathrm{T} &\longrightarrow {}^4\mathrm{He}\,(3.5\ \mathrm{MeV}) + \mathrm{n}\,(14.1\ \mathrm{MeV}) \\ \mathrm{D} + \mathrm{D} &\longrightarrow \mathrm{T}\,(1.01\ \mathrm{MeV}) + \mathrm{p}\,(3.02\ \mathrm{MeV}) \\ \mathrm{D} + \mathrm{D} &\longrightarrow {}^3\mathrm{He}\,(0.82\ \mathrm{MeV}) + \mathrm{n}\,(2.45\ \mathrm{MeV}) \\ \mathrm{D} + {}^3\mathrm{He} &\longrightarrow {}^4\mathrm{He}\,(3.6\ \mathrm{MeV}) + \mathrm{p}\,(14.7\ \mathrm{MeV}) \end{aligned} \tag{1.2}$$

The values in brackets indicate the kinetic energy associated with each particle produces by the reaction; and each one is characterized by its own "probability", or cross-section, expressed in m^2: it carries the meaning of an area surrounding the target particle such as if the incident particle traverses it, the reaction is initiated. Out of all reactions, the most desirable one would be a deuterium-only fusion: this because the availability would be virtually infinite fuel-wise, since deuterium is easily obtained from heavy water, that is present in fixed quantity in seawater (about 1 part out of 6000). The ^{3}He reaction instead has the highest net energy gain, and also all of its by-products are electrically charged, making them possible to confine longer inside the bulk plasma and help maintain the fusion temperature. In the end though, cross-section is the actual decisive criterion that need to be considered: Figure 1.1 reports the experimental cross-section data for fusion reaction in function of the incident particle, and it is easy to see how the D−T reaction dominates the other two in the relevant range of energies. The difference is such that at this moment in history the deuterium-tritium reaction is the only one being researched for power production purposes.

This reaction though does not come without drawbacks: tritium is naturally radioactive, with a half-life of 12.3 years; this means that it is not present in nature, and must be produced ad hoc. The most common reactions to produce tritium involve Lithium atoms and fast neutrons:

$$\begin{aligned} {}^6\mathrm{Li} + \mathrm{n} &\longrightarrow \mathrm{He} + \mathrm{T} + 4.8\ \mathrm{MeV} \\ {}^7\mathrm{Li} + \mathrm{n} &\longrightarrow \mathrm{He} + \mathrm{T} - 2.5\ \mathrm{MeV} \end{aligned} \tag{1.3}$$

One reaction is exothermic, hence desirable in a fusion plasma; the problem is that the natural fraction of ^{6}Li available is extremely smaller than the other option. The actual design choice for use into fusion reactors is to produce tritium through these reactions directly inside the vacuum vessel, by coating particular zones with lithium, called Breeding Blankets, and exploiting the fast neutrals generated by the fusion reactions. This shifts the problem of availability from tritium to lithium, that can boast a relatively high diffusion over Earth's upper crust.

1.4 Plasma definition

Given the range of energies (and hence temperatures) in which fusion cross-sections are meaningful (easily in the 10 keV range), it is easy to see how they can happen

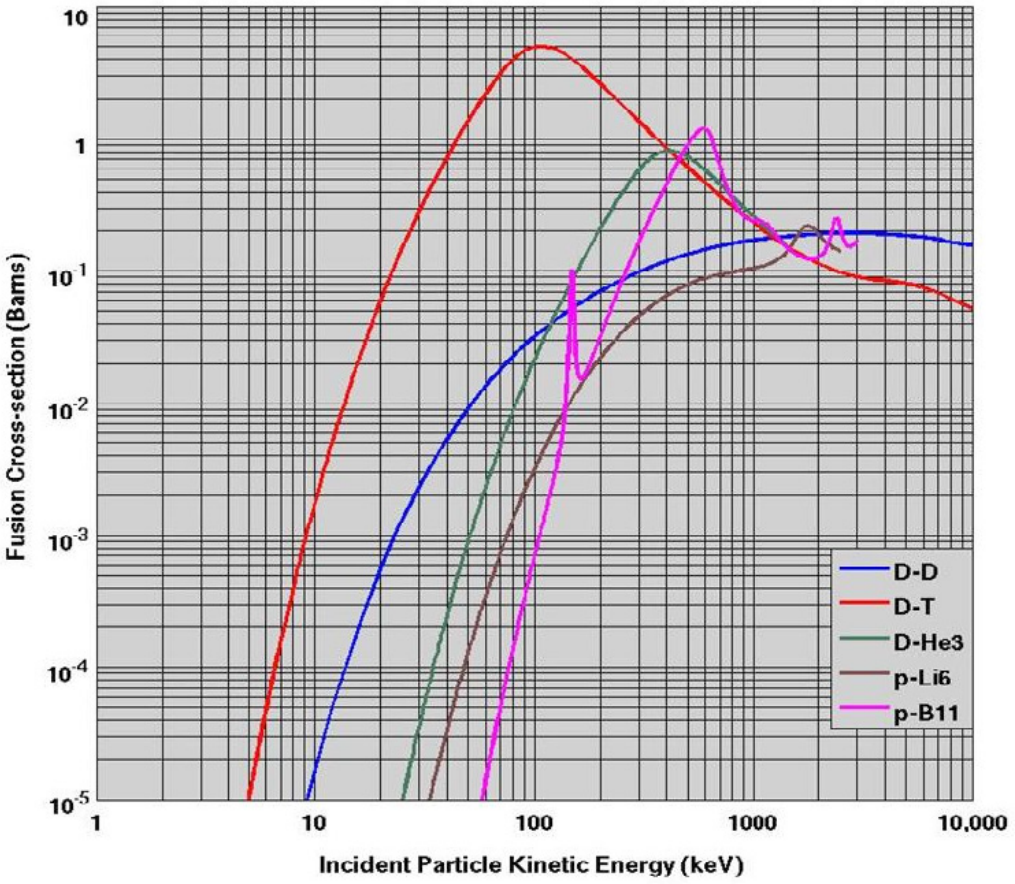

Figure 1.1: Cross-section of some typical nuclear reactions as a function of the energy of the incident particle. One barn equals 10^{-28} m^2 [2].

only between elements in plasma condition. Plasma, considered as the fourth state of matter, is defined as a quasi-neutral ionized gas characterized by high temperatures, electric conductivity and displaying collective behaviour. There are a number of criteria that distinguish a simple ionized gas from a fully developed plasma:

- The conductivity and hence the ability to shield external electric fields: in plasma, positive and negative charges are free to move independently, and over a certain spatial length charge imbalance due to fields disappears. The parameter that gives the order of magnitude of said distance is called Debye length:

$$\lambda_{\mathrm{D}} = \sqrt{\frac{\epsilon_0 T_{\mathrm{e}}}{n_{\mathrm{e}} e^2}} \tag{1.4}$$

  where T_{e} and n_{e} are the electron temperature and density. This means that in order to have plasma, the macroscopic length of its main dimension L must verify that $L \gg \lambda_{\mathrm{D}}$: with this condition it is ensured that there is no

macroscopic charge concentration, making the ionic and electronic densities equal in average.

- The number of particles contained in a sphere of radius λ_D must be far greater than one:

$$N_D = \frac{4}{3}\pi\lambda_D^3 n \gg 1 \tag{1.5}$$

This ensures that the particles are numerous enough to make averages and integral quantities meaningful, and describable with distribution functions.

- Another criterion regards the role of collective effects compared to internal collisions. To describe this ratio, it is possible to use the plasma frequency ω_p, indicating the time scale for the plasma to shield inhomogeneities, and the collision frequency ν_c indicating the average time between collisions for particles. The ratio of these two quantities ω_p/ν_c is thus an index of how much collisions have influence in the particle behavior. In a plasma, this parameter has to be far greater than one, indicating a prevalence of ranged collective effects on local collisionality. What it also entails is the need when describing the system of considering not only conventional fluid dynamics, but also electromagnetism: magnetohydrodynamics (MHD).

1.5 Plasma confinement

To create the right conditions for fusion, particles must be confined close to each other: aside from gravitational confinement, plasma can be confined either inertially or magnetically. Experiment on inertial confinement for fusion relies on extreme heating and compression of a target pellet of deuterium and tritium by high power laser beams. There is interest on the research field, reaching record energy in recent years (70% of the injected energy from fusion reactions [3]), but production of energy from said source still remains impractical, due to the extremely pulsed nature of the fusion reaction.
The main focus is then on magnetic confinement: its concept is based on the behavior of plasma particles in electromagnetic fields, following magnetohydrodynamics laws. By assuming a single fluid approximation, where electron and ions are weighted together as

$$\rho_s = \rho_e + \rho_i\,, \tag{1.6}$$

$$\mathbf{v}_s = \frac{\rho_e \mathbf{v}_e + \rho_i \mathbf{v}_i}{\rho_e + \rho_i}\,, \tag{1.7}$$

new variables are obtained to use in the differential equations. The ideal MHD laws (no resistance) are as follows:

$$\text{Conservation of mass: } \frac{\partial \rho_\mathrm{s}}{\partial t} + \nabla \cdot (\rho_\mathrm{s} \mathbf{v}_\mathrm{s}) = 0, \tag{1.8}$$

$$\text{Conservation of momentum: } \rho_\mathrm{s} \left(\frac{\partial}{\partial t} + \mathbf{v}_\mathrm{s} \cdot \nabla \right) \mathbf{v}_\mathrm{s} = \mathbf{J} \times \mathbf{B} - \nabla p, \tag{1.9}$$

$$\text{Conservation of energy: } \frac{\mathrm{d}}{\mathrm{d}t} \left(\frac{p}{\rho_\mathrm{s}^\gamma} \right) = 0, \tag{1.10}$$

$$\text{Ideal Ohm's Law: } \mathbf{E} + \mathbf{v}_\mathrm{s} \times \mathbf{B} = 0, \tag{1.11}$$

$$\text{Ampère's law: } \nabla \times \mathbf{B} = \mu_0 \mathbf{J}, \tag{1.12}$$

$$\text{Faraday's law: } \frac{\partial \mathbf{B}}{\partial t} = -\nabla \times \mathbf{E}, \tag{1.13}$$

$$\text{Solenoid condition: } \nabla \cdot \mathbf{B} = 0, \tag{1.14}$$

where p is the pressure, γ is the specific heat ratio, $\mathbf{J}$, $\mathbf{B}$ and $\mathbf{E}$ are the current density, magnetic flux density and electric fields. Solving the motion differential equation under these constraints yields a gyrating motion of the fluid around the magnetic field lines, at a typical distance and frequency:

$$r_L = \frac{m|v_\perp|}{q|B|} \quad \textit{Larmor radius} \tag{1.15}$$

$$\omega_c = \frac{q|B|}{m} \quad \textit{cyclotron frequency} \tag{1.16}$$

where $|v_\perp|$ is the module of the component of the velocity perpendicular to the $\mathbf{B}$ vector.
The best and easiest topological choice to confine the plasma is to close the magnetic field lines on themselves in a toroidal shape. However, this not enough: due to the manifestation of destabilizing forces, mainly related to the toroidal form (tendency to expand and flatten the curved magnetic lines) and MHD instabilities, it is necessary to "twist" the magnetic field lines, by adding a poloidal component (the so-called *rotational transform*) to the already present toroidal confining one.
Two possible methods to obtain the needed field configuration have been developed: the Pinch family and the Stellarator family.

- In the Pinch family of devices, the rotational transform is obtained by generating and driving a large toroidal plasma current, that in turn creates the needed poloidal component. Based on the ratio of the toroidal and poloidal magnetic components at the plasma edges, an additional distinction can be made between Reversed-Field Pinch (RFP) (with negative ratio) and the Tokamak (with positive ratio).

- In the Stellarator family of devices, the rotational transform is generated by the presence of accurately shaped external coils, leading to a currentless confined plasma.

All of them have notable pros and cons, but the most researched and the most diffused technology at the moment is indeed the Tokamak, for its relative simplicity and versatility; as such, a brief explanation for it will be reported.

1.5.1 The Tokamak configuration

The tokamak configuration has been invented in 1952, named after a Russian acronym for *toroidal'naya kamera s magnitnymi katushkami*, "toroidal chamber with magnetic coils". Since then, it has been the most promising axisymmetric toroidal configuration for high temperature plasma confinement. The system is constituted by:

- The toroidal magnetic coils, consisting in a elevated number of radially symmetrical 'D'-shaped coils, usually superconductive, due to the extremely high currents needed to maintain the desired magnetic fields. Their shape is accurately optimized to resist electromechanical stresses and provide large space to the fusion plasma within. Magnetically they are the main source of the confinement field, compensating part of the outward kinetic pressure of the travelling particles.

- The poloidal magnetic coils, divided into central solenoid and position control coils; and similarly to the toroidal ones they can be superconductive. The central solenoid concatenates the whole vacuum vessel, behaving as the primary of a transformer with respect to the ionized gas within as the secondary, hence able to transfer energy through ohmic dissipation; the other poloidal coils run around the tokamak, and they provide the field necessary to maintain shape and position of the plasma volume.

- The Heating and Current Drive auxiliary systems, indicating a set of devices dedicated to helping maintain the power balance inside the plasma volume and thus the fusion conditions by injecting power through various methods, for example Neutral Beam Injection of Radio-Frequency Antennas, and also helping to drive the overall plasma current. The neutral beam injection will be treated in detail in Chapter 2.

- Radial saddle coils, mainly dedicated to fine-tuned control of MHD instabilities.

- Power supply and COntrol & Data Acquisition Systems (CODAS), as well as the vacuum and cooling subsystems, and everything else dedicated to the accurate operation of the tokamak.

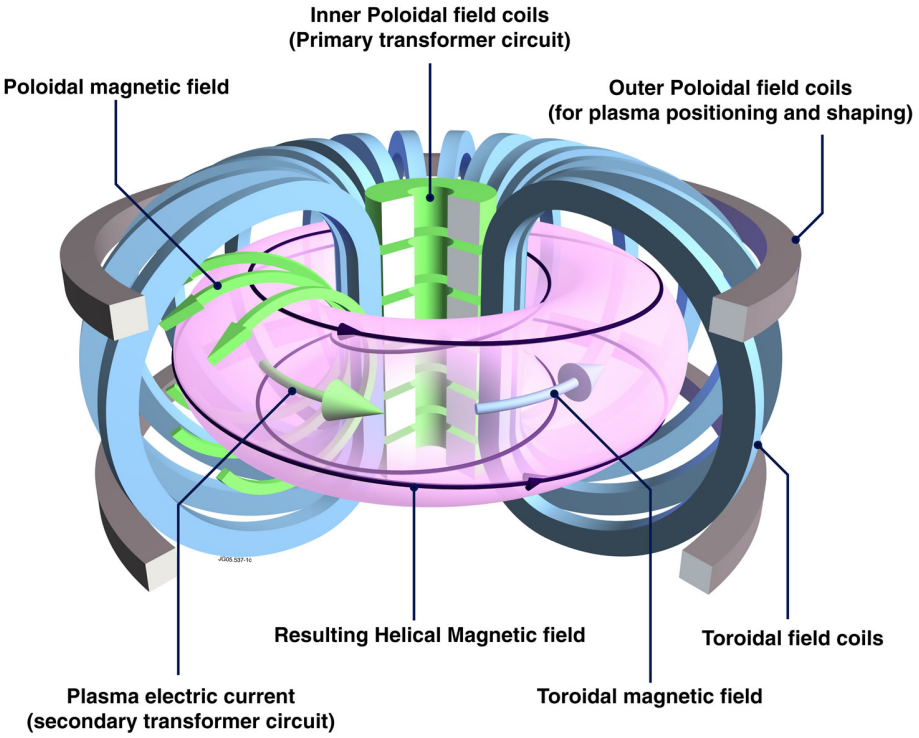

Figure 1.2: Scheme of the tokamak configuration and positioning of the magnetic system. [Courtesy of EUROfusion]

Before a discharge the central coil is charged to its nominal current and shorted, the vacuum vessel is filled with the initial charge of plasma gas and the position control coils are powered, ready to contain the plasma that is about to form. At the start of the pulse operation, a massive inductively-coupled discharge in the gas is provoked by the flux swing generated by the switching of the main central coil on a discharge resistor, in a great equivalent L/R circuit fashion. The discharge is then maintained through the help of additive heating systems, for the whole so-called *flat-top* phase. At the end of the available flux swing, it is necessary to stop the discharge in a controlled way, to avoid the quenching of the plasma current, that could cause extreme electromagnetic stresses on the vessel components.
The plasma is contained within the volume intercepted by toroidally closed magnetic flux lines, but all of those particles that migrate outside of the confinement (because of collisions, neutralization, diffusion mechanisms or the fusion reaction itself) are bound to intercept the walls of the vessel. While this is necessary to actually extract energy from the fusion process, there is the need to control the deposition in such a way as to avoid localized concentrations of thermal loads and damage. The walls are actively cooled, for those neutral particles that can no longer be confined (e.g. neutrons from the fusion reaction), whereas the outer envelope surface of the plasma volume that encloses all of the closed flux lines (called Last Closed Flux Surface)

is modified in shape, in order to direct at least the charged stray particles away from the burning plasma and into a part dedicated to thermalization and dispersion of the particle energy. This component presents itself in both *limiter* and *divertor* configuration, each with its pros and cons, and illustrated in Figure 1.3: most of the actual designs makes use of a divertor, due to its ability to dissipate higher thermal fluxes by intercepting exhaust at an angle and its greater distance from the burning plasma, reducing the chance of sputtering impurities reaching the main chamber. The component itself is very critical to a good operation of the tokamak, but its behaviour is strongly dependent on the plasma and its dynamics, that are quite hard to model in a simulation. This is one of the reasons behind the need of a dedicated facility to the accurate study of this delicate component and plasma-wall interactions in reactor-like environments, without risking to lose years of research because of a wrong extrapolation of a low-power design: that facility, DTT, and its auxiliary heating systems are the main scopes of this thesis, and will be explored in detail in Chapter 3 and 4.

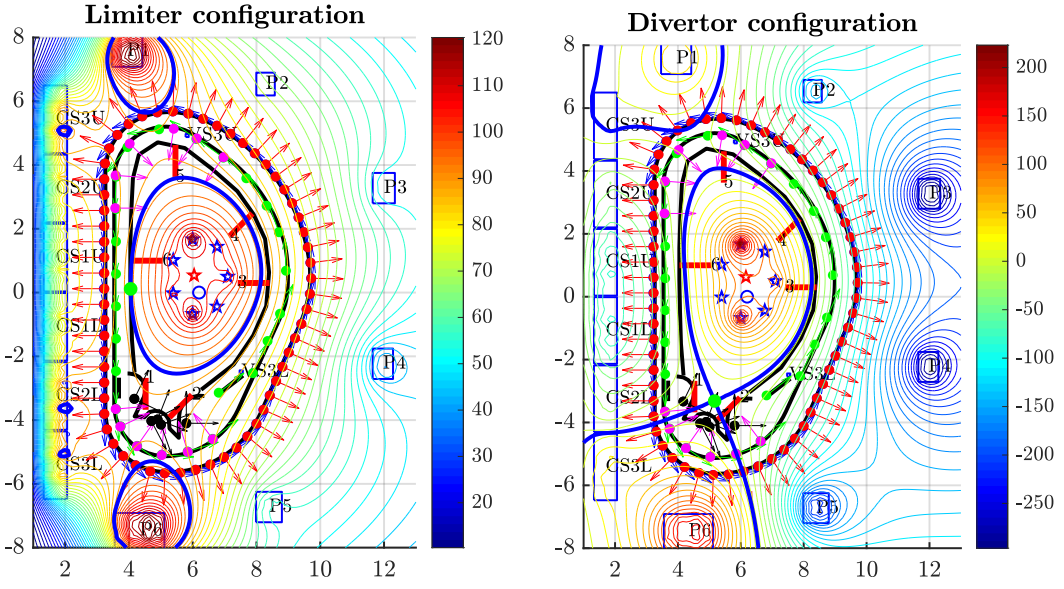

Figure 1.3: Results of a simulation on a poloidal section of ITER. Evidenced for the two configurations are the magnetic flux lines, as well as the Last Closed Flux Surface in blue.

What does it take to have a self-sustaining reactor? An estimate can be made through the Lawson criterion, in which a simple zero-dimensional power balance is carried between power intake of the reactor and various losses from plasma, it can be shown that in order to obtain a self-sustaining reaction, some key parameters such as

the particle density n, the average confinement time τ_E and the plasma temperature T can be combined to form a parameter called *triple product* $n\tau_E T$, that needs to be higher than a given threshold. This value must be met by the tokamak specifics to be able to reach the so-called *break-even* condition, in which the power generated by the fusion reaction is equal to the power lost and the auxiliary heating used to maintain optimal fusion conditions. In particular the most desired type of power balance, called *ignition*, and defined as the condition in which the heating of the plasma due to the fusion reaction itself is sufficient to cover the other power losses without the need of auxiliary heating can be obtained if the triple product verifies the condition:

$$n\tau_E T \ \geq 5 \times 10^{21} [\mathrm{m}^{-3}\,\mathrm{keV\ s}] \tag{1.17}$$

As plasma confinement technologies progress, it is possible to reach longer confinement time scales, and consequently increasing density and temperature; in over fifty years the steps made in that sense have been giant leaps towards the objective of reactor-like and ignition power gain, as can be seen in figure 1.4. The next important step in this path (and red dot in the figure) will be the reaching of the break-even condition in the largest international scientific effort in the field of thermonuclear fusion, ITER.

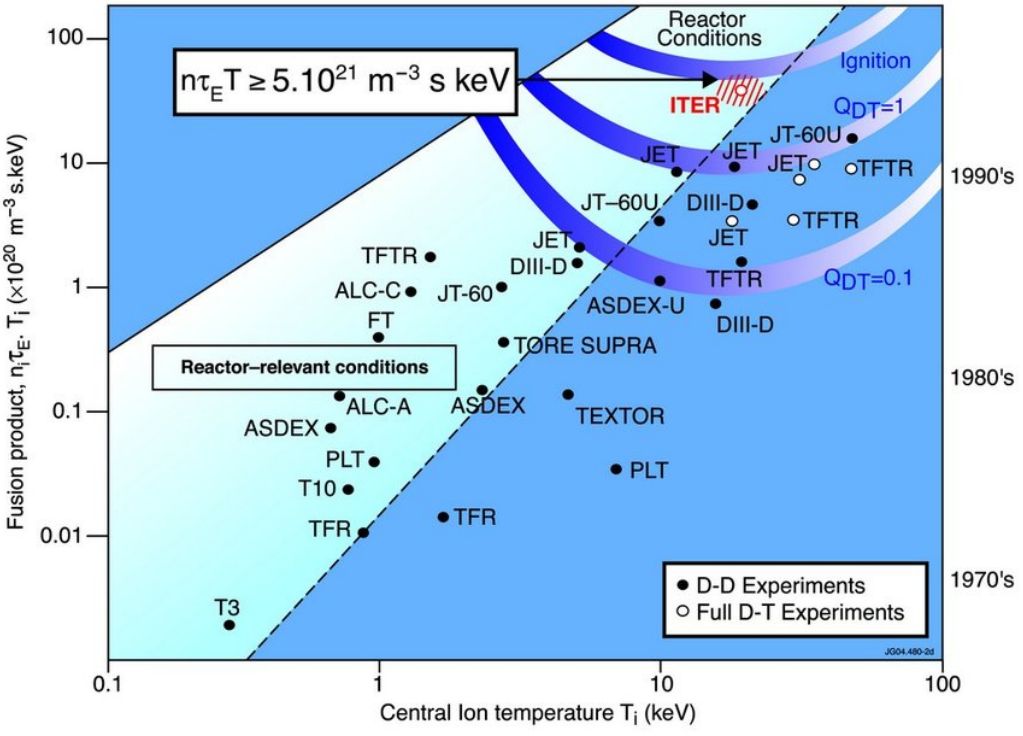

Figure 1.4: History of experimental tokamaks' triple products, reported as a function of the core temperature. It can be seen how the Lawson curves present a minimum at around $T \approx 15$ keV. [Courtesy of EUROfusion]

1.6 ITER

The International Thermonuclear Experimental Reactor (ITER) is the focus of all of the international scientific community effort revolving around nuclear fusion, involving the European Union, United States, China, India, Japan, South Korea, Russia, etc. for a total of 35 countries that are working together towards the realization of the world's largest experiment on fusion. The building site of the experimental reactor has been chosen to be Cadarache, in France, with the assembly phase planned to end with the first plasma milestone in 2025.
ITER has been designed to prove the feasibility of reactor-like power gain, with the objective to generate through fusion over 10 times the injected heating power used (defined as the gain factor Q), and maintain the fusion reaction for long periods of time. A glance to the main parameters of ITER can be found in table 1.1, and the cutaway in figure 1.5 shows the inherent inner complexity of such a machine.

ITER parameters	**Value**
Power by fusion [MW]	500
Gain factor Q	≥ 10
Pulse duration [s]	3600
Plasma type	D−T
Maximum plasma radius [m]	6.2
Minimum plasma radius [m]	2.0
Plasma current [MA]	15
Toroidal magnetic field [T]	5.3
Auxiliary heating:	
- Neutral Injectors [MW]	33
- RF Antennas [MW]	40
Plasma volume [m^3]	830
Device height [m]	26
Device diameter [m]	29

Table 1.1: ITER experimental reactor main properties [2].

With its considerable size (about ten times the plasma volume of the largest device in operation) and overall power, diagnostic availability and operating range, ITER will also permit the investigation of an array of new physical regimes and technological issues that up to now were impossible to explore, due the reduced dimensions: for the first time, there will be tests on the production of tritium directly during the discharge through in-vessel breeding blankets, as well as important data

on the divertor component. These finds will be key in developing the next step of the research towards the demonstration of the technological and economic feasibility of a nuclear fusion power plant, what is known as the DEMO project.

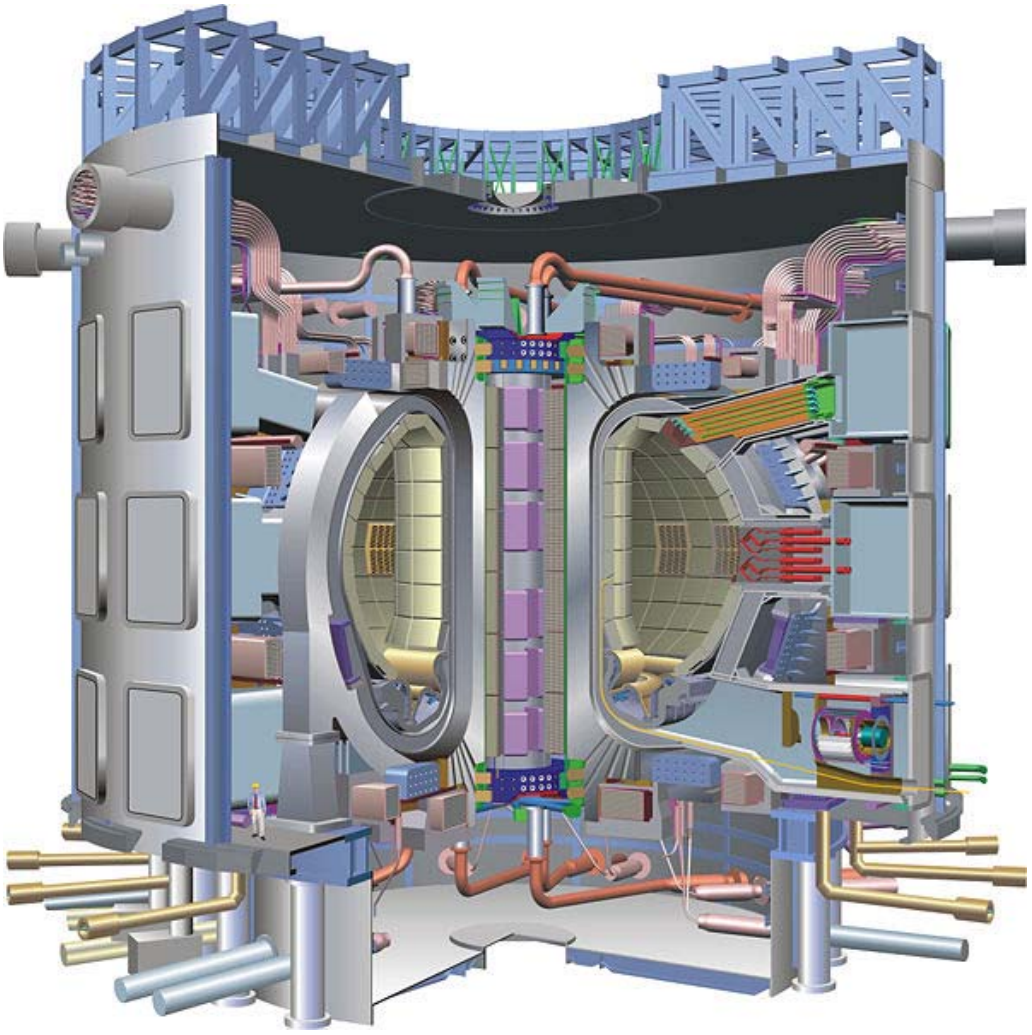

Figure 1.5: 3D cutaway of ITER configuration. The size can be perceived by the human figure in the picture [Courtesy of ITER].

Chapter 2

Neutral beam heating overview

SUMMARY - Neutral beam heating is considered nowadays the most important method to supply additional power in many fusion experiments around the world. The concept is straightforward: neutral atoms penetrate through the confining magnetic field and are ionized in the plasma via Coulomb collisions with electron and ions. The fast ions generated in this way are then confined by the magnetic field as well. If their kinetic energy is large compared with the plasma temperature, they deliver their energy to ions and electrons by collisions, heating up the plasma. Fast neutral atom beams are generated via charge exchange neutralization of ion beams. This chapter sums up the physical basis of generation and neutralization of an ion beam.

2.1 Introduction

Neutral Beam Heating relies on the concept of accelerating, neutralizing and injecting high energy neutral particles within a magnetically confined thermal plasma:

- First, ions are generated within a plasma in an Ion Source.
- The desired particles can then be accelerated through electrostatic means to the desired energy through an Accelerator.
- The charged fast beam passes through a Neutralizer, evolving the majority of the beam into fast neutrals.
- The non-neutral by-products are deflected through electrostatic means onto a dedicated device, the Residual Ion Dump (RID), isolating the neutral beam.
- This neutral beam can either be dumped in a Calorimeter to measure its power, or directed towards the tokamak: the beam can penetrate the magnetic field, following straight lines until being ionized by the thermal plasma. Then, through to Coulomb collisions, the energy is transferred to the bulk.

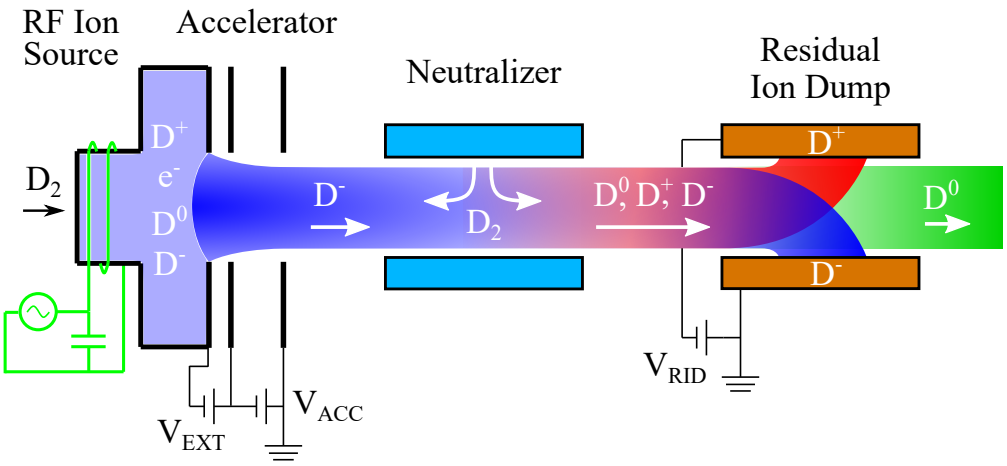

Figure 2.1: Simple schematic detailing the NBI principle. V_{EXT} and V_{ACC} are the extraction and acceleration voltages of the accelerator, while V_{RID} is the deflection potential of the Residual Ion Dump.

A schematic of the process is presented in Figure 2.1. Every part will be explained within their own section.

The first proof of principle experiments took place in the early 1970s at the Princeton Large Torus (PLT), where an NBI discharge managed successfully increase the ion temperature of the plasma from 1 to 4 keV [4], all the way to the first demonstration of a net-current-free stellarator plasma at Wendelstein 7-A in 1980, setting the basis for the extensive future stellarator research programme; NBI were also the key instrument in one of the biggest discoveries in magnetic plasma confinement, the H-mode (high-confinement mode), at the ASDEX tokamak in 1982 [5], which became the baseline discharge scenario that will be used in ITER.

All in all, NBIs are deeply intertwined with the history of fusion research; as a heating system they can achieve different objectives:

- Deep and localized core plasma heating, due to its ability to penetrate the magnetic confinement within a specific interaction zone.
- Possibility of heating both electrons and ions due to Coulomb collisions.
- Current Drive and Momentum injection, to help with plasma confinement.
- Key to H-mode access.
- Low-power beams can be used as diagnostic beams, able to obtain data from the core plasma and study particle transport.

For these reasons, NBI heating represents a dominant part in most of the larger tokamaks of the past, present, and planned, as reported in Table 2.1. This chapter

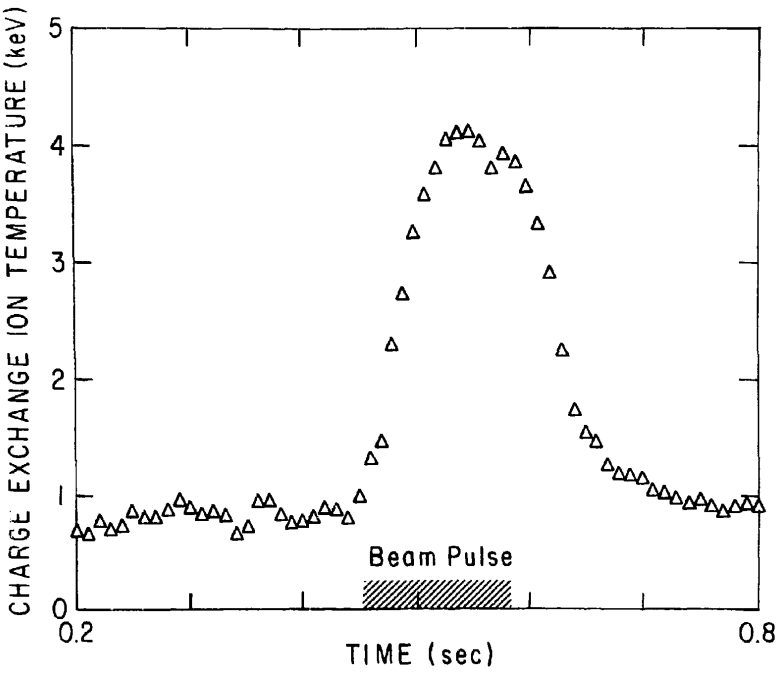

Figure 2.2: Charge-exchange ion temperature as a function of time during the discharge. A peak ion temperature of 4 keV is attained during injection of 1.6 MW of H^0 into a D^+ plasma [4].

will not focus on the physics of the interactions of a fast beam with a hot magnetized plasma, which is a completely separate matter and not strictly on topic of the thesis. Instead the engineering of the NBI in its different parts and principles will be presented, to have an idea of the inner workings of the system.

2.1.1 Positive or Negative NBIs

Even before starting to discuss the different components of an NBI, a question must be answered: what type of particle should be injected? As for the species that should be used, it stands to reason to accelerate the same species as the type of plasma present in the tokamak (e.g., a H^0 beam for an hydrogen plasma) as to not "pollute" the system and yield energy uniformly. But what about the charge with which the acceleration is applied, does it make a difference?
A measurement campaign at JT-60U [6] investigated the matter with either positive (H^+ or D^+) or negative (H^- or D^-) beams at different energies, and evidenced how the neutralization efficiency of a beam in gas (described later) would drop sharply to zero after about 50 keV amu^{-1} for positive beams, while remaining about constant at 60 % for negative beams (Figure 2.3). Since the energy of the beam is directly linked to its penetration depth in a plasma, and tokamaks are constantly increasing in size to enhance their reactor capability, negative NBIs (NNBI) are the necessary choice

	R_0	a	I_p	B_t	Installed heating power [MW]				
	[m]	[m]	[MA]	[T]	P-NBI	N-NBI	ECRH	ICRH	LH
ITER	6.2	2.0	15	5.3	-	50	20	20	-
JET	2.96	1.25	4.8	3.45	34	-	-	10	7
JT-60SA	2.97	1.17	5	2.25	24	10	7	-	-
TFTR	2.4	0.8	2.2	5	40	-	-	11	-
DTT	2.19	0.70	5.5	6	-	10	33	8	-
KSTAR	1.8	0.5	2.0	3.5	11.5	-	1	-	-
EAST	1.7	0.4	1.0	3.5	8	-	4	3	4
DIII-D	1.67	0.67	2.0	2.1	20	-	5	4	-
ASDEX-UG	1.65	0.5	1.2	3.1	20	-	8	8	-

Table 2.1: Collection of main parameters and H&CD power mix for some of the most important past, present and future tokamaks (as of 2022).

to make. This aspect would be fine, if not for the fact that negative ion sources and systems are extremely more complex to model, build and operate with respect to their positive counterparts; some of these issues will be discussed later.

2.2 The Accelerator

To start the discussion, it is better to first illustrate the main mechanism of NBI operation: the beam extraction and acceleration. A particle beam can be extracted from an emitter by applying a potential between the emitter and a second plate electrode, in a diode configuration. Let us consider the ideal case, consisting of:

- Infinite extension in y and z;
- A zero potential emitter and a collector plate at $x = a$ and at potential V_a;
- No initial particle velocity;
- Infinite charge availability;
- Only a single species of particle interested.

In this configuration, before the extraction, the potential plot would be of a single line from 0 to V_a, as in a normal DC capacitor; however, after the release of the charged particles with a current density J, their own space charge causes the potential curve to flatten near the emitter. If the current density is increased, the first derivative V' of the potential in x (proportional to the electric field E) will eventually reach

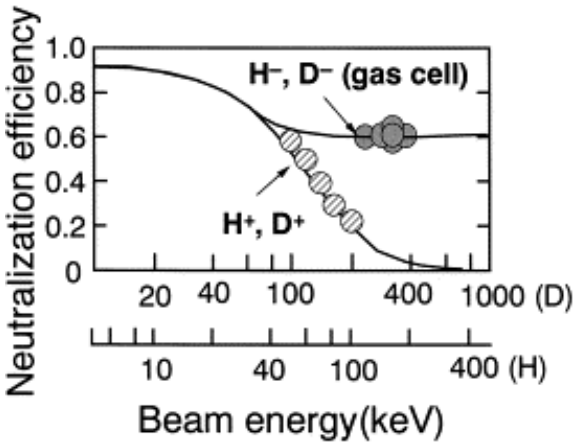

Figure 2.3: Measured neutralization efficiency as a function of the beam energy in the 1998 JT-60U campaign [6].

0: after this point, no additional current can be extracted for this combination of potential and geometry.
By using the hypotheses to solve the Poisson equation near the emitter, and imposing $V'(0) = 0$, the Child-Langmuir equation is obtained:

$$J_s = \frac{4\epsilon_0}{9} \cdot \sqrt{\frac{2eZ}{m}} \cdot \frac{V^{\frac{3}{2}}}{a^2} \ , \tag{2.1}$$

where J_s is the maximum current density that can be extracted, ϵ_0 is the vacuum permittivity, e is the elementary charge and Z is the ion charge state. By multiplying J_s by the aperture area, the current I_s is obtained.

The formula can be modified for different extraction geometries, but it always stays as a proportionality law between the current and the three-halves power of the potential, where the constant of proportionality is called *perveance* P of the extraction system.

$$P = \frac{I_s}{V^{\frac{3}{2}}} \ \left[\mathrm{A\ V^{-\frac{3}{2}}}\right] \tag{2.2}$$

The perveance contains within all information of the extraction setup: it can be shown that different systems with the same perveance produce the same beam shape. Realistic particles however usually start from a curved boundary that comes to form between the plasma and the acceleration regions, the *meniscus*, individuated by the boundary at which particles begin to feel the acceleration. This shape can be approximated by a spherical surface, resulting in the Langmuir-Blodgett perveance correction formula [7]:

$$P_D = \sqrt{\frac{eZ}{m}} \cdot \frac{5.5 \times 10^{-8}}{d^2} \left(1 - 1.6\frac{d}{R}\right) \ \left[\mathrm{A\ V^{-\frac{3}{2}}\ cm^{-2}}\right], \tag{2.3}$$

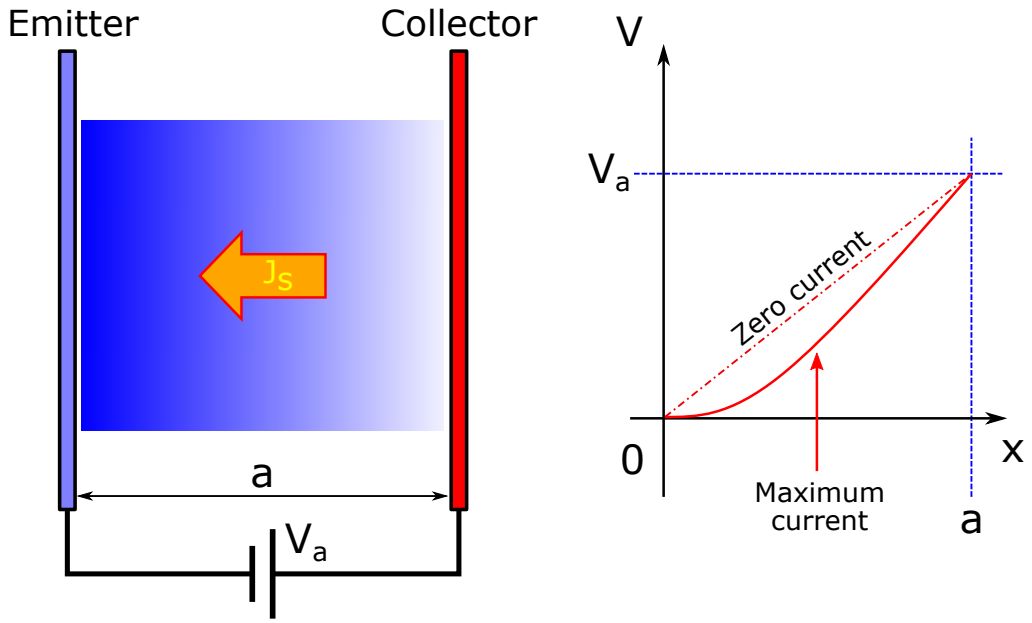

Figure 2.4: Schematic representing the setup for the Child-Langmuir law.

where P_D is the perveance per area unit, d is the distance between the two electrodes, and R is the curvature radius of the meniscus. From these two formulas, it is possible to understand that to extract a large current density, d should be small, with a high applied V.
An experimental study at UKAEA in 1973 [8] confirmed that by sweeping the so-called aspect ratio, defined as ratio between the chosen aperture radius r and the electrode distance d, the best optical performance and highest currents extracted were obtained for $r/d < 0.5$ (Figure 2.5). This adds insight to the ideal extractor design, which should minimize d, but also the aperture radius as well: to obtain large currents, a multi-aperture array is necessary.

Experimental spectroscopy and calorimetry on beams suggest a simple way to describe the shape with which beamlets propagate, by fitting the power profile with two Gaussian curves:

- The core component is the most focused part, characterized by a small *divergence* θ_{RMS}.
- The halo component contains ill-focused particles, characterized by a large θ_{RMS}.

To better understand and characterize different accelerators, the definitions of *deflection* and *divergence* are given.
The average deflection of a beamlet is defined as the mathematical average of the

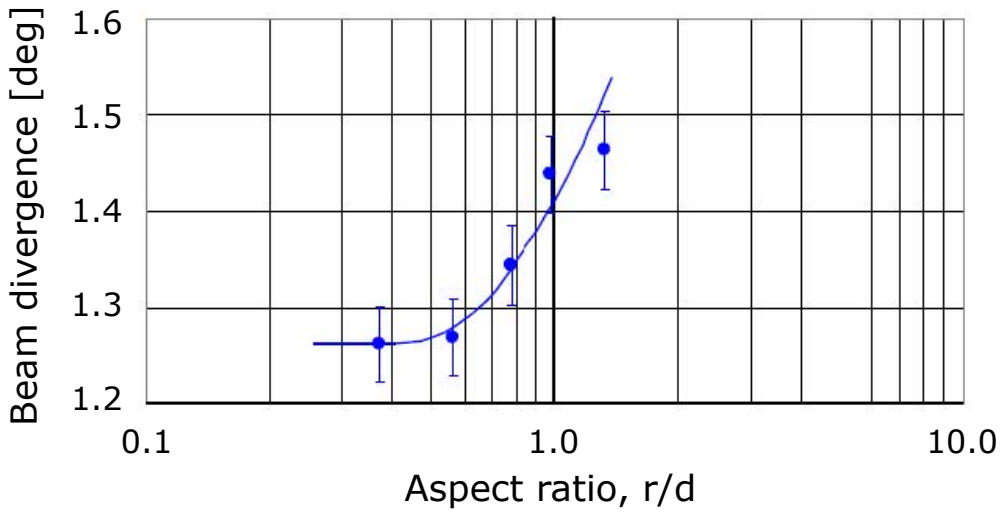

Figure 2.5: Sweep of the aspect ratio and relative minimum beam divergence for a test beamlet [8].

ratio of one of the two transverse velocity components and the main axial velocity component between all of the particles of a beamlet; its value is a measure of the beam direction. Its value is measured in millirad (mrad), and for an accelerator oriented along the x axis, in case of a beamlet containing N test particles, the average deflection can be calculated as

$$\theta_{y\,(z)} = \frac{1}{N}\sum_{k=1}^{N}\frac{v_{y,k\,(z,k)}}{v_{x,k}}. \tag{2.4}$$

The divergence is defined as the RMS value of the ratio of the total transverse velocity component and the main axial velocity component (with respect to the beam center in the phase space) between all of the particles of a beamlet (i.e., the width of the respective Gaussian) and represents the rate at which the beamlet is expanding in size. Its value is measured in mrad, and calculated as

$$\theta_{RMS} = \sqrt{\frac{1}{N}\sum_{k=1}^{N}\left(\frac{v_{y,k}}{v_{x,k}} - \theta_y\right)^2 + \left(\frac{v_{z,k}}{v_{x,k}} - \theta_z\right)^2}. \tag{2.5}$$

These definitions are very important, as they often represent the figure of merit of an accelerator.

As for the formulas, real setups however hardly match the idealized conditions of the Child-Langmuir law:

- Particles are not infinitely available from the ion source.
- Particles near the extraction apertures are in thermal equilibrium (hence possessing with their own non-zero velocity).

- The plasma edge possesses its own potential gradient (the sheath), which should be accounted for.

All of these reasons (and many others) set us apart from the predictions, moving from a space-charge limited regime toward a current limited regime, where even if the extraction potential is increased the current no longer increases: reducing this effect by increasing the available particles as much as possible by optimizing the ion source is one of the challenges of neutral beam injection.
After the delicate process of extraction, the acceleration to the desired energy is next.

2.2.1 Accelerator design

Particle accelerator science has a more than two centuries long history, from the first electron guns in vacuum tubes in the 19th century, all the way to the Large Hadron Collider at CERN, that with its 6.8 TeV beam stands at the frontier of knowledge. Its use in the fusion field though focuses less on the extremely fast, and more on the extremely powerful, aiming to deliver both velocity and quantity (equivalent to "potential" and "current") in the MW range.

Extensive experimental research and different successful campaigns onboard tokamaks have gradually perfected the design towards the adoption of Multi-aperture, Multi-Grid (MaMuG) type accelerators, where the acceleration potentials are subdivided between intermediate grids, improving the beam directivity and quality. Each one of these intermediate grids has evolved in time a particular shape, that will be described in the following subsections.

2.2.1.1 Plasma Grid

The Plasma Grid (PG) is the most peculiar of the different grids:

- It serves as a separator between the ion source and the accelerator region.
- The extraction apertures are housed within.
- The plasma side is extremely important for the generation of negative ions through *surface production* which requires a special coating and a strictly controlled temperature through the cooling system; more details in this are reported in the Ion Source chapter.
- In some accelerators, a large current runs through the PG to generate an useful magnetic field within the source, improving the negative ion generation; more details in this are reported in the Ion Source chapter.

The shape of the grid on the ion source side has a conical shape with an angle of around 45°, repeated for each aperture: this is supposed to improve drastically the chance of surface-generated negative ions to be extracted, rather than being

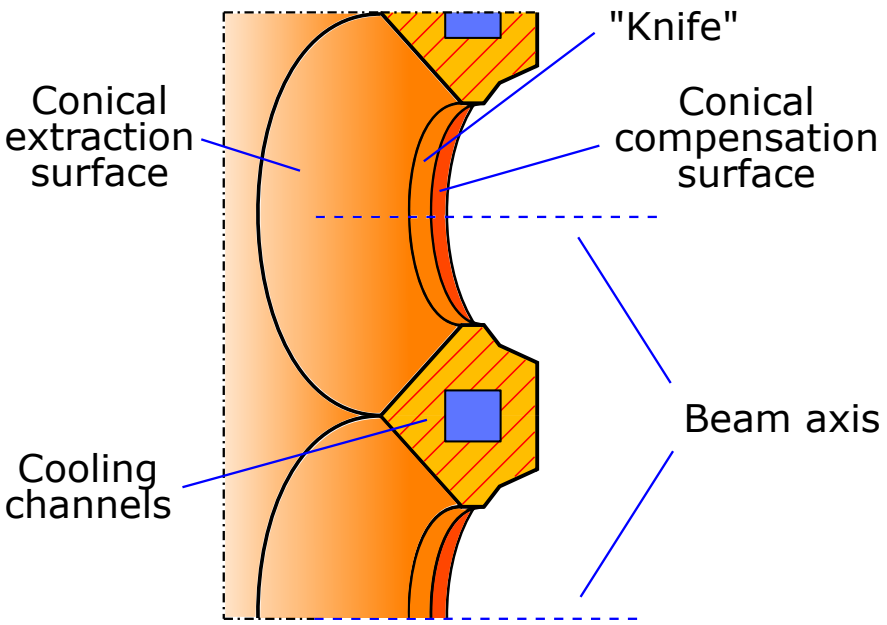

Figure 2.6: Typical PG profile used in most NNBIs.

simply emitted back towards the plasma with a flat surface. More details on surface production will be reported on Section 2.3.3.2. On the accelerator side, a similar conical shape is adopted but for a different reason: with the beam formed, even by supposing that all particles start parallel to each other, the same-charge repulsion would very quickly defocus the beam. Intuitively, it is possible to "bend" the electrode to provide an inward field component that compensates the inner repulsion of the newly-formed beam: J. R. Pierce in 1940 found an exact solution to this problem for planar symmetry in idealized conditions [9], with possible generalizations to cylindrical and spherical geometries. Realistic applications however are a little more nuanced, with designs refined to work on a variety of scenarios. A typical PG profile is presented in Figure 2.6.

2.2.1.2 Extraction Grid

The Extraction Grid (EG) has a determinant role:

- As the name implies, it is the second electrode in a Child-Langmuir diode; its voltage and distance from the PG determines current extracted and optics of each beamlet.
- The beam in its proximity is still fairly slow; this means that the EG is the best place to implement *beam steering techniques*, since the particles can be affected by the electrostatic field for longer. More details will be given in the Beam Aiming section.

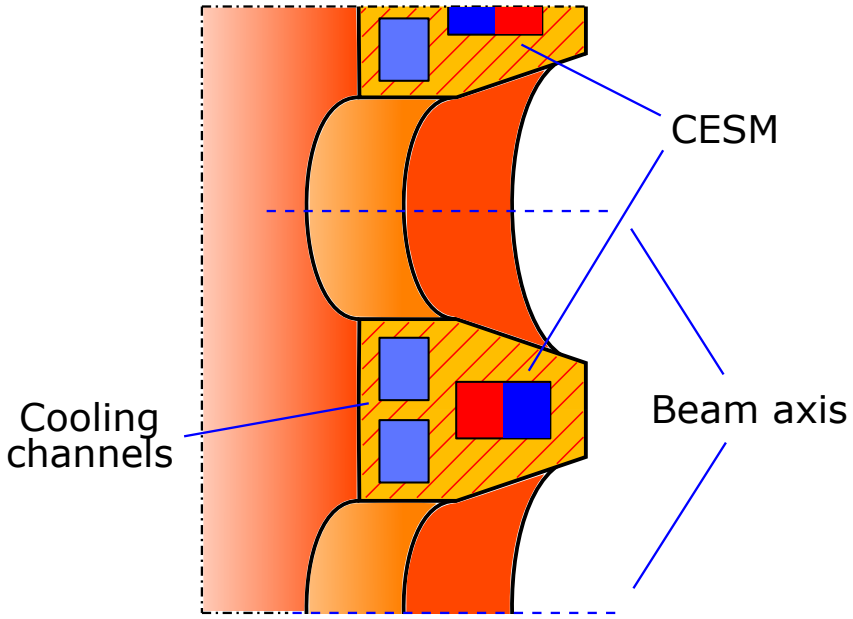

Figure 2.7: Typical EG profile used in most NNBIs.

- The slower beam also means that when crossing the grid, the space-charge repulsion is more visible; a conical shape is then usually adopted for the EG, to increase clearance.
- The extraction process does not unequivocally extracts negative ions, but electrons as well (*co-extracted electrons*), with well-conditioned sources yielding ideally a ratio of electrons per negative ion of less than 1. These electrons must be stopped as soon as possible, and the EG serves this purpose by hosting a series of Co-extracted Electrons Suppression Magnets (CESM) in alternating directions, that deflect the unwanted electrons upon the grid itself. This however causes undesired alternated deflection of the ion beam as well (the Criss-Cross Deflection Effect, or CCDE).

The face closer to the PG is flat, at the desired extraction distance with a simple cylindrical aperture, then gradually tapering to a larger diameter when reaching the other side. Since the grid is subjected to direct electron load due to CESM action, the cooling system within the grid must be carefully designed to be as effective as possible while leaving enough space for magnets. A typical EG profile is presented in Figure 2.7.

2.2.1.3 Acceleration Grid

The Acceleration Grid (AGs) has usually multiple copies of itself, subdividing the desired potential jump into more manageable steps; the separation also helps with

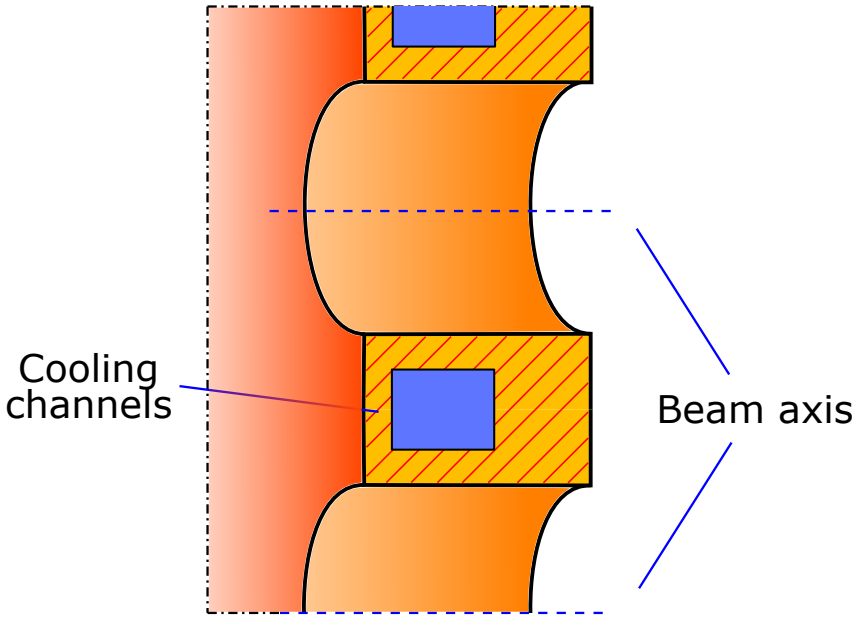

Figure 2.8: Typical AG profile used in most NNBIs.

beam optics, since beamlets are "tethered" in their direction by the aperture arrays, that otherwise would be affected more by mutual repulsion. The last AG is called Grounded Grid (GG), being at ground potential. They have the simple design of a cylindrical aperture array, since the only objective with these grids is acceleration without optical distortion. These grids are also the ones that are mostly heated by poorly-focused particles, formed neutrals, and electrons: enhanced cooling must be enforced to avoid failure. A typical AG profile is presented in Figure 2.8.

2.2.1.4 Beam losses

Within the delicate accelerator system, there are multiple sources of losses that worsen the extraction efficiency, cause additional heat loads, or worsen the quality of the beam; the most important ones are:

- Stripping losses: due to the presence of background neutral gas within the accelerator flowing in from the ion source and the NBI vacuum vessel and the low electron detachment energy for negative ions, it is highly probable that collision reactions may prematurely neutralize or even ionize the particles, reducing the available extracted current. The formed neutrals and electrons have poorly focused trajectories, leading to significant heating of the accelerator; in the case of the positive ions, they are accelerated backwards toward the ion source, with a very small footprint and high heat flux (the *back-streaming ions*). The most important reactions for a H^- (or D^-) beam are listed in Table 2.2.

- Core and Halo components: while in ideal conditions the halo component would disappear, real ion sources always feature a part of beam impinging on the grids. Efforts in determining what and how exactly the halo is forming are ongoing; possible explanations are high-divergence extraction of ions from the PG apertures, plasma dis-uniformities, and out-of-source ion formation.
- External fields: the accelerator is subjected to a number of external fields, namely the CESM magnets, the PG filter field, and the tokamak poloidal stray field. Each one affects the direction of flight of the beamlets and can lead to impingement if not accounted for.

Formula	Reaction
$\underline{H}^- + H_2 \longrightarrow \underline{H} + H_2 + e$	Single stripping
$\underline{H}^- + H_2 \longrightarrow \underline{H}^+ + H_2 + 2\,e$	Double stripping
$\underline{H} + H_2 \longrightarrow \underline{H}^+ + H_2 + e$	Ionization
$\underline{H}^- + H \longrightarrow \underline{H} + H + e$	Atomic stripping

Table 2.2: List of the main beam–gas collision reactions. The underlined species belong to the beam.

2.2.2 Beam aiming

Similarly to children of loving parents, extracted beamlets need guidance: they need directions to reach their dream career (reaching safely the tokamak) and they need protection against bad influence of their peers (beam-to-beam repulsion); to help them, the parents have their methods (beam-steering devices) to apply where they have the biggest effect.
The next paragraphs contain informations about the most common techniques used in accelerators.

2.2.2.1 Aiming strategy

In high-performing fusion accelerators, beamlets proceeding perfectly parallel towards a tokamak are not a good idea: the tokamak blanket is one of the most important components in a reactor setup, and large side apertures to let the beam inside would disrupt the configuration, as well as letting dangerous neutron radiation in the NBI. To minimize the size of the beam at the exit of the connecting duct, aiming strategies are enforced on the beamlets to focus in a desired point by deciding in what direction to aim each beamlet aperture.
Logic would dictate to simply connect each beamlet from the chosen aperture array to the focus point in the tokamak, obtaining a triangular beam with a constantly

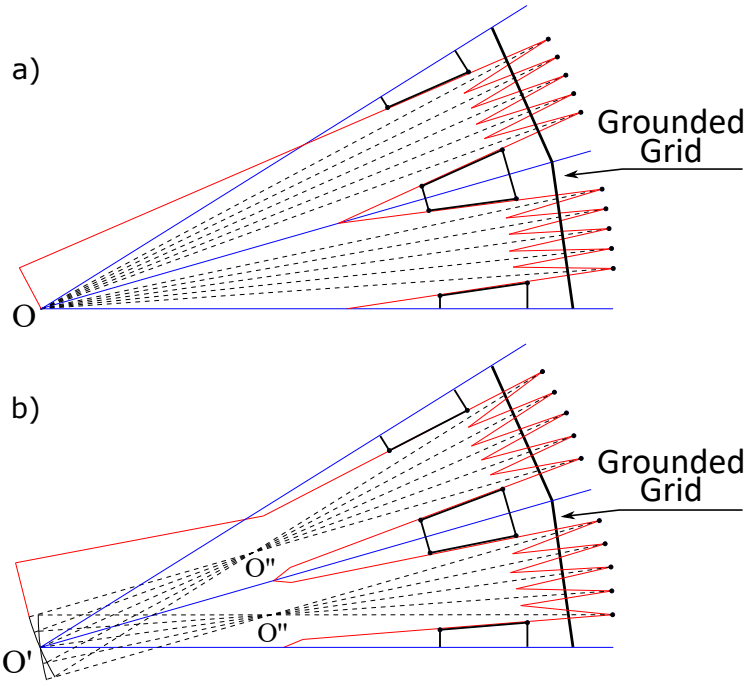

Figure 2.9: Scheme detailing a horizontal section of the a) common focus and b) multi-focus aiming strategies.

decreasing cross-section. This is what is called *common-focus* aiming strategy, and has the advantage of minimizing the port needed for the beam to enter the tokamak. This is not the only possible solution: a *multi-focus* approach is also available, implemented in the ITER NBI beamline design:

- In the horizontal (z axis) direction, each aiming plane has its main axis aligned to the main focal point, while each beamlet of the respective group is aimed at about halfway along the main axis.

- In the vertical (y axis) direction, all aiming planes and beamlets are aimed at the main focal point.

This approach has the advantage of considerably reducing the horizontal beam cross-section near critical Beam Line Components (BLCs) that would otherwise be more exposed to direct beam interception and higher heat loads (illustrated in Figure 2.9). in addition to this there is the fact that the first of the BLCs would suffer from the first impact of the beam halo component: an early focusing can help distribute these heat loads over a larger surface. A potential drawback of the closer focusing is that steering devices need to be even more effective in their action; these are discussed in the next paragraph and in the chapter about the optimization of DTT.

2.2.2.2 Beam steering

Beam steering involves placing along the accelerator some "aiming devices" in order to achieve the desired aiming strategy or correcting undesired effects (such as the CCDE) with the least amount of additional components as possible.
These devices are either electrostatic or magnetic in nature; some examples are:

- Steering Grids (SG): a thinner grid juxtaposed to the main one, but with its own aperture slightly offset in the intended steering direction; effective for small corrections with almost no impact on beam shape.
- Folded Grids: the ideal method to guide a charged beam is to provide an electric field directed in exactly the intended trajectory, hence the possibility to "fold" flat grids to follow the aiming strategy; this method is obviously more complex to manufacture with respect to flat grids.
- ADCMs: Alternate Deflection Compensation Magnets are a proposed way to mitigate the CCDE problem on accelerators. They are used in combination with CESM magnets, and are orientated as to strengthen the deflecting field on the source side, while weakening it on the other; choosing the right size can nullify the deflection effect, with only a slight beam offset remaining.

These methods are illustrated in Figure 2.10. The list is by no means exhaustive, as many fine-tuning tweaks can be done by manipulating the shape of the electrostatic field.

2.2.2.3 Beam repulsion

The beam repulsion is the logical result of trying to force same-charged beamlets close to each other. The total effect on a beam is the combination of the repulsive electrostatic component and the attractive magnetic effect of same-direction currents, with the final result of a widening beam, wider and wider when closer to the outer envelope.
To compensate this effect, a particular device is indicated: the electrostatic kerb. They consists of small, metallic stripes placed near the outer apertures with the intent of locally deforming the electrostatic field and creating an asymmetry (Figure 2.11). They have a strong deflection effect on the nearest beamlets, but can also significatively deform the beam envelope, so they should be used sparingly. They work best in the low-energy zone, near the EG, in combination with other aiming devices.

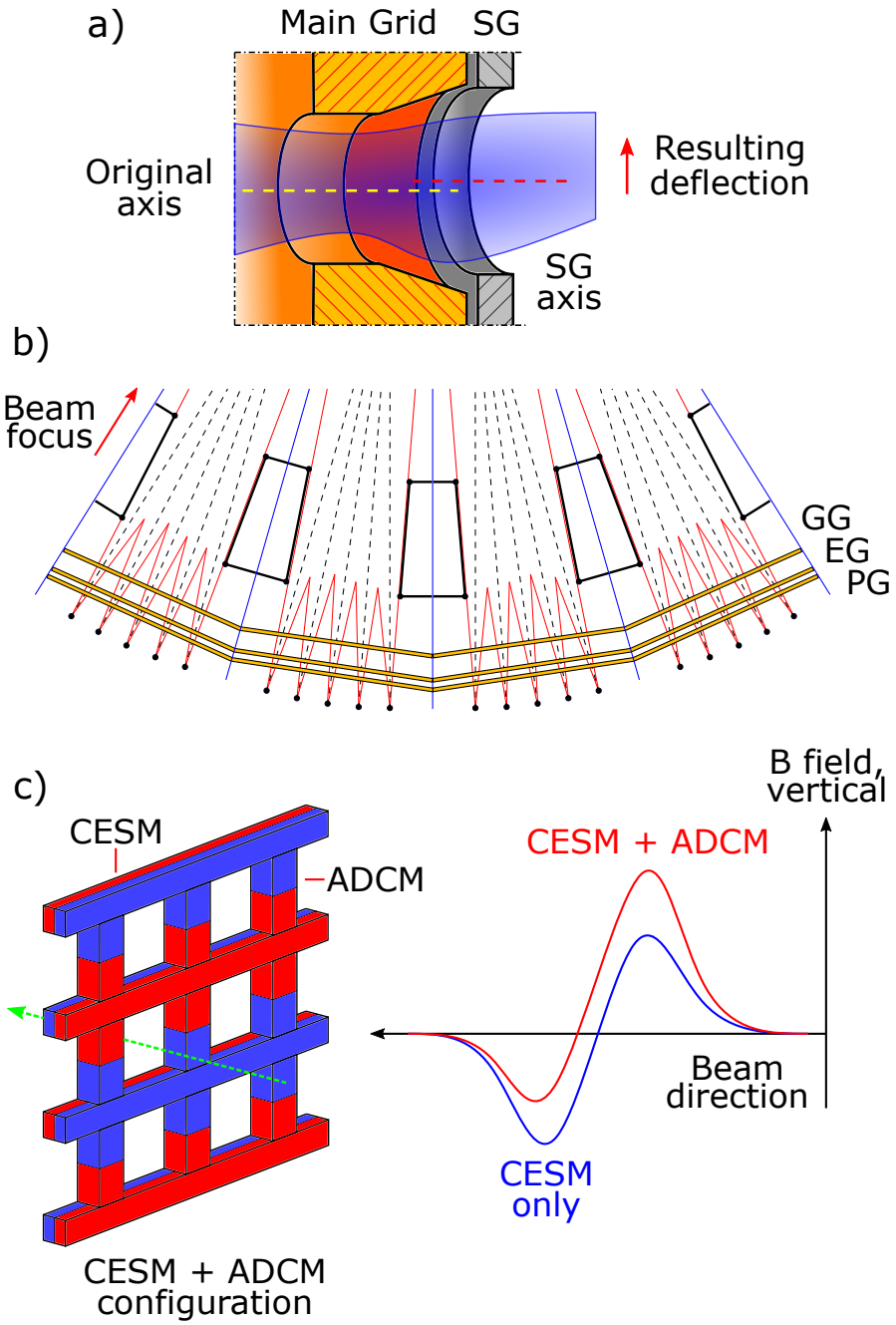

Figure 2.10: Sketches of the described beam steering devices: a) Steering Grid principle; b) Folded grids converging on a single focus point; c) CESM and ADCM combination, with a plot of the resulting vertical magnetic field.

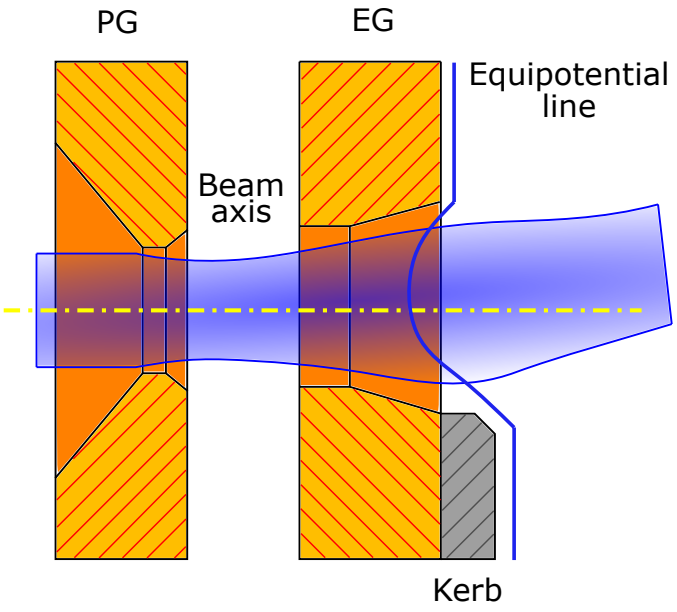

Figure 2.11: Scheme of the concept behind the electrostatic kerb.

2.3 The Ion Source

The negative Ion Source is such a complex system that multiple experiments have been set up with the single objective of investigating and maximizing performance of this component.
Plasma-based ion sources are based on a controlled leakage of particles from the source (the extraction process), and an adequate mechanism to heat plasma electrons. Confined laboratory plasma has a number of basic properties that are useful to remember:

- Quasi-neutrality: in stationary conditions, the sum of all plasma-to-wall currents (diffusion current) and extracted (or injected) currents is zero (no accumulation of charge is present).
- Plasma voltage: in typical cases, diffusion of electrons to walls is faster than ions due to mass difference; as a consequence the source plasma develops a small positive voltage Φ_p with respect to the wall, that is proportional to the electron temperature T_e.
- Plasma sheath: most of the voltage drop is contained within a region called the plasma sheath, around 10 Debye lengths long (λ_D) from the walls. The remaining potential (which is proportional to the ion generation rate) favours transport of ions to the sheath.

What follows is a brief description of the principal concepts behind ion generation from plasma.

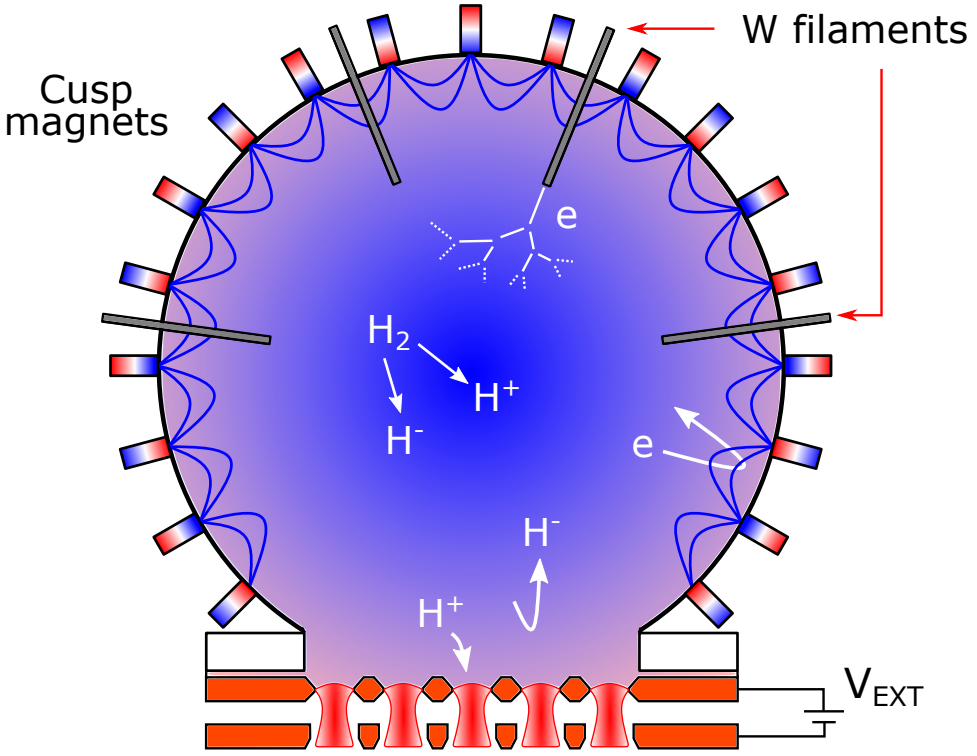

Figure 2.12: Simplified schematic of a positive arc-driven ion source.

2.3.1 Arc-driven sources

Arc-driven ion sources were the first to be developed and applied to early positive NBI, since they are based on the well-understood mechanism of thermionic emission combined with a "magnetic bucket" type of confinement to limit the plasma wall losses. They still have a large use in most large NBIs (such as JT-60 NBIs) due to their proven track record in ion generation.
In these sources, a tungsten filament at the edge of the vessel emits fast electrons that ionize the neutral gas injected by a dedicated line. These charged particles are accelerated by the electric field between filaments and the source walls, generating plasma through electronic avalanche; the final achievable plasma density is directly correlated to the power flowing through the filament, P_{arc}. The walls of the plasma chamber are covered in magnets in cusp configuration, deviating drifting charged particles back into the plasma and helping in maintaining the density as high as possible. A schematic of a typical arc source is presented in Figure 2.12. The downside to this type of sources is that the filaments eventually erode and break in an unpredictable manner, forcing shutdowns and maintenance.

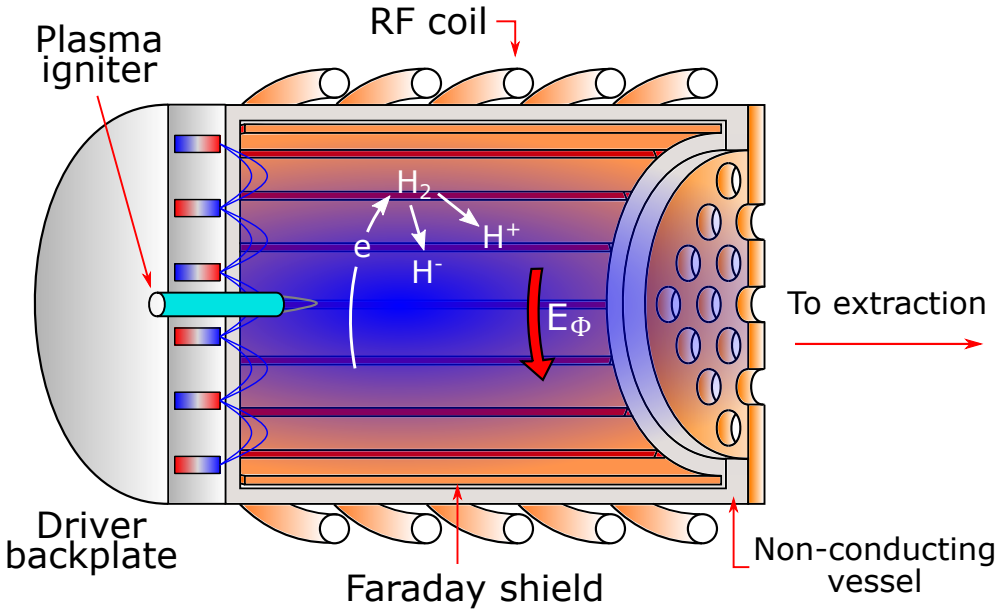

Figure 2.13: Simplified schematic of an ICP source.

2.3.2 Inductively-coupled sources

Inductively-coupled plasma (ICP) sources use Radio-Frequency (RF) coils near the plasma to transmit energy through electromagnetic waves to the free charges within. The main vessel is made of inert material (such as quartz or alumina), with an inner copper Faraday shield to protect the vessel from sputtering, and a cusp-covered backplate to limit plasma losses. The RF coil covers the cylindrical driver, the region where the plasma is heated, ensuring a close coupling between coil and plasma (similar to the primary and secondary windings of a transformer). The Faraday shield has multiple longitudinal mutually-covering slits so that eddy currents may be prevented, while being opaque to particles.
In this configuration, the coil produces a time-varying azimuthal electric field component (typical frequency of 1 MHz), stronger at the edges. The plasma, after being primed by an ignition filament, starts responding to the external field accelerating the particles and generating its own exclusion field, limiting the external effect to the penetration depth δ. The fast particles ionize the neutral injected gas, creating the desired ions.
The clear advantage with respect to arc-driven sources is the lack of eroding filaments, making the system more reliable. They are however more complex to operate, requiring RF power supplies and load matching systems to maximize power absorption. A schematic of an ICP driver is presented in Figure 2.13.

2.3.3 Negative ion generation

When trying to apply these concepts towards negative ion production, it was noticed that the resulting population of negative ions was far too low, mostly due to the low binding energy of the additional electron. The attention moved towards studying the underlying mechanisms of ionization, and create sources able to magnify the negative ion population. A brief description of the important reactions and the resulting improvements made is reported in the next sections.

2.3.3.1 Volume generation

With volume generation is intended the system of reactions involving the ionization of neutral hydrogen (or deuterium) molecules, and taking place within the plasma itself. The most important reaction is the dissociative electron attachment:

$$H_2[v'' > 0] + e[\text{slow}] \longrightarrow H_2^- \longrightarrow H^- + H \tag{2.6}$$

This reaction is the most prominent for volume production, and is mostly due to slow electron collision with ro-vibrationally excited ($v'' > 0$) hydrogen molecules. The excitation of H_2 can happen through either wall interaction and *recombinative desorption* or due to impact of fast electrons generated by the plasma driver. This aspect however highlights an additional detail about the need for a slower electron population; in the specific case of negative ion sources, two plasmas separated by a magnetic filter are required:

- A warmer plasma region, where hydrogen molecules are partly dissociated or excited;
- A colder plasma region, where negative ions can be easily formed and survive long enough to be extracted.

This magnetic filter is achieved for larger sources by running a large current within the Plasma Grid and generating a transverse magnetic field of several mT: this field is strong enough to mirror back high-energy electrons, but allows ions and low-energy electrons to drift through.
A setup of this type has several advantages such ad reduced destruction of desired negative ions and reduced co-extraction of electrons at the apertures; but also introduces plasma dis-uniformities and drifts, due to $\mathbf{E} \times \mathbf{B}$ forces arising from field interactions; studies on mitigating this effect are still ongoing.

2.3.3.2 Surface generation

Surface generation is intended as the system of reactions that use a solid surface (in this case, the PG) as a catalyst substrate and electron donor. The process is based on the lowering of the work function W of the surface, which represents the

minimum binding energy for electrons in a solid; if the electron affinity E_a of the particle is higher than W, then the probability of electron capture is proportional to

$$p \propto \exp\left(\frac{E_a - W}{v_\perp}\right). \tag{2.7}$$

To lower W as much as possible, the PG plasma side has a special Mo coating, with Cs being accurately evaporated within the chamber. This is a very important reaction, requiring a very accurate control of surface temperature and evaporation parameters, since both neutral atoms and ions can be effectively converted in negative ions when coming into contact with the walls.
After generation, the negative ions are removed from the source by the plasma sheath potential, ensuring a constant flow. To help the extraction process, the plasma facing side of the Extraction Grid has a conical shape, so that emitted ions may be captured more easily by the sheath potential. Experiments with caesiated surface extraction also usually report that the largest part of the negative ions are produced by surface interaction, and also are characterized by a low fraction of co-extracted electrons ratio (less or equal to 1).
Problems with surface generation comes from the poor reproducibility of result, and the sheer number of parameters that need to be controlled in order to have a satisfying (sometimes unexpected) result, once referred to by a researcher on the field as "almost alchemy". Studies and experiments are still ongoing.

2.4 Drift region and Beam Line Components

After being successfully extracted and accelerated, the beam is free to travel the rest of the distance to the tokamak; however, being still a charged beam, it is susceptible to external factors and to itself. A brief description of what happens in the drift region and of the components placed along the beam trajectory is reported.

2.4.1 Beam propagation

One of the paragraphs in the Accelerator design sections was dedicated on how beams react to each other and how to correct it, but what happens when the accelerator is no longer present?
Studies in the '70s for applications of ion beams in space demonstrated that ion beams cannot propagate freely in a vacuum: particles are repelled by Coulomb interactions that would constantly widen the beam, until the beam is not recognizable any more. However, this is no longer true if the propagation medium is not a vacuum, but a low-density gas. As it travels, the beam collides with the background gas with the following reactions:

- $\underline{H}^{\pm} + H_2 \longrightarrow \underline{H}^{\pm} + e + H_2^{+}$, the ionization of background gas by a beam particle;
- $\underline{e} + H_2 \longrightarrow 2\,e + H_2^{+}$, the ionization of background gas by a fast electron;
- $\underline{H}^{-} + H_2 \longrightarrow \underline{H}^{0} + \underline{e} + H_2$, the stripping of a beam particle (only for negative beams).

The potential well generated by the travelling beam traps the produced secondary charges of the opposite sign, compensating the repulsion. This phenomenon is called Space-Charge Compensation (SCC, Figure 2.14) and it has been proven to be such a fast and strong effect for the correct background density that it allows the beam to travel virtually undisturbed for long distances.
The compensation effect in the positive and negative beam cases is slightly different: since the carriers of opposite charge in the positive case are electrons, they are smaller and faster, thus harder to trap within the potential well, leading to under-compensation of space-charge. On the other hand, with a negative beam, the charge carriers are H_2^{+}, heavier than the beam: positive charges tend to cluster more near the potential well due to inertia, leading to over-compensation.
When considering the simulation aspect, the presence of the SCC is extremely important: by assuming it taking place instantaneously and perfectly, it allows for simpler particle tracing simulations where the role of space-charge between particles can be safely ignored.

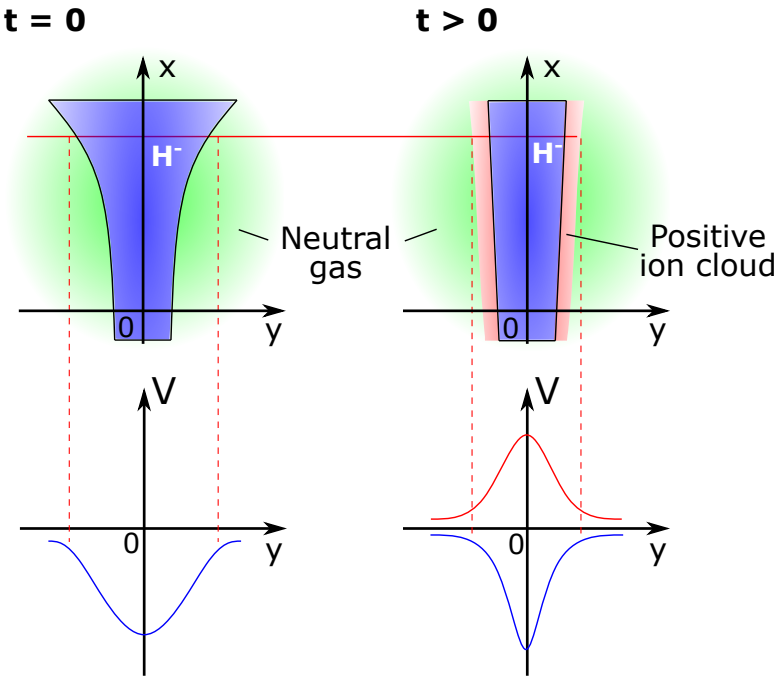

Figure 2.14: Scheme representing the principle behind SCC in the negative beam case.

2.4.2 Neutralizer

The Neutralizer is the first of the Beam Line Components, and absolves the role of the "N" in the NBI acronym. The beam enters the component placed at a small distance from the GG and undergoes a series of collision reactions with the background gas pumped within. The main, more significant reactions (equivalent for deuterium) are:

- The main neutralization reaction: $\underline{H}^- + H_2 \longrightarrow \underline{H} + e^- + H_2$;
- The re-ionization of neutral particles: $\underline{H} + H_2 \longrightarrow \underline{H}^+ + e^- + H_2$;
- The double re-ionization of negative particles: $\underline{H}^- + H_2 \longrightarrow \underline{H}^+ + 2\,e^- + D_2$.

Increasing density along the line of sight of a totally negative D^- beam increases the neutralization rate; however, as the useful D^0 fraction rises, the other undesired reactions grow as well, up to a point of maximum neutralization rate. To obtain the ideal neutralization rate, a fixed gas *target thickness* must be maintained within its walls: target thickness is defined as the integral of gas number density along a path line, and represents how many 'obstacles' (i.e. particles in a particle collision model) are present along a given measure line. The value can be maintained high with low gas input by having very narrow and tall beam channels to reduce the gas conductance and hence the needed gas throughput; this is to avoid excessive particle fluxes for the vacuum system to remove. The target thickness at the maximum is

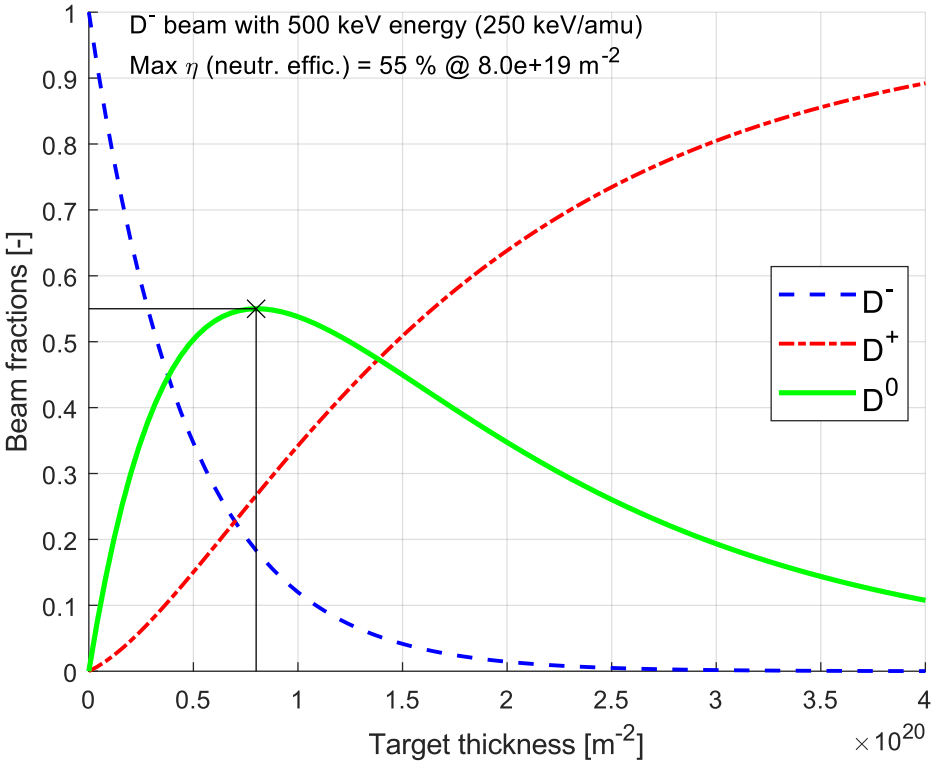

Figure 2.15: Resulting beam fractions plot as a function of target thickness for a given 500 keV deuterium beam.

used as an indication on how to combine number density and length in the NBI to guarantee the maximum rate of reaction for neutral deuterium. As an example, the maximum neutralization rate achievable for a 500 keV D^- beam (such as in DTT NBI or MTF) is 55 %, with a target thickness of about 8.0×10^{19} m^{-2} (see Figure 2.15). The front of the Neutralizer is particularly interested by undesired heat loads due to the halo beam component and fast electron population impinging on the columns of the slits. This usually call for the installation of dedicated Leading Edge Elements (LEE) with enhanced cooling to protect the component. A conceptual design for a Neutralizer is reported in Figure 2.16.

2.4.3 Residual Ion Dump

At the Neutralizer exit, the beam has only been 60 % converted into neutrals; the rest, according to Figure 2.15, is equally distributed between positive and negative ions. These particles are potentially dangerous as they carry a significant part of the power that will be deflected by the tokamak field upon the vessel if not controlled: this is the role of the Residual Ion Dump. The RID can be magnetic (as in ASDEX

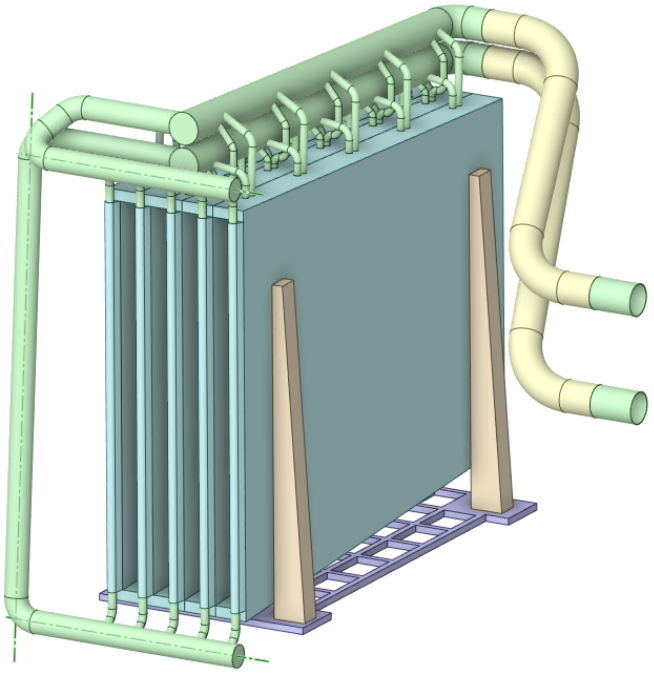

Figure 2.16: Conceptual design of a Neutralizer, with the cooling system and the LEE in place.

and JT-60) using an Ion Bending Coil and an Ion Dump; or electrostatic (as it will be in ITER NBI), where plates at different potential separate and deposit the ions upon themselves. As over 40 % of the initial beam power is lost in this component, the cooling system must be dimensioned accordingly.
The heat load peak is small and defined, since the entire beam feels the effect at the same time, landing in the same spot; to spread it more evenly, a time-varying ramp voltage can be added to the base RID voltage, shifting the heat load along the plates. A conceptual design for a RID is reported in Figure 2.17.

2.4.4 Calorimeter

After the RID, the beam is ready to enter the tokamak chamber; however, to be sure of the characteristics of what is actually being injected (i.e, energy and power) and not prematurely release an undesired beam, a calorimeter is present between RID and the exit duct. This device must be able to withstand the full power of the beam, with heat load densities rivalling those that can be reached the tokamak's own divertor (around tens of MW m^{-2}). For these reasons in high-power NBIs, the calorimeter is a tube calorimeter, where the there is no plate in-between the beam and the cooling, and the swirl tube technique is used. A conceptual design for a tube calorimeter is reported in Figure 2.18.

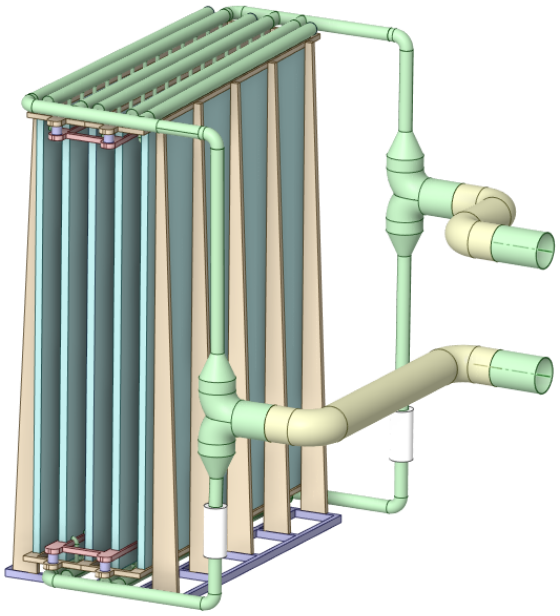

Figure 2.17: Conceptual design of an electrostatic RID. The cooling pipes towards the charged plates must pass through apposite insulators.

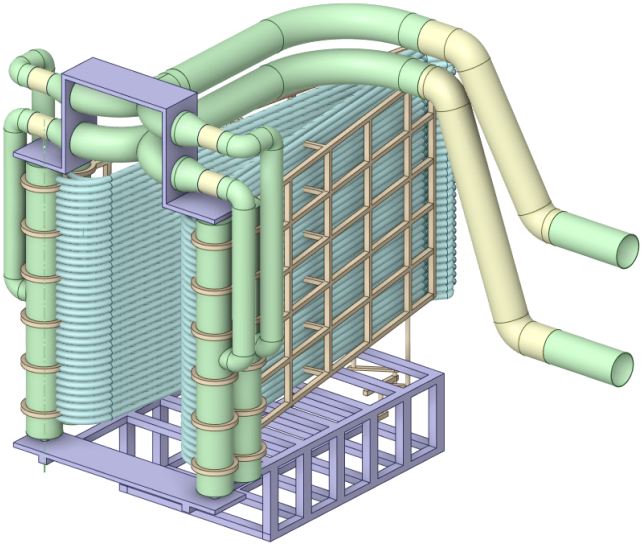

Figure 2.18: Conceptual design of a tube calorimeter.

Chapter 3

Divertor Test Tokamak NBI, design and materials

SUMMARY - The Divertor Test Tokamak (DTT) as a experimental facility will require both power and control to replicate fusion-like heat deposition conditions to test new Plasma Facing Components and divertor. A consistent part will be delivered through NBIs, which will have a single air-insulated beam source, inspired by the Japanese NBIs of JT60 and LHD, but using a RF source concept instead as in ITER NBI, accounting for about 10 MW of heating power. For DTT NBI, there will be also, for the first time, the possibility of constructing complex copper components (such as the grids or the Faraday shield) through the Additive Manufacturing techniques.

3.1 Introduction

In 2012, the European Fusion Development Assembly published "Fusion electricity - a road-map to the realization of fusion energy" [10], devising a strategic vision towards the ambitious objective of attaining generation of electrical power by a Demonstration Fusion Power Plant (DEMO) by 2050. One of these missions portraits the need in the near future of defining and designing a particular experimental facility, denominated Divertor Test Tokamak (DTT), dedicated to aggressive R&D in the matter of power exhaust and Plasma Facing Components. In fact, as described in the article, whereas in ITER some choices in the matter have already been made and will be thoroughly tested once the experiment effectively starts, there is no guarantee that the ITER baseline strategy (since that after all, it is an experiment) will be able to be extrapolated to what are the DEMO requirements (a full-power reactor). The lack of alternative solutions would potentially delay the realization of fusion by 10-20 years. By building a separate facility to work in parallel with ITER, the aim is to cover with on-field experience the gap in Plasma Facing Components knowledge during the design process from proof-of-principle devices to actual full-power experiments like

ITER and future DEMO-like reactors, that cannot simply be filled with numerical simulations.
Some of the most evident problems in the analysis of fusion exhaust are:

- Available experiments operate in Scrape-Off Layer (SOL) and plasma bulk conditions very different from those expected in DEMO-like reactors;
- As a consequence, simulations too are based on SOL models that are not reliable in extrapolating to DEMO;
- The impact of different configurations for a key component like the *divertor* is something to be evaluated accurately by experimentation;
- Other problems might arise from integration of a possible solution with other key tokamak subsystems, as in vacuum pumping, etc.

It is also a great opportunity of collaboration between numerous research teams throughout the national border, each one with its own part to handle; and also on occasion to shine the spotlight of fusion research on Italy, with such an important project.

3.2 DTT test facility

DTT will be a new experimental fusion facility, whose construction is starting at ENEA C.R. Frascati, Rome, Italy. The location already hosts an ENEA research center and housed the FTU tokamak experiment, easing authorizations and licensing procedures. Initial budget has been fixed at about 500 M€; a dedicated DTT team, composed of ENEA, CNR, INFN, RFX and other European Universities with direct experience on several other similar devices, has already distributed that amount between the complex of vessel, magnetic coils, cooling/pumping, Heating & Current Drive, power supply and diagnostic systems. All of their choices have been listed and justified in the latest Interim Report [11] and more recent paper by R. Ambrosino [12]. Some of the main parameters for DTT are listed in table 3.1.

Parameter	**Value**
R [m]	2.19
a [m]	0.7
Aspect ratio	3.1
I_p [MA]	5.5
B_T [T]	6
Pulse length [s]	100

Table 3.1: Main DTT parameters (for Single Null configuration) [12].

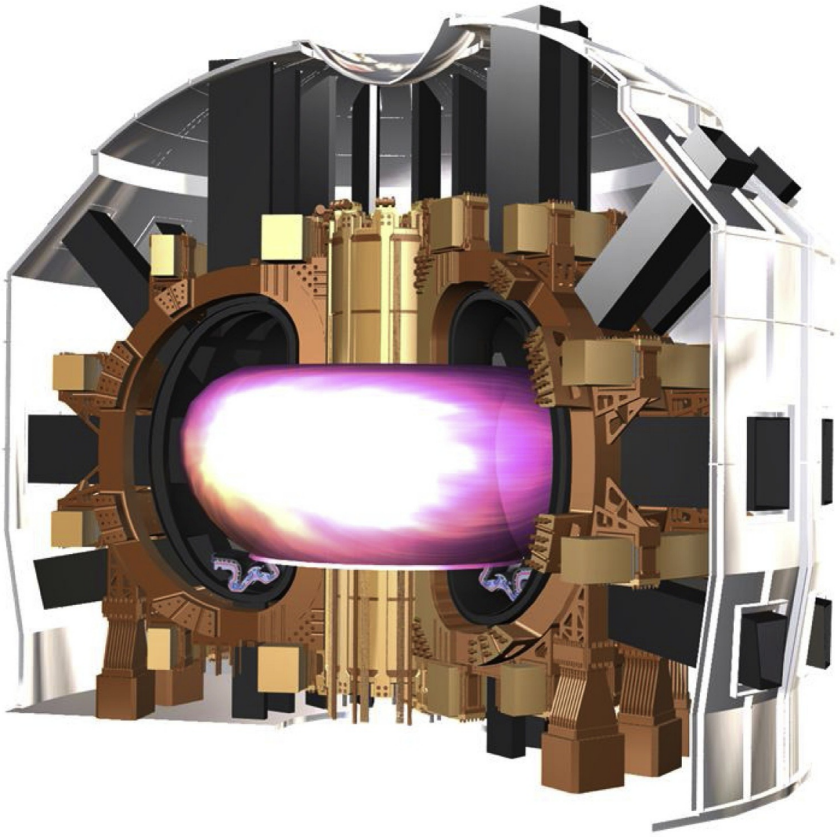

Figure 3.1: Sectional CAD rendition of DTT [12].

Since the DTT experiment is finalized to study the power exhaust in a fusion reactor-like environment, particular care was dedicated in determining the ideal parameters for bulk plasma, the divertor and the SOL regions. In order to have the needed versatility on experiments, a total amount of 45 MW in additional heating power will be installed in successive phases (as described in Figure 3.2) after the completion of main vessel and coil systems, subdivided between different H&CD types of devices. The additional heating will be covered for about 6 MW with Ion Cyclotron Resonance Heating (ICRH) and 29 MW with Electron Cyclotron Resonance Heating (ECRH), both using antennas to couple EM waves with particles in the plasma, at frequencies that are close to the resonance cyclotron frequency of each. In doing so, particles are continuously accelerated in resonance during their alternate revolving motion, increasing their kinetic energy and thus their temperature.
The rest of the power (about 10 MW) will be appointed to a Negative NBI system, to reliably accelerate high energy neutral beams able to cross the plasma bulk and heat its center.

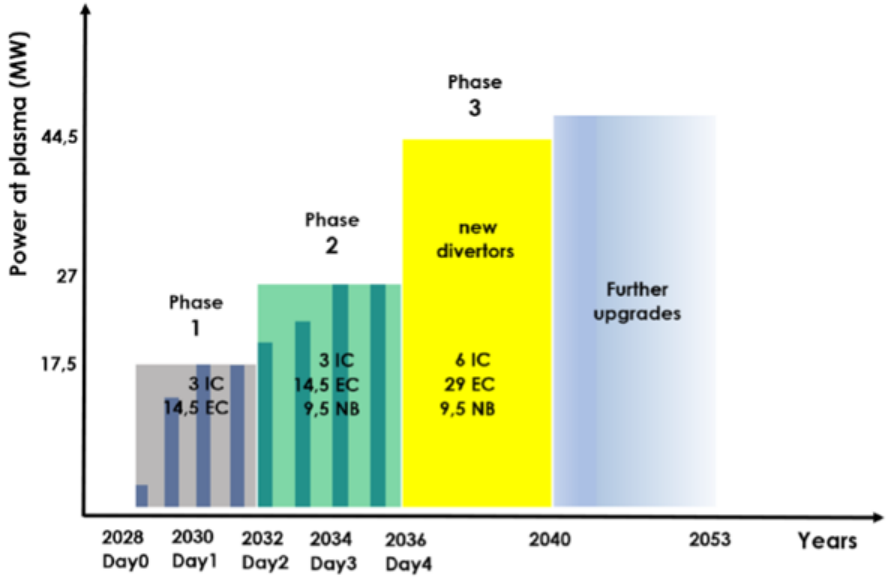

Figure 3.2: Schematic planning of the DTT H&CD operations. The NBI will be present starting from Phase 2. [Courtesy of DTT]

3.3 DTT NBI overview

Following an overall detailing of the structure will be presented, with a more in-depth look at the NBI systems that are going to be adopted in the DTT injector.

3.3.1 Energy and injection parameters

An NBI system based on the acceleration of positive ions would inject efficiently particles into the plasma with energies in the order of 80-120 keV. This range of energy however would lead to a too peripheral power deposition for DTT. In order to heat particles in the core at the density that is expected to be reached, a negative-ion-based NBI system at higher energies ($E \geq 300$ keV) is then proposed. Presently a 510 keV beam energy is considered as the most interesting value, being a good compromise among costs, size and performances. The acceleration voltage has been subdivided in three, obtaining a voltage gap per acceleration stage of 167 kV, less than the one that was adopted in ITER NBI. In order then to reduce the shine-through, magnetic ripple losses and help the current drive, an accurate assessment of the injection angle α_{inj} has been carried out, using dedicated transport codes ORBIT and METIS. This simulation showed good heating footprint and reduced losses for angles of injection of $\alpha_{\text{inj}} = 35$ °at the first wall, at a 3400 mm tangency radius.

3.3.2 Beamline conceptual design

The conceptual design follows from the above physics requirements, and considers as main guidelines the maximization of flexibility, RAMI (Reliability, Availability, Maintainability, Inspectability) and efficiency, also minimizing cost and weight. The definitive version of the design will provide, as has been mentioned, 510 keV of beam energy, through the acceleration 40 A of D^- from 1280 grid apertures; the grids will be five in total, of which one for extraction and three for acceleration.

The overall beam will be divided into four separate vertical blades: such a choice permits to minimize the minimum length of the neutralizer to have an acceptable reaction ratio, and also allow for better deflection control. For this device, the target wall plug efficiency is $\approx 30\%$, meaning that improvements must be made as to transfer successfully at least 30% of the absorbed electric power into the plasma bulk, without problems during the pulse.

The accelerator grids, situated in the beam source, are a critical component, since (as it has been discussed) they have a rather complex design, with very small cooling channels, apertures for the negative ions and grooves for the electron deflection embedded magnets. The possibility of manufacturing by means of copper electrodeposition on a milled base plate made of pure copper has already been proven in recent works from Consorzio RFX [13]. Still, as electrodeposition is a rather complex manufacturing process, the possibility to manufacture the grids by Additive Manufacturing is currently being considered. The printing process requires though the use of particular techniques to achieve high thermal conductance, for which an important effort in process and material characterization is being made by the INFN colleagues of the Padova branch. A presentation is given in section 3.4.

The main components of the injector assembly, shown in figure 3.3, recuperate some different concepts from other existing NBIs from around the world: similarly to the NBIs of JT-60 [14] and LHD [15], a design with an air-insulated beam source is proposed, to reduce the vacuum volume, increase the source accessibility and avoid the need of a complex air-to-vacuum bushing to connect the SF_6 insulated Transmission Line to the vacuum vessel. A drawback of this solution is the required clearance between the ion source and the surrounding structures (at least 2.5 m, to avoid electrical discharges).

The DTT design differs though from the Japanese scheme in the choice of ion source: in fact, it is proposed to use the same RF source concept adopted for ITER, developed by IPP Garching [16] in Germany, creating ions through Inductively Coupled Plasma as described before. Other BLCs will be ITER-like too, while the vacuum vessel will be without large flanges (differently from ITER) to reduce cost and weight: only small flanges are foreseen for pumping, diagnostics and BLC supplies,

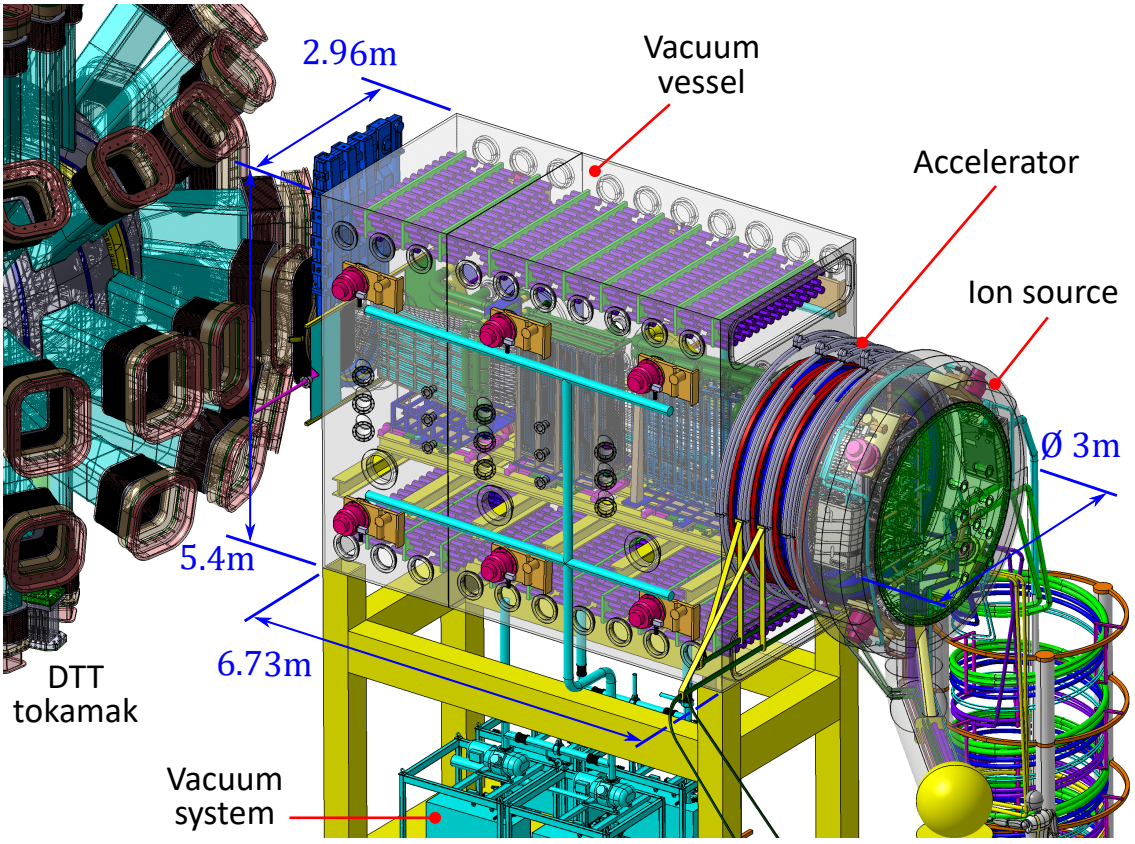

Figure 3.3: Overall view of DTT NBI in its position near the DTT tokamak. The main dimensions are also reported.

while the BLC maintenance is planned to be from behind, by removing the beam source and setting the components on rails.

Another critical R&D program that is being carried out is the manufacturing process for a rather unusual component, the insulating rings of the accelerator. These rings are interposed between the acceleration grids; as such they must be quite large (diameter of 3 m and length of 0.5 m) and must fulfill several important functions, i.e. to maintain the electrical insulation between the acceleration stages, and to support the beam source while being perfectly leak tight and having a vacuum compatible surface on the internal side. This kind of technology has been explored with the Japanese JT-60 air-insulated NBI by using Fiber-Reinforced Polymer (FRP) rings; in Italy for DTT the job has been assigned to the Pisa branch of the INFN, where the design phase is ongoing.

The DTT NBI will be featuring a typical fore-vacuum system using screw and Roots pumps plus an Ultra-High Vacuum (UHV) system based on turbo-molecular pumps on the lateral sides of the vacuum vessel. During beam operation however the

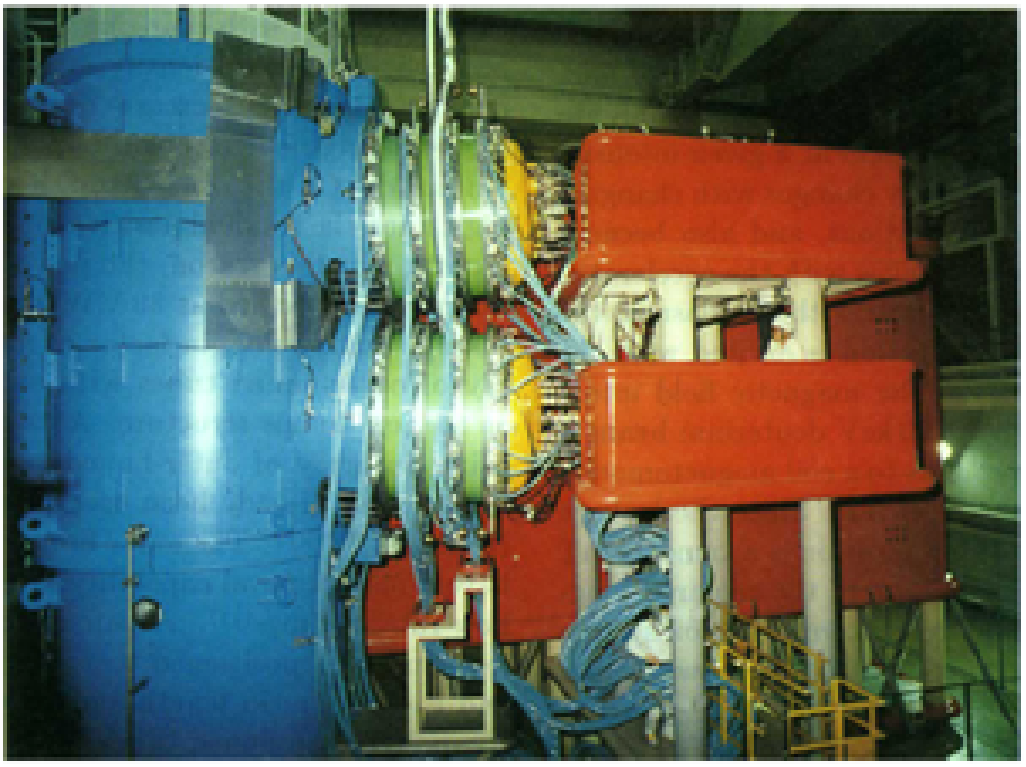

Figure 3.4: Detail of the JT-60 NBI system, showing the beam sources and the FRP rings [14].

main pumping will be entrusted to a relatively new application to the fusion field: Non-Evaporable Getter (NEG) pumps, organized in "pumping walls" configuration covering the top and bottom walls of the vessel. NEG materials are composites (such as Zinc-Aluminum Oxide [17]) capable of capturing surface-impinging gas particles and diffusing it in its bulk; it is usually arranged as compressed powder discs piled one over the other to form columns, then arranged in hexagonal formation (Figure 3.5). Many combinations of orientations and positioning have been tested to maximize the capture coefficient for the pumping structure, that in recent simulations has managed to reach a value of about 0.1. With respect to the enormous cryopumps adopted in ITER NBI, these pumps have the advantage of working at ambient temperature and needing electricity only during regeneration by heating, once saturated.

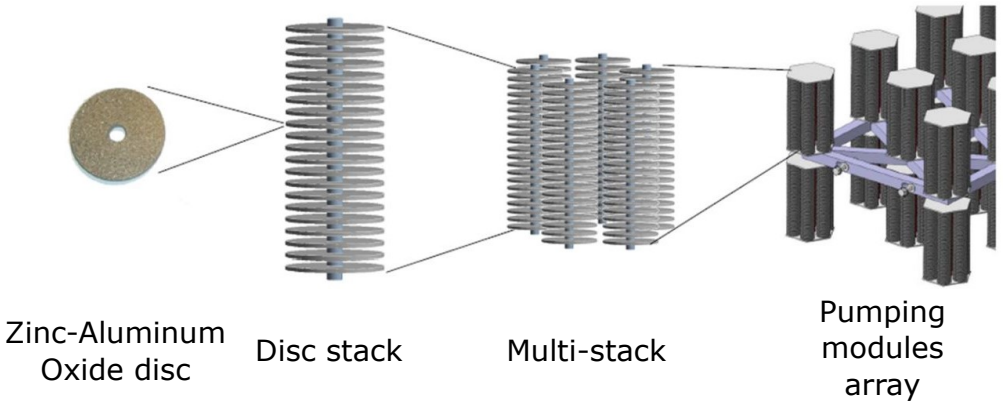

Figure 3.5: Schematic representation of Non-Evaporable Getter pumping modules.

3.4 Additive Manufacturing

Over the past decades, Fast Prototyping using polymers powders heated on deposited on successive layers has become well known and established as the "3D printing" widely known to the public. What is of recent availability is the technology behind electron beams and power lasers, able to locally melt metal powders deposited by a nozzle. That, coupled with Computer-Aided Design (CAD), poses the prospect for layer-by-layer fabrication of complex, custom metal or alloy products impossible to be achieved by more conventional processing of wrought or cast precursors, also reducing manufacturing time and costs. These components include simple geometries, including various sizes of cylindrical and rectangular block products as well as more complex mesh and foam components which are especially novel because they can be fabricated in complex systems with high specific strength and stiffness [18]. More in detail, between all of the available techniques, the one being considered for DTT NBI is Selective Laser Melting (SLM).

In SLM, melting is achieved through a focused laser beam of chosen frequency and power: the laser is focused by a CNC driven mirror onto a metallic powder bed, then re-coated mechanically after each pass to form the successive layers; scanning can be selective along the x–y plane, growing in the z direction, in a neutral atmosphere of Argon or Nitrogen.

As for the particular case of DTT, the main problems of printed components are the porosity for some materials (an important parameter for water-cooled grids in a vacuum environment) and the difficulty of effectively melting some metal powders, including pure copper, without the appropriate wavelength lasers. This leads to incomplete melting and high porosity, with low properties of strength and heat transfer. This is due to the fact that pure copper reflects almost all of the typical frequencies used in AM lasers, aside from the green-red light range, which are still not very diffused. So, in order to fuse copper, there is the need to increase the power,

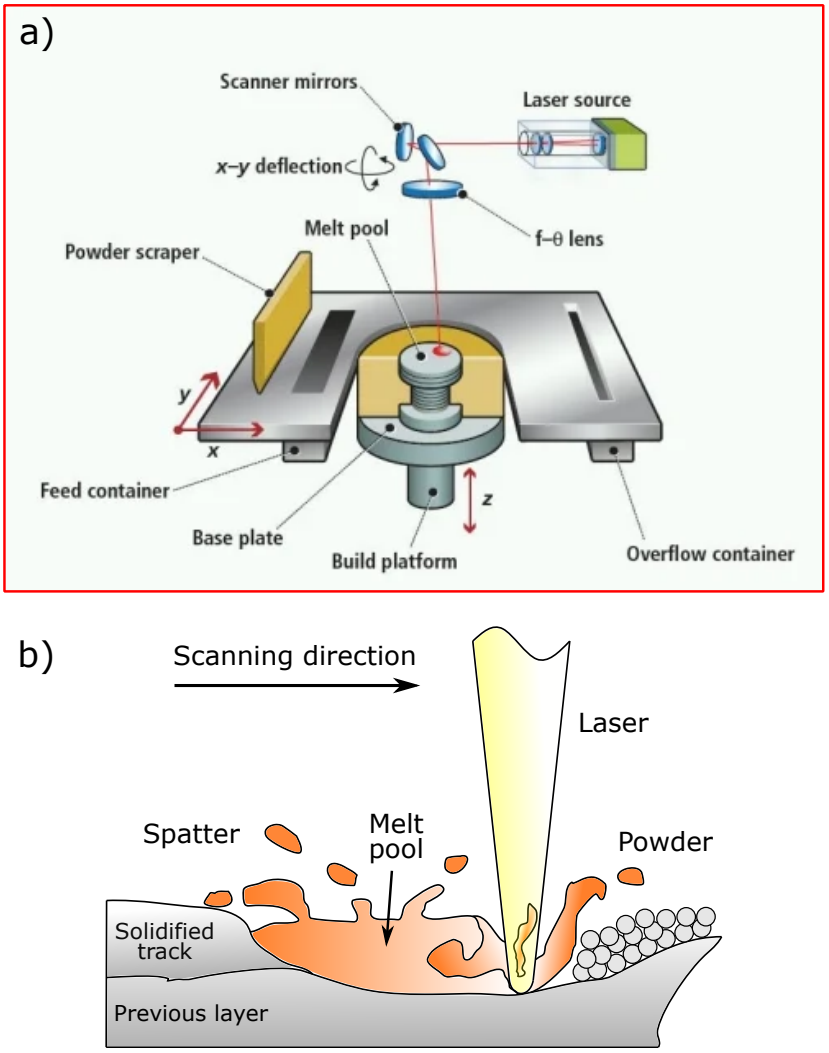

Figure 3.6: a) Conceptual design of an SLM system [19], b) Zoom of the melt pool.

change the laser frequency, or introduce impurities/use alloys. This is a drawback, because pure copper would be the best choice for the acceleration grids, with its mechanical strength, high thermal and electric conductivity: the most promising alternative that is proficiently printable have been identified in mixed copper powder alloys, namely 99% copper powder (with O and P impurities) and CuCrZr. This last alloy has normally a particularly low thermal conductivity with respect to the pure copper; however, it is possible to treat CuCrZr components by heating them at around 600° C for a determined period of time (called "aging"): this leaves the crystalline domains the time and energy to reorganize themselves and dramatically increase their conductivity.
These procedures are being investigated by the DTT NBI design team: some compa-

nies showed interest on developing advanced technology on additive manufacturing and lasers for these materials and have been asked to produce some test components for accurate analysis of parameters as the mechanical strength, porosity and thermal conductivity, using different printers and printing directions. Some results are presented in Table 3.2.

		EOSINT M280, 400W			EOS M290, 1kW	TRUMPF Truprint, 1kW
		Pure Cu	**99% Cu**	**CuCrZr**	**Pure Cu**	**Pure Cu**
Horiz. printing	Yield strength [MPa]	113	255	272	160	140
	Tensile strength [MPa]	160	313	366	225	221
	Young module [GPa]	109	155	142	125	136
Vert. printing	Yield strength [MPa]	89	238	248	165	137
	Tensile strength [MPa]	103	259	318	223	200
	Young module [GPa]	85	150	131	125	124
General	Thermal conductivity [W m^{-1} K^{-1}]	137	312	322	389	396
	Relative density	89%	98%	99.5%	99.8%	99.8%

Table 3.2: Main parameters for grid material candidates and different printers.

The obtained results show as expected that by using high power infrared or green lasers, the production of fully dense parts with high thermal conductivity is quite feasible; it also confirmed that pure copper is not processable on lower laser powers. These experiments also evidenced the suitability to application of the CuCrZr alloy: by tuning the heat aging process it is possible to obtain a material with higher strength than pure copper and a thermal conductivity not lower than 300 W m^{-1} K^{-1}. Currently, some Extraction Grid prototypes are being built and tested, to check for possible issues during manufacture, using both pure copper and the CuCrZr alloy.

Chapter 4

Functional Optimization for DTT NBI

SUMMARY - The DTT NBI device is a trailblazer in many of its aspects, from the beam source, the vacuum pumping system, short focus distance etc., all the way to reliably flexible operation. All of these aspects influence each other to various degrees, and required new integrated techniques to properly assess their effects. This section describes the design and simulation work that was done in order to meet the DTT NBI requirements.

4.1 Introduction

As mentioned in Chapter 2, a NBI is a very complex system, that forces engineers to blend together the very small (details on the scale of fractions of millimetres) to the very large (the beam travels tens of metres), while in a vacuum. It stands to reason from a numerical standpoint to, where it is possible, divide and conquer the two worlds, individuating two separate domains:

- The beam source assembly, composed by the RF beam source proper and the electrostatic accelerator; the latter dictates the shape of the beam using apertures only few millimetres large.
- The BLCs, the vacuum vessel, and the duct assembly, responsible of making the charged beam available to the tokamak; each one of them would require a crane to even adjust slightly, due to their size.

This is what was done during the optimization effort for DTT NBI, developing different sets of models finely tuned to the size of the problem.

This chapter has two main sections: the one on the beam source (more specifically the design of the accelerator) and the part on full-NBI modelling (regarding vacuum, external fields, and particle tracing). Both are dedicated to increase the wall-plug efficiency of the system, while satisfying board requirements.

4.2 Beam Source subset

This section will be dedicated to explain the design choices and showcase the results of simulations regarding the Beam Source assembly. However, since the RF source for DTT NBI is foreseen to be of the same type as in SPIDER and MITICA [20, 21], less attention is needed in their design; the main focus in this thesis will be on the electrostatic accelerator. The final objective is to first design a system capable of satisfying beam quality and aiming prerequisites, and secondly estimate the resulting heat loads due to beam operation (key inputs in cooling estimations).

The first step to accelerator design is to determine the *aiming strategy*; this decision is dictated by external constraints, like the shape of the plasma source or the maximum encumbrance for the NBI. Being able to implement it efficiently at the accelerator level is one of the most important aspects in improving beam transmission, and consequently the NBI efficiency.

4.2.1 DTT NBI aiming strategy

Derived from the available space for the system, the DTT NBI total focal length will be of about 12 m, making it a rather short device especially when compared with other similar systems, such as the similarly powered JT-60 NBI (with its 22.7 m [22]) or even the future ITER NBI (totalling 25.4 m [23]), while using plasma sources of similar sizes: this means that the NBI will have a strongly converging beam envelope, that may require particular attention when designing the beamlet steering systems.

The accelerator assembly is divided in sixteen equal *aiming planes*, each one hosting a 5 by 17 beamlet array, illustrated in Figure 4.1. Each one is slightly inclined, as to with their surface be tangent at the center to the spherical surface centered at the focal point and the radius equal to the focal distance. In this way, each plane is already directed towards the desired focal point, and needing smaller steering adjustments. From a beam trajectory standpoint they are also equal, meaning that all successive finer aiming corrections can be developed on a single plane and then extended to all without problems, which simplifies the work considerably. Another decision to make is in what direction to aim each beamlet aperture. Logic would dictate to simply connect each beamlet from the chosen aperture array to the focus point in the tokamak, obtaining a triangular beam with a constantly decreasing cross-section, in *common-focus* aiming strategy fashion.
For DTT NBI however the choice fell upon a *multi-focus* approach rather than a common-focus one, since priority was given to minimize heat loads and maximize beam transmission. A potential drawback of the closer focusing is that steering devices need to be even more effective in their action; this is discussed more in detail in the next paragraph.

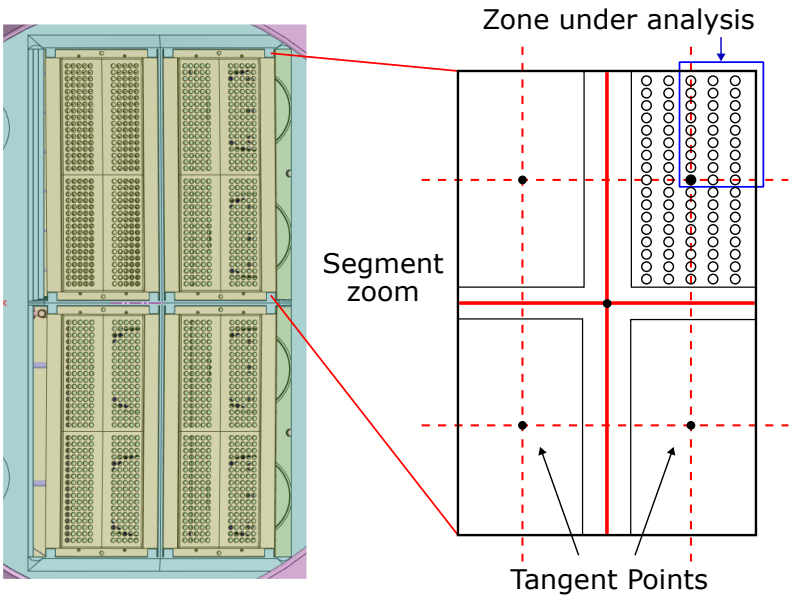

Figure 4.1: Scheme detailing how the grids are segmented and each plane aligned in the direction of the focal point. Due to symmetry, analysis can be restricted to the area enclosed by the blue rectangle.

4.2.2 The DTT NBI accelerator

As per usual, the desired beam energy must be reached through the use of an electrostatic accelerator. The proposed design divides the acceleration of the particles in five separate electrostatic grids (illustrated in Figure 4.2), over which the total accelerating voltage is spread:

- The Plasma Grid (PG) at about -510 kV, separating the beam source cavity from the accelerator, is where the negative deuterium ions and electrons are extracted; during operation, a strong current flows through to generate the magnetic filter inside the cavity to increase ion yield.
- The Extraction Grid (EG) at -500 kV: the small potential difference and grid distance must be finely tuned to maximize beam extraction and improve beam optics; the still low-energy beam here can be easily steered to match the aiming strategy.
- The Acceleration Grid 1 (AG1) at -333 kV, providing the first great potential jump to the particles. It is the start of the simple linear acceleration phase.
- The Acceleration Grid 2 (AG2) at -166 kV, providing the second.
- Grounded Grid (GG) at ground potential; also delimiting the end of the Beam Source subset domain.

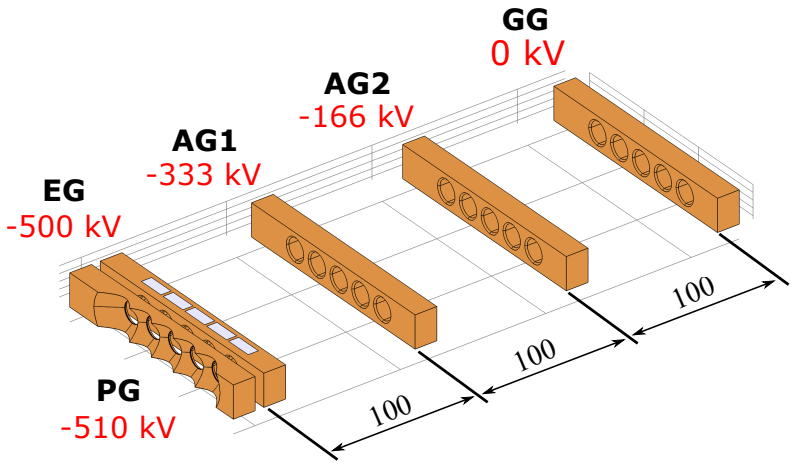

Figure 4.2: Horizontal section of a beam group of the accelerator assembly. The distance between grids (in mm) is reported.

The aiming strategy previously described can guarantee a significant improvement of the overall transmission efficiency, but needs a proper device, acting at the electrostatic level, able to shape the field and steer the beamlets correctly. Similar systems regularly apply electrostatic aiming devices such as those described in section 2.2.2.2, but these were found to be either not effective enough in aiming (when trying to preserve the beam shape) or deforming excessively the beam shape (when trying to meet the desired beam directions) in the DTT NBI case, mostly due to its relatively short focus distance and adopted multi-focus aiming strategy. This motivated a significant design effort to identify a method to supply the desired aiming to the beam, and culminated with the proposal of a new type of aiming device, the Hyperlens Grids (HGs).

4.2.3 The Hyperlens Grids

The idea underlying this proposal is to provide substantial deflection in the most homogeneous way possible for all the particles in each beamlet (conserving beam shape) and being able to control them individually to a certain degree (to achieve the different target deflections), both horizontally and vertically. A possible approach has been found by adapting the concept of "folding" the grid to a single beamlet basis: for each aperture, the entrance should be flat, as usual; the exit instead would have an inclined plane as surface, shaping the nearby electric field to guide particles in the same normal direction (as in Figure 4.3). By connecting then each aperture's "aiming plane" with flat junctions as to not modify the nearby electrostatic field shape, a lens-like profile naturally emerges. Combining this with the steering grid concept, it is possible to imagine interchangeable, lens-shaped on one side (hence

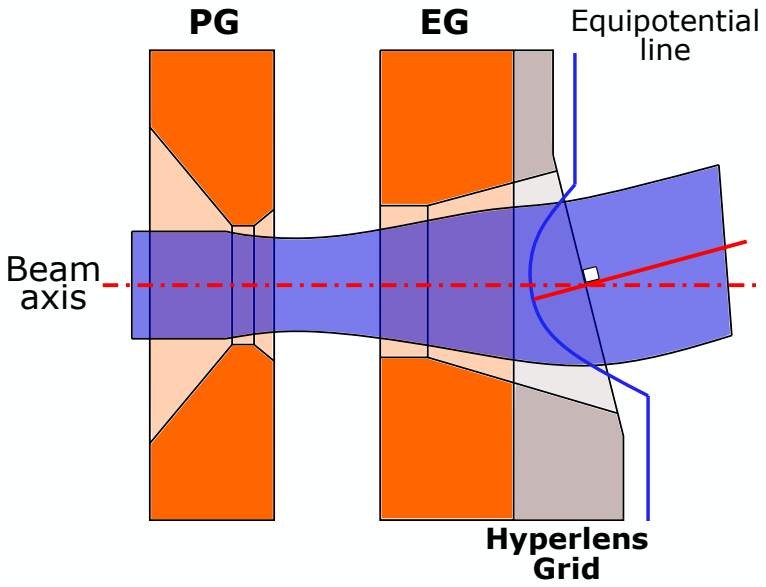

Figure 4.3: Diagram detailing the concept at the base of the Hyperlens Grid: the grid shape locally deforms the electric field imposing a specific direction to the beamlet.

the name Hyperlens), thin grids to attach to the main, simpler flat one. It also easy to see the direct correlation between the slope found at the exit and deflection (taller slope means greater deflection) and how this effect can be decomposed in horizontal and vertical components, allowing the beam to have two separate focal points and then add them by superposition of effects. The steering effect can also be split between grids, to minimize the overall length of the accelerator and avoiding undesired beam loads: this is due to the fact that inside the apertures beams feel little electrostatic pull and start to diverge due to self-charge, and if the channel is too long due to excessive additional grid thickness it may start to impinge inside the aperture itself. Since there is no real way to pre-emptively account for all beamlet-beamlet interactions and superposition of effects here is not totally between independent parameters, the design needs iterations to match requirements.

The Hyperlens Grid concept has been applied to the DTT accelerator: achieving the ideal aiming can be reduced to the matter of finding the correct set of slopes to apply to the grid construction. Further simplification can be achieved by checking the symmetries of the problem: thanks to how the aiming strategy in DTT is set up, all of the 5 by 17 beam group arrays are formally equal, and also symmetric around their centre. This means that only 2 columns (plus the centre column) by 8 rows (plus the centre row) need to be simulated. The idea is then to create two 3 by 9 matrices (2+1 row beamlets by 8+1 column beamlets), containing the slope values in the horizontal (Δh_{ij}) and vertical (Δv_{ij}) directions that can be chosen all independently from each other. The Hyperlens Grid can be visualized as similar to an elevation map on a grid: to obtain the four corners of the desired plane for the

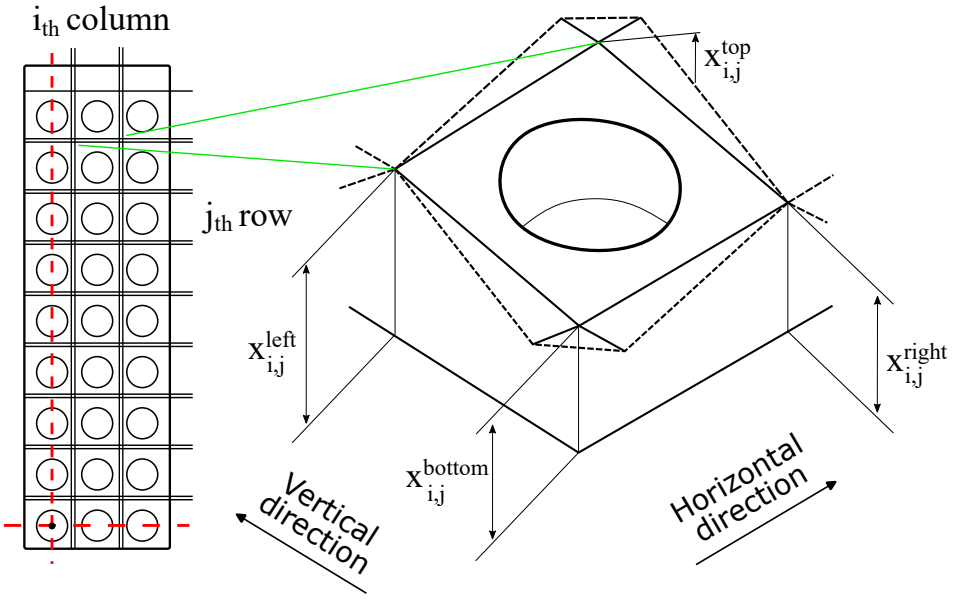

Figure 4.4: Scheme illustrating the principle of the complete Hyperlens profile. Its modular nature is evidenced in dashed lines: these hexagonal shapes allow a continuous junction even if the aiming planes have not the same inclination.

ij-th beamlet (represented by the x coordinates in the model) the slope values must be combined accordingly.

$$x_{i,j}^{top} = \sum_{n=1}^{i} \Delta h_{n,j} + \sum_{m=1}^{j} \Delta v_{i,m} \tag{4.1}$$

$$x_{i,j}^{left} = \sum_{n=1}^{i-1} \Delta h_{n,j} + \sum_{m=1}^{j} \Delta v_{i,m} \tag{4.2}$$

$$x_{i,j}^{right} = \sum_{n=1}^{i} \Delta h_{n,j} + \sum_{m=1}^{j-1} \Delta v_{i,m} \tag{4.3}$$

$$x_{i,j}^{bottom} = \sum_{n=1}^{i-1} \Delta h_{n,j} + \sum_{m=1}^{j-1} \Delta v_{i,m} \tag{4.4}$$

This procedure has to be repeated for each of the beamlets. One aspect to pay attention to is that now there is the possibility that adjacent aiming planes are not always equally inclined, and consequently they cannot be connected by a simple planar junction; they can be connected by triangles instead, obtaining a hexagonal modularity. This is illustrated in Figure 4.4, with the final CAD product presented in Figure 4.5. Now that the shape of the grid is established, other important design aspects must be considered.

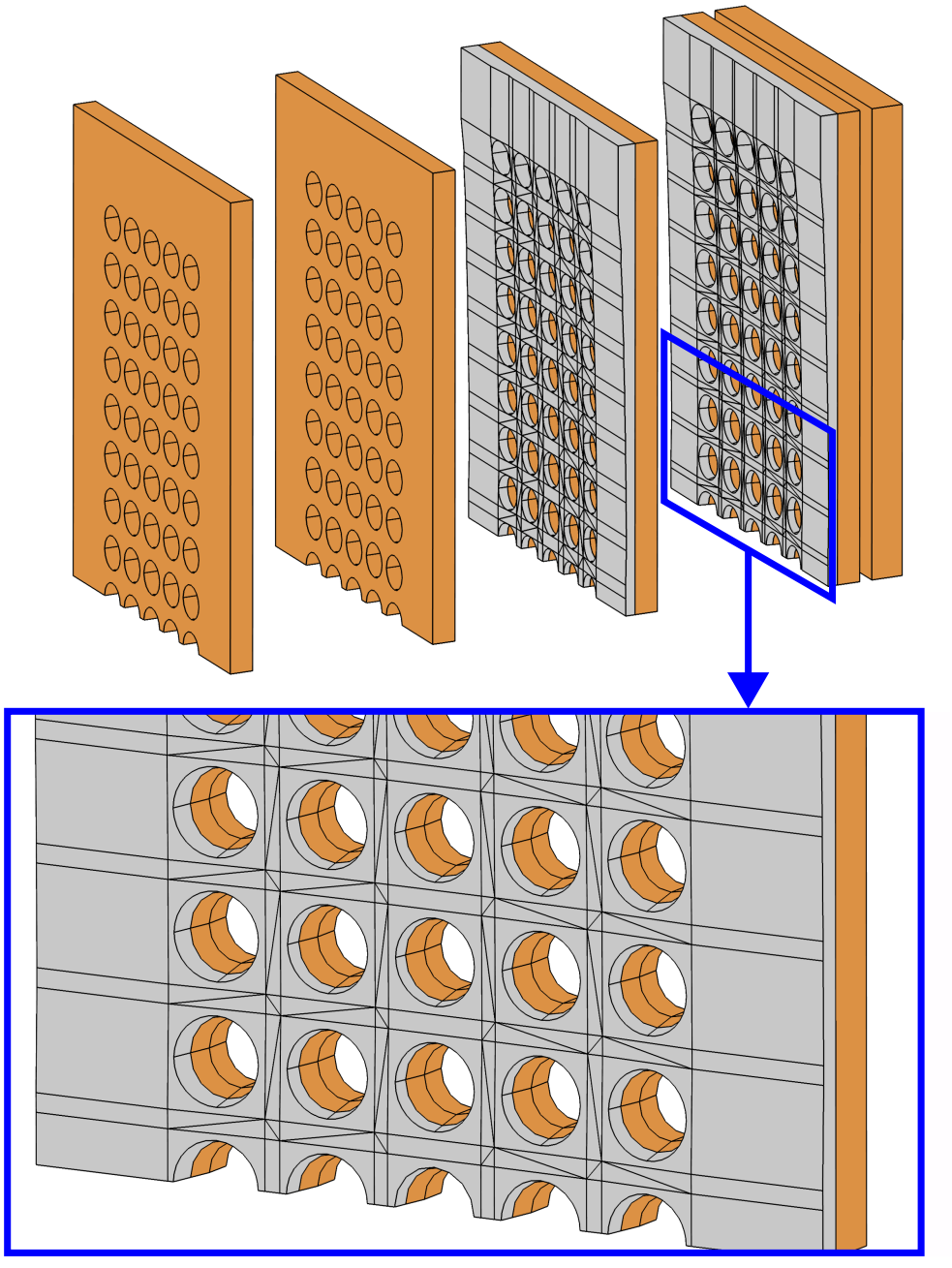

Figure 4.5: 3D render of the DTT NBI accelerator assembly in a 40-beamlet subset, where the HGs have been applied. A detail of the HG is present.

4.2.3.1 Multiple Hyperlens Grids

A decision must be made about how many additional HGs are necessary in the accelerator: this is usually the result of a trial and error process, since not all HGs give the same performance due to the different energy of the particles in the beams between grids. In fact, even supposing that HGs can impart the same transverse velocity component to the beam, the final direction is dictated by the ratio with the axial velocity, that constantly increases. In this early design iteration, the use of only two identically sloped HGs was found to be sufficient; the additional constraint helps to keep the design parameters as simple as possible. More advanced systems could tailor the steering effect differently for each grid.

4.2.3.2 Offset of beamlet apertures

Usually beamlet apertures are placed in regular arrays at fixed distances across the grids; for DTT NBI however, with its strongly converging beam shape, this approach does not allow clear sight lines towards the focus point. On top of this, said sight lines are not perfectly straight as one might assume: as particles gain axial energy under constant acceleration, while the transverse energy stays the same, they draw quasi-parabolic trajectories within the accelerator, more pronounced at the edges of the beam segment. To avoid impingement the solution is to follow the quasi-parabolic beam trajectories, starting from a regular beamlet array at the GG (20 mm horizontal, 22 mm vertical spacing), increasing linearly the distances on the earlier grids based on the focus angle (as a first order correction), then slightly modifying the position of each aperture on each grid (as a second order correction). Obviously these offsets must be obtained after an iterative process; they have already been implemented in the first design.

4.2.3.3 Criss-Cross Deflection Effect compensation

There are various methods to compensate this effect: in DTT NBI it has been chosen to pre-emptively shift the PG apertures in the opposite alternate direction of about 0.5 mm, such as to have ideally the beamlets placed at the centre again after the EG and thus not interfere with the effect of the HGs. This approach introduces a significant simplification for the successive simulations: by assuming that the beamlets are centred at the EG, there is no need to simulate the effect of the suppressing magnets on the ion beam, removing the magnetostatic aspect from the formulation.

4.2.4 Particle Tracing simulations

Each iteration of the design of the accelerator must be evaluated from a beam trajectory standpoint, and the main figures of merit that are used are the average deflections and the divergences of each beamlet. To this purpose, a set of two different codes was used, each one tailored to analyse in detail one of the two different aspects:

- SLACCAD, a ray-tracing axial-symmetric code, capable of modelling the beamlet self-charge, responsible for the space-charge limited emission. This is essential to obtain the formation of the so-called *meniscus*, defined as the surface where the particles start to accelerate due to the electric field and that is essential as an initial boundary condition for successive simulations. This degree of accuracy allows for determination of the beamlet self-divergence, the most important quantity that determines the quality of the particle beam.
- COMSOL® Multiphysics, a commercial Finite Element Method (FEM) code, whose formulation of 3D coupled electromagnetic field-particle interactions allows to evaluate beamlet-to-beamlet repulsion and the effect of HGs. The exit directions are then post-processed and confirmed with the reference values.

The requirement of DTT NBI is to reach a design that guarantees:

- Any beamlet not exceeding 7 mrad of exit divergence, in order to have properly focused beamlets and limited power dispersion.
- Any beamlet with a deflection error not exceeding 2 mrad with respect to the ideal direction dictated by the aiming strategy.

After applying the described procedure and following through some iterations with different sets of grid thicknesses, the requirements have been satisfied by using two HGs of thickness varying between 2.5 and 8.5 mm, with an exit divergence ranging from 2.65 to 4.66 mrad. An example of the SLACCAD simulations is reported in Figure 4.6. This range of values instead of a single number is due to the fact that these grids have a variable thickness: the electrostatic path is different for each beamlet, so it follows that also the exit divergence is not single-valued but rather in a range. Also, the extraction voltage (the voltage gap between PG and EG) was object of a parametric sweep to determine the minimum range of values of the divergence; said minimum was found with an extraction voltage of 7.5 kV. The maximum absolute error in the beam direction is calculated as

$$\epsilon_{max} = \max_i(\sqrt{(\theta_{y,i} - \theta'_{y,i})^2 + (\theta_{z,i} - \theta'_{z,i})^2}), \tag{4.5}$$

where θ' indicates the ideal deflection in either y or z, and i spans the number of beamlets considered in the simulation. The result of the COMSOL simulation is reported in Figure 4.7. The value ϵ_{max} in this configuration was found to be 1.83 mrad.

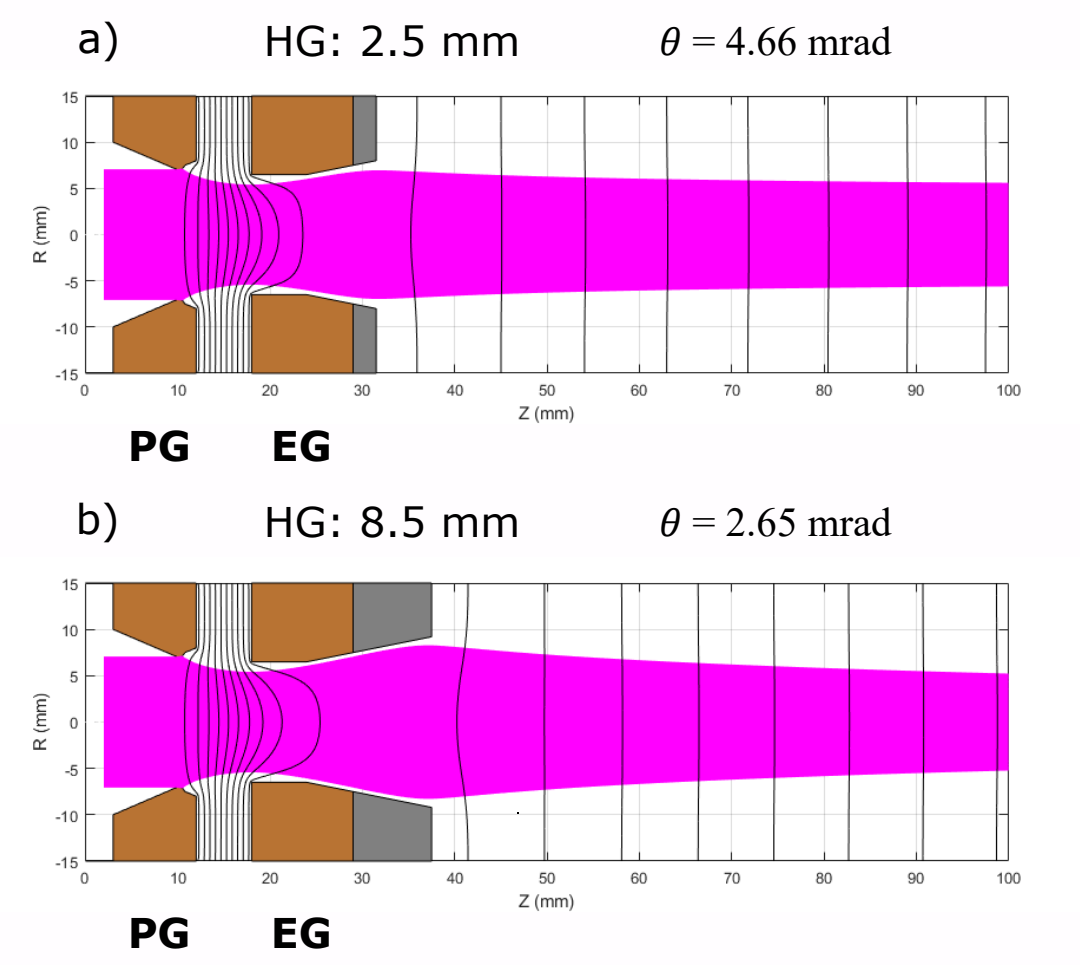

Figure 4.6: Detail of the SLACCAD simulations on beam divergence. a) and b) refer to the limit cases for the HG.

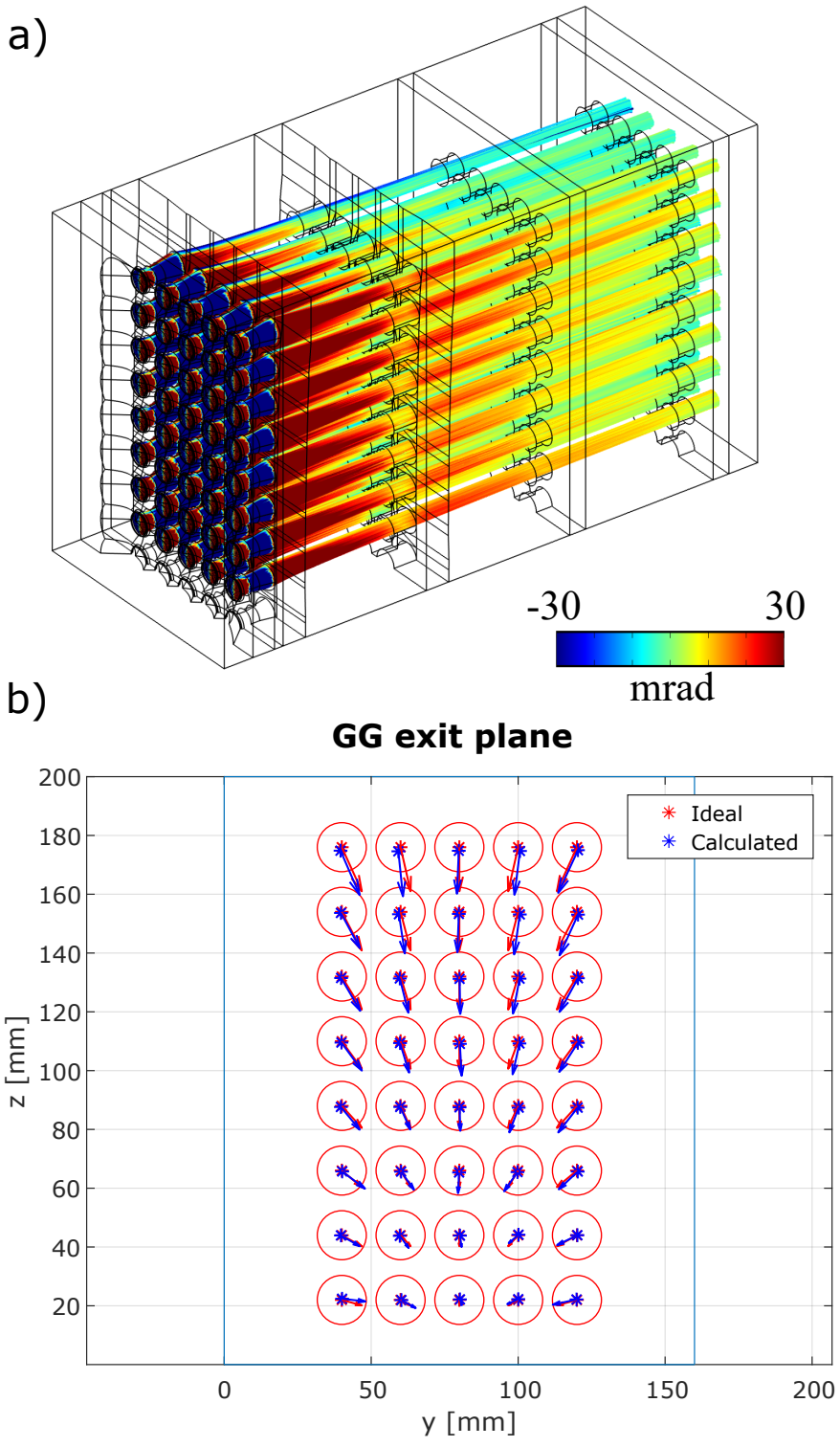

Figure 4.7: Main results of the Particle Tracing simulations: a) Trajectory plot of a 40-beamlet subset of a beam group, where the color represents the particle deflection; b) graph comparing the calculated average deflection for each beamlet (blue) to the reference directions (red).

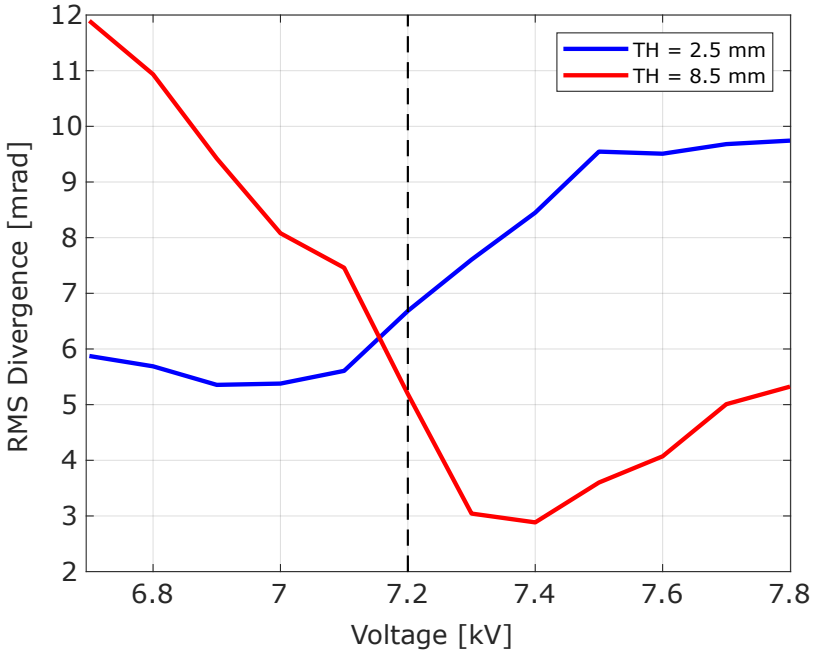

Figure 4.8: Parametric results from SLACCAD: the only value of the extraction voltage where both of the limit cases are under 7 mrad is around 7.2 kV.

4.2.5 Off-nominal scenarios

A desired additional aspect from the plasma physicists' point of view is the possibility for the NBI to achieve even different acceleration energies from the nominal, expanding the available scenarios. This possibility however must be carefully evaluated, since every part of the accelerator is already dimensioned to full power. For the Hyperlens Grids in particular, a round of simulations has been carried out to evaluate the accelerator performance drop in the most important off-nominal operation case: half of the nominal acceleration voltage (255 kV) and same current. Off-nominal operation now requires a strategy in how to distribute the potential across the grids: dedicated simulations in SLACCAD underlined the importance of maintaining the same voltage jumps where the beam is still slow (i.e., near PG, EG and AG1) rather than uniformly decreasing them: this conserves the well-tailored steering effects of the nominal case, limiting the defocusing effect of a slower beam to the latest stages of acceleration where aiming is less important. Secondly, the extraction voltage has to be slightly re-tuned in order to obtain satisfying optics from the beamlets, having changed the electrostatic field distribution: a parametric simulation for the two limit cases of thickness value of the HGs while changing the extraction voltage can identify a new minimum value. The SLACCAD simulations have given interesting results in terms of divergence, identifying the new extraction voltage as 7.2 kV with divergence that ranges from 5.19 to 6.68 mrad, as shown in Figure 4.8. Using the best case from

SLACCAD, the COMSOL multi-beamlet simulation has been run to obtain the exit deflection map as in the nominal case. Results show as expected an increase in the maximum absolute error in deflection, reaching 4.11 mrad, explainable by a set of reasons:

- Obviously the energy reduction: even if HGs affect the transverse velocity components in the same fashion, the axial component is still reduced by a factor of $\sqrt{2}$, magnifying the already present error.
- While maintaining the voltage in the early grids does help with conserving focus, the HGs still lose a small part of their deflection efficacy due to the flattening of the electrostatic lenses.
- Slower beamlets and particles have more time to interact, repelling each other farther than the nominal case.

This is still a very important result, since it provides insight on how to expect the beam to behave at least down to half-energy, by worsening its beam qualities of about a factor of two. This fact will be used later in the full-NBI simulation section to estimate a power-energy characteristic for DTT NBI.

4.2.6 Accelerator heat loads

In this section the calculations regarding the projected power losses in the DTT NBI electrostatic accelerator will be described, pointing out eventual simplifications and temporary design choices. Heat loads in an electrostatic accelerator are due to direct beam interception (that should be nominally null, but may happen during operative condition variation) and, especially in a negative ion-based system such as DTT, from these main parasitic particle-background gas reactions:

- Stripping reactions: $\underline{\mathrm{D}}^- + \mathrm{D}_2 \longrightarrow \underline{\mathrm{D}} + \mathrm{e}^- + \mathrm{D}_2$;
- Double stripping reactions: $\underline{\mathrm{D}}^- + \mathrm{D}_2 \longrightarrow \underline{\mathrm{D}}^+ + 2\,\mathrm{e}^- + \mathrm{D}_2$;
- Background ionization reactions: $\underline{\mathrm{D}}^-(\mathrm{or}\,\underline{\mathrm{D}}) + \mathrm{D}_2 \longrightarrow \underline{\mathrm{D}}^-(\mathrm{or}\,\underline{\mathrm{D}}) + \mathrm{e}^- + \mathrm{D}_2^+$.

In these reactions the underlined $\underline{\mathrm{D}}$ identifies the fast particles accelerated from the source. Other non-negligible sources of particles are the particle-wall impacts that lead to both sputtering and additional electron emission. Accurate heat load determination requires to combine into a single simulation all of the separate aspects of electromagnetics and reactions hypothesized up until now, and often lead to reconsiderations of aspects and problems that did not surface earlier. The code used for the evaluation is the Monte-Carlo code EAMCC, which starting from a predefined electrostatic potential map (here separately evaluated in SLACCAD) and accompanied by the magnetic field from the grid magnets with a tentative

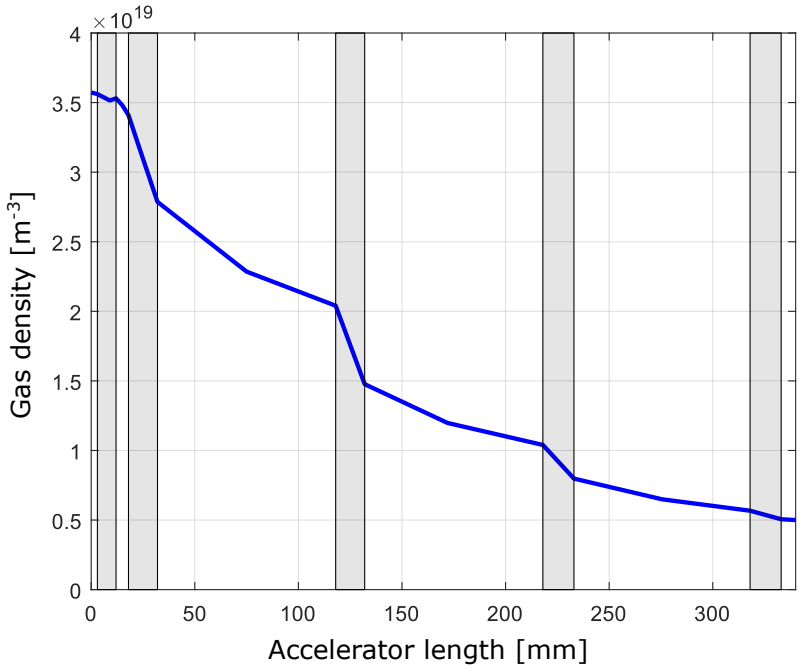

Figure 4.9: Background gas density plot in the MITICA-like assumption. The grey outlines represent the grids' positions.

background gas density profile is able to track secondary particle generation. This is not limited to particle-particle collisions either, but also particle-surface interactions can be evaluated in the case of impact; this makes EAMCC a really comprehensive code to work with in the determination of heat loads.

4.2.6.1 Accelerator gas density

The first step is to hypothesize a background gas distribution. The DTT beam source is rather complex in shape, with a number of tweaks to increase pumping inside the accelerator; an accurate and non-isothermal simulation would require a full-scale model simulation (on a still in some parts uncertain geometry) on a vacuum code tweaked to account for particle-wall thermal interactions (such as the code AVOCADO), which it would be best suited for a later stage of simulation. An interesting first-order approximation is to adapt a previous simulation obtained using AVOCADO for one of MITICA NBI accelerator scenarios, rescaling the result to only the 5 grids of DTT; the profile is illustrated in Figure 4.9. This hypothesis is still quite conservative as gas flow in MITICA is quite high, and a number of design choice improvements to reduce the background gas density are not being considered.

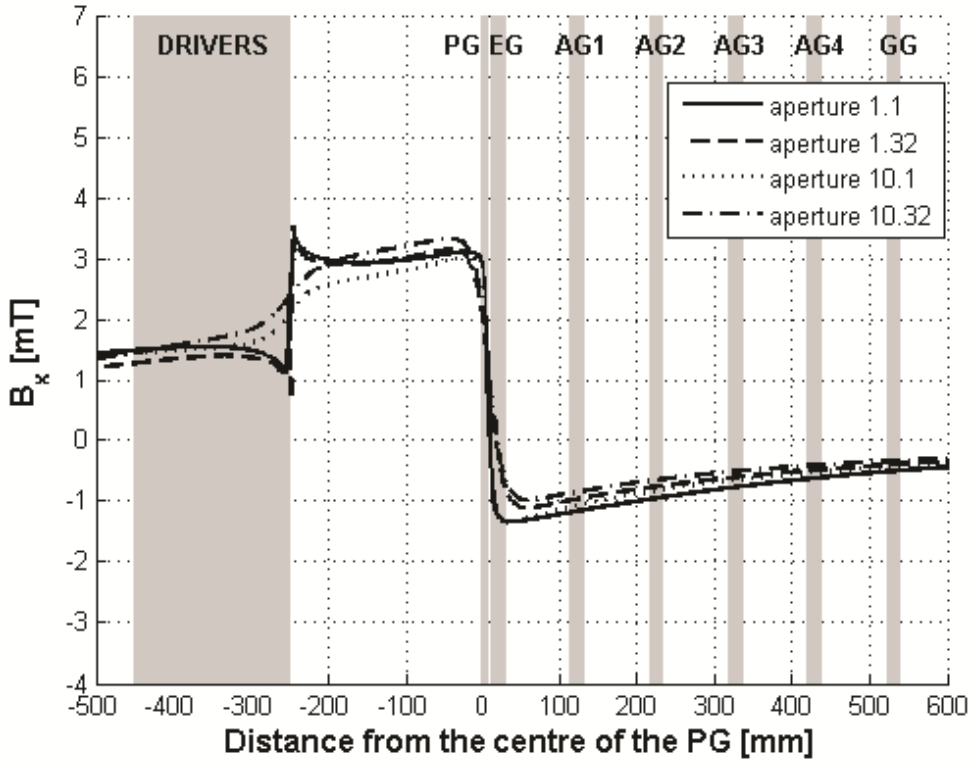

Figure 4.10: Horizontal filter field expected to be used in MITICA NBI. Inside the accelerator an almost constant horizontal field of 1 mT is present [24].

4.2.6.2 Grid heat loads

Next is the actual evaluation of the heat loads on the different grids of the accelerator using EAMCC. The extraction voltage has been fixed at 7.5 kV, corresponding to an exit divergence of about 4.6 mrad. The size of the correction magnets has been altered from the design value that was inherited from the MITICA geometry, since their effect was too strong for the DTT beam. Since the distance between beamlets is not constant on each grid to follow their convergent shape, it is difficult to give now a definitive size estimate. What has been done is working on the relative position of magnets with respect to the beamlet axis on a simple 20 by 22 mm domain. An additional horizontal field created by the filter current flowing in the PG has been added along the whole accelerator in similar way to what is designed to happen in MITICA (see Figure 4.10), helping in deflecting stripped electrons upwards (or downwards, based on the current direction). However, EAMCC only supports cylindrically symmetric geometries, so it is not possible to simulate the effect of CCDE correction by PG shifting, and a little beam interception on the grid is inevitable. The simulation is divided in two separate ones: a first, dedicated only to the deuterium ions, and a second only for the co-extracted electrons, supposing

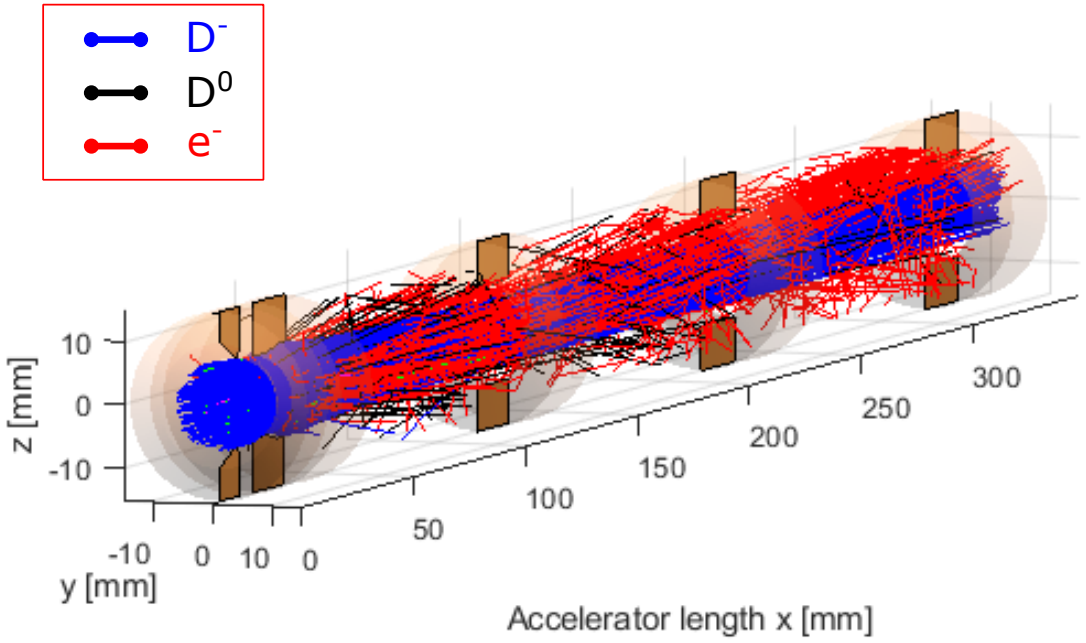

Figure 4.11: Trajectory plot of the EAMCC ion simulation. The electrons are being curved upward by the filter field.

for simplicity that they can be considered separately, and they do not influence each other. The results reported are the sum of the two simulations unless stated otherwise, and are reported in Figure 4.11, 4.12, and 4.13.

The provided gas density profile has proven to be really conservative: the remaining deuterium negative ion fraction is 72 %, which is far from the ideal objective of 80 %, and is mostly linked to the high density in the zone immediately outside the PG, where the stripping cross-section is the highest. The resulting electrons are accelerated up to nominal voltage and generating the greatest part of the heat load, as reported in Tables 4.1 and 4.2.

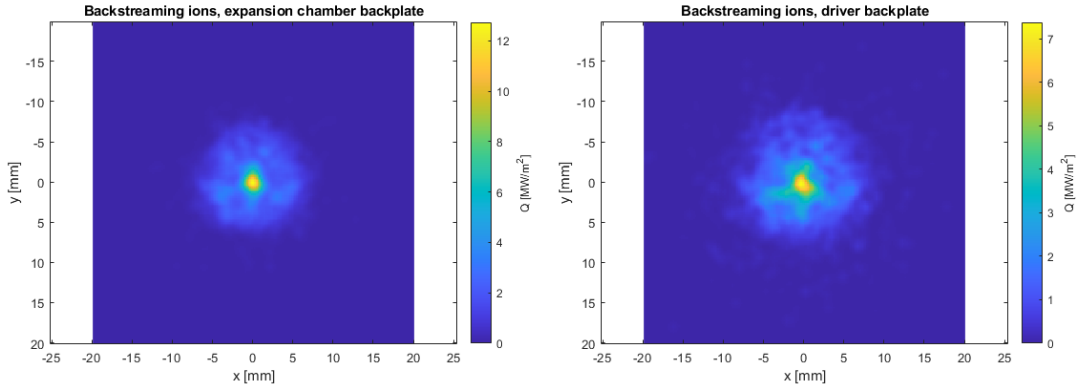

Figure 4.12: Set of plots with the heat load distribution from back-streaming ions on the driver and expansion chamber backplate.

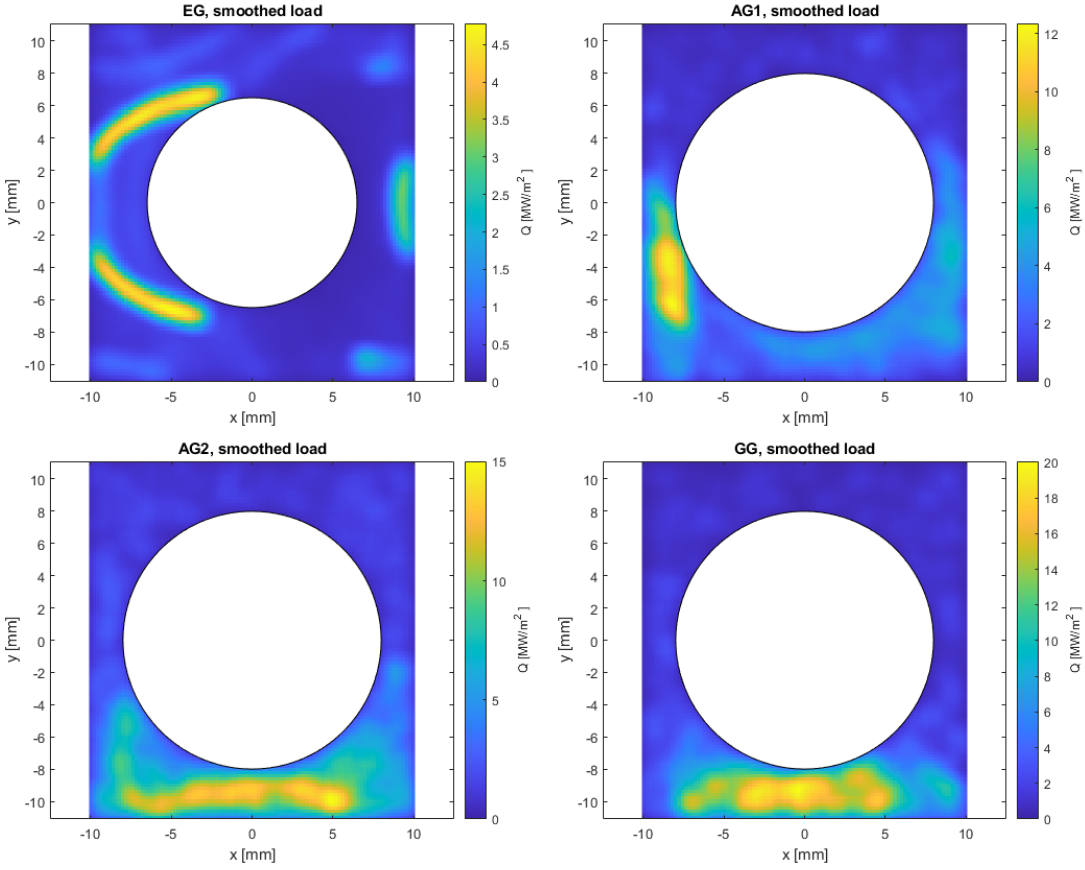

Figure 4.13: Set of plots with the heat load distribution on the accelerator grids.

	EG			AG1			AG2			GG		
	Front	Hole	Back	Front	Hole	Back	Front	Hole	Back	Front	Hole	Back
D^- [W]	0	7	1	13	7	0	9	20	0	8	18	0
D_0 [W]	0	1	0	8	2	0	4	2	0	6	4	0
D^+ [W]	0	1	2	0	0	1	0	0	0	0	0	0
D_2^+ [W]	0	13	12	0	2	3	0	0	1	0	0	0
e^- [W]	249	34	0	618	244	7	993	259	14	1051	224	1
Total	249	56	15	639	255	11	1006	281	14	1065	246	1

Gridwise total	EG	AG1	AG2	GG	Total
Beamlet tot. [W]	320	905	1302	1312	3839
Acc. tot. [kW]	432.2	1230.8	1770.7	1784.3	5221

Ion source load	Beamlet tot. [W]	Acc. tot. [kW]
Back-streaming ions	326	443

Table 4.1: Set of tables reporting the heat load distribution by species and by grid, with the estimated totals for the whole accelerator.

Net Current	Back	PG	EG	AG1	AG2	GG	Exit
Ion sim. [mA]	1.94	0.01	0	-3.1	-3.92	-3.6	-29.82
Coex. sim. [mA]	-0.01	-0.5	-36.16	-1.04	-0.46	-0.19	-0.11
Total [mA]	1.93	-0.49	-36.16	-4.14	-4.38	-3.79	-29.93
Acc. total [A]	2.62	-0.67	-49.18	-5.63	-5.96	-5.15	-40.70

Table 4.2: Net current component on each grid, backplate or transmitted.

4.3 Full-NBI modelling

After the due estimations at the beam source level made in the previous paragraphs, this section is dedicated instead to the NBI in its entirety. The first part is dedicated to a new method to design BLCs, based on the bigaussian approximation for the beamlets, applied to the DTT case. Once established the geometry, the discussion moves onto the vacuum system, the external stray field, and internal heat loads on the BLCs, as inputs and outputs of the full-NBI particle tracing simulation.

4.3.1 The beam-fitting BLC design

The first step to determine the beamline geometry is developing a code parametrizing the BLCs' main dimensions only based on optics assumptions and minimum or fixed quantities, for example a minimum plate thickness or RID length. To start, the neutralizer and RID are subdivided in four equal "sectors", one for each beamlet group, so that only one can be determined and the others obtained by rotation. In this setup, each sector contains a beam channel, with the walls of the neutralizer fins and the RID plates as delimiters. The key component in this work is the adoption of a more detailed approach to BLC modelling: usually, BLCs are designed as simple channels large enough to fit a fixed divergence beam plus some clearance on either side. This approach somewhat ignores how beamlets behave experimentally, and has the disadvantage of not being able to know the interception losses due to beam divergence until after an appropriate particle simulation is run, that can lead to undesired hot-spots in the heat loads. Taking advantage of the conceptual design phase for DTT, a new approach was developed and applied: the beam-fitting design. With this method, each beamlet is modelled through the commonly adopted Gaussian power distribution approach and fully characterized by its $1/e$ divergence ϵ, which is defined as the angle between the main beamlet axis and the locations where its power density function in space is reduced by a factor of $1/e$. If the beam is supposed aligned to the z axis, starting from a point source in the origin, and a symmetric beam is adopted so that $\epsilon_x = \epsilon_y = \epsilon$, the normalized power density space distribution is defined as

$$F(x, y, z) = \frac{1}{2\pi\sigma^2(z)} \exp\left(-\frac{x^2 + y^2}{2\sigma^2(z)}\right), \tag{4.6}$$

where

$$\sigma(z) = \frac{z \tan\epsilon}{\sqrt{2}}. \tag{4.7}$$

Experimental particle beams however are better described by the superposition of two different Gaussian distributions sharing the total power of the beamlet at a given ratio, called the bigaussian approximation: the part of the beam with the more focused particles (thus smaller ϵ) is called *core*, while the remaining part with more ill-focused particles (and larger ϵ) is called *halo*. If f_c and $f_\mathrm{h} = 1 - f_\mathrm{c}$ are the respective beam fractions for core and halo, and F_c, F_h are the two Gaussian distributions characterized by core divergence ϵ_c and halo divergence ϵ_h, each beamlet can be described as

$$F_\mathrm{b}(x, y, z) = f_\mathrm{c} F_\mathrm{c}(x, y, z) + f_\mathrm{h} F_\mathrm{h}(x, y, z). \tag{4.8}$$

In designing a beamline, the most critical aspect to be kept into consideration is the transmission efficiency of the system. This value is ultimately dictated by the most limiting component in size, which in all fusion NBIs is always the connecting duct between the NBI vacuum vessel and the tokamak: the port size and duct must be as

small as possible to fit between the confining magnets, to not disrupt the blanket configuration, reducing neutron fluence, and to limit gas flow between the two.
For a square port (particular case of a rectangular port) of half-width s and at a distance from the point source L, the normalized power transmitted is

$$p(s, L) = f_{\mathrm{c}} \operatorname{erf}^2\left(\frac{\alpha}{\tan \epsilon_{\mathrm{c}}}\right) + f_{\mathrm{h}} \operatorname{erf}^2\left(\frac{\alpha}{\tan \epsilon_{\mathrm{h}}}\right), \tag{4.9}$$

where $\alpha = s/L$.

A small additional step is necessary: since Equation 4.9 supposes a point source for the beam, it is necessary to determine first a starting distance L_{rb} such that, at that distance, the beam reaches a fixed starting beam radius (in this case, $r_{\mathrm{b}} =$ 7 mm); the formula yields a value of about $L_{\mathrm{rb}} = 0.6$ m that should be added to all other distance values when determining slit width.
Equation 4.9 can be numerically inverted, so that for a desired passing power fraction p_{t} at a distance L, the needed slit half-width s_{t} is

$$s_{\mathrm{t}} = s\left(p_{\mathrm{t}}, L\right) = p^{-1}\left(p_{\mathrm{t}}, L\right). \tag{4.10}$$

In DTT the size of the duct exit has already been determined, which in turn fixes the maximum power fraction that can be transmitted through. Determining this value is a little more convoluted than simply applying Equation 4.10, because of the multi-focus aiming strategy. To obtain a simple estimate of the passing power in a multi-focus setting, a single sector is considered (since they are formally equal) and the beamline is imagined "straightened" for simplicity. By drawing in such a setup (illustrated in Figure 4.14) the multi-focus strategy, each beamlet of the group has more space to pass on one side of the central axis, and less on the other. Due to the secondary focus being exactly at half the distance of the primary, this space is exactly the original inter-axis beamlet distance mirrored (d = 20 mm or $2 \cdot \mathrm{d}$ =40 mm). If L_{pf} is the primary focus length and s_{duct} is the half-width of the duct, the passing power fraction can be obtained as follows:

$$p_1 = \frac{p(L_{\mathrm{pf}}, s_{\mathrm{duct}} - 2 \cdot \mathrm{d}) + p(L_{\mathrm{pf}}, s_{\mathrm{duct}} + 2 \cdot \mathrm{d})}{2} \tag{4.11}$$

$$p_2 = \frac{p(L_{\mathrm{pf}}, s_{\mathrm{duct}} - \mathrm{d}) + p(L_{\mathrm{pf}}, s_{\mathrm{duct}} + \mathrm{d})}{2} \tag{4.12}$$

$$p_3 = p(L_{\mathrm{pf}}, s_{\mathrm{duct}}) \tag{4.13}$$

$$p_{\mathrm{tot}} = \frac{2 \cdot p_1 + 2 \cdot p_2 + p_3}{5} \tag{4.14}$$

The beam properties used were those of a bigaussian beam of 85 % to 15 % ratio between core and halo components, with respectively $\epsilon_{\mathrm{c}} = 3$ mrad and $\epsilon_{\mathrm{h}} = 30$ mrad: with the multi-focus aiming strategy and the decided duct size, the expected analytical power transmission is of about 90 %. The value p_{tot} is the driving factor of design, and to make sure that it is respected, none of the components between source

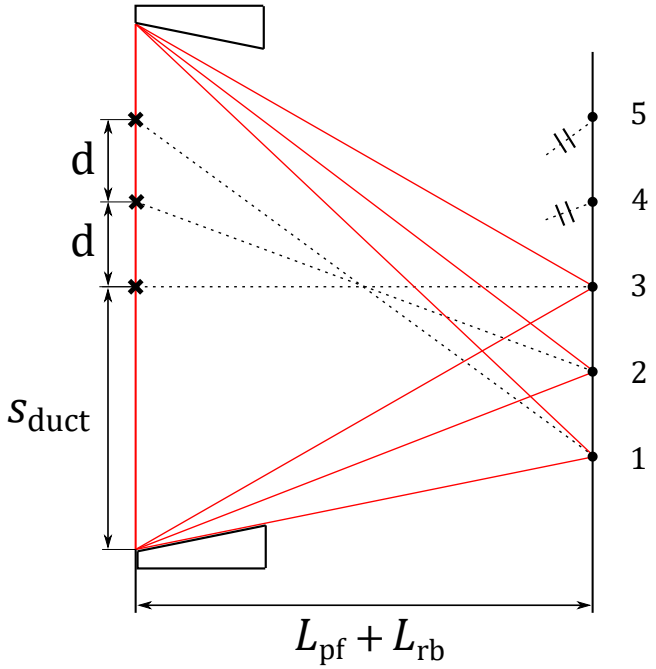

Figure 4.14: Geometry sketch to illustrate the reasoning behind the multi-focus passing power estimate.

and duct exit may scrape more from the beams: in other words, a minimum buffer distance derived from Equation 4.10 (varying as the beam expands along its sight line) from all beamlets' axes must be kept as they travel through the BLCs. An important simplification that can be made is that since the BLCs design consists of very tall but thin channels to reduce internal gas conductance, usually the vertical (y) direction is not an issue until the duct; this means that the BLCs can be designed in 2D without problems.
This decision however affects the p_t, which would effectively increase, given that the duct appears no longer limited vertically; to this purpose, a distinction is made between a $p_{t,\text{tot}}$ and $p_{t,\text{hor}}$, where $p_{t,\text{tot}}$ represents the effective total power transmission in a three-dimensional duct, while $p_{t,\text{hor}}$ represents the same quantity but restricted to the horizontal plane, which is the one that will be used in the design phase. The two are directly related, and for convenience only the latter will be used: whenever p_t is mentioned, it is $p_{t,\text{hor}}$.

4.3.1.1 Geometric procedure

To draw the delimiting surfaces of the BLC channels, two sets of instructions are sufficient: one for the starting edge and another for each successive point. The starting edge is the closest edge of the BLCs to the tokamak (in this case, the RID

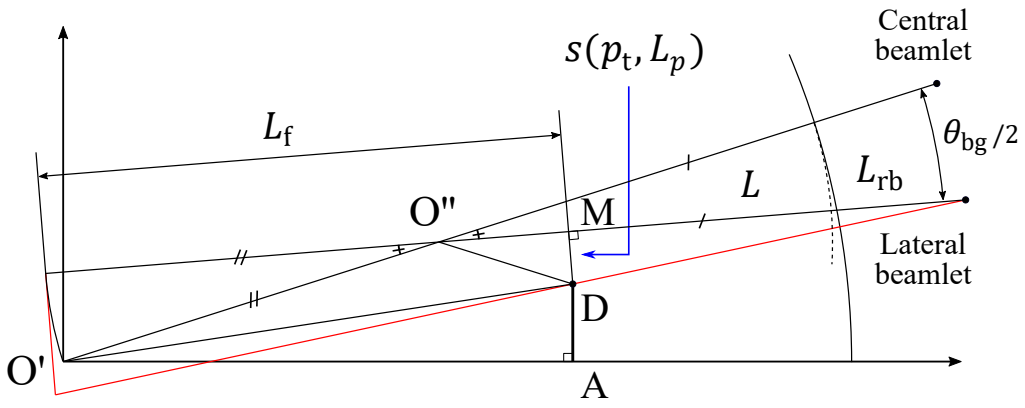

Figure 4.15: Geometry sketch for determining the initial point of the beam-fitting configuration.

plate), that due to the expanding nature of the beam also represents the smallest thickness of the plates; as such, it is one of the boundary conditions and it should be chosen appropriately. By having the independent variable L defined as the sum of the BLCs' (neutralizer and RID) lengths along the lateral beamlet line of sight and choosing the correct p_t (different from p_{tot} in a multi-focus setting), it is possible to determine the necessary wall clearance s of the outermost beamlet of a channel at the distance $L_p = L + L_{rb}$, while the segment $\overline{AD}$ is half of the desired minimum thickness. To complete the sector, the beam group angular span is necessary; said angle is obtained as

$$\theta_{bg} = \frac{\Delta d_{bg}}{L + MO''} , \tag{4.15}$$

where $\Delta d_{bg} = 80$ mm is the inter-axis distance between the first and the last beamlets. Once the remaining distance to the focus point L_f is fixed, the other quantities can be obtained as

$$M\hat{O}''D = \tan^{-1} \frac{s\,(p_t, L_p)}{L_f - O'O''} , \tag{4.16}$$

$$O'\hat{O}''D = 180° - M\hat{O}''D - \frac{\theta_{bg}}{2} , \tag{4.17}$$

$$\overline{O''D} = \sqrt{(L_f - O'O'')^2 + s^2\,(p_t, L_p)} , \tag{4.18}$$

$$O'D^2 = O'O''^2 + O''D^2 - 2 \cdot O'O'' \cdot O''D \cdot \cos\left(O'\hat{O}''D\right) , \tag{4.19}$$

$$\overline{O'A} = \sqrt{O'D^2 - AD^2}. \tag{4.20}$$

The segment $\overline{O'O''}$ is simply the secondary focus distance, and is known; the first point of the configuration is then individuated by $D = (O'A, AD)$.

Any other delimiting point can be obtained by following the second set of instructions:

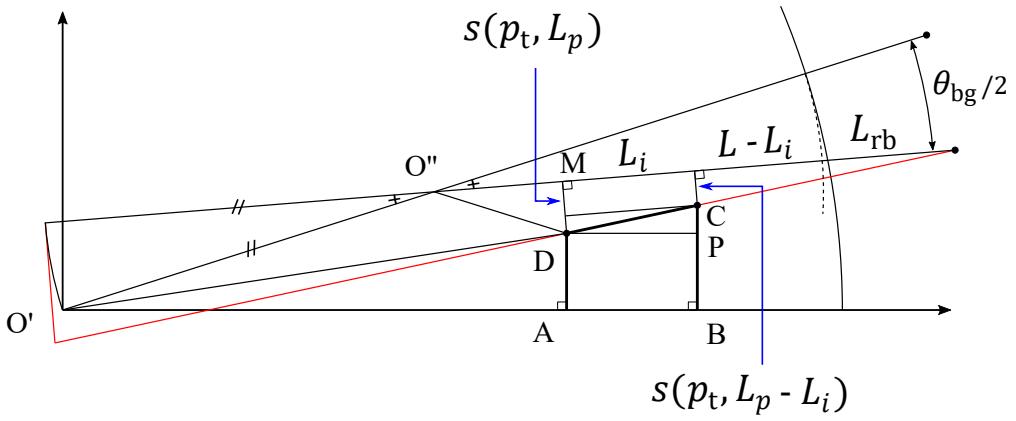

Figure 4.16: Geometry sketch for determining the successive points of the beam-fitting configuration.

if L_i is the length along the beamline of the BLC in question, then

$$M\hat{D}C = \tan^{-1}\frac{L_i}{s\left(p_t, L_p\right) - s\left(p_t, L_p - L_i\right)}\,, \tag{4.21}$$

$$M\hat{D}O'' = 90° - M\hat{O}''D\,, \tag{4.22}$$

$$O''\hat{D}O' = \sin^{-1}\left(\frac{O'O''}{O'D}\sin O'\hat{O}''D\right)\,, \tag{4.23}$$

$$O'\hat{D}A = \cos^{-1}\frac{AD}{O'D}\,, \tag{4.24}$$

$$C\hat{D}P = 270° - M\hat{D}C - O''\hat{D}O' - M\hat{D}O'' - O'\hat{D}A\,, \tag{4.25}$$

$$\overline{CD} = \sqrt{L_i^2 + \left(s\left(p_t, L_p\right) - s\left(p_t, L_p - L_i\right)\right)^2}\,, \tag{4.26}$$

$$\overline{AB} = CD \cdot \cos C\hat{D}P\,, \tag{4.27}$$

$$\overline{CP} = CD \cdot \sin C\hat{D}P. \tag{4.28}$$

The delimiting point is then $C = (O'A + AB, BP + CP)$. To mirror the sector, its angular span is necessary; said angle is obtained as

$$A\hat{O}'D = \tan^{-1}\frac{AD}{O'D}\,, \tag{4.29}$$

$$D\hat{O}'O'' = 180° - O'\hat{O}''D - O'\hat{D}O''\,, \tag{4.30}$$

$$\theta_{sec} = 2 \cdot \left(A\hat{O}'D + D\hat{O}'O''\right). \tag{4.31}$$

By mirroring the $ABCD$ polygon about the center beamlet axis, the final geometry is obtained; the sector (as in Figure 4.17) can be patterned with respect to the centre with an offset of θ_{sec} to obtain the whole horizontal section.

The routine uses the correct set of BLC lengths and distances of L_N (Neutralizer

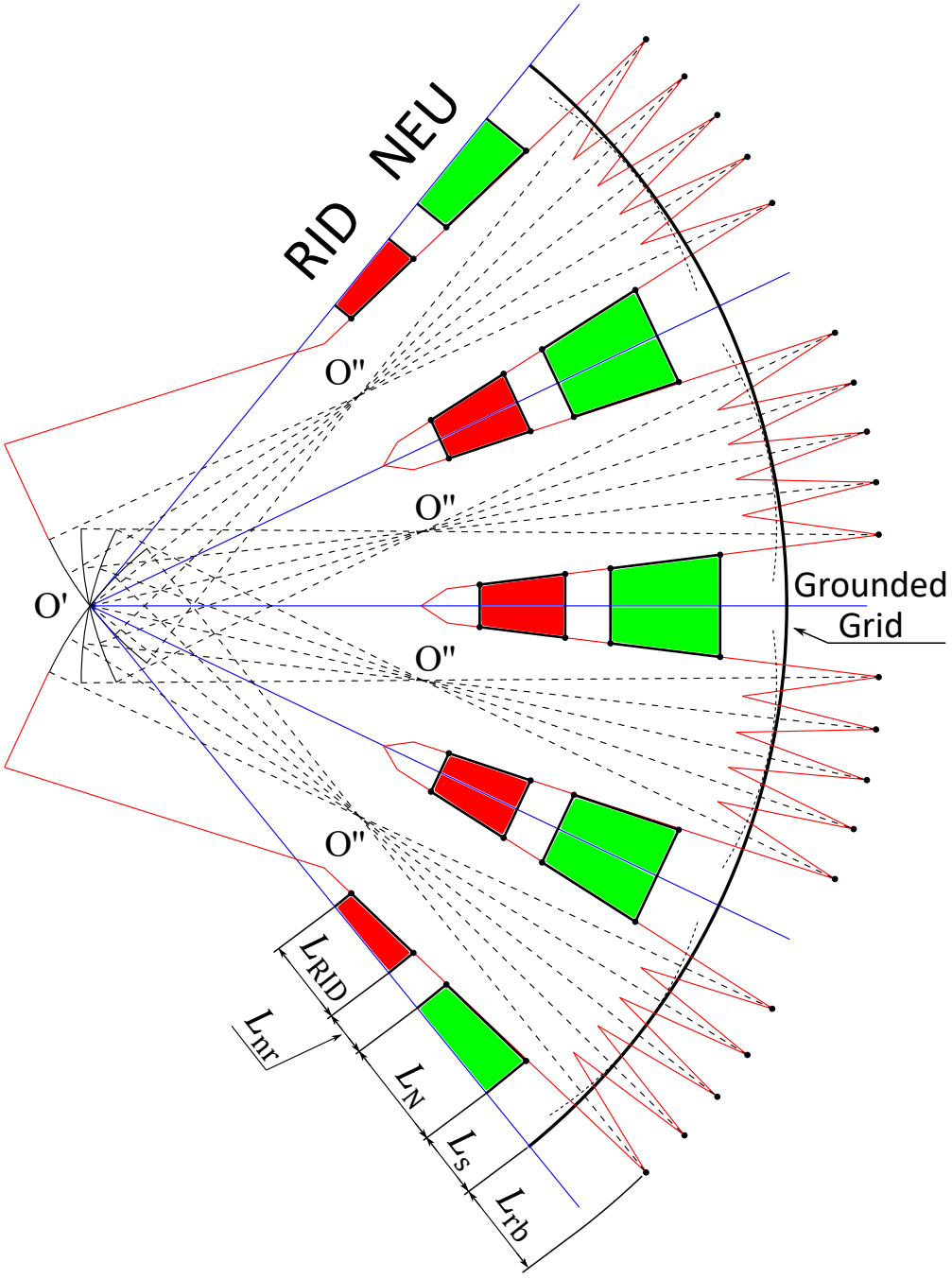

Figure 4.17: Geometry sketch for the entire horizontal section of the beam-fitting configuration.

length), the distance between GG and the neutralizer L_{s}, the distance between neutralizer and RID L_{nr}, and the RID length L_{RID}. The resulting geometry was the basis for the complete three-dimensional CAD developed for DTT.

4.3.2 Vacuum analysis

The next important aspect to consider from the operational standpoint is the distribution of pressure inside the vacuum vessel of the NBI. Its importance stems from the need of keeping pressure as low as possible to avoid undesired ionizing reactions, while maintaining an average pressure in the neutralizer of about two orders of magnitude higher than the rest to maximize neutralization. As it was mentioned, to achieve such a feat the beam itself is organized in vertical thin blades, so that the neutralizer may have a low-conductance cross-section and gas may tend to stay more inside the component, increasing the average pressure; all the while NEG pumping modules are displaced to concentrate pumping in key areas, such as the duct intake port.

The simulation takes place once again in COMSOL using the angular coefficient method, a Boundary Element Method (BEM) formulation applicable to the molecular regimes which combines view factor computation (typical of thermal radiation problems) between elements to the cosine law of emission for incident particle fluxes [25]. The result is a map of values containing the distribution of the particle fluxes, pressure, and density; said map can be extended to out of boundary points for internal evaluations in post-processing (i.e. the beam flight-line).
The beams must travel for almost 12 m, where the details of few centimetres on the grids and components are quite irrelevant and needlessly memory-intensive to incorporate; an extensive simplification of geometry has been done, maintaining only the most important features.

The sources of gas in this system are several:

- The principal obviously is the neutralizer gas outlet, as mentioned before; the quantity is subdivided between the separate slits and must be calibrated to obtain the ideal target thickness for the neutralization reaction at this particular energy (500 keV), that is the integral of particle number density along the flight line of the beam.

- Secondly, source of gas is the beam source itself, since it uses gas to produce plasma; the same extraction apertures behave then as gas outlets, contributing negatively to accelerator performance with premature neutralization, all the way into the vacuum vessel. A commonly used, overestimated value for this throughput is 2.8 Pa m^3 s^{-1} at 0° C.

- Another important source of gas is the tokamak itself, but it is very hard to obtain an estimate of the entity of the gas intake, given the complexity and

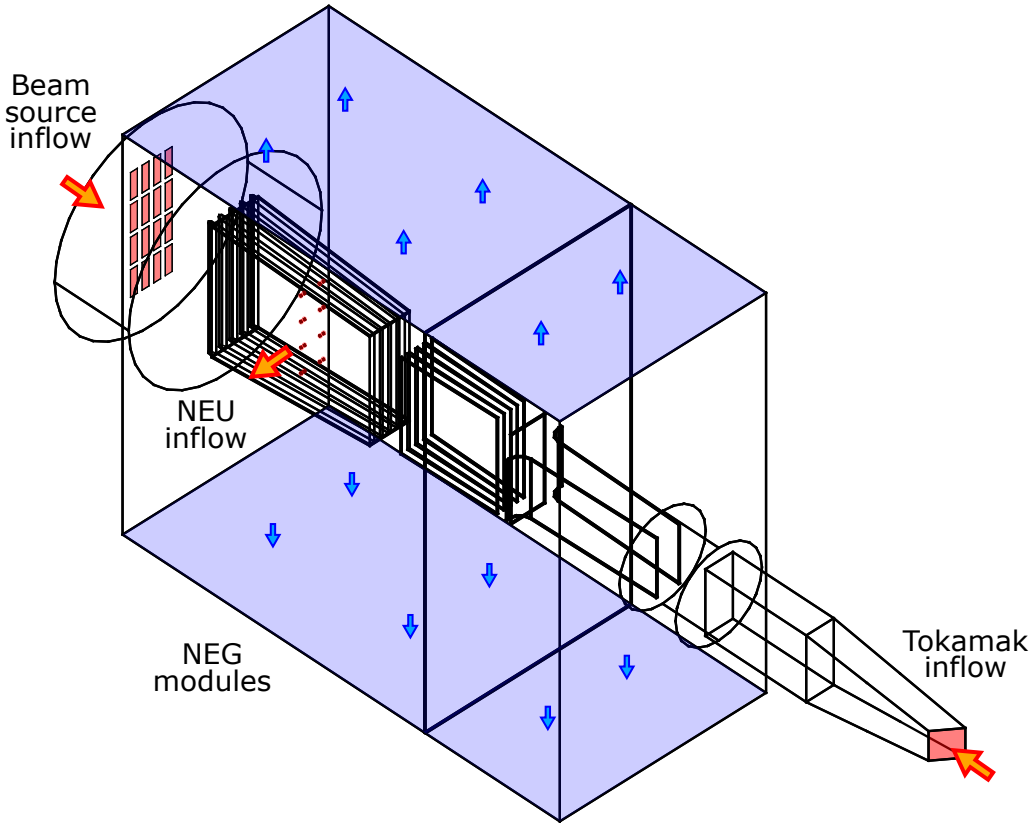

Figure 4.18: Simplified geometry of DTT NBI used in vacuum simulations.

variability of plasma edge simulations and possible working conditions. The argument deserves its own paragraph and is discussed later.

- A difficult to evaluate contribution is the one from gas detached from the walls by impinging particles, since it is tied to optics and external fields and is distributed along the whole NBI. It is usually safe to forego the contribution from optics given its small value, in favor of the contribution arising from the impinging re-ionized beam in the duct region.

As for the gas sinks, the upper and lower surfaces of the vessel are considered covered in NEG pump modules, with a tentative capture coefficient of 0.1; to enhance the effect of pumps near the duct entrance, where the beam is more subject to re-ionization, a gas baffle has been placed at the exit of the RID to separate the two regions: this limits the effect of the neutralizer gas in the duct region, lowering the average pressure in the duct itself. The simulation geometry is illustrated in Figure 4.18.

Parameter at port	Value
Avg. atomic specific flux (D^0) [$m^{-2}s^{-1}$]	7.131×10^{20}
Avg. molecular specific flux (D_2) [$m^{-2}s^{-1}$]	1.512×10^{20}
Atomic temperature (D^0) [eV]	1.62×10^3
Molecular temperature (D_2) [eV]	5.64

Table 4.3: Deuterium species at tokamak port.

4.3.2.1 Plasma Edge boundary conditions

The boundary conditions at the plasma edge near the tokamak were refined using data obtained from plasma scenario simulations in DEMO, kindly provided by F. Subba of EUROfusion WPPMI. Between the different expected gases inside the tokamak, the main interest for duct losses is on deuterium: knowing this, the expected fluence of deuterium atoms and molecules at plasma edge has been given. The data is the result of an axisymmetric plasma equilibrium, averaged along the first wall on a 20 cm square region, centred at the equatorial plane ($z = 0$). Values are reported in Table 4.3.

The presence of atomic deuterium generated from tokamak reactions adds complexity to the vacuum model, and so it does the information on gas temperature, changing in principle the whole formulation of the problem to accommodate for heat exchange between walls and particles. This is quite hard to accomplish, requiring data on how much energy particles can exchange per hit (the accommodation coefficient k_{ac}); and requiring being able to track how, as it thermalizes, the atomic deuterium forms molecules: as it stands, an ideal "correct" solution would not be as simple as considering the two species separately and summing the contributions. Even if the contribution of atomic deuterium is ignored, the calculation may be relatively easier, since no reactions now happen alongside the duct; however, the temperature difference, transpiration and the thermalization process are still present.

A simplification can be made by applying some conservative reasoning and using these facts:

- The reionization cross-section for atomic and molecular deuterium are different: 2.890×10^{-21} m^2 for D^0 and 6.278×10^{-21} m^2 for D_2.
- In a vacuum, when gases at different temperatures come in contact, *thermal transpiration* happens (see Figure 4.19): since gas density is inversely proportional to the square root of the temperature, as the gas cools down along the duct the density rises, up to the point of thermalization. From there on, the problem to solve is again isothermal.

Taking these statements into account and assuming a "fast" thermalization of incoming particles, it is possible to imagine for the whole process to happen just outside the

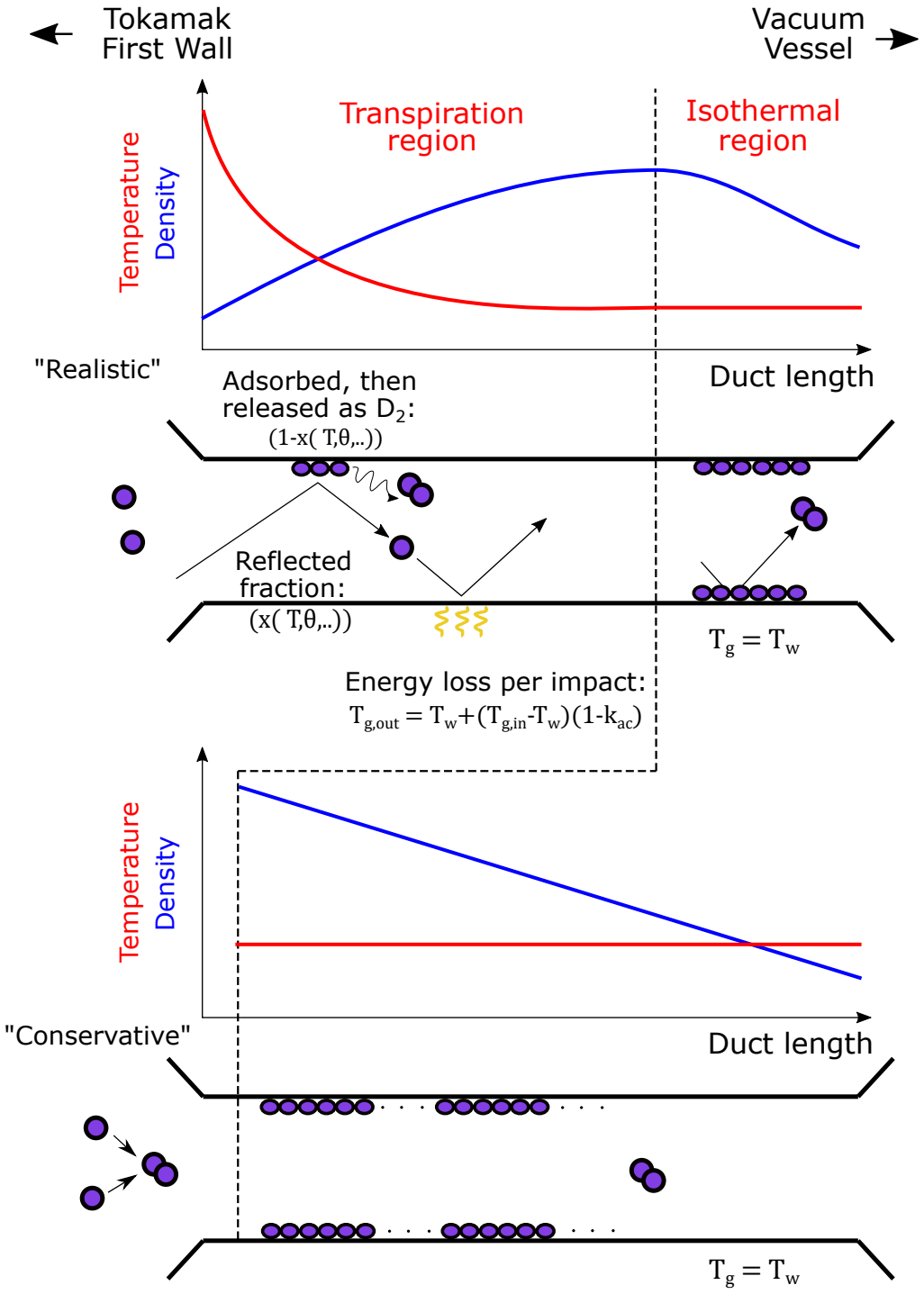

Figure 4.19: Scheme detailing the simplifications of this approach to the problem. $T_{g,out}$ and $T_{g,in}$ are the gas temperatures after and before a wall impact, T_w the wall temperature, k_{ac} the accommodation coefficient. The transpiration zone is concentrated at the duct port, while keeping the calculated flux constant.

duct on the tokamak first wall, and for the atomic deuterium to fully react into molecules there as well. In practice, this would mean to halve the atomic D specific flux contribution (since they fully reacted into molecular form), consider only one species (D_2), and to have an isothermal problem again. This can be considered conservative since the problem is now being solved in a "colder" state with respect to the ideal one, meaning higher densities; and, because the gas species left of the two is the one that reacts easier with fast neutrals, also higher losses.

Carrying out the calculations using the numbers in Table 4.3: by combining J_{D^0} and J_{D_2}, the total specific flux $J^*_{D_2} = \frac{J_{D^0}}{2} + J_{D_2} = 5.077 \times 10^{20}$ m^{-2} s^{-1} is obtained. Multiplying by a port area of about 0.264 m^2, the molecular flux $\Phi^*_{D_2} = 1.340 \times 10^{20}$ s^{-1} is obtained. This value is equivalent to a throughput at 0°C of $Q^*_{D_2} = \Phi^*_{D_2} \cdot k_B \cdot 273.15$ K $= 0.505$ Pa m^3 s^{-1}.

This throughput value can then be used in the vacuum simulation as a boundary inflow from the tokamak. Still, this is a rather rough approximation: gas in vacuum is obviously better approximated where the temperature is fully modelled. Some numerical codes are able to keep track with additional degrees of freedom for incoming and exiting gas temperature on walls (for angular coefficients methods) usually requiring iterative solutions, or accurate modelling of energy transmission per impact of the test particles (in Monte Carlo codes).

4.3.2.2 Target thickness

Established all of the above, before the calculation of the density profile, only the neutralizer throughput needs to be addressed, and that is established by looking at the ideal *target thickness* for a 500 keV beam. Using the COMSOL isothermal model through subsequent simulations, the value is adjusted in order to obtain the ideal target thickness from the Grounded Grid apertures up to the end of the neutralizer. The optimum target thickness in the model used is achieved by imposing a throughput at 0°C of 21.7 Pa m^3 s^{-1}. The resulting number density along a beam line of sight is reported at Figure 4.20. All this information will then be exported and used in the determination of heat loads with a successive particle tracing simulation, where the probability of reaction is evaluated at each time step using the local density value.

4.3.3 Stray field compensation

A tokamak magnetic system is by definition composed by a main toroidal coil system providing the principal confinement for the plasma, and a poloidal (vertical and radial) coil system dedicated to provide flux swing, vertical stability, shape control, etc.. The toroidal system aims to approximate a perfect toroidal configuration, but by obviously having only discrete sets of coils, part of the field "leaks" through the gaps, creating the so-called ripple field which causes additional plasma losses; this field however decays quickly with increasing radial distance, so it is not a problem for far enough devices. However, this is different for the poloidal system, whose

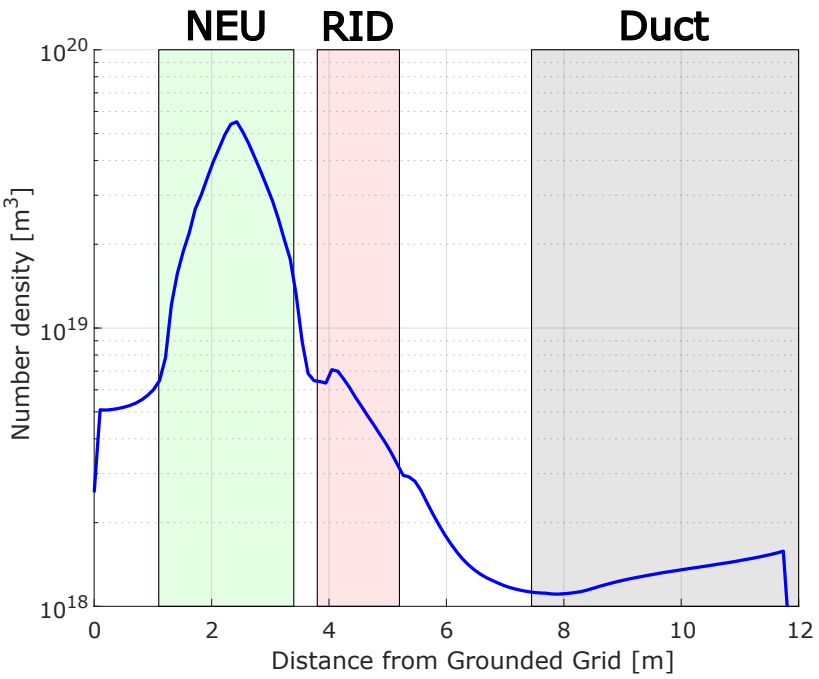

Figure 4.20: Result of the vacuum simulations using the aforementioned boundary conditions.

solenoidal structure allows for free expansion of the magnetic dipole field around the tokamak, with the field decaying slowly. This field is referred to as the *poloidal stray field* (Figure 4.21). Due to the nature of their operation related to fast, charged particle beams, NBIs are particularly susceptible to external electromagnetic fields; when coupled to a large tokamak where high magnetic fields are a requirement, issues regarding charged beams are bound to arise. This is especially true for DTT, where the NBI is being positioned fairly close to the tokamak (within about 7 to 15 m from the magnetic axis), while being subjected to scenarios devised to be ITER and DEMO-like. Confirmation about the entity of this problem was obtained during the first particle tracing simulations, which made use of a full map of the tokamak's magnetic field to determine wall power losses on the Beam Line Components (BLCs): the field was confirmed strong enough to deflect 99 % of the beam upon the neutralizer; the remaining 1 % being the part of the beam that managed to neutralize before being deflected in the short space between the Grounded Grid (GG) and the neutralizer. This motivated a significant research programme to identify a method of suppressing the stray field effect.

4.3.3.1 Stray Field Shielding System

The correction for the stray field has been already implemented to various degrees in all existing operating tokamaks featuring NBI such as JT-60 [26] and ASDEX-UG

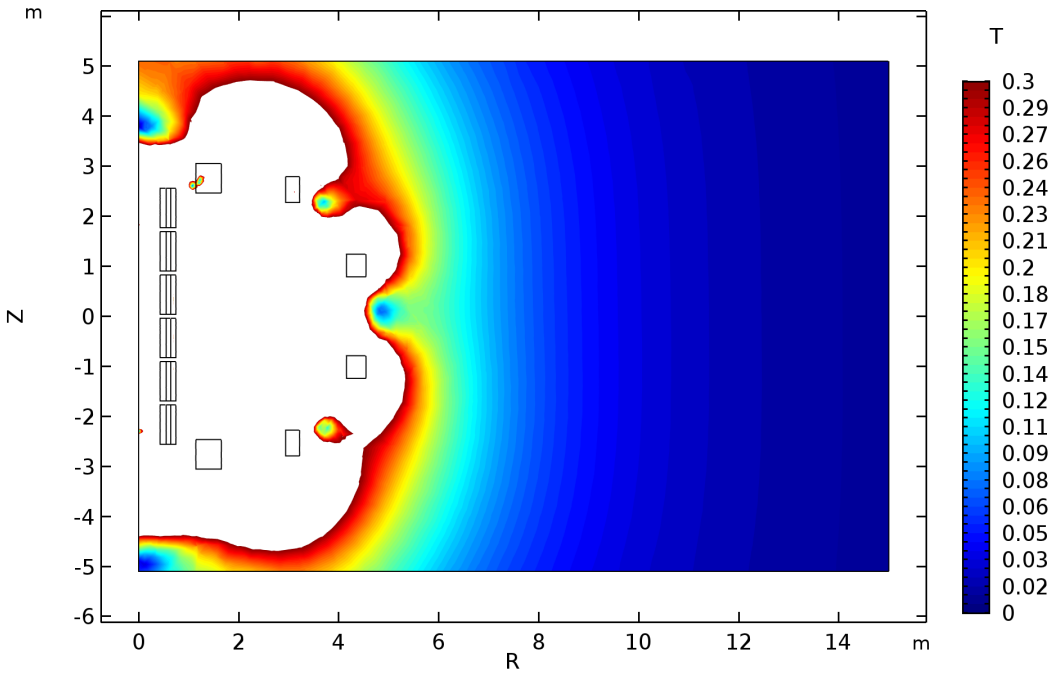

Figure 4.21: Contour plot for the absolute value of the magnetic flux density, showing the extension of the poloidal stray field. The value range is limited to appreciate the field in the farthest region.

[27], and ITER NBI itself is going to feature a large Magnetic Field Reduction System (MFRS) [28, 29]; the DTT version will be denominated Stray Field Shielding System (SFSS). All of the considered design solutions are based on one of the following systems, or both (illustrated in Figure 4.22):

- A passive ferromagnetic structure (Passive Shield, PS), dedicated to re-routing the field around the desired regions.
- If that is not enough, also an Active Coil (AC) system to suppress the constant "error" given by the passive shield and to follow the evolution of the stray field as it evolves in time during a discharge.

The region that these shields need to protect is usually the one where charged particles are present, meaning the beam source, the electrostatic accelerator, and the neutralizer, until the Residual Ion Dump (RID). For the scope of this paper, the region to shield has been restricted to the region after the GG, since the beam source and the accelerator are complex components that require their own specific set of codes to evaluate external effects; these regions will be object of a separate work. The ideal placement of these components depends on each particular case:

- Outside the vacuum vessel, occupying more space and needing to enclose

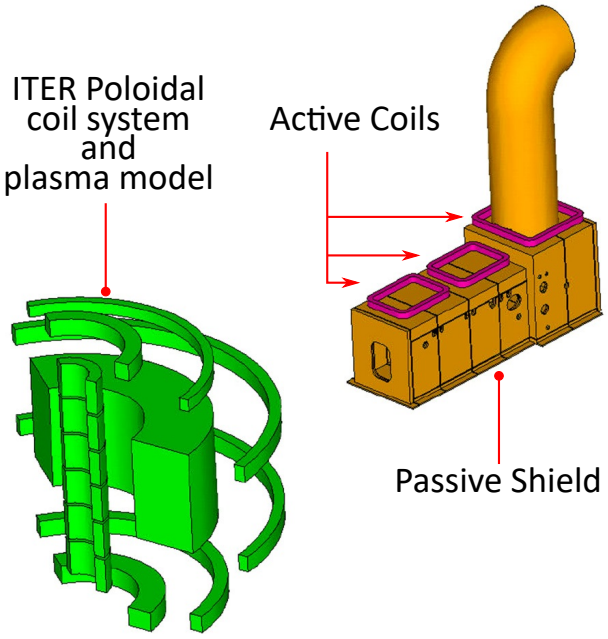

Figure 4.22: An older ITER MFRS design [29] as an example of a stray field compensation system.

regions larger than needed, but with no drawbacks on the beam itself and easily accessible.

- Inside the vacuum vessel, minimizing the region to shield, but with potential issues due to the beam operation, e.g. obstruction of gas flow, voltage holding, coil feed-through if used, etc..

In the case of DTT NBI the space constraints, the air-insulated beam source requiring a large external clearance, and the possible adverse effects of having a large iron mass very close to the tokamak fields, make the use of passive external shielding unattractive.
Efforts in designing the SFSS concentrated around this fact, producing a series of proposed designs which are the object of the paper:

- The first design is an external active coil system, which is very useful in determining the entities of the quantities at play needed to suppress the stray field; referred to as the "reference" case due to its status of first solution proposed.

- The second design is a fully passive internal shield, wrapping tightly around the interested region; it was proposed to analyse the possibility of avoiding coils entirely.

- The third design is the combination of the second design with additional active coils (located in this case inside the vacuum vessel), in order to increase the minimization of the stray field.

Each of the designs will be described in detail in the following paragraphs.

4.3.3.2 Problem setup

Before going into the detail of each design, the simulation procedure is described. First, the poloidal stray field must be obtained: to achieve this, a sector of the DTT tokamak (one sixth) containing the outline of DTT NBI has been modelled using the commercial multi-physics Finite Element Method (FEM) code COMSOL®. The simulation is a linear magnetostatic problem, to shorten computational time. The material used in the passive structures is always the same iron model material, characterized by a relative permeability of $\mu_{Fe} = 4000$.

To limit the volume needed to properly simulate the tokamak without edge effects, the model is set up to have an axisymmetric coordinate system ($\mathbf{i}_\phi$ for toroidal direction, $\mathbf{i}_r$ for radial, $\mathbf{i}_z$ for vertical), with symmetry conditions placed at the two section planes delimiting the simulation domain, while the upper, lower and rear side of the domain contain a special layer called *Infinite Element Domain*, wherein the mesh elements are artificially scaled up in length during calculation to emulate a very large domain for a fraction of the volume. An example domain is reported in Figure 4.23. To calculate the stray field, information is needed on the particular scenario that is being implemented, and since the coil currents vary considerably for the same scenario, also the time of the discharge considered must be specified. Given the preliminary nature of the work, it was decided to focus on the baseline Single Null (SN) DTT scenario, and to simplify the computational effort, only the time of maximum field within the NBI (found to be immediately after the phase of flat-top, at $t = 89$ s) was considered.

Once established the boundary conditions of the tokamak, the type of SFSS to test must be chosen: if the design features a Passive Shield, its geometry is added to the model to determine the new resulting stray field distribution. The field within the whole NBI is not necessary at this step, so a small subset enclosing the space between the GG and after the Neutralizer (where the charged beam will travel through) is individuated and denominated the *evaluation volume* V, which will be the target of shielding and field minimization. If the design features Active Coil(s), they are also added to the model; however the procedure for choosing the correct set of coil currents needs to be considered. To do this, a separate simulation for each coil or coil pair imposing a test current of 1 A when all of the other sources are turned off is carried out, and the resulting field within the evaluation volume V is exported for each one.

During exploration of the stray field shape and strength, the vertical component B_z was found to be predominant within the NBI region, as a consequence of the

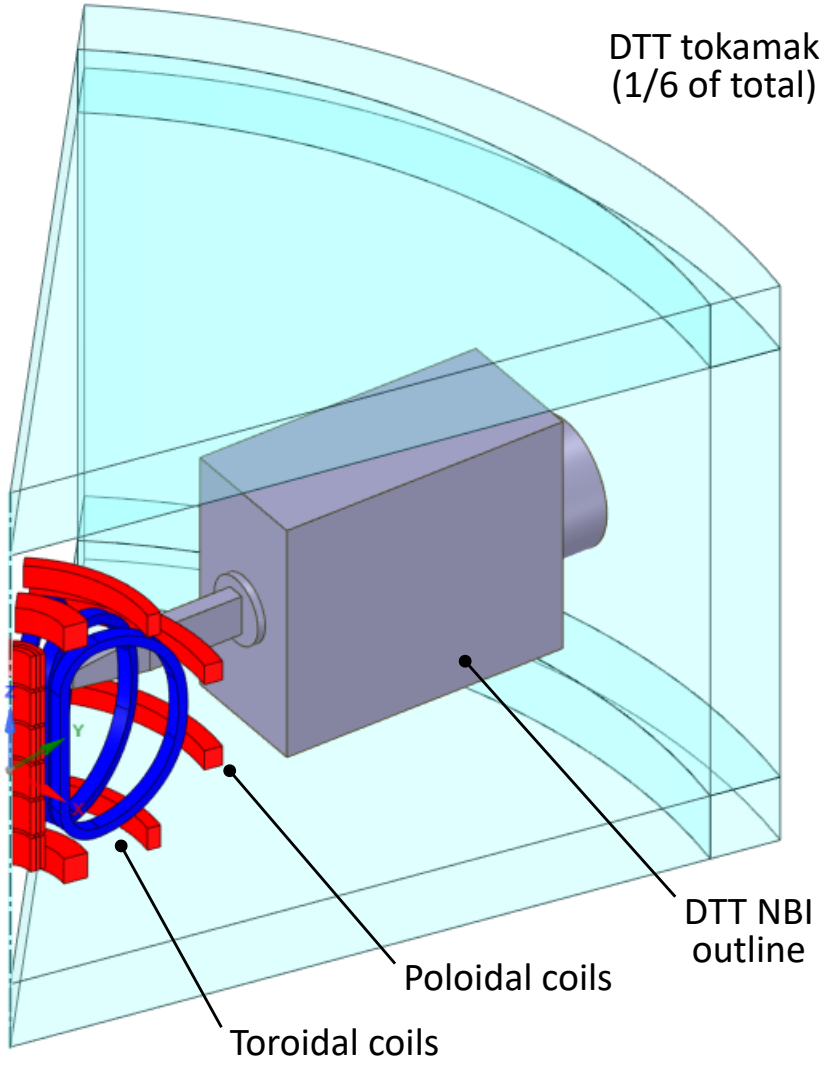

Figure 4.23: Simulation domain of the magnetostatic problem in COMSOL.

NBI location along the equatorial plane ($z = 0$). Coupled with the fact that this component is the main responsible for the particle losses on the tall and thin walls of the Beam Line Components (BLCs) due to its sideways deflection, it is safe to restrict the scope of minimization to only the B_z component of the stray field. In linear conditions, this allows to directly scale the coil fields by the imposed currents and add them to the stray field for each point within the volume V. This results in an overdetermined system of the type

$$\sum_{i}^{N_c} B_{c,i_z}(P) \cdot I_{c,i} + B_{s_z}(P) = 0, \ P \in V \tag{4.32}$$

where N_c is the total number of coils or coil pairs, $B_{c,i_z}(P)$ is the vertical field generated at point P per each ampere of current through the i-th coil, $I_{c,i}$ is the current flowing to the i-th coil and $B_{s_z}(P)$ is the vertical field generated at point P by the stray field. To minimize this system various optimization methods can be utilized; in this case, the fastest way to obtain a result is to simply look for the least squares solution to the system: the current vector $\mathbf{I_c}$ thus obtained can be used for one final simulation with all field sources are active, and the whole NBI field exported.

In parallel, if the chosen SFSS has internal components, the neutral gas distribution may be affected, and needs to be recalculated to later estimate the correct beam evolution: COMSOL allows to simulate the vacuum system as well. The formulation used by this code is an isothermal angular coefficient method, which treats gas flow akin to radiation exchange: the code calculates the view factors between elements and models diffusion off of the walls using a cosine law of reflection.

The final step is to combine the exported compensated field and gas distribution in a full-NBI particle tracing simulation (the exact same type that will be described in the dedicated section), where it is possible to evaluate directly the efficacy of the chosen SFSS configuration by the most important quantity: the neutral power successfully transmitted to the plasma (Figure 4.24). This aspect is the basis of the main figure of merit used in this work, the *compensation efficiency* η_{stray}, defined as

$$\eta_{stray} = \frac{P_{pl}}{P_{pl,\,\text{no-field}}} \tag{4.33}$$

where P_{pl} is the neutral power reaching the exit of the NBI duct, and $P_{pl,\,\text{no-field}}$ is the same quantity calculated in a completely stray field-free case: this number can be used as an additional factor within the efficiency tower to obtain the NBI wall-plug efficiency and is tied to each specific SFSS. If the value is satisfactory, then other quantities come into consideration such as current magnitude needed (if active), encumbrance, saturation, etc.. The calculated value for $P_{pl,\,\text{no-field}}$ that will be used is 9.94 MW.

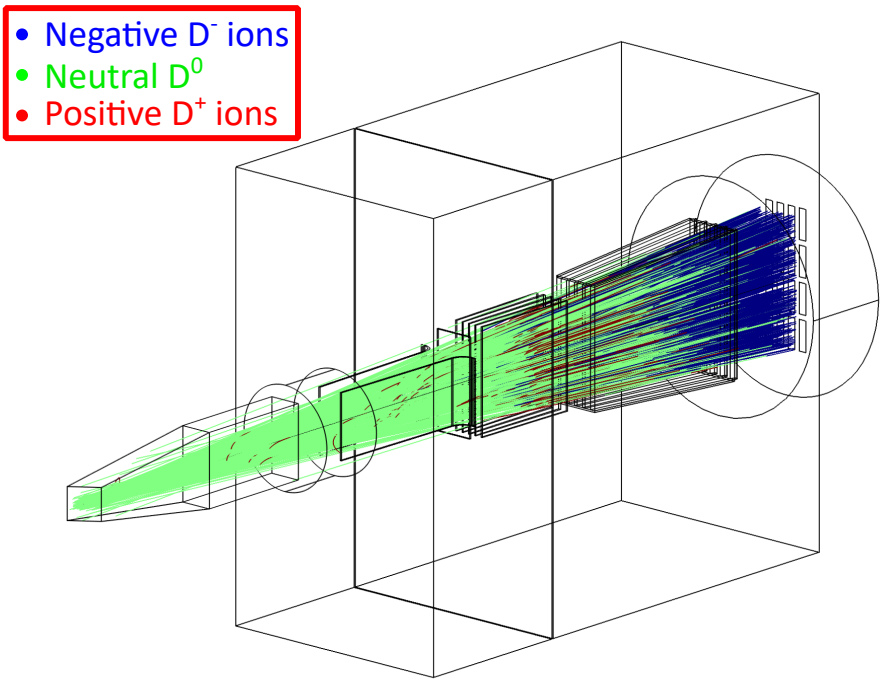

Figure 4.24: Result of a particle tracing simulation in COMSOL.

4.3.3.3 Case 1: external nested Active Coils

This design was the first functioning result that was found during the early design phase, when passive shields were still not being considered for simplicity, and the effort was aimed at finding a solution external to the NBI vacuum vessel: this would be quite desirable to avoid accessibility issues and to avoid disrupting the internal gas flow. At the time the whole simulation procedure described in the earlier paragraph had still not been fully developed: the 3D field was obtained from a poloidal snapshot of the SN scenario, then artificially adding the toroidal field. This explains the different placement of heat loads for this case, especially in the duct region; since this is only a reference case anyway a conformation of the models was not done, the most important part being anyway the poloidal field. The solution comprises 4 pairs of nested coils, a larger one with other three placed within side-to-side. The geometry is detailed in Figure 4.25. Each coil pair works in Helmholtz configuration (same current and orientation), and their particular geometry allows them to follow accurately the shape of the stray field; unfortunately, to achieve this precision, the main external coil pair and the other three work antagonistically, leading to extremely high design currents. Other pairings were tried in order to try and cancel this antagonistic relation, but none other managed as good a result as this one. The optimized coil currents are reported in Table 4.4; the compensation efficiency is an impressive $\eta_{stray} = 0.987$.

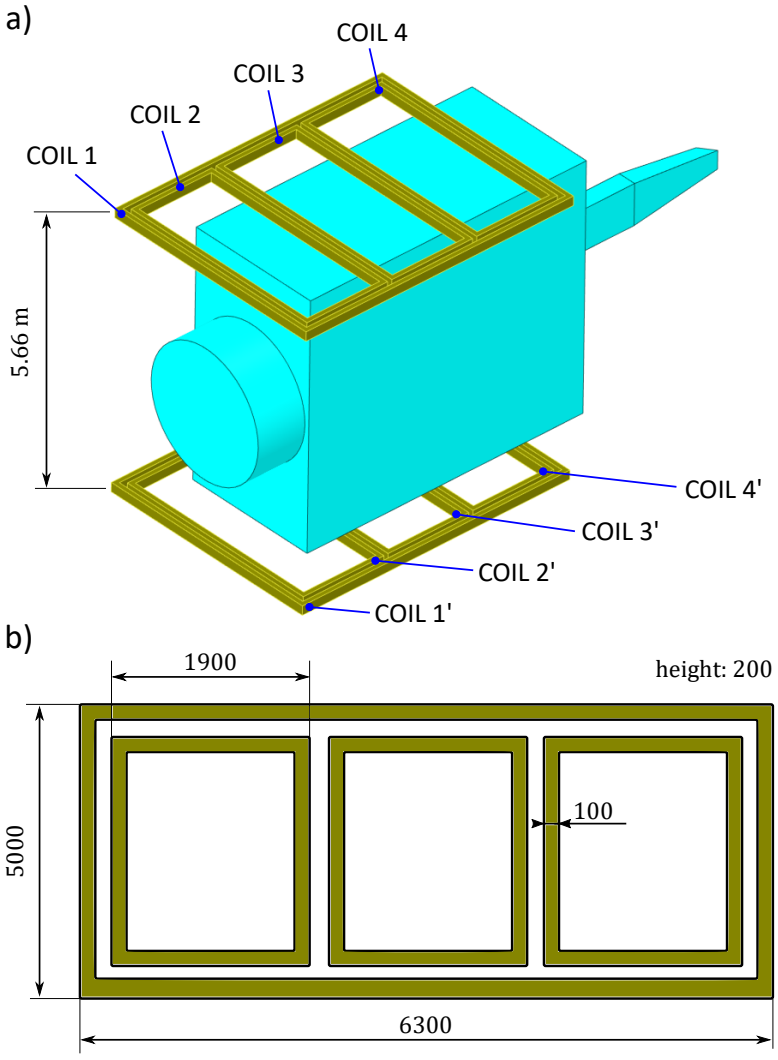

Figure 4.25: Case 1, a) View of the external coil system applied to DTT; b) detail of the coil dimensions (not to scale).

Coil pair	Design currents [kAt]
Coil 1 - 1'	644
Coil 2 - 2'	-657
Coil 3 - 3'	-636
Coil 4 - 4'	-479

Table 4.4: Design currents of Case 1. The sign of the currents depends on the orientation of the external field.

4.3.3.4 Case 2: internal Passive Shield

This design is the diametrically opposite approach to the previous: after realizing that any external coil would need very high currents to produce meaningful correction effects due to the large distance between them (the vessel is about 5.5 m tall), the option of introducing passive shields was taken into consideration. Still, when deciding whether using a large, external shield or a smaller, internal one, the issue of field leakage within the shielding region became apparent: to put it simply, when a shield encloses a region but presents an aperture on its surface, the magnetic field will "leak" inside for a distance proportional to the smallest dimension of said aperture. For an external shield, this means that the whole vessel should be covered in iron, leaving only the duct aperture, or that at the very least the shield should overextend over the desired volume V to minimize for the leakage. Both of these options however would require a massive amount of iron near the DTT tokamak, which is not acceptable; internal shields were therefore considered. Apertures must still be present to allow beam passage, but leakage can be controlled by overextension after the neutralizer, and application of a *Barrier Grid* (BG) on the GG (Figure 4.26). This BG will rest on the GG with apertures large enough to not affect the beam, serving as a "lid" to the rest of the shield in a very delicate zone that otherwise would be subjected to unmitigated field leakage.

As mentioned before, having an internal shield changes the background gas distribution; especially in this case, where the shield is wrapped tightly around the neutralizer, the flow to the pumps in the zone between GG and neutralizer is completely blocked, potentially causing issues of premature stripping inside the accelerator due to increased gas density. To mitigate this, an array of apertures is foreseen all around the shield, their radius chosen as to reduce leakage while allowing gas flow to a suitable degree. The result is an almost perfect insulation of the shielded region, and quite promising for a fully passive system (with compensation efficiency $\eta_{stray} = 0.961$). A quick scan of the diameters for apertures on the shield individuated a 100 mm diameter as sufficiently limiting field leak; on the sides, apertures are placed and offset as to maximize empty space while avoiding saturation. The apertures did help in decreasing the gas density outside the GG (to about 50 % more than the original case) but the gas flow from the neutralizer still had to be adjusted in order

to have the ideal target thickness and maximize neutralization.

4.3.3.5 Case 3: internal PS and AC system

The last design considered is an improvement upon the second case: the Passive Shield is the same, while adding a single Active Coil pair in Helmholtz configuration. Their geometry follows the shield in its inclination and is tailored to fit within the beam source aperture with no mechanical interference (Figure 4.27). The result of increased complexity is improved field minimization: $\eta_{stray} = 0.981$. The most important positive aspect is that now only one pair of coils is sufficient, and that the required current to minimize the worst-case field is 33 kAt, one order of magnitude less than the external coil design, due to them being far closer now.

4.3.4 Particle tracing simulation

All of the previous steps, namely the geometry definition, the neutral gas density distribution, and stray field compensation, are necessary inputs for the full-NBI particle tracing simulation in COMSOL. This overarching, all-encompassing multi-physics simulation takes all of the aspects that interact with the particle beam, and it can give extremely important feedback on the goodness of the previous design choices, as well as providing an important input for the designers, the expected heat load distribution.
The simulation is a time-dependent one, where a pre-established number of macro-particles N are launched in the domain with an initial energy E_{beam} and direction based on divergence and aiming strategy. Each macro-particle represents a flow of real particles, based on the original imposed extracted current I_{ext}. These particles are subjected to the Lorentz force while moving in an electromagnetic field, while at each time-step a fraction of the beam is neutralized or ionized with an algorithm based on local gas density and cross-section to derive the reaction rate ν. Their final point of impact is collected and averaged for each element composing the geometry, obtained the desired heat map. The total heat load depends on the background gas density, while the heat load distribution is mainly determined by the external electromagnetic fields: the maps will change depending on the plasma scenario, the time of the discharge, and also when switching SFSS types. To keep the results as simple as possible, the same field conditions as the ones used in the SFSS exploration will be used; however, this does not mean that during the rest of the discharge more critical hot-spots may not arise even with a reduced field. Time-dependent results will be explored more in detail in the future, once that a final SFSS design will have been chosen. The simulation consists of two separate instances, one for the negative deuterium ion beam and another for the transmitted electrons, described in the next paragraphs.

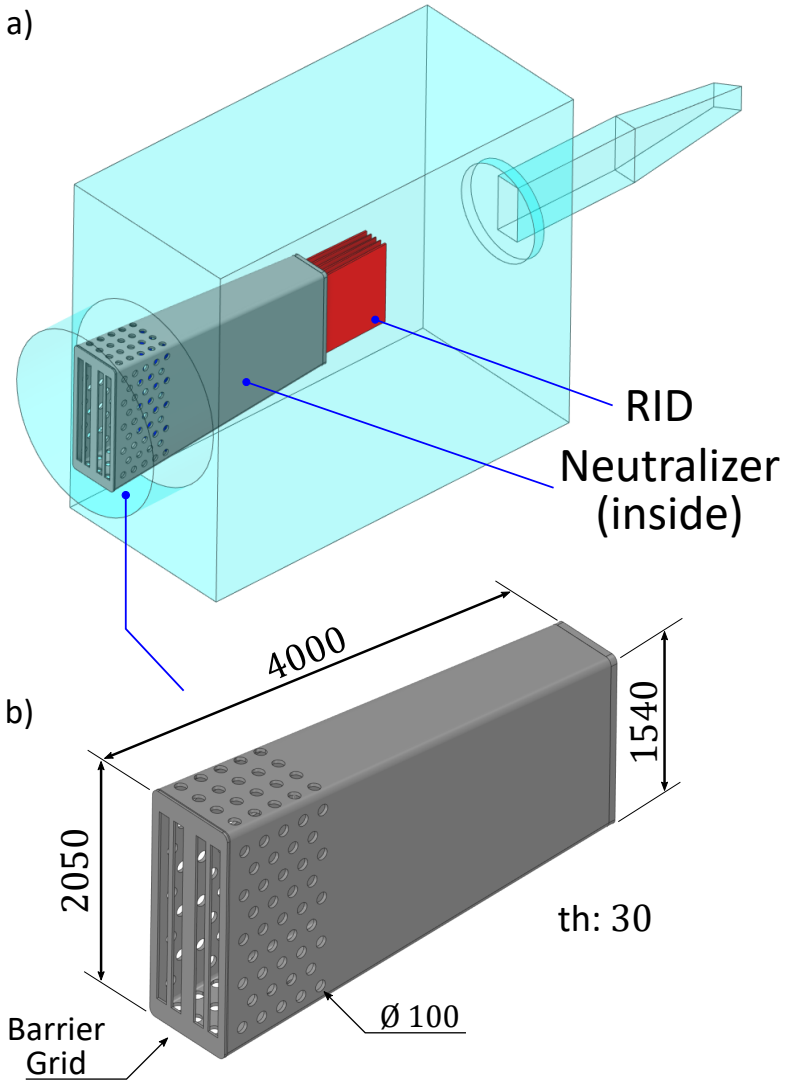

Figure 4.26: Case 2, a) View of the internal passive shield applied to DTT; b) detail of the shield.

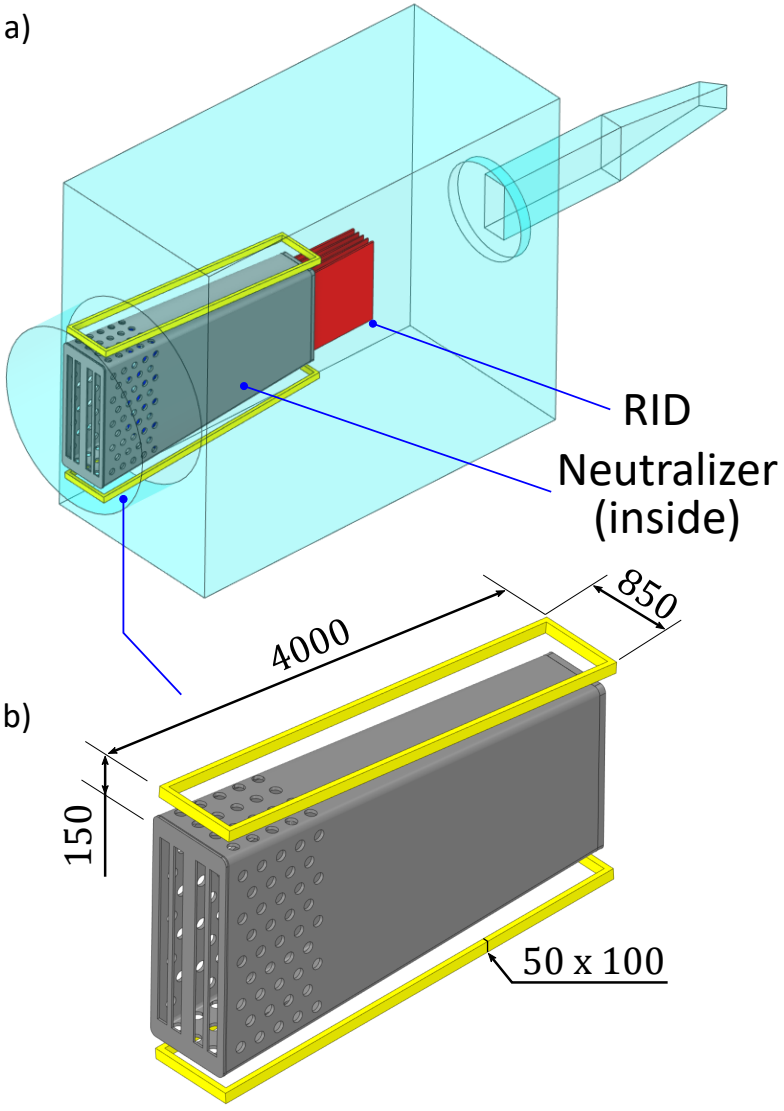

Figure 4.27: Case 3, a) View of the internal combined active and passive compensation applied to DTT; b) detail of the internal coil geometry.

4.3.4.1 Deuterium beam heat load simulation

Aside from the already discussed boundary conditions, for the deuterium beam there are a number of additional ones that need to be implemented, mostly regarding the beam structure and initialization:

- The particles' position and direction are derived by starting from a 2D-Gaussian velocity distribution, its width dictated by the $1/e$ divergence chosen for the beam and peak related to the 510 keV energy, and truncated at 3σ to avoid particles with impossibly wide trajectories.
- Each beamlet is composed by a core and halo fraction in a 85 % to 15 % ratio and different divergences, with each of their guiding centres laying on the surface of a spherical GG and aimed following the multi-focus strategy.
- The total current assigned to the particles is 40 A, equal to the current extracted from the 1360 apertures (radius 7 mm) with an extracted current density of 250 A m^{-2} and an extraction efficiency of about 0.8. This current is also subdivided between core and halo components, with their respective fraction.
- The external fields considered are the one generated by the RID at 8 to 15 kV (depending on the compensation type) and the already discussed poloidal stray field of the tokamak.

4.3.4.2 Transmitted electrons heat load simulation

Transmitted electrons are the results of either stripping reactions that happen all along the accelerator, or the result of surface detachment from neutral impacts near each one of the grids. This means that the electrons that manage to exit the accelerator have a peculiar energy distribution, starting from very low energies (electrons generated late) all the way to nominal energy (generated deep in the accelerator) with very sharp peaks near the energies corresponding to the grid potentials; the majority of them with casual directions. This makes the simulation process only slightly more complex with respect to the deuterium ion beam case, since particles do not have the same velocity and positions cannot be decided arbitrarily. It was decided to use the already available output from the EAMCC code from Section 4.2.6, which is able to give a snapshot of the particles exiting the accelerator. Filtering for electrons, it is possible to use this data as the input for the heat load simulation, with the due observations:

- The particles per beamlet in EAMCC are far more than the heat load code can handle, it is necessary to reduce the number of electrons while maintaining the energy distribution. To do this easily the electrons are sorted by increasing energy, then picking one each x times such that the resulting set is at least under the maximum number of particle allowed. The resulting energy distribution is reported in Figure 4.28.

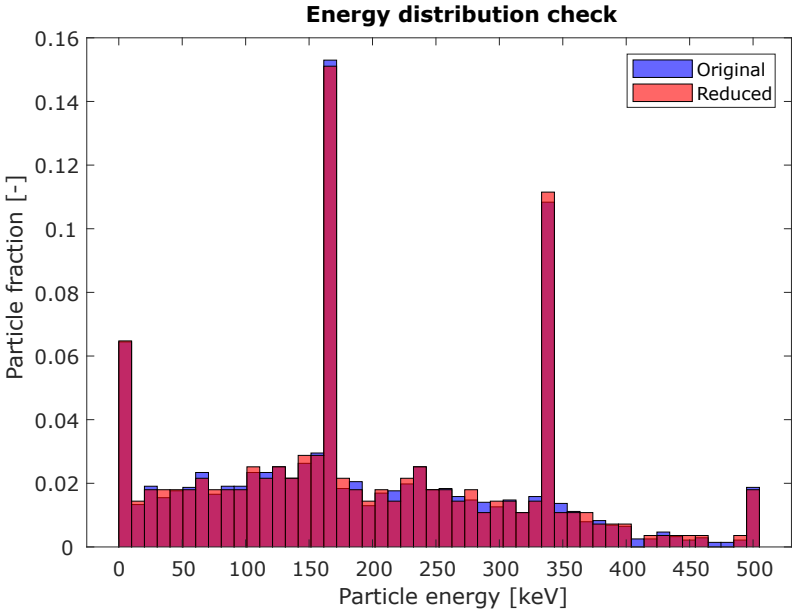

Figure 4.28: Particle energy distribution before and after the sample reduction. The purple zone indicates the overlap between the two distributions, which is almost complete.

- Simply arraying the resulting set of starting points and velocities over the GG would lead to blatant non-physical concentrations of heat loads, so randomization is absolutely necessary, as it was done for the deuterium beam. This time however both positions and velocities are already determined, so randomization should come in small perturbations to the original set. The positions were shifted randomly around a 1 mm circle, while the velocities were shifted randomly around a 5° spherical sector, paying attention to maintain the magnitude. Both randomizations are uniform. On top of these perturbations, the usual horizontal and vertical aiming contributions due to the grids must be added. The final result is illustrated in Figure 4.29.

- The last step is determining the current fraction carried by these electrons in order to compute the release frequency. In this particular case in EAMCC 50000 starting negative ions were used, and 2778 electrons reached the exit. This means that electrons are carrying $\frac{2778}{50000} \cdot 100\% = 5.56\%$ of the total current.

The simulation can then be run for a limited runtime: this is due to the small mass of electrons, that makes them more susceptible than ions to the external fields, and thus their gyration orbits can take longer to track; also, since a lot of electrons have very small energies, it would take a very long simulation time to reach an end surface. Taking this into consideration, the simulation is stopped after 50 μs, when the majority of the energetic electrons has stopped. The only BLCs that are

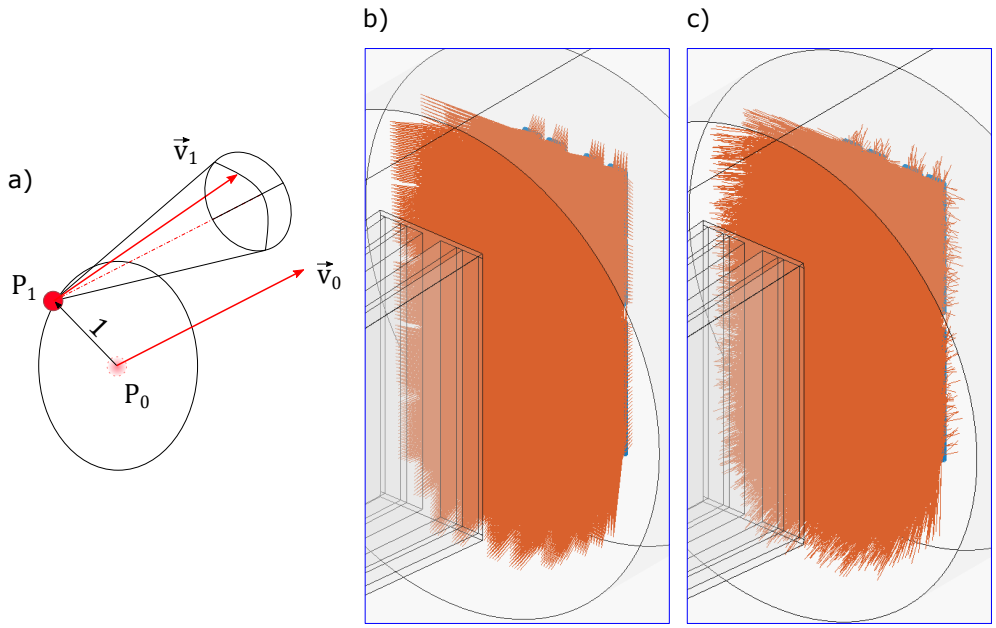

Figure 4.29: Example of the randomization process for the electrons. a) illustrates the procedure for a particle, while b) and c) show the particle distribution before and after the randomization procedure.

significantly interested by the electron loads are the neutralizer and the passive shield, when present; while some electrons may travel across the vessel to the RID or even the walls of the vessel itself (if there is no passive shield) their impact on heat loads are fairly limited and shadowed by the far larger deuterium loads.

4.3.4.3 BLC heat load distribution results

This section contains the heat load maps on the BLCs for the different SFSS designs (Figures 4.30, 4.31 and 4.32) and those for the beam duct (Figures 4.33, 4.34 and 4.35), as well as the total power balances (Tables 4.5a, 4.5b and 4.5c). A particular case is that of the simulation for the calorimeter (Figure 4.36), that has been performed without field to obtain the nominal case of the expected beam footprint.

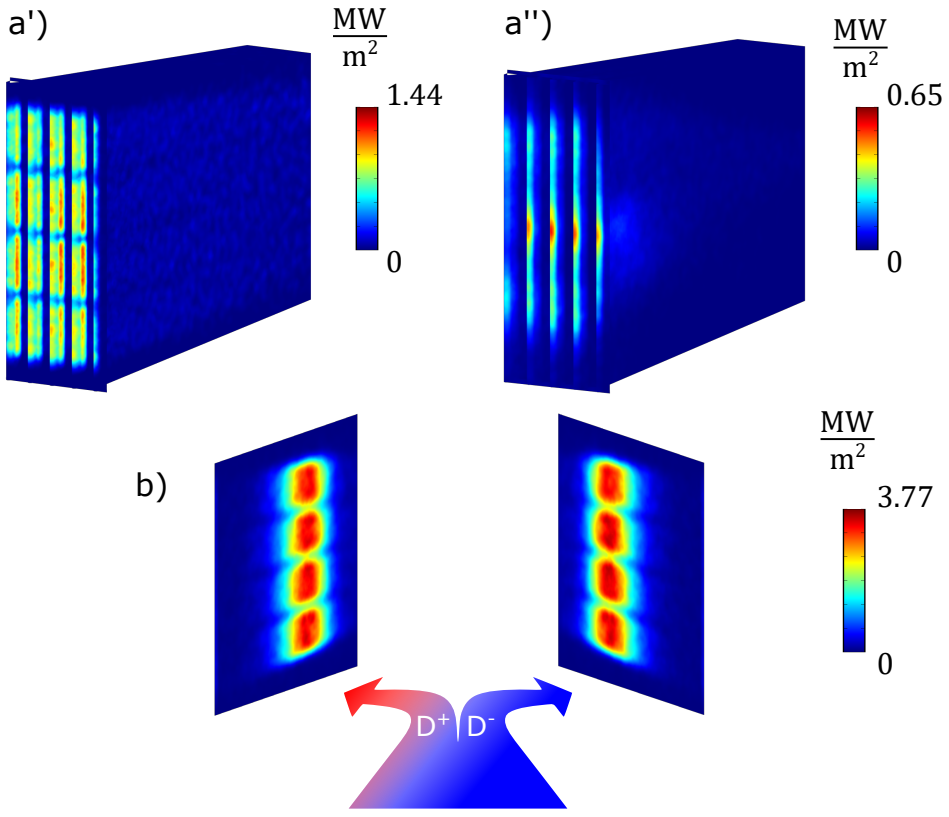

Figure 4.30: Heat load maps for Case 1: a') Deuterium heat loads on neutralizer; a") electron heat loads on neutralizer, b) Heat loads on two plates of the RID.

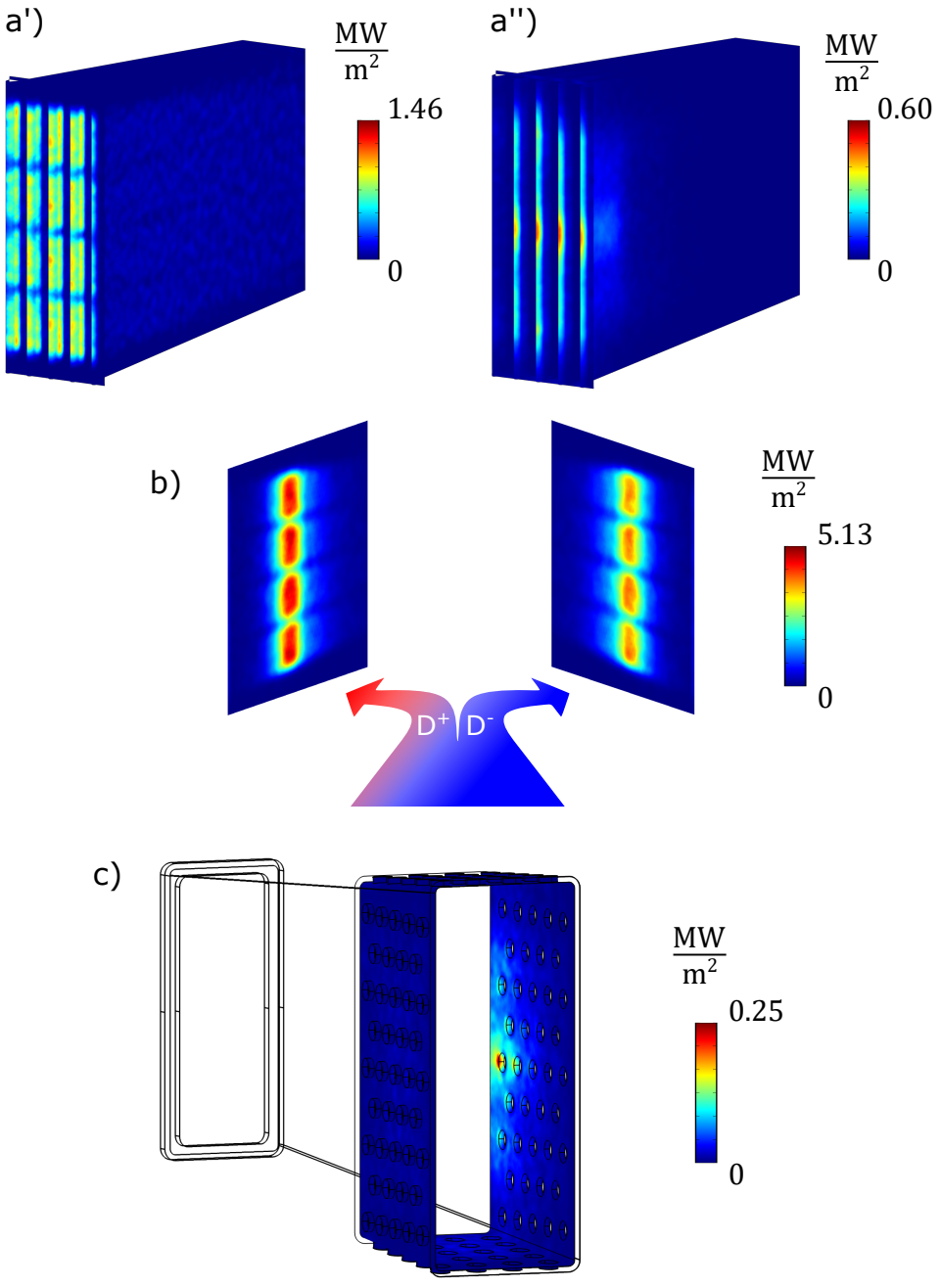

Figure 4.31: Heat load maps for Case 2: a') Deuterium heat loads on neutralizer; a") electron heat loads on neutralizer, b) Heat loads on two plates of the RID, c) Electron load on the internal shield.

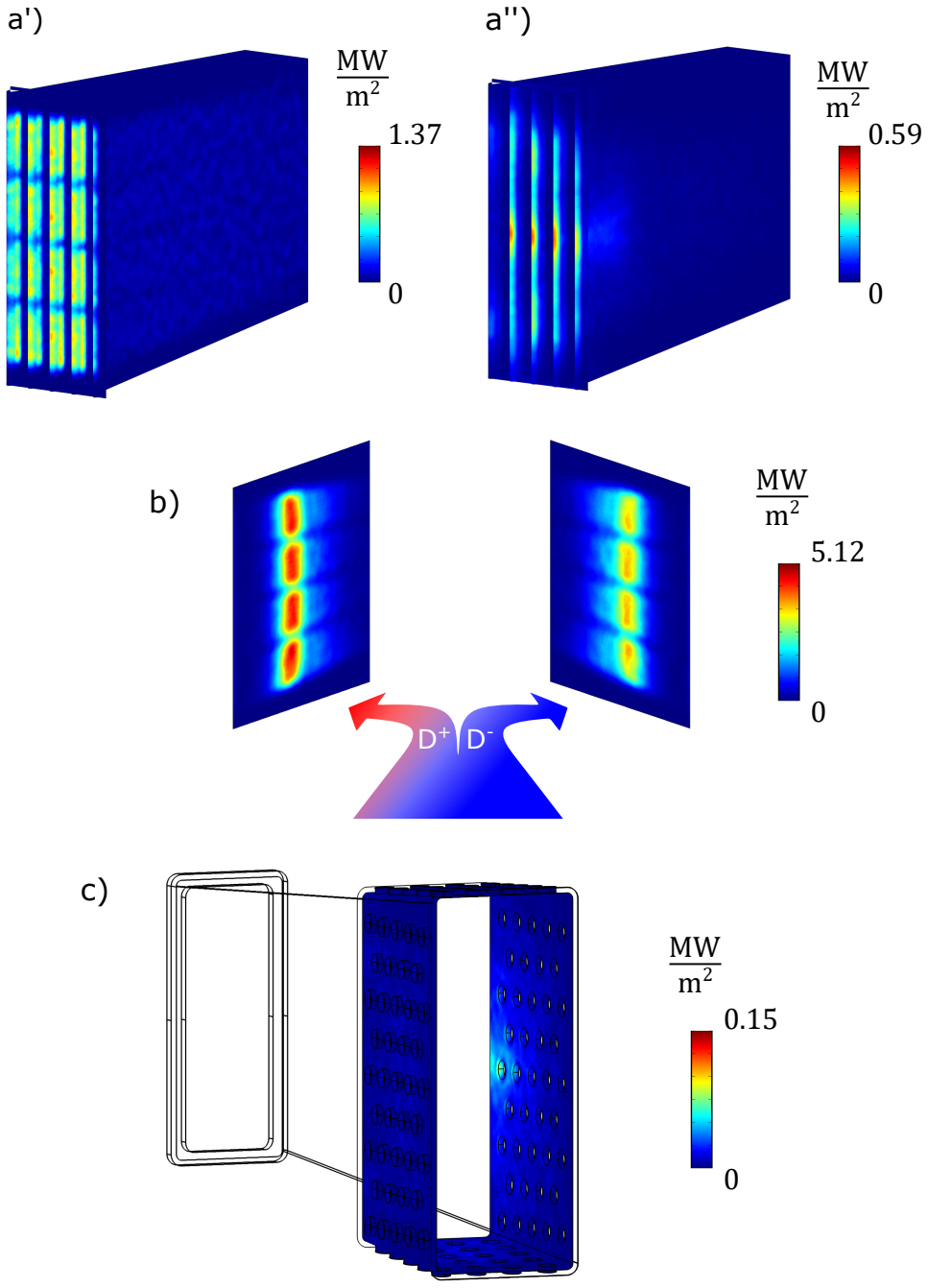

Figure 4.32: Heat load maps for Case 3: a') Deuterium heat loads on neutralizer; a") electron heat loads on neutralizer, b) Heat loads on two plates of the RID, c) Electron load on the internal shield.

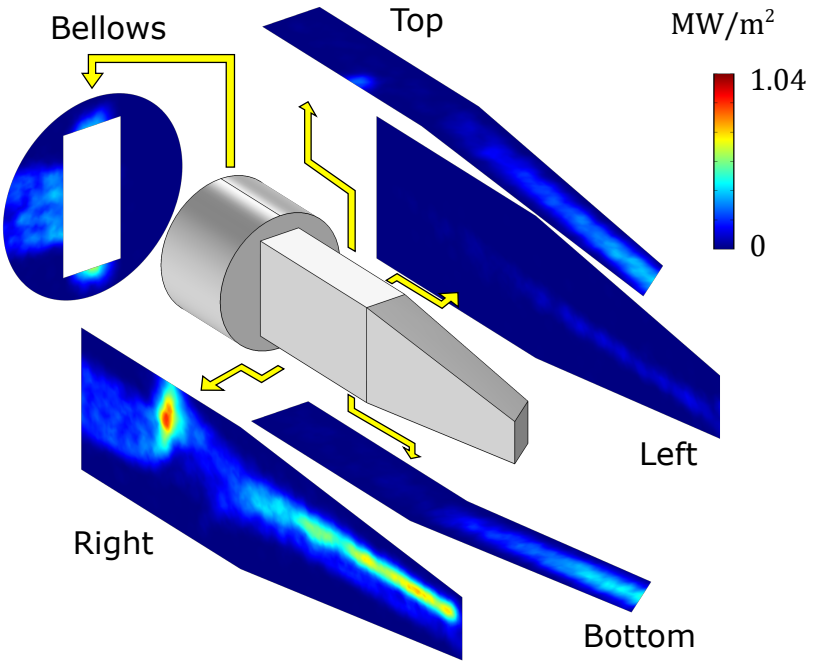

Figure 4.33: Beam duct heat load maps for Case 1. As mentioned before, the difference in the position of the heat loads with the successive others is due to a different method of field evaluation used in this case.

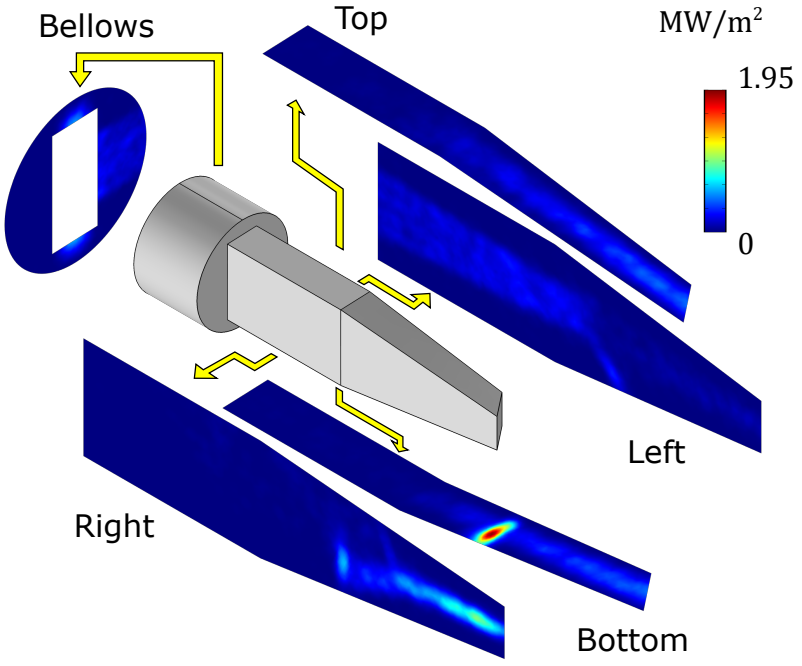

Figure 4.34: Beam duct heat load maps for Case 2.

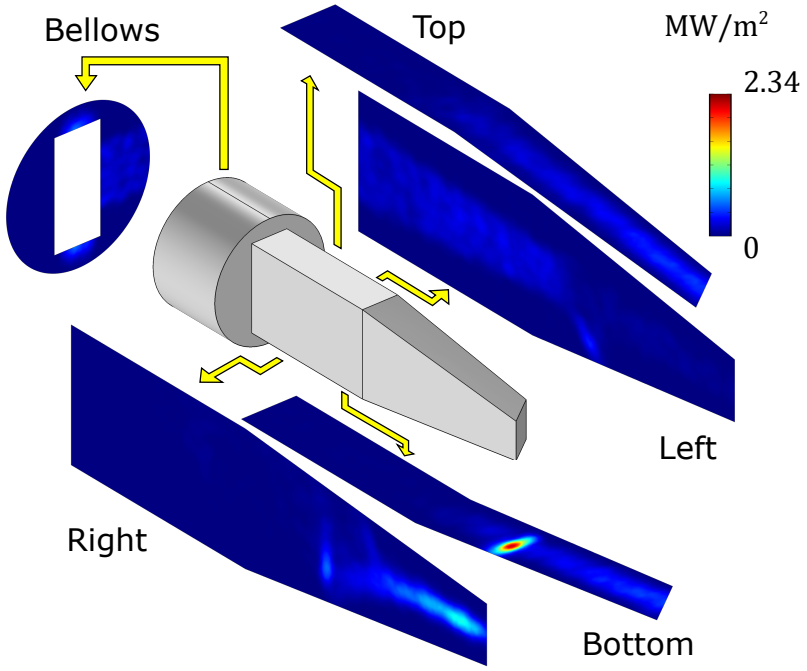

Figure 4.35: Beam duct heat load maps for Case 3.

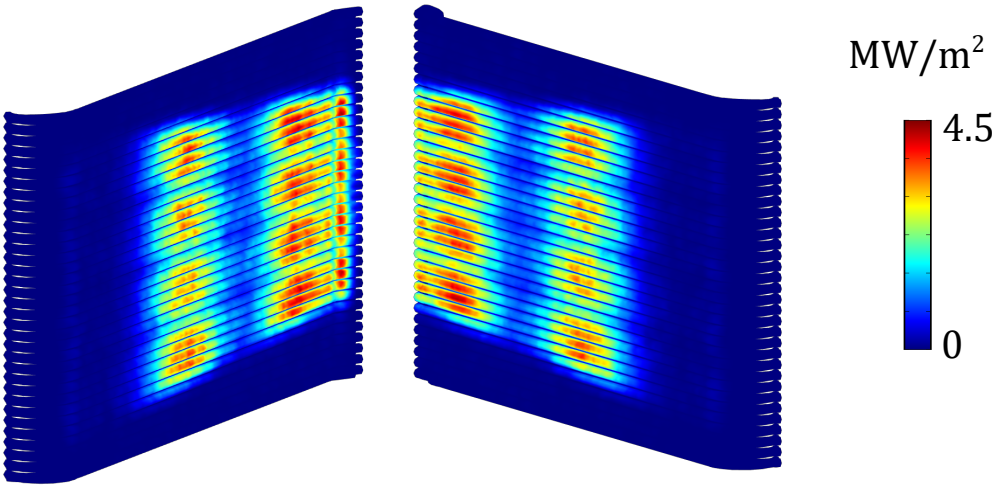

Figure 4.36: Heat load map for the two halves of the calorimeter. The separate hotspots on the panels are due to the effect of multi-focus aiming.

Power balance	**D [MW]**	**e^- [MW]**
Neutralizer	2.15	0.398
RID	9.16	0.008
Calorimeter (open)	0.50	/
Duct	0.69	/
Other	/	0.059
To plasma	9.81	/
Total	22.31	0.465

(a) Power balance of the particle tracing simulations of Case 1.

Power balance	**D [MW]**	**e^- [MW]**
Neutralizer	2.22	0.397
RID	9.47	≈ 0
Calorimeter (open)	0.51	/
Duct	0.60	/
Other	0.01	0.068
To plasma	9.55	/
Total	22.36	0.465

(b) Power balance of the particle tracing simulations of Case 2.

Power balance	**D [MW]**	**e^- [MW]**
Neutralizer	2.13	0.404
RID	9.35	0.005
Calorimeter (open)	0.51	/
Duct	0.60	/
Other	0.02	0.056
To plasma	9.75	/
Total	22.36	0.465

(c) Power balance of the particle tracing simulations of Case 3.

Table 4.5: Set of tables collecting the power balances of the particle simulations for DTT NBI. The slight discrepancy in the total deuterium power is due to different potentials assigned to the RID, increasing the beam energy accordingly.

4.3.4.4 Estimation of off-nominal NBI power to energy characteristic

The NBI can be an important tool for plasma physicists to achieve a given scenario, with its ability to penetrate deep into the plasma core and deposit heat. It is for this reason that, as with all instruments, versatility in operation becomes desirable. The objective is to derive an estimate of a possible power vs. energy characteristic that this iteration of the DTT NBI design is able to yield, to use as reference when designing plasma scenarios.
The procedure adopted uses the nominal energy and half-energy operating conditions as edge cases, to then interpolate the intermediate energy cases in a linear approximation. The half-energy case has been discussed in section 4.2.5, where the potential distribution strategy between grids has been described.
As mentioned, this distribution strategy coupled with a good source conditioning allows for operation with the same extracted current density for all intermediate cases, justifying the linear approach. However, for energies lower than half of the nominal, several optics issues arise (insufficient acceleration and focusing, with the beam impinging inside the accelerator), that would require treating the extracted current density as a variable and not constant. For now, the focus is in the half to nominal energy range.
The expected power reaching the plasma in the nominal case has already been determined in the previous sections and can be easily rounded up to the expected 10 MW; what is missing is the corresponding value for the half-energy scenario. To obtain this value, a full-NBI particle tracing simulation as in the previous sections can be set up, but with reduced energy (with consequently reduced target thickness in the neutralizer) and appropriately chosen values for the core and halo divergences. As it was mentioned at the end of section 4.2.5, the half-energy scenario roughly doubles the divergence of the beam: this means that, to simplify, a 6 mrad core and 60 mrad halo beam can be considered as a starting point for the simulation. This beam and energy managed to yield 4.75 MW of D^0 to the plasma; a plot of the estimated characteristic is reported in Figure 4.37.

4.4 Conclusions

Within this chapter, an in-depth description of the most important design choices adopted for DTT NBI was given, from the finer details of the accelerator grids, to beam aiming and full-NBI particle tracing simulations.
The DTT NBI accelerator will feature Hyperlens Grids, additional components to be placed in contact with the main grids in order to shape the electrostatic field and provide the correct aiming to each particle beamlet, with a beam quality expected to be satisfying the requirements. The same suite of codes used to design the accelerator of ITER NBI has been applied to DTT NBI, obtaining a first estimation of the internal accelerator losses and heat load maps.

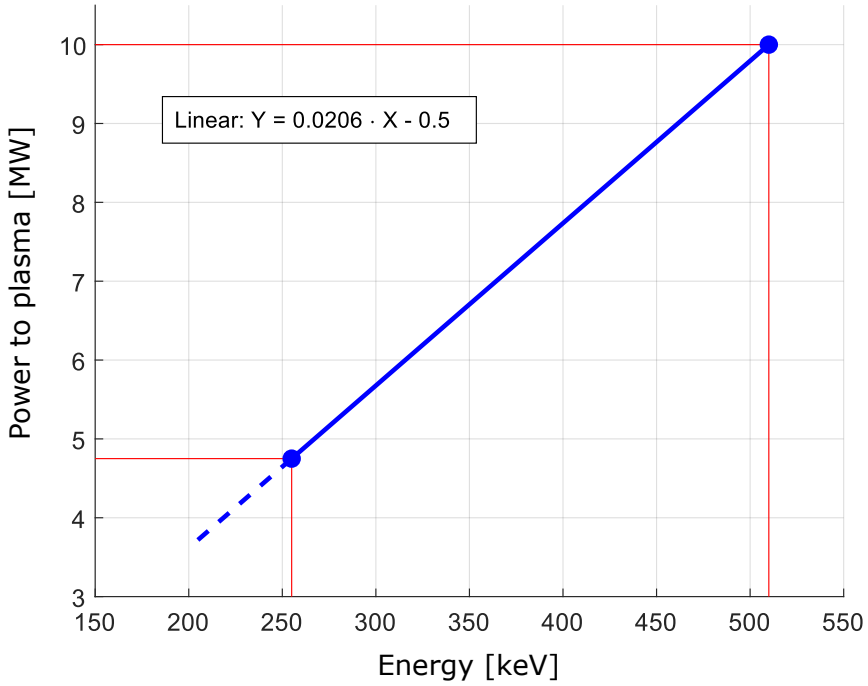

Figure 4.37: Power vs. energy characteristic for DTT NBI.

Regarding the entire NBI, the new concept of beam-fitting BLC components and multi-focus aiming strategy have been adapted to the DTT requirements, reducing particle heat loads; coupled with the study of the vacuum conditions within DTT NBI and stray tokamak field issues, a new design for the NBI has been successfully derived. Particle loads heat maps and efficiency of the NBI in different operating conditions have been obtained through a dedicated suite of models for particle tracing.

Chapter 5

Parallel work on DEMO NBI

SUMMARY - A DEMOnstration fusion power plant will be the next step after ITER, with the objective of developing a reliable and cost-effective power plant to demonstrate its usefulness in baseload power production. To improve the injector efficiency, the concept of plasma-enhanced neutralization was proposed: in the Beam Driver Plasma Neutralizer (BDPN) case, the beam itself ionizes the background gas, and high plasma density is ensured by an efficient magnetic confinement. The physics of this device have already been the scope of several papers, but the assumed geometry was never adapted to fit a realistic, divergent DEMO NBI beam, which is the objective of this chapter.

5.1 Introduction

Following in the future footsteps of ITER, a DEMOnstration fusion plant is foreseen to be the next step towards baseload power generation by thermonuclear fusion, with the aim of proving the technological and commercial feasibility of a complete power plant. To achieve this, a higher duty cycle with longer plasma discharges is required and recirculating power must be reduced by increasing efficiency of the auxiliary heating systems. For the European DEMO the pre-conceptual design [30] developed in the period 2014–2020 assumes 50 MW from each candidate heating system, Electron Cyclotron Resonance Heating (ECRH), Ion Cyclotron Resonance Heating (ICRH) and Neutral Beam Injection (NBI) heating. Since 2021 the baseline design assumes ECH only, but NBI as well as ICH continue to be developed as a risk mitigation strategy. The NBI design assumes 50 MW of power injected from two or three 1 MeV beamlines with an accelerated negative deuterium ion current of 40 A. The energy efficiency of NBI is limited mostly by the upper bound on neutralization efficiency for negatively charged beams through neutral gas, which forces the system to lose $\gtrsim 45$ % of its power in the form of non-neutralized ions impinging on the residual ion dump. Compounded by early stripping losses, re-ionization losses, geometrical transmission losses and limited power supply efficiency these losses limit the wall-plug efficiency, i.e. injected power divided by total system power consumption, of typical

negative-ion-based NBIs to about 30 % [31].
A possible remedy is provided by the plasma neutralizer. In this concept the gas inside the neutralizer has a degree of ionization of several percent, enhancing the neutralizer efficiency for the negative beam [32]. Experiments have proven increased neutralization [33], but until now they have been using external arc sources to generate plasma, introducing additional complexity and power consumption.
In 2013 E. Surrey and A. Holmes proposed the concept of a plasma neutralizer where the beam itself would ionize the background gas along its path [34], called the beam-driven plasma neutralizer (BDPN). The beam deposits energy in the neutralizer mostly in the form of stripped fast electrons (272 eV for a 1 MeV D^- beam) and fast electrons generated by the beam through background gas ionization (called Rudd electrons). These fast electrons cause secondary ionization. In order to achieve a plasma density and degree of ionization sufficient for enhanced neutralization the walls are lined with cusp magnets. In a follow up in 2019 I. Turner and A. Holmes [35] gave a more detailed description of a possible design for the BDPN and improved Surrey's and Holmes' original zero-dimensional model. For an ITER-like NBI ion beam they predicted an achievable neutralization efficiency of up to ≈ 80 %.
The model was further amended by Starnella et al. [36], who introduced several previously overlooked loss mechanisms, which led to a reduction of the predicted achievable neutralization to ≈ 68 %. This latest model calculates also temperature of the neutralizer gas besides the degree of ionization and neutralization efficiency. The main inputs are the neutralizer main dimensions, cusp field strength and magnet separation as well as filling pressure. The model is iterative and takes several CPU hours to converge.
The BDPN design assumed by Starnella features a box-like neutralizer which, unlike the gas neutralizer for ITER, has no internal channel-separating walls in order to reduce plasma losses. All walls are lined with permanent magnets in Halbach configuration and there is a magnetic field across the beam entrance and exit slits created by magnets that sit in bars between the slits. As the absence of internal walls increases the gas conductance, the entrance and exit bars are extended towards the outside in the shape of "fins" (Figure 5.1b) as a compensatory measure to restrict the gas conductance. The design used is of a conceptual nature only and not optimized for the integration into an actual beamline. This chapter attempts to improve on this, by optimizing the shape parameters of the BDPN together with those of the ion source and the RID in order to maximise the neutral yield of the entire beamline, i.e. the flux of injected neutral D per D^- ion current extracted from the ion source, rather than the neutralisation yield of the BDPN as a stand-alone component. This requires the consideration of

1. the geometrical transmission losses for neutral D by all BLCs along the entire beamline and its dependence on BLC geometry parameters, using the same beam-fitting design used for DTT in Section 4.3.1;

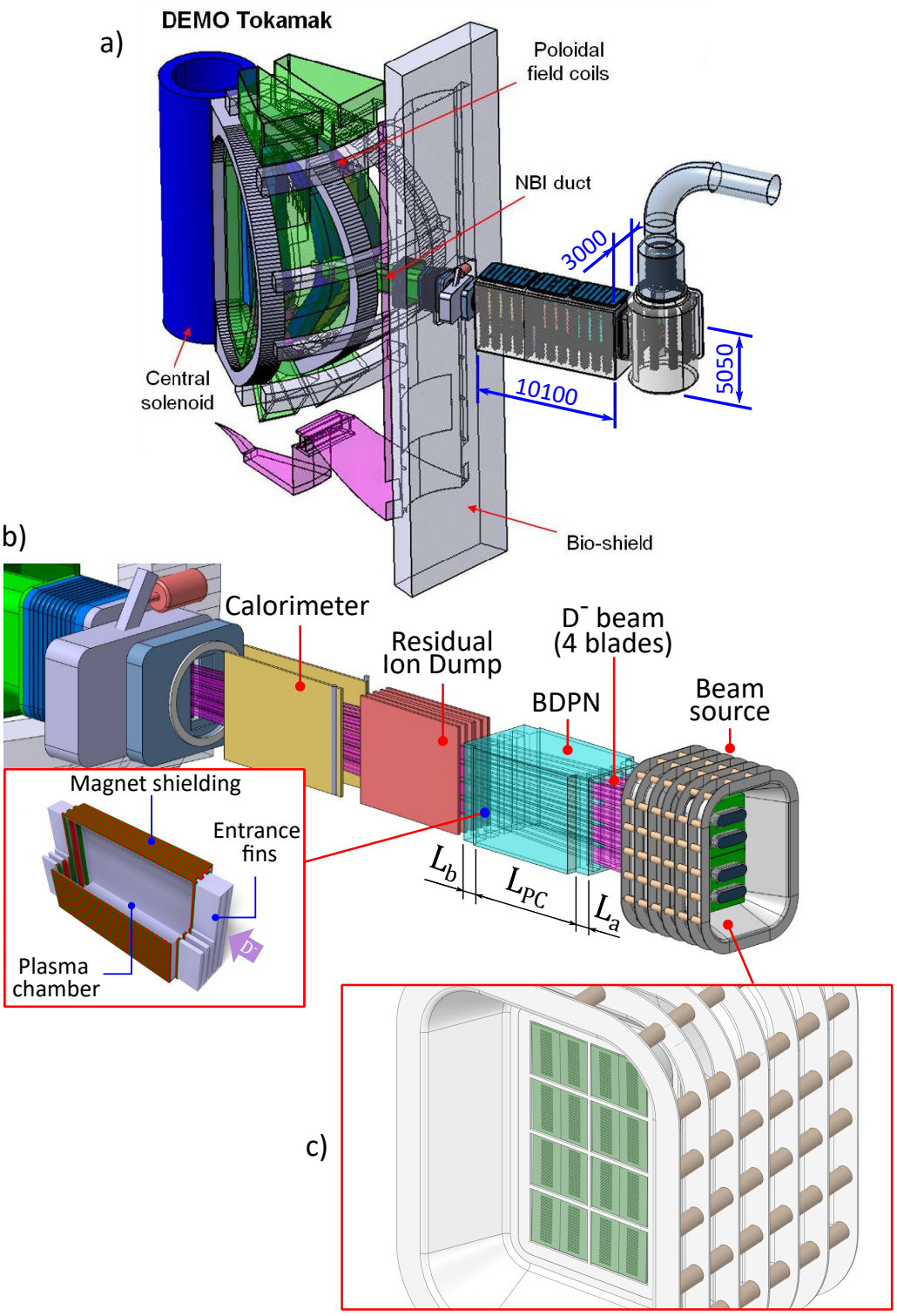

Figure 5.1: Pre-conceptual design for DEMO NBI (2022). a) isometric cutaway of the DEMO tokamak and NBI assembly with the main dimensions of the injector vacuum vessel; b) view of the main DEMO NBI components in the version featuring the BDPN, with a section view showing the BDPN geometry and a possible magnetic configuration [36]; c) detail of the beam source, showing the chosen layout of the beamlet array.

2. the dependence of the plasma density and degree of ionization in the BDPN on BDPN dimensions and gas density;

3. the gas temperature in the BDPN and gas conductance out of the BDPN in order to determine the required neutralizer gas flow;

4. the neutral gas profile depending on the gas flow and pumping speed and spatial pump distribution in order to calculate reionization losses;

5. the species evolution of the extracted D^- beams along the entire beamline.

In order to make this optimization more manageable, a general shape for the BLCs is prescribed, leaving only their dimensional parameters free for optimization within an allowed range. Besides being convenient for the exercise, such restrictions will also exist in practice, e.g. in the form of a maximum allowed beamline envelope or a maximum tolerable opening in the breeding blanket.

5.2 Problem setup

The starting point is the current pre-conceptual design for DEMO NBI (Figure 5.1), with the focus point situated in the blanket; the design distance from the neutralizer to the focus point is maintained. However, the neutralizer length is free to change, by repositioning the ion source accordingly. On the vacuum side, the present cross-section of the NBI vessel is kept.
One also needs to decide how the beamlet array is organized: having tall beam columns is preferable for reducing gas conductance between the fins of the BDPN and in the channels of the RID. Furthermore, a cross section that is not too different from a square is beneficial for the BDPN because it keeps the volume-to-loss-surface ratio high and number of entrance slits should be even for reasons of symmetry of the magnetic cusp field. Hence the original layout with 4 by 4 beamlet groups array, each one consisting of 5 by 16 beamlets, appears to be a reasonable choice that can be carried over. However, while the vertical spacing between beam groups can be fixed beforehand because all of them pass through the same slits and channels, the horizontal spacing needs to be a free parameter to allow the surrounding component geometry to change.
A couple of further external constraints are needed to avoid unfeasible solutions: the maximum horizontal dimension of the ion source is set to 1.5 m and the maximum allowed length of the neutralizer is 4 m. The chosen work flow is as follows:

- Find the relations that determine the values of the BDPN and RID dimension parameters necessary to achieve a set value for the geometrical transmission losses. The geometry parameter space is then mapped for allowed solutions that are compatible with all external constraints, such as the size constraints mentioned above or a minimum allowed wall thickness.

- For every allowed point in the discretized parameter space from above the plasma density and neutral gas temperature in the BDPN is calculated using a parametrized scaling obtained with Starnella's model [36]. This calculation is carried out for various gas flows into the neutralizer. For each of these calculations the gas density distribution is calculated using a parametrized geometry in an FEM code. Said gas distribution can be used to solve numerically the system of equations describing the evolution of the D^- beam through background gas collisions, and giving us the neutral beam equivalent current injected into the torus.

- The geometry–gas-flow combination that gives the maximum neutralized beam fraction is the desired solution.

- Particle tracing simulation through the whole NBI beamline are then performed in order to calculate the resulting heat loads on the BLCs and to double-check the beam evolution and the transmission calculation.

5.2.1 Parametric geometry description

The basis of the parametric geometry is the same beam-fitting BLC design that was used in the previous chapter, Section 4.3.1, when designing the DTT beamline. The main difference with the previous case is the adoption in DEMO NBI of a common focus aiming strategy, to minimize the impact of the duct aperture to the tokamak environment. It also has the advantage of being more intuitive and slightly simpler in formulation. Figure 5.2 shows a schematic of the beamline geometry as a horizontal cross section. The grounded grid position is on the circle on the right. All beamlets are focused to a common point O on the left where they intersect both horizontally and vertically in order to minimize the beam width in this position. Differently from the multi-focus case, the beam width in point O can be determined by the divergence of a single beamlet. In between the grounded grid and the focus point are the two beamline components of interest. The first in beam direction is the BDPN, characterized by an entrance fin length L_a, an inner length L_PC (Plasma Chamber length) and an exit fin length L_b. The second component is the RID with a length L_RID in a distance L_nr from the neutralizer. For simplicity it is assumed that all beamlet starting points as well as the BDPN and RID entrance and exit surfaces lie on spheres around point O. The neutralizer and RID are once again subdivided in four equal "sectors", one for each beamlet group, so that only one needs be determined and the others are obtained by rotation. The first task is to find an algorithm that determines the lengths and widths of the channels in the BDPN and RID that guarantees a requested geometrical transmission while satisfying all external constraints. It must be noted that Fig. 5.2 is only a schematic in which the angles and hence the width-to-length ratio are strongly exaggerated.

For these calculations it is assumed $f_\mathrm{c} = 0.85$, $f_\mathrm{h} = 0.15$, $\epsilon_\mathrm{c} = 7\,\mathrm{mrad}$ and

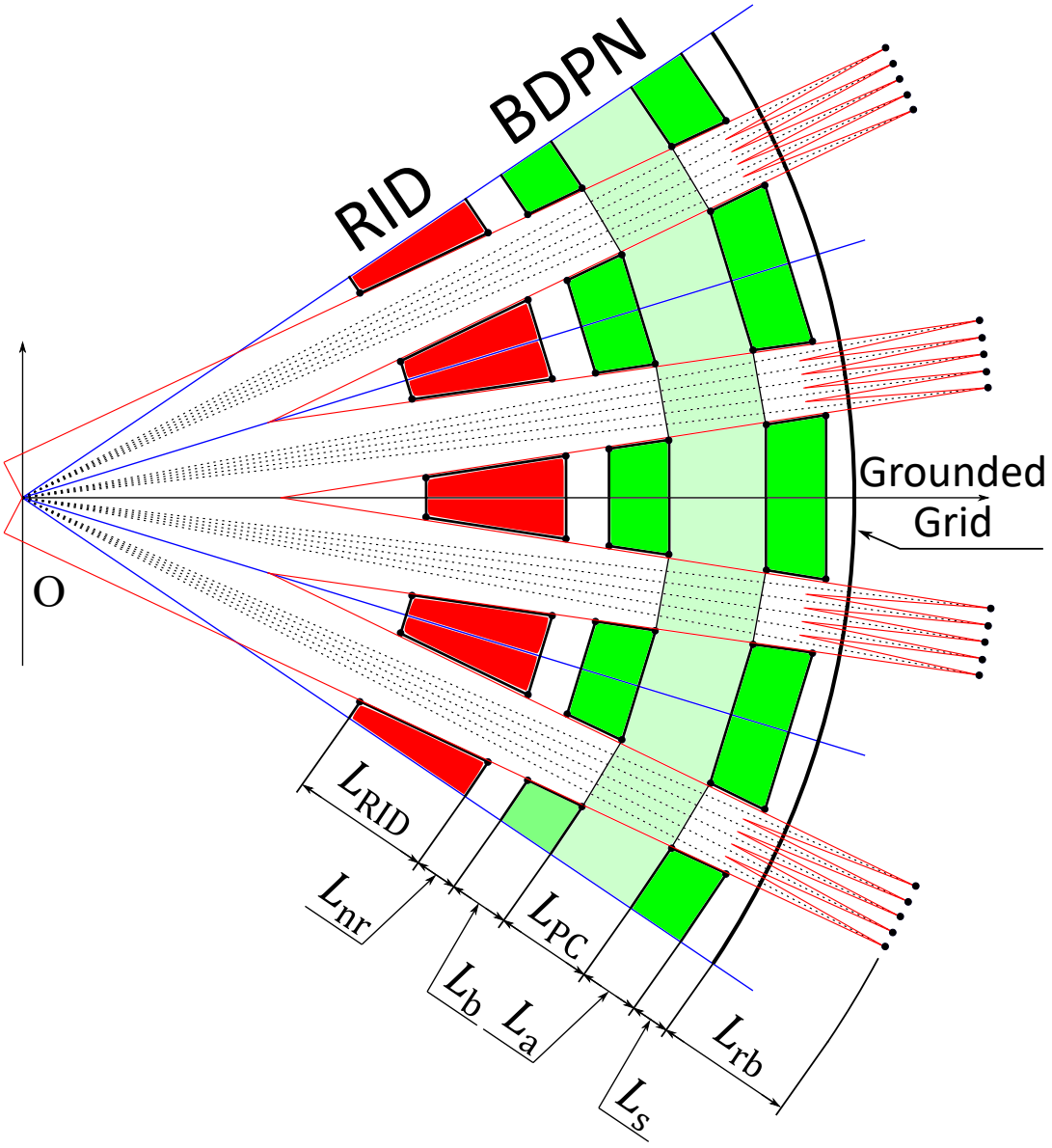

Figure 5.2: Geometry sketch of a horizontal section of the NBI BLCs in this parametric model.

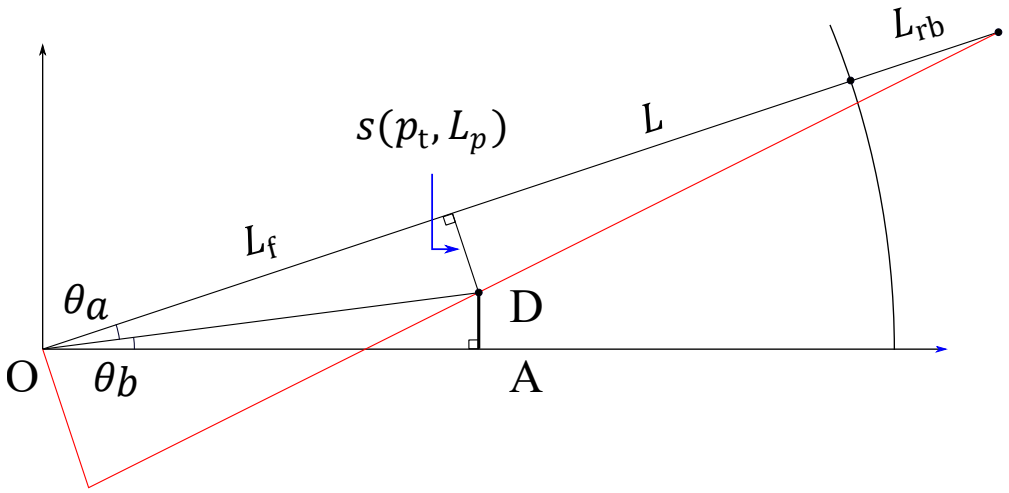

Figure 5.3: Geometry sketch for determining the initial point of the beam-fitting configuration.

$\epsilon_h = 15$ mrad, as specified for the ITER NBI. As all beamlets are being focused from a long distance to a single point in the middle of the port to reduce the exit beam cross-section as much as possible, it is reasonable to equate the full beam transmission to the one of a single, centred beamlet expanding towards the exit; this means that Equation 4.8 can be used to analytically estimate the transmission, without further derivation. In the case of DEMO NBI, where the size of the duct aperture is still in discussion, using a designer's approach the size of the duct is chosen according to a desired p_t. However, attention must be paid, since for the reasons mentioned earlier all apertures in the breeding blanket must be as small as possible.
As mentioned before, beamlets start from point sources, while having in reality a finite size ()$r_b = 7$ mm): a backward displacement L_{rb} of about 0.7 m of the beamlet point sources with respect to the Grounded Grid is necessary with this beam.

5.2.1.1 Geometric procedure

Similarly to what has been done for DTT, to draw the delimiting surfaces of the BLC channels the first step is to find the delimiting edge that is farthest downstream. For every beamlet this is the downstream edge of the RID channel wall that the beamlet is closest to. It is hence also sufficient to consider only the horizontally outermost beamlets for the respective RID channel edge. By having the independent variable L defined as the sum of the BDPN and RID lengths along the closest beamlet line of sight and postulating a desired p_t, the necessary wall clearance s of the outermost beamlet of a channel at the distance $L_p = L + L_{rb}$ can be determined, while the

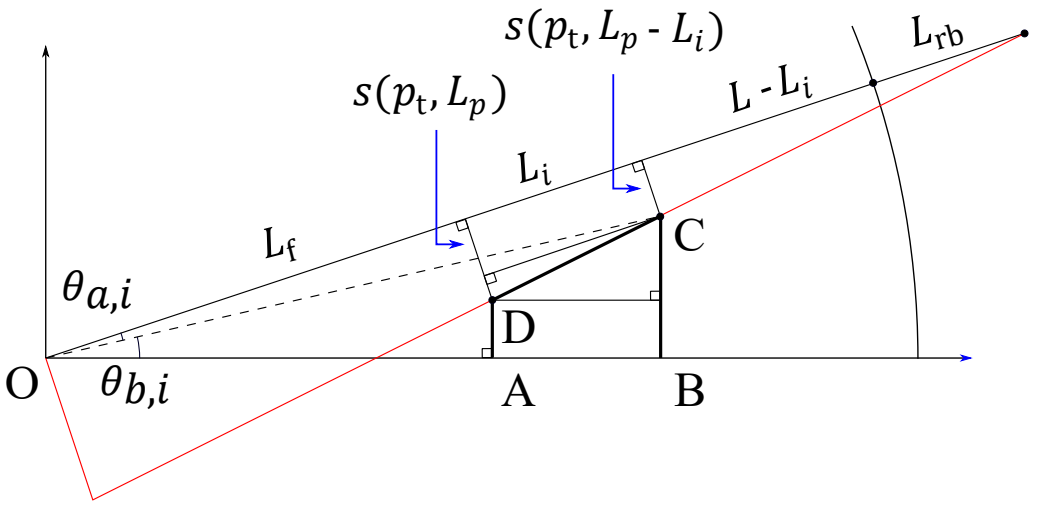

Figure 5.4: Geometry sketch for determining the successive points of the beam-fitting configuration.

segment $\overline{AD}$ is half of the allowed minimum thickness of the RID plate between two channels. Once the remaining distance to the focus point L_f is fixed, the other quantities can be obtained as

$$\theta_a = \tan^{-1} \frac{s\left(p_\mathrm{t}, L_p\right)}{L_\mathrm{f}} \,, \tag{5.1}$$

$$\theta_b = \sin^{-1} \frac{\overline{AD}}{\sqrt{L_\mathrm{f}^2 + s^2\left(p_\mathrm{t}, L_p\right)}} \,, \tag{5.2}$$

$$\overline{AO} = \sqrt{L_\mathrm{f}^2 + s^2\left(p_\mathrm{t}, L_p\right) - AD^2}. \tag{5.3}$$

The value $\theta_t = \theta_a + \theta_b$ is important since it describes the inclination of the first beam with respect to the initial horizontal axis; the first point of the configuration is then individuated by $D = (AO, AD)$.

Any other delimiting point can be obtained by following the second set of instructions: if L_i is the distance along the beamline of the point in question starting from the initial base point, then

$$\theta_{a,i} = \tan^{-1} \frac{s\left(p_\mathrm{t}, L_p - L_i\right)}{L_\mathrm{f} + L_i} \,, \tag{5.4}$$

$$\theta_{b,i} = \theta_t - \theta_{a,i} \,, \tag{5.5}$$

$$\overline{BC} = \sqrt{\left(L_\mathrm{f} + L_i\right)^2 + s^2\left(p_\mathrm{t}, L_p - L_i\right)} \sin\theta_{b,i} \,, \tag{5.6}$$

$$\overline{CD} = \sqrt{L_i^2 + \left(s\left(p_\mathrm{t}, L_p\right) - s\left(p_\mathrm{t}, L_p - L_i\right)\right)^2} \,, \tag{5.7}$$

$$\overline{AB} = \sqrt{CD^2 - \left(AD - BC\right)^2}. \tag{5.8}$$

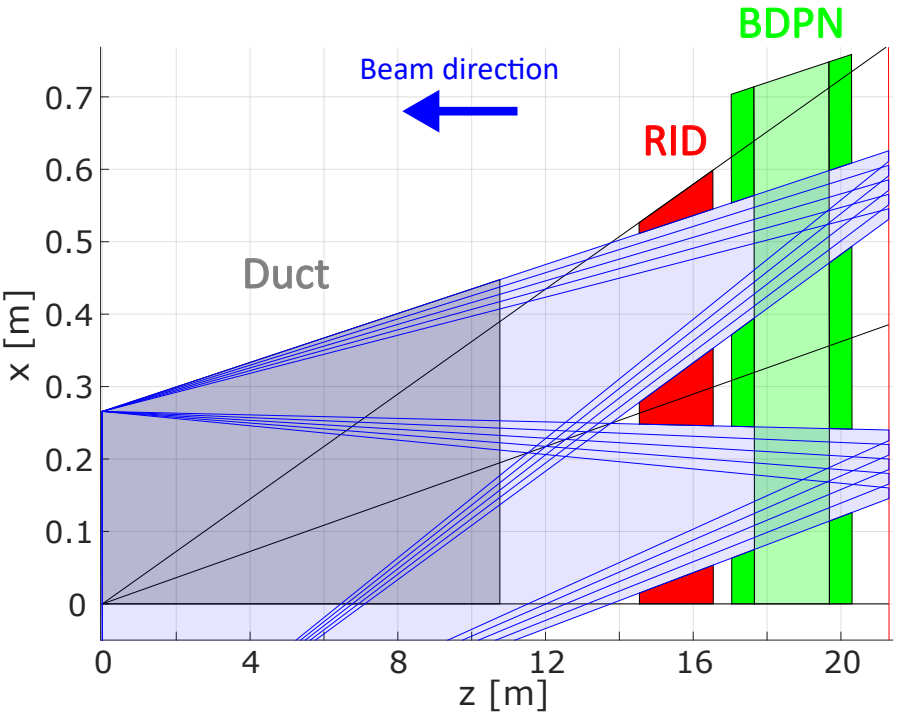

Figure 5.5: Plot of the geometry section of a possible beam-fitting solution for the BDPN. Not to scale.

The delimiting point is then $C = (OA + AB, BC)$. To complete the sector, the beam group angular span is necessary; said angle is obtained as

$$\theta_{\mathrm{bg}} = \frac{\Delta d_{\mathrm{bg}}}{L_{\mathrm{f}} + L} \ , \tag{5.9}$$

where $\Delta d_{\mathrm{bg}} = 80$ mm is the inter-axis distance between the first and the last beamlets; the sector angular span is then $\theta_{\mathrm{sec}} = \theta_{\mathrm{bg}} + 2\theta_t$. By mirroring the $ABCD$ polygon about the center beamlet axis, the final fin geometry is obtained; the sector can be patterned with respect to the centre with an offset of θ_{sec} to obtain the whole horizontal section.

An example of this procedure applied to the whole NBI is shown in Figure 5.5: the here presented code can be run starting from a given combination of L_{PC} and $L_{\mathrm{a}}, L_{\mathrm{b}}$ (fin length, assumed to be equal), with all other quantities (the distance between GG and the neutralizer L_{s}, the distance between neutralizer and RID L_{nr}, the RID length L_{RID}, the remaining focus length L_{f}) kept constant.
In order to discriminate between feasible and non-feasible solutions, the resulting total neutralizer width is compared to the maximum width allowed – which, given the shape of the beam, is the most stringent boundary condition, since it affects directly

the size of the necessary beam source – and marked accordingly in the parameter space.

5.2.2 Parametric FEM model description

The next step uses the information acquired during the geometry set exploration and builds for each one a 3D model of DEMO NBI based on the varying geometry of the BDPN. The gas flow in free molecular regime in this model is then solved once again by the FEM commercial code COMSOL® with the objective of obtaining the gas density distribution, while being controlled by a MATLAB® script for post-processing. The geometry, shown in Figure 5.6, is inspired by the latest DEMO NBI pre-conceptual design [30] and tries to capture the main features of the system while simplifying it as much as possible to shorten computation time. The setup of the gas sources and sinks is also based on earlier reports on vacuum analysis in DEMO NBI (from [37]); these are:

- The gas inflow into the neutralizer, Φ, which is varied between simulations, is distributed among 5 gas inlets inside the plasma chamber.
- The gas immission from the source through the accelerator, is set at $Q_{\mathrm{s}} = 3$ Pa m^3 s^{-1}.
- The gas entering the NBI duct from the tokamak, set at a conservative $Q_{\mathrm{c}} = 2$ Pa m^3 s^{-1}.
- The vacuum system is modelled by "pumping walls" on the top and bottom parts of the vessel, with a tentative capture coefficient $C_{\mathrm{s}} = 0.1$.

The formulation of the model is isothermal, but the code still allows for surfaces at different temperatures within. The neutral gas in the neutralizer is heated by the transiting beam and this can be taken into account by assigning to the inner walls of the neutralizer the same temperature of the gas. The temperature gradient effect can be emulated in the passage between plasma neutralizer and room temperature by setting the appropriate value of T_{NEU} on the inner side.
The explorative nature of the problem at hand would in principle require a separate vacuum simulation for each variation of the gas inflow Φ or neutralizer temperature T_{NEU}, which becomes immediately unreasonably time-consuming. To avoid this, the idea is to represent the variation of inflow and temperature through an appropriate weighted interpolation: this approach takes the solutions at the extremes of pre-established exploration boundaries (in this case, the solutions at minimum and maximum allowed inflow, minimum (room) and maximum allowed temperature) calculated by COMSOL and combines them through appropriate weighting in MATLAB to obtain an intermediate solution, which in a linear problem (as it is in this case) is very close to the one that would have been obtained by direct model evaluation.

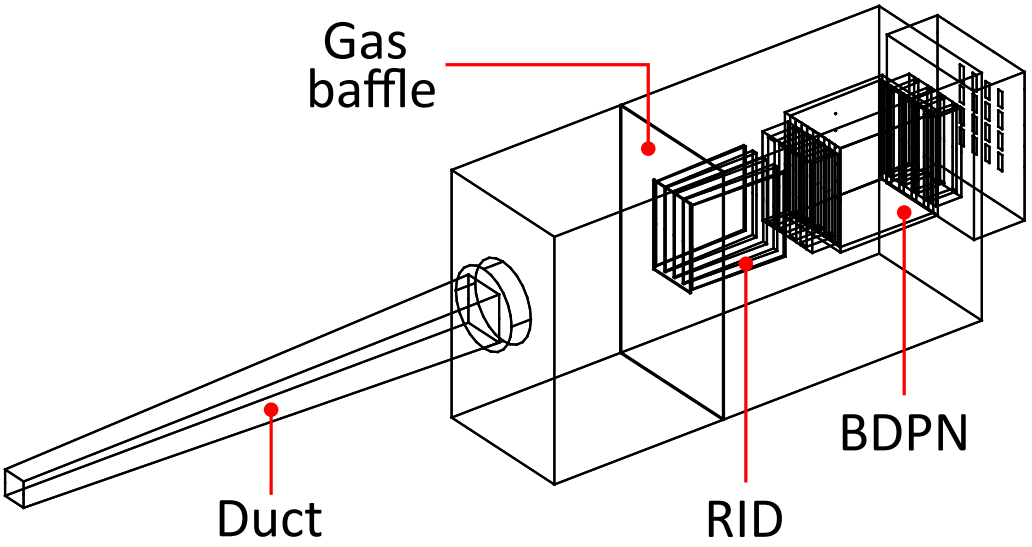

Figure 5.6: Geometry plot of the working DEMO NBI FEM model.

The set boundaries are between 300 and 600 K for the neutral gas temperature, and between 4×10^{21} and 2×10^{23} s^{-1} for the neutralizer particle inflow. These boundaries were selected by trial and error, while trying to capture the full picture of the BDPN response to different flows and temperatures. If $(T_\mathrm{m}, T_\mathrm{M}), (\Phi_\mathrm{m}, \Phi_\mathrm{M})$ are the set boundaries, the weights are defined as

$$\begin{aligned} w_{T_\mathrm{M}}(T) &= \sqrt{\frac{T - T_\mathrm{m}}{T_\mathrm{M} - T_\mathrm{m}}},\ w_{\Phi_\mathrm{M}}(\Phi) = \frac{\Phi - \Phi_\mathrm{m}}{\Phi_\mathrm{M} - \Phi_\mathrm{m}}, \\ w_{T_\mathrm{m}}(T) &= 1 - w_{T_\mathrm{M}},\ w_{\Phi_\mathrm{m}}(\Phi) = 1 - w_{\Phi_\mathrm{M}}. \end{aligned} \tag{5.10}$$

If $G = \{k = (i,j) |\ i \in \{T_\mathrm{m}, T_\mathrm{M}\}, j \in \{\Phi_\mathrm{m}, \Phi_\mathrm{M}\}\}$ are the possible binary combinations of the respective cases, the new interpolated density is then obtained as:

$$w_k(\Phi, T) = w_i\, w_j;\ k \in G\,, \tag{5.11}$$

$$n(\Phi, T) = \sum_{k \in G}^{|G|} n_k \cdot w_k. \tag{5.12}$$

This interpolation is the main component of the overall MATLAB exploration algorithm which applies the BDPN scaling and loops through the available inflow values looking for the maximum neutralized beam fraction.

5.2.3 The BDPN scaling

In order to obtain the ionization degree and neutral gas temperature, the BDPN model of Starnella et al. [36] would have to be run for every point in the parameter space exploration described above. Starnella's code is a zero-dimensional balance code that models the various populations of ions and electrons with their numerous interactions and loss channels (such as wall losses, impact dissociation, dissociative recombination, etc.) using as input the fast negative ion beam, BDPN geometry, and filling pressure, then yielding the resulting equilibrium temperature and expected ionization degree. As one single BDPN model run takes several CPU hours, this is highly impracticable. To work around this problem the BDPN model was run for a reduced number of neutralizer lengths L_{PC}, widths and heights as well as gas flows while maintaining all other numerous variables, such as the strength of cusp magnetic field, cusp spacing, etc., constant. The resulting data is stored as a multi-dimensional lookup table and the desired model outputs for a specific parameter combination can simply be obtained by interpolation. The dependences of gas temperature and ionization degree on neutralizer length as read from this table are shown in Figure 5.7.

5.2.4 Exploration algorithm

Once a point in geometry parameter space is deemed beam-optically viable and its weighted interpolation of the density is available from the lookup table, the exploration algorithm is engaged. Its purpose is to systematically scan the inflow parameter space available in the BDPN scaling lookup table while making sure that the solution is consistent regarding gas temperature and gas flow. This is done as follows:

- The throughput loop is engaged: for each given value of Φ, the average density inside the neutralizer is computed as a function of temperature between boundaries T_{m} and T_{M}.
- This curve is intersected with the gas-temperature-vs-average-density curve from the BDPN scaling at the corresponding fixed neutralizer dimensions. The temperature at the intersection point is the working temperature T at which the calculation must continue.
- The final neutral density distribution is obtained by weighted interpolation using the given Φ and T , while through the neutralizer average density and BDPN scaling the plasma density is obtained.
- The neutral gas distribution and plasma density allow one to derive the beam fraction evolution through the NBI using cross-section data from literature (from Barnett [38] and Berkner [32]).

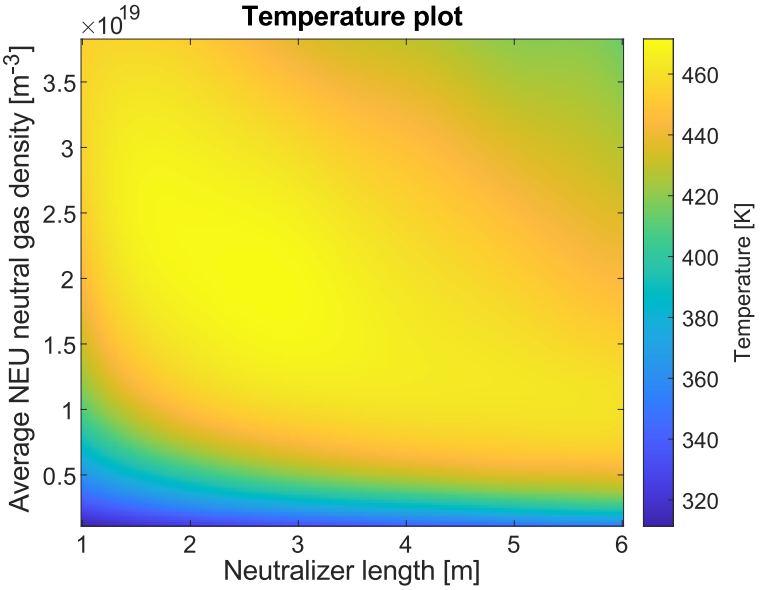

(a) Temperature scaling for the BDPN. For a fixed neutralizer length, the denser the gas the more diluted the heating effect of the beam; for very low densities, the beam travels unaffected and does not heat the gas.

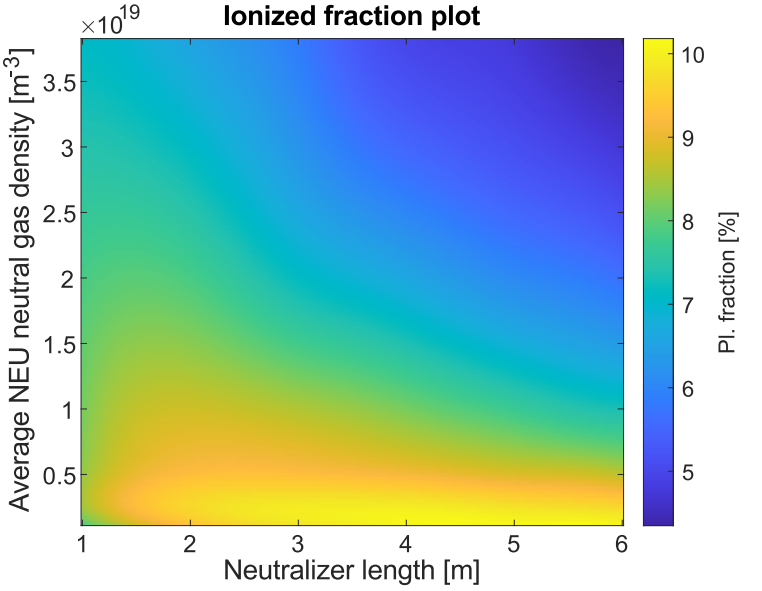

(b) Ionization degree scaling for the BDPN. For a fixed neutralizer length, the denser the gas the more diluted the ionizing effect of the beam.

Figure 5.7: Plots of the BDPN scaling over their definition domain, at constant height and width.

- The process repeats for each allowed value of Φ; the one that has the highest neutralized beam fraction at the exit of the NBI duct is deemed the optimum solution for the given geometric set. Other important quantities (such as corresponding specific inflow and temperature) are stored, ready to analyse the next geometry.

In this fashion it is possible to obtain a correlation between an optically viable geometry identified by the couple (L_a, L_{PC}) and respective quantities such as neutralized beam fraction at NBI exit, needed gas inflow, temperature; among which it is easy to look for the one with the highest neutral power.
As the entire algorithm could be hard to follow on text alone, 5.8 contains a detailed flowchart of the process.

5.2.5 Particle Tracing simulation

The results of the previous step, namely the neutral gas density distribution, the plasma density distribution, and the geometry, are the inputs for the full-NBI particle tracing simulation in COMSOL. The outputs are the final transmitted neutral fraction to the plasma, as well as the heat loads due to particle loss on the various BLCs. The other boundary conditions are set as follows:

- The particles' positions and directions are derived by starting from a 2D-Gaussian velocity distribution, whose width is dictated by the $1/e$ divergence chosen for the beam and peak related to the 1 MeV energy, and truncated at 3σ to avoid particles with very wide trajectories.

- Each beamlet is composed of a core and a halo fraction, with each of their guiding centres lying on the surface of a spherical GG and aimed towards the centre that coincides with the focus point.

- The total current assigned to the particles is 40 A, equal to the current extracted from the 1280 apertures (radius 7 mm) with an extracted current density of 254 A m^{-2} and a supposed efficiency of the accelerator of 0.8. This current is subdivided between core and halo components, with their respective fraction.

- The beam evolution is modelled through a collision algorithm using the same cross-sections as in 5.2.4 to derive the reaction rate ν.

- The only external fields considered are the one generated by the RID at 50 kV and the confinement magnetic field at the extremities of the BDPN; for now other sources (such as tokamak poloidal stray fields) have been ignored.

In order to gauge the deflection effect of the end confinement magnets on the crossing charged particle beams, a tentative magnet configuration has been adopted with a feasible square cross-section of 20 mm of Sm-Co magnets.

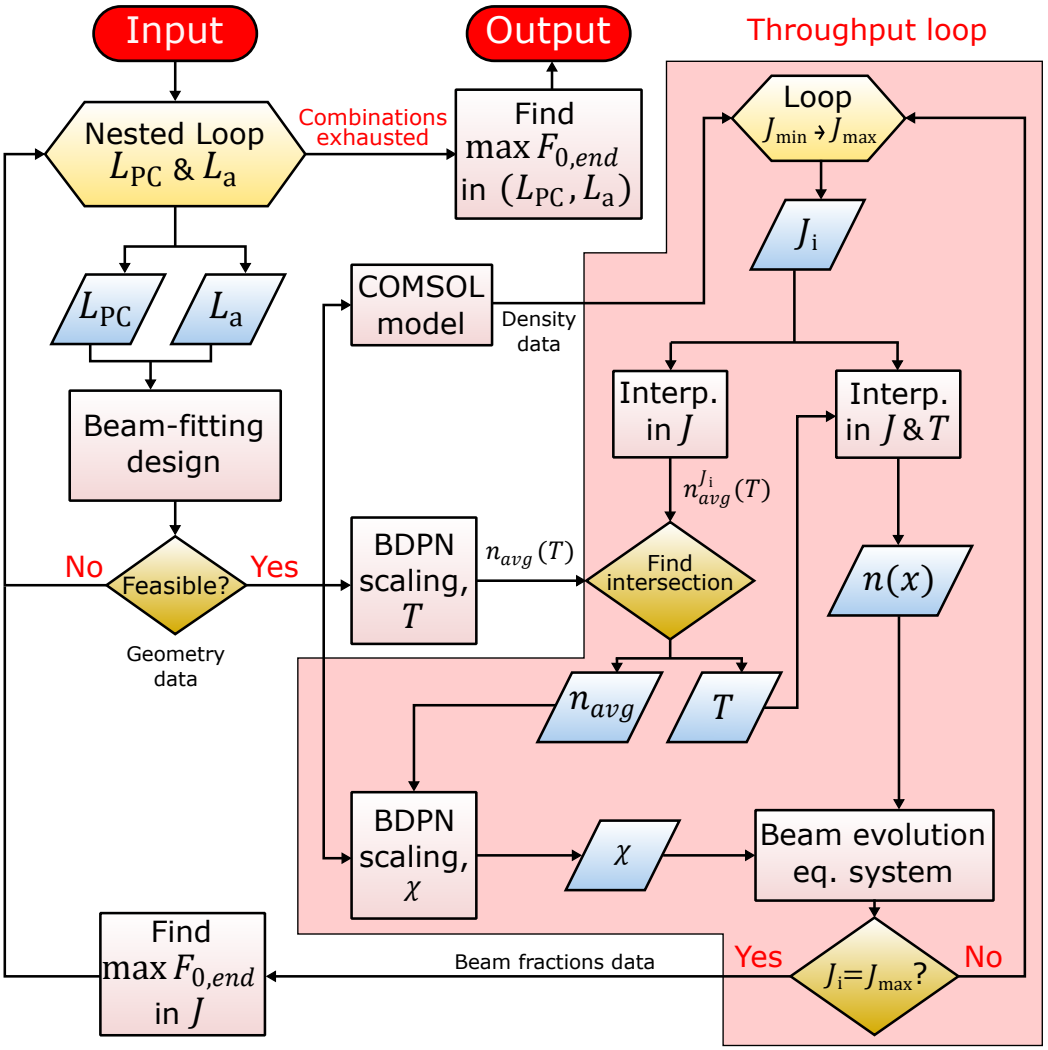

Figure 5.8: Algorithm flowchart of the optimization process, illustrating the role of the BDPN scaling.

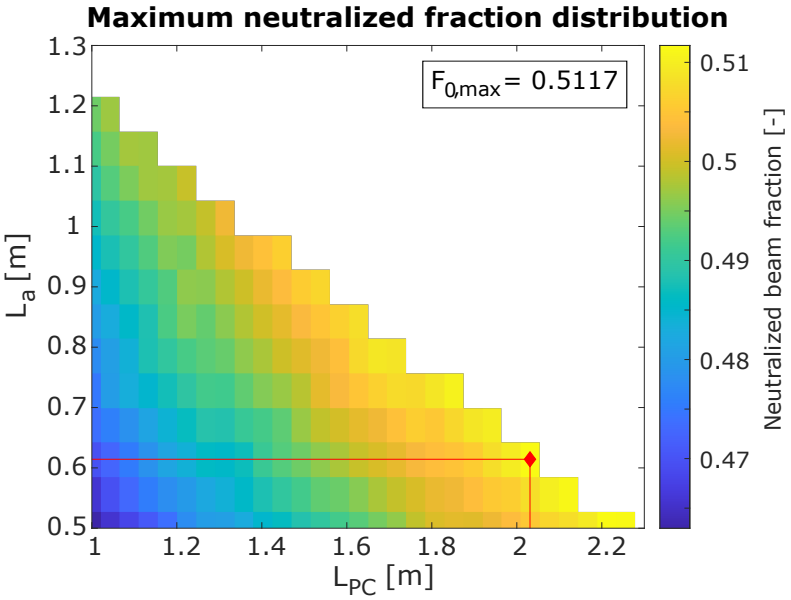

Figure 5.9: Map of the BDPN plasma chamber length (L_{PC}) and fin length ($L_{\mathrm{a}} = L_{\mathrm{b}}$) parameter space showing the injected neutral fractions at optimal gas flow for each neutralizer configuration. The global maximum is indicated by a red diamond, while the white area on the top-right represents forbidden combinations.

5.3 Results

5.3.1 Results of the BDPN model

The parameter exploration yielded interesting results; by collecting each feasible combination of fin and neutralizer length with their respective maximized neutral fraction at the NBI exit in a plot, one can visualize where the absolute highest value is located (Figure 5.9). It is important to specify that these numbers are not wall-plug efficiencies, but rather neutralization yields, and only part of the latter. An estimate of the wall-plug efficiency by using the available data will be given later in the the chapter.

The maximum value is 0.5177, located at $L_{\mathrm{PC}} = 2.03$ m, $L_{\mathrm{a}} = L_{\mathrm{b}} = 0.614$ m, with a gas inflow of $\Phi = 1.01 \times 10^{22}$ s^{-1} (equivalent to 38 Pa m^3 s^{-1} at 0°C). The triangular shape of the solution space is a consequence of the maximum width constraint, with the upper edge marking the points where the overall neutralizer length $L_{\mathrm{NEU}} = L_{\mathrm{a}} + L_{\mathrm{PC}} + L_{\mathrm{b}} = 2L_{\mathrm{a}} + L_{\mathrm{PC}}$ is at its achievable maximum.
Another aspect can be appreciated while looking at a plot showing the evolution of the neutral fraction along the beamline as a function of the gas input (Figure 5.10). Intuitively, when trying to maximize the neutral fraction, one would place the working point of the neutralizer as close to the available maximum as possible; however, the plot in Figure 5.10 shows a different picture: the ideal beam evolution

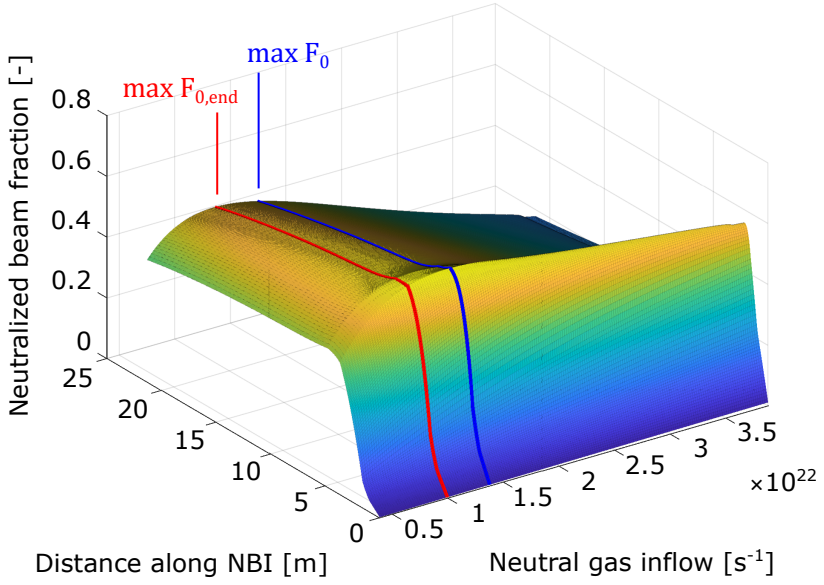

Figure 5.10: Plot of the evolution of the neutral fraction along the NBI (right to left) as a function of gas inflow. The red line represents the beam evolution that has the maximum neutral fraction at the NBI exit, while the blue line represents the one that reaches the maximum at the end of the neutralizer.

granting maximum neutral fraction at the beamline end, $\max F_{0,\mathrm{end}}$) is at lower neutralizer gas flow than that which achieves maximum neutralization ($\max F_0$) at the neutralizer exit. This is due to the increased gas requirement to obtain the maximum neutralizer performance, which in turn increases the density after the neutralizer and the reionization losses, losing more than what was gained.

5.3.2 Comparison with a gas neutralizer

Since the BDPN has been proposed as a replacement for the gas neutralizer (GN), it is important to compare the BDPN result in a meaningful way with a GN. An "equivalent" gas neutralizer (GN) is investigated, where equivalent refers to:

- Same maximum allowed encumbrance (length and width).
- Same beam quality and desired power fraction.
- Same beam-fitting design applied, equivalent to a BDPN but with a constant $L_{\mathrm{PC}} = 0$.
- Same maximization of neutral fraction by tuning the gas inflow; there are now however 3 gas inlets for each one of the 4 channels (for a total of 12 apertures).

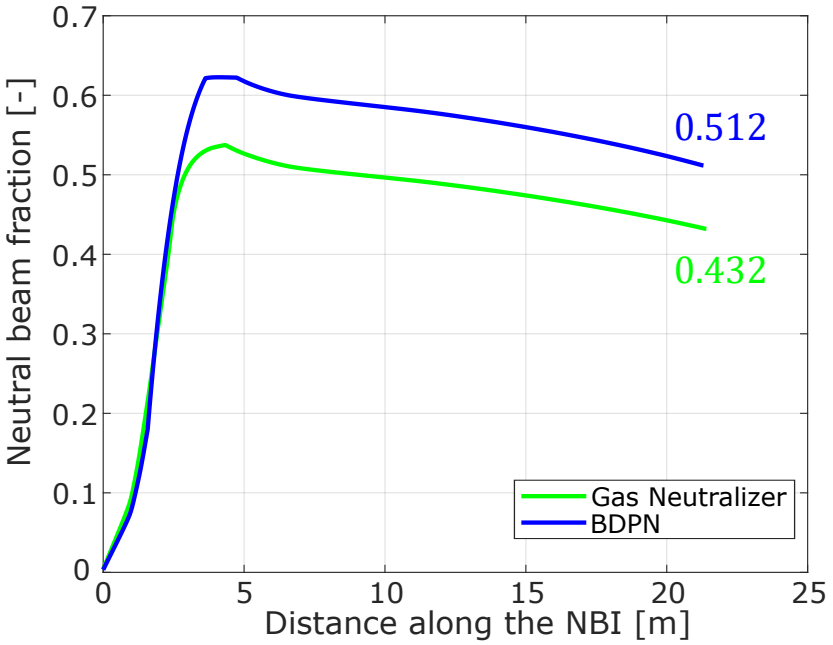

Figure 5.11: Comparison between GN (green) and BDPN (blue). The maximum neutral fraction at the exit of the NBI is shown.

The best neutral beam evolution in both cases are shown in the same plot to highlight the difference between them (Figure 5.11), as well as the neutral gas distribution (Figure 5.12). The comparison shows that a GN achieves around 8 percentile points less than that its BDPN counterpart ($F_{0,\mathrm{end}} = 0.432$, compared against 0.512), with a similar length of 2.86 m. The total inflow needed for the GN in this case is $\Phi = 1.09 \times 10^{22}$ s^{-1} (41 Pa m^3 s^{-1} at 0°C, very close to the BDPN value of 38 Pa m^3 s^{-1}). This close match between the needed gas inflows can be explained by the adoption of longer entrance and exit fins in the BDPN with respect to the proposed design by Turner and Holmes, effectively choking the flow from the larger Plasma Chamber, coupled with a significantly lower neutral gas target thickness requirement for the BDPN, derived by the plasma model: in the best configuration, the BDPN required 6.81×10^{19} m^{-2} of neutral gas for a 1 MeV beam, compared with 1.10×10^{20} m^{-2} for a GN.
Starting from this result, it is possible to derive an estimate of the NBI wall-plug efficiency in the two cases in a similar fashion as what has been done in [30]: by substituting in the chain of efficiencies the new values from the results, the wall-plug efficiency is 0.30 for the GN and 0.34 for the BDPN (Table 5.1).

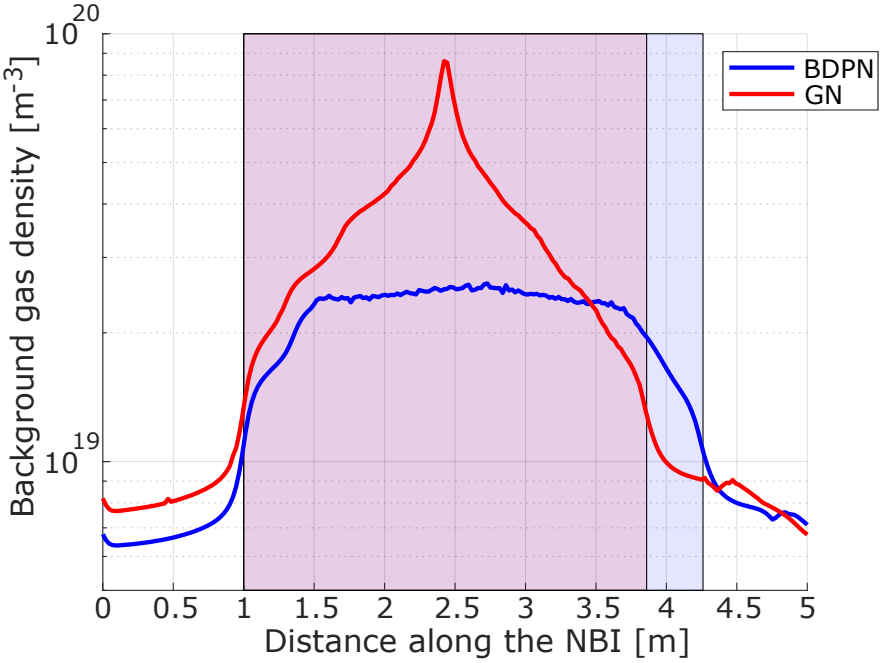

Figure 5.12: Comparison between the background gas distribution between GN and BDPN in the Neutralizer region. The Neutralizer outline in the two cases is reported.

5.3.3 Results of the Particle Tracing model

The Particle Tracing model has been run to determine the heat loads distribution, the power balance, and deliver an important cross-check to confirm the earlier results (Figure 5.13). To assess the impact of entrance and exit end magnets on the trajectory of the beam ions, an otherwise identical simulation but without magnets was also run, obtaining an "ideal" case to compare against.
Furthermore, to cross-check if the beam-fitting design is able to transmit the desired power, another simulation without reactions and external fields was also launched. The results are listed in Table 5.2.

The simulations show a very close match between the analytic estimation of transmission and the numeric result, confirming the premise of the beam-fitting design approach. Another important confirmation to get is on the neutral fraction achieved: in MATLAB this value is obtained through a system of differential equations, while in COMSOL the beam evolution is obtained through particle collision algorithms. To check this aspect, it is possible to divide the neutral fraction at the end of the NBI in the no magnet case (0.4820) by the numerical transmission (0.9192) to obtain the effective numerical neutral conversion fraction 0.524, to be compared with the original $F_{0,\max}$ of Figure 5.11 (0.512). The two values differ for merely about 3 %, which given the degree of approximations made is a very good result.

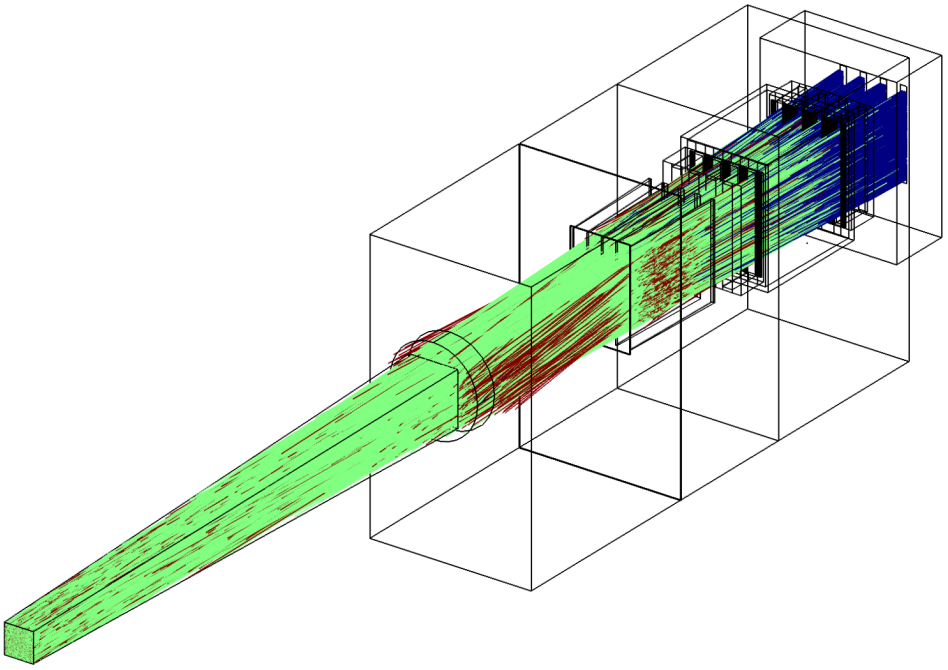

Figure 5.13: Trajectory result plot of the Particle Tracing model. In blue are the D^- ions, in green the D^0 neutrals, and in red the D^+ ions.

As a consequence of the beam-fitting approach, the heat load power density is evenly distributed, with peaks around 0.95 MW m^{-2} for the Neutralizer fins and 3.44 MW m^{-2} for the RID panels (Figure 5.14).

The data in Table 5.2 underlines also the importance of choosing the appropriate magnet configuration at the ends of the BDPN: with the one used in the model, inserted as a first tentative, the deflection is enough to cause additional losses of 2 MW.

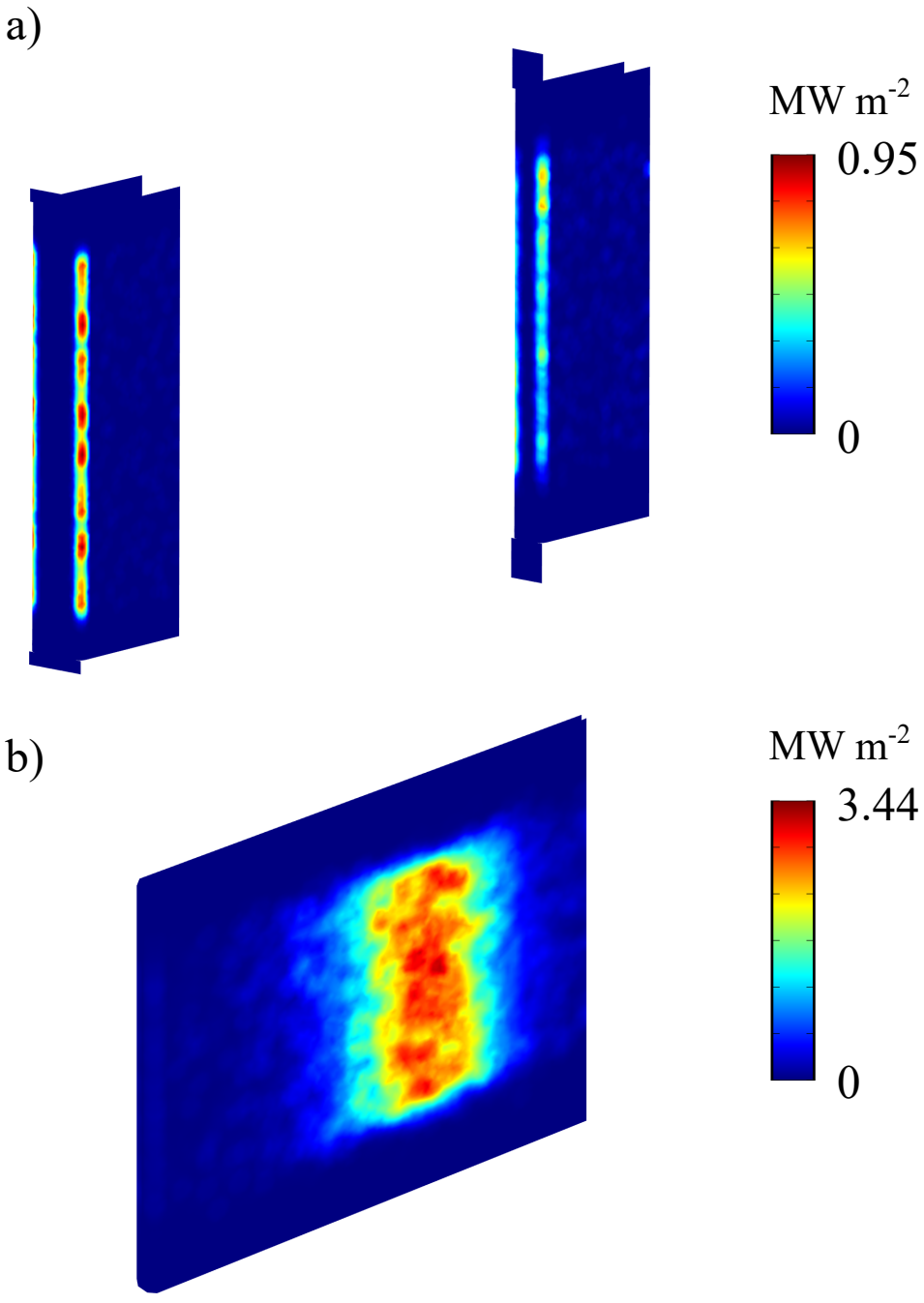

Figure 5.14: Heat load maps for the interested BLCs. Figure a) is the central set of fins of the neutralizer, while Figure b) is the central plate of the RID.

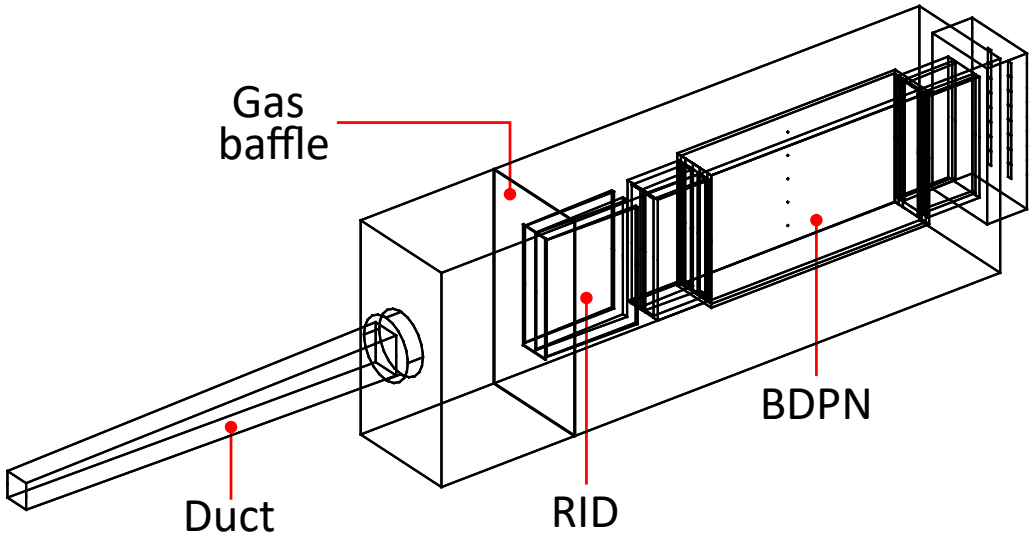

Figure 5.15: Geometry plot for the two-blade beam design.

5.3.4 Possibility for further improvement

The presented results constitute an optimization under the initial boundary conditions that have been set, and are therefore not a global optimum. The optimization exercise has also shown how different quantities influence each other. These trade-off relations can be used to imagine new possible geometric configurations where some constraints are more relaxed, and better performance can be achieved.
For example, a two-blade beam design has been proposed, obtained by reshaping the beam group array from the 4 by 4 into a 2 horizontal by 8 vertical beamlet groups configuration, similarly to a previously considered DEMO NBI design [39]. The height of the vessel and BLCs is then appropriately increased to fit the new beam shape, resulting in the geometry of Figure 5.15. The advantage of such a configuration is that the width of the BLCs is greatly reduced, and almost constant as the beamline gets longer: this is due to the expansion boundary of the side beamlets being almost completely compensated by the focusing towards the center. Obviously this cannot go to extreme lengths, since also the blanket aperture must scale accordingly, however it allows for a significantly longer neutralizer.
The BDPN scaling was extended in order to cover neutralizer lengths up to 6 m, and the optimization routine run again.
The highest value of neutralization efficiency of 0.56 (5 percentile points more than the four-blade beam) was found on the extreme upper right corner of its parameter space plot (obtained in the same way as Figure 5.9), which means that the space size chosen this time (up to $\max(L_a, L_{PC}) = (1.5\text{ m}, 6\text{ m})$, as large as the scaling currently allows) was still too small to contain the global maximum. Still, this trial proves that different approaches to the choice of geometry may lead to even more enhanced neutralization rates.

5.4 Conclusions

Within this chapter, for the first time, a complete DEMO NNBI beamline with a BDPN has been modelled and its parameters optimized, assuming realistic geometry and boundary conditions. Considering geometric transmission, the degree of ionization achieved in the plasma neutralizer as a function of its geometry and feed gas flow, the neutral gas distribution and the beam species evolution along the whole beamline, the neutral yield from the grounded grid of the ion source's accelerator to the beamline end, i.e. the injected D^0 flux divided by the accelerated D^- flux, is about 48 % with a wall-plug efficiency of the beamline of 0.34. This is about 6 percentile points more neutral fraction and about 4 percent more wall-plug efficiency than a gas neutralizer, obtained while applying the same algorithm and boundary conditions.
The optimization exercise has highlighted some more and some less intuitive trade-offs. Obviously making the BDPN, and thus the whole beamline, longer means that the duct opening in the breeding blanket either has to be larger or leads to more geometrical losses. However, the combined optimization of neutralizer geometry and gas flow in order to obtain an optimal neutral flux at the beamline end favours a longer neutralizer. Interestingly, for a given geometry the gas flow that results in the highest neutral fraction at the exit of the neutralizer is higher than the gas flow that creates the highest neutral fraction at the beamline end. This is due to the additional reionization losses downstream of the neutralizer, which overcompensate the increased neutralisation in the BDPN. Understanding the various trade-offs is indispensable in driving the future design effort.
Obviously, the values reported here are optimizations under a particular set of boundary conditions: these were guided by the space envelope of the current NBI beamline design for the European DEMO, which has a gas neutralizer, but are to some extent arbitrary, as every one of them can be disputed. However, the optimization framework developed here can be used to guide the design under any set of external boundary conditions once these are known.

	Ref.	Option 1	Option 2
	ITER HNB	2022 DEMO NBI (GN)	2022 DEMO NBI (BDPN)
Extracted current density [A m^{-2}]	289	251	224
Total extracted current [A]	57	50	44
Nominal acceleration voltage [MV]	1	1	1
Aux/extraction overall efficiency	0.9	0.9	0.9
Gross power [MW]	63	55	49
Stripping/halo losses efficiency	0.7	0.8	0.8
Accelerated current [A]	40	40	35
Source/neutralizer transmission	0.95	0.95	0.95
Neutralizer efficiency	0.55	0.54	0.62
Beam line/duct transmission	0.8	0.82	0.8
Estimated power to plasma [MW]	16.67	16.67	16.67
Injector overall efficiency	0.26	0.30	0.34

Table 5.1: Main parameters and efficiencies for the different DEMO NBI options. The first column is from [30], while the others incorporate the results obtained here.

	No Mag. field	w/ Mag. field
Initial power	40.04 MW	
Neutralizer	0.671 MW	0.705 MW
RID	14.90 MW	15.04 MW
Exit (D^0)	19.30 MW	17.29 MW
GG - plasma	48.20 %	43.18 %

	Numeric	Analytic
Transmission	91.92 %	91.90 %

Table 5.2: Results of the particle simulations for the BDPN. Upper table from top to bottom: initial power launched at the GG, power lost in the neutralizer, power dumped in the RID, power at the beamline exit injected into the torus, fraction of injected initial power; Lower table: comparison of geometrical transmission calculated by analytic and numerical means.

Chapter 6

Parallel work on SPIDER

SUMMARY - The SPIDER source is an experimental device located at Consorzio RFX with the objective of testing the extraction of a negative ion beam (H^- and D^-) of the same size as an ITER NBI ion source. After concluding its first successful Caesium campaign, the experiment is currently in a shutdown phase; the possibility of installing the Electron Dump component is under discussion. To make a sensible decision, a number of simulations and considerations need to be made; this chapter contains the work made during the activity on the task «PROJ_24 "Decision on electron dump"».

6.1 Introduction

Within the programmed activities dedicated to the improvement of Neutral Beam Injectors destined for ITER [40], the SPIDER (Source for Production of Ion of Deuterium Extracted from RF plasma) experiment has been built at Consorzio RFX. The main objectives of SPIDER are a $H^-(D^-)$ extracted current density larger than 355 (285) A m^{-2}, 1280 extraction apertures, beam energy of 100 keV and a pulse duration up to 3600 s. For the plasma generation, an ITER-size Radio-Frequency (RF) ion source is foreseen, with a design based on the ELISE experiment located at IPP Garching [41]. Its operation is vital to discover and study the phenomena and issues linked to generation and acceleration of high currents of negative ions, bridging the knowledge gap towards the full-size ITER NBI system; the future RF-based NNBIs will greatly benefit from the results of SPIDER.

Starting from the first version of the SPIDER accelerator design in 2008 [42], various additional components have been proposed and investigated by the RFX team: in particular, after noticing a possible issue with excessive electron loads within the vacuum vessel, a new component – the Electron Dump (ED) – has been designed and manufactured in order to catch the electrons exiting the accelerator [43]. This component is a based on an array of actively cooled pipes placed at the exit of the GG, intercepting any particle straying too far from the intended beam path (see Figure 6.1).

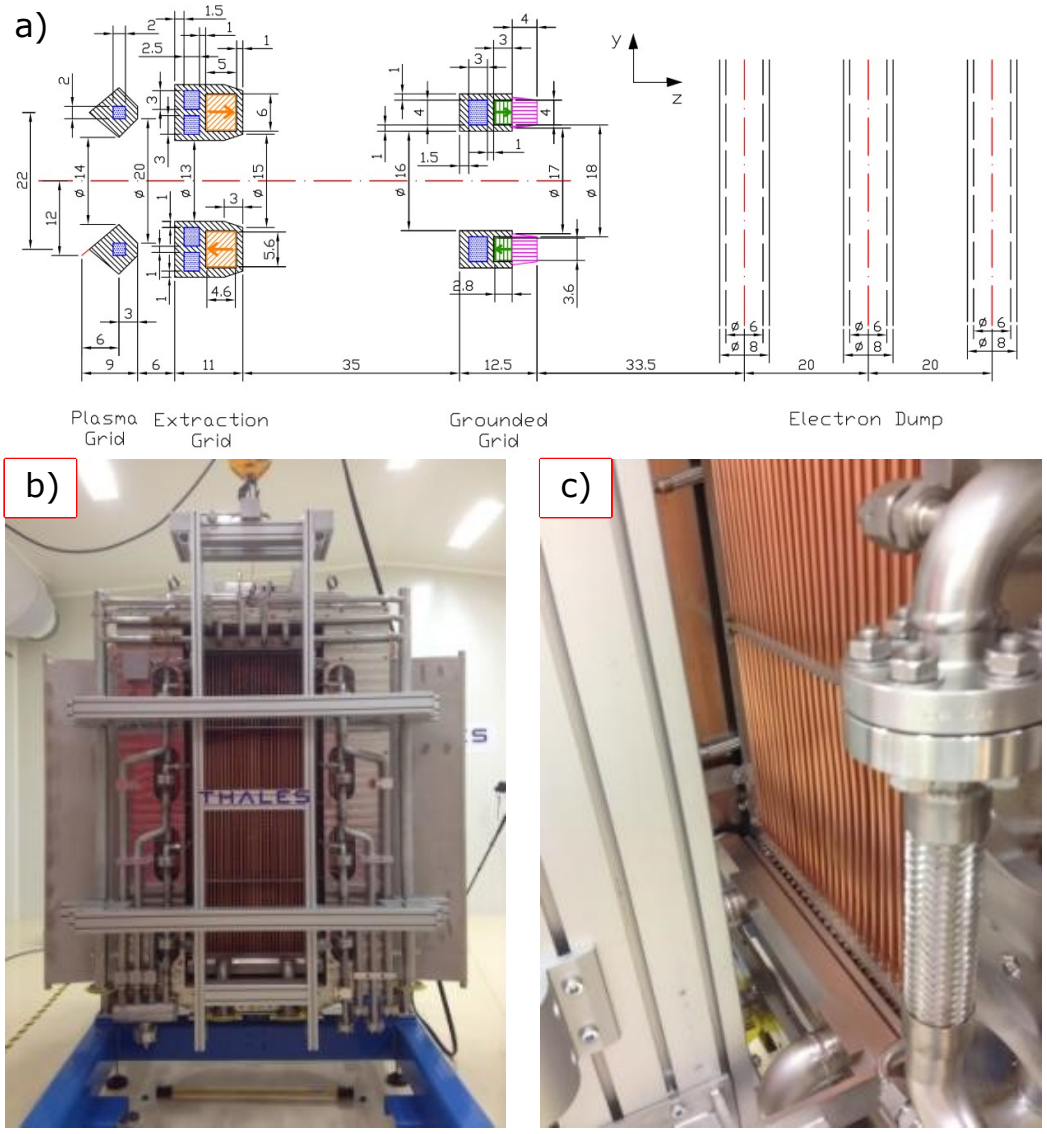

Figure 6.1: a) Dimensions in the accelerator and ED region [43]; b) ED mounted on the SPIDER beam source; c) detail view.

Given the current 2022 shutdown of SPIDER after the successful Caesium campaign, there is the possibility to install the ED, but this sparked a debate on whether to proceed now (considerably increasing complexity, due to the number of pipes) or wait for the next shutdown. My Ph.D. at Consorzio RFX allowed me the precious chance to get involved in the decision process for this important experiment, supporting the debate with various simulations on particle tracing, heat load determination, and temperature distribution.
This chapter is dedicated to illustrate the simulations that helped to deliberate on the matter of the ED.

6.2 ED Particle tracing and thermo-mechanical evaluations

To provide additional insight on the role of the ED inside of SPIDER, additional particle tracing simulations were conducted using a simplified approach. The objective is to obtain updated heat maps of the particle loads that would form on the internal components of SPIDER, both with and without the ED.

The codes used for this work are MATLAB® to initialize the starting particle arrays for each species considered, then imported into the commercial FEM code COMSOL® to obtain the heat maps on the desired components and the temperature distribution. The initial trajectory data used in this set of simulations comes from a dedicated SPIDER paper [43], where a full-power SPIDER experiment was simulated in EAMCC and the transmitted power after the GG was estimated (with results reported in Table 6.1).

Species	**Power [kW]**	**Current [A]**
H^-	5720	57.2
H	330	(11.1)
H^+	10	0.2
e^-_{str}	330	7.1
e^-_{coex}	170	1.9

Table 6.1: Power balance of transmitted power by species for a full-power SPIDER experiment. e^-_{str} refers to electrons generated by stripping, and e^-_{coex} to electrons coextracted.

To freely change the divergence and CCDE deflection of the main negative hydrogen ion beam, the original trajectory data from EAMCC was not used; instead, a routine to generate gaussian-distributed particle sets at the desired energy, divergence and deflection (the same as in the DTT and DEMO simulations) was implemented.

Since the divergence and deflection of the beam are being modified, it is difficult to reflect this change on the neutral hydrogen particles and stripping electrons without additional dedicated simulations; for simplicity, the neutral hydrogen "current" (more correctly a particle flux) is being merged with the main negative beam, reaching 68.3 A, while the electrons are imagined to be constant in their trajectories in all configurations. The positive hydrogen ions are being ignored. This overall negative ion current will be subdivided between a core part (the 85 %, corresponding to 58.06 A) and a halo part (the 15 %, 10.24 A). The proposed scenarios to be investigated are:

- A simulation of the footprint of a single 5 by 16 beam array upon the diagnostic calorimeter STRIKE, both with and without the ED, for the following cases:
    1. **Nominal**: beam with 7 mrad core, 75 mrad halo, 0 mrad of CCDE deflection.
    2. **Optimistic**: beam with 7 mrad core, 75 mrad halo, 20 mrad of CCDE deflection.
    3. **Average**: beam with 15 mrad core, 75 mrad halo, 20 mrad of CCDE deflection.
    4. **Realistic**: beam with 30 mrad core, 75 mrad halo, 20 mrad of CCDE deflection.
- A simulation of a quarter of the SPIDER source where the particle loads of the "realistic" case are projected on the Vessel and In-Vessel Components, coupled with a thermal analysis to determine the peak temperature of the vessel. This simulation will be done too with and without the ED.

6.2.1 Limited STRIKE-only simulations

For these simulations, the beam array is limited to a single 5 by 16 beam group, with the current scaled down accordingly. The domain of the simulation is a simple parallelepiped, where the end face represents the upside face of the STRIKE calorimeter, placed at 495 mm from the GG. More details on the geometry are represented in Figure 6.2.

Following are the heat load maps for the main ion beam and the co-extracted electrons, as well as the percentages of passing negative ions through the ED in the three cases (Table 6.2). A separate case where only the stripping and co-extracted electrons are considered is also present, in order to gauge their possible disturbance on beam power analysis.

From Table 6.2, it can be observed that the ED has a variable effect on the extracted beam, that depends on the beam optics. In fact, with a high-quality beam (nominal case) the whole beam core (having in this case a divergence of 7 mrad) and about 3/4 of the halo (having in this case a divergence of 75 mrad) are

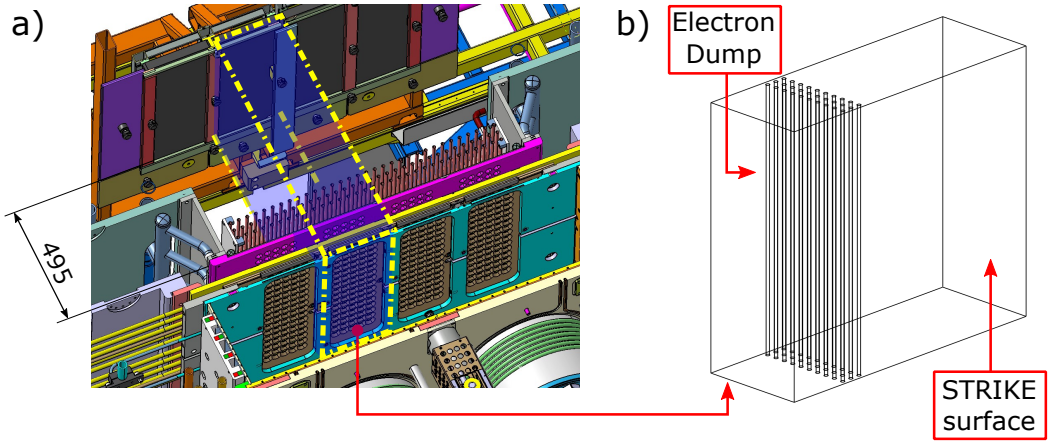

Figure 6.2: Limited STRIKE-only subset simulation: (a) CAD of the region to be simulated; (b) considered domain in COMSOL.

passing through the ED. The numbers significantly change by considering the realistic scenario (similar to what was observed during the 2021 experimental campaign). In this case, also a fraction of the beam core (estimated around 5 %) is dumped. On the other hand, the amount of dumped halo in this case is only slightly changed from the nominal case. In the realistic case, the 5 % interception of the beam core is due to the fact that in this case the core divergence is significantly higher (30 mrad) than the nominal one and to the presence of a certain CCDE (of ±20 mrad, depending on the row number).

An important fact to be highlighted here is that the beam halo is in any case strongly dumped by the ED. In fact, the interception of halo is in any case around 25 % of the one exiting from the GG. This amount is slightly less than 25 % in the nominal case, where the CCDE is assumed to be completely compensated, and slightly more than 25 % in the other three cases, where a residual CCDE of 20 mrad is considered. In any case, such a high ratio of halo interception suggests that the possibility to characterize the halo during operations with ED is strongly reduced if not impossible.

This would be an important drawback of mounting the SPIDER ED in the successive campaign, where one of the most important goals will be to measure the halo power in view of MITICA. In fact, the halo power that will hit the grids of the MITICA accelerator (especially AG4 and GG) has been simulated but never proven by experiments. The current design of the MITICA grids is based on the simulations reported in [44]. From Figure 8c of this paper, it can be observed that the heat load on AG4 and GG is mostly given by the halo particles. Experiments to confirm the numbers of Figure 8c of [44] are strongly needed to prepare the experiments in MITICA, and the SPIDER experiment is probably the most suitable experiment to do this, as its three grids are similar to the first three grids of MITICA (PG, EG

		Core	Halo	Total
With ED	**Nominal**	100 %	76.3 %	86.5 %
	Optimistic	99.8 %	74.1 %	85.2 %
	Average	99.0 %	74.1 %	84.8 %
	Realistic	94.8 %	74.1 %	83.0 %
No ED	**Nominal**	Always 100 %		
	Optimistic			
	Average			
	Realistic			

Table 6.2: Passing fraction of beam components with or without the ED for the four cases considered.

and AG1) and the ion source is also very similar. Figure 6.3 reports the footprints of the beamlets on STRIKE considering the same four scenarios (nominal, optimistic, average, and realistic). In this case, the effect of the ED is not significant, as the footprints without the ED are in all cases very similar to the ones with ED. Figure 6.4 reports the footprint of the co-extracted electrons and the footprint of all electrons (co-extracted and stripped) on STRIKE. In both cases, it can be observed that the heat load by the electrons is foreseen to be low and distributed on the STRIKE surface, so that it is expected to give no particular problems to the measurement of the beam footprints shown in Figure 6.3. Figure 6.5 shows the loads expected on the ED tubes. It can be observed that the peak power density is about 5 times larger in the realistic case (5 MW m^{-2}) than in the nominal one (1.1 MW m^{-2}). Additional detail can be obtained from Figure 6.6, where each contribution to the heat load is listed separately: it can be observed that this large difference is mostly given by the contribution of the beam core, that is null in the nominal case but very high in the realistic case. Table 6.3 reports the amount of heat load on the tubes due to the core, halo, stripped and co-extracted electrons. It can be observed that the contribution of the core is very different in the four considered scenarios. Table 6.4 reports the total amount of heat load on the ED tubes and on the overall ED. It can be observed that the total heat load is about 50 % higher in the realistic case (1.01 MW) than in the nominal case (0.68 MW).

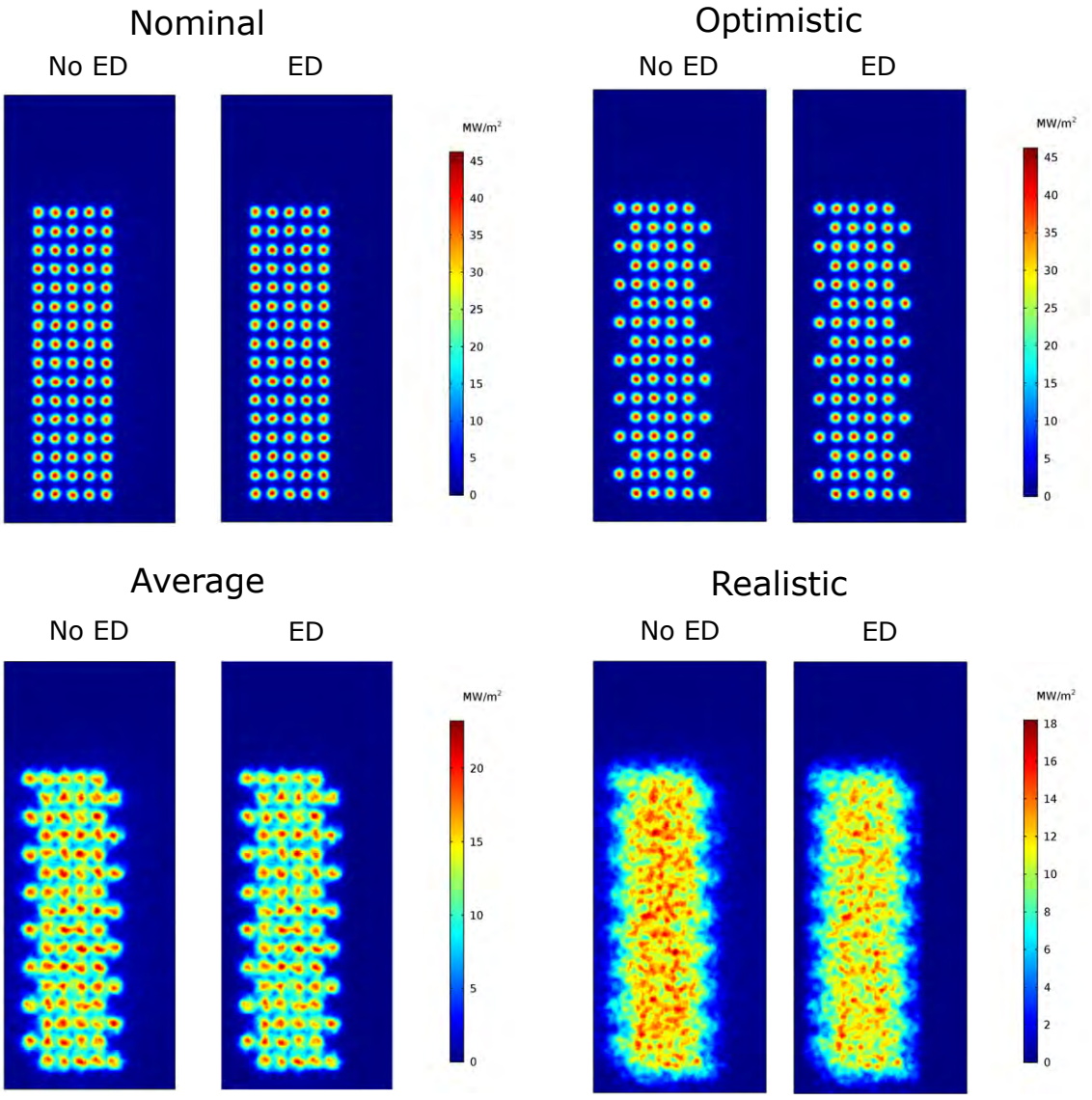

Figure 6.3: Heat maps of the main beam simulation, in the four different cases described.

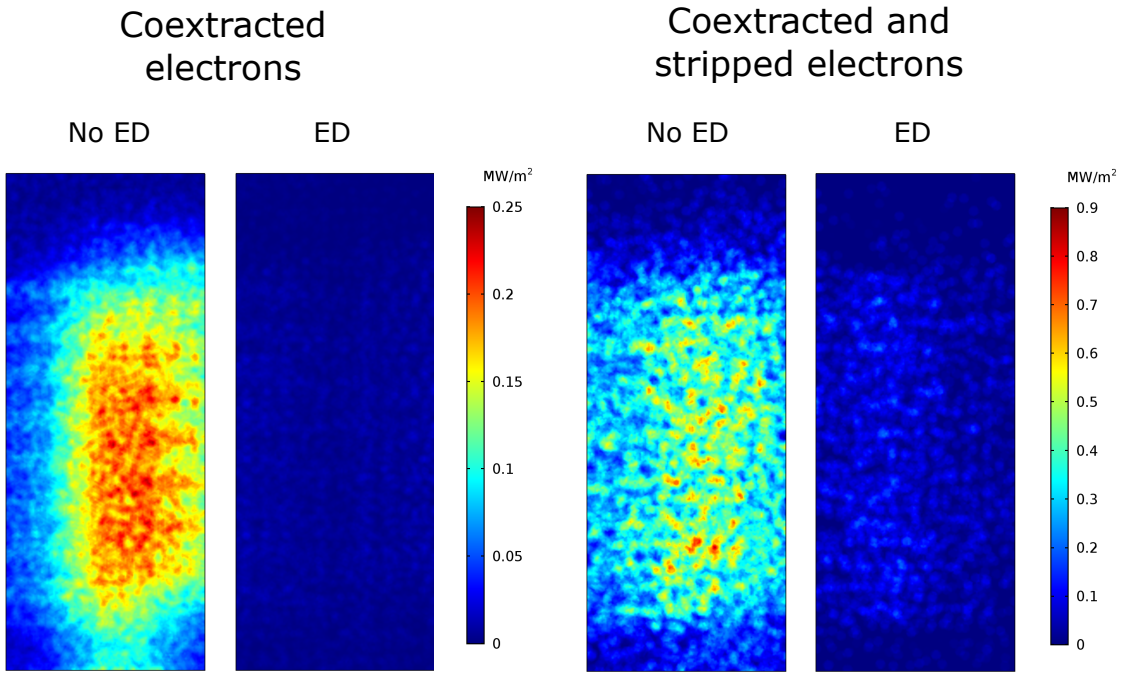

Figure 6.4: Heat maps of the co-extracted electron population (on the left) and of the whole electron population (on the right) on STRIKE, with and without the ED.

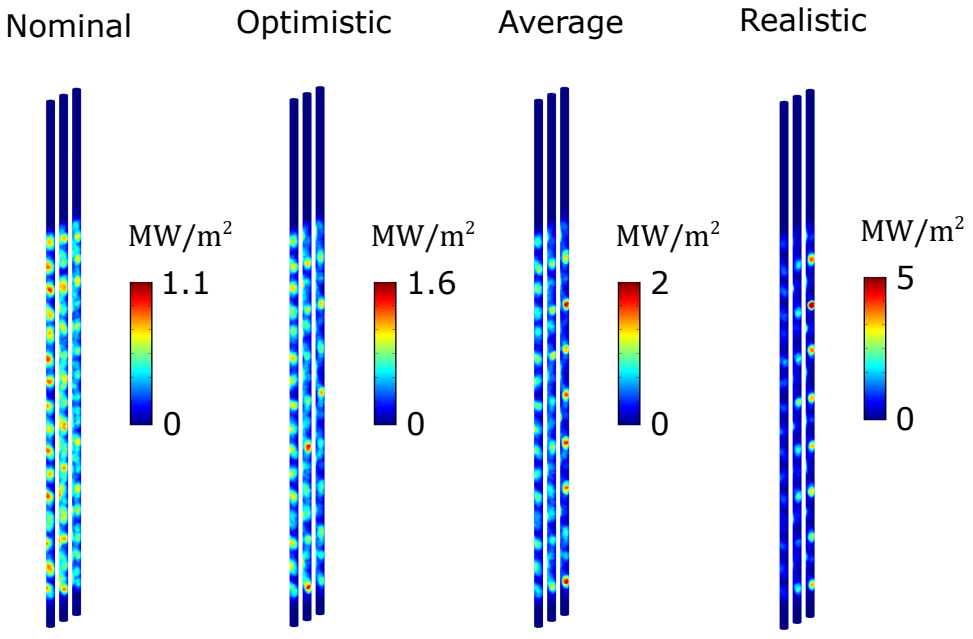

Figure 6.5: Total Heat maps on the ED in the four different cases considered; the one regarding the co-extracted electrons is excluded here.

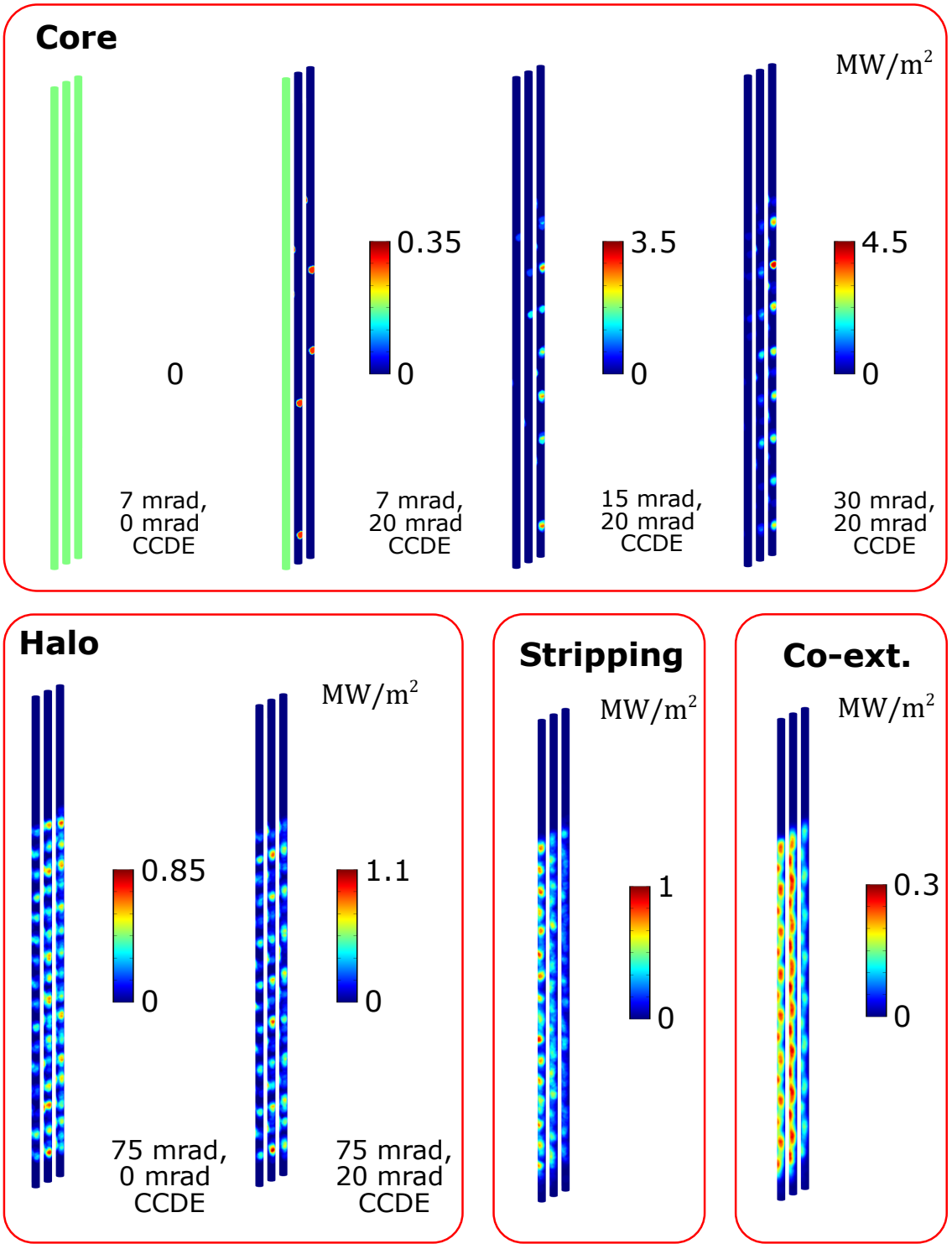

Figure 6.6: Heat maps on the ED, subdivided by contribution.

	Core				Halo		Electrons	
Pipe No.	**N.**	**O.**	**A.**	**R.**	**N.**	**O., A., R.**	Strip. el.	Co-ext. el.
1 [kW]	0	0	0.03	0.18	0.56	0.70	1.56	0.78
2 [kW]	0	0.06	0.08	1.05	1.22	1.24	1.20	0.80
3 [kW]	0	0.05	0.52	2.62	1.33	1.31	0.76	0.36

Table 6.3: Power load by contribution on the most heated ED pipes, at the center of each beam group.

Pipe No.	**Nominal**	**Optimistic**	**Average**	**Realistic**
1 [kW]	2.90	3.04	3.07	3.22
2 [kW]	3.22	3.30	3.32	4.29
3 [kW]	2.47	2.50	2.97	5.07
Total [MW]	0.68	0.71	0.76	1.01

Table 6.4: Total power balance on the most loaded ED columns, and the total ED load for one beam segment, obtained by multiplying the single beamlet power by 80.

6.2.2 Thermo-mechanical simulations on the ED

The heat loads on the ED were taken from the previous paragraph and imported in a new multi-physics simulation of heat transfer, turbulent flow, and mechanical stress, using once again the COMSOL code. This evaluation must be done to detect the temperature distribution on the ED itself, the maximum ΔT in the water temperature, the maximum solid displacement caused by the heat load, and the resulting stresses on the material. The material considered is pure copper, and the model consist of a single pipe with 8 mm external diameter, 1 mm thickness, 400 mm length, upon which the different heat loads in the different cases are applied. The water mass flow for each pipe is set to 0.3 kg s^{-1}, with a starting temperature of 35 °C. From the mechanical standpoint the pipe is fixed at one end while free to expand longitudinally, and subject to gravity. From Table 6.5, it can be observed that the temperature increase of the water is in all cases acceptable because very contained. On the other hand, the temperature of the tube surface can reach higher values, with the maximum temperature of around 65 °C in the nominal case and of around 85 °C in the realistic case, as shown in Figure 6.7. These values are still considered as acceptable for copper. The out-of-axis thermal deformations of the tubes are about proportional to the temperature peaks; hence they are also larger in the realistic case compared to the nominal case. In particular, the deformation along the x direction (horizontal transverse) is the most critical one and is plotted in Figure 6.8. From this figure, it can be observed that even in the most critical case (realistic) the tubes are bowing with a maximum out-of-axis deformation in the x

direction of about 0.14 mm, which is considered acceptable as it is just 1.1 % of the nominal distance between the tubes in x direction (12 mm). The stresses in the tubes have been evaluated as well in each of the four cases: the stress is almost null along the tubes, reaching a significant value only at the lower edge of the pipe. Considering for this point an infinitely rigid constraint of no rotation, the peak values of the Von Mises stress are evaluated as in Table 6.6. Considering that the stress peaks are extremely localized and calculated with conservative boundary conditions infinitely rigid constraint of no rotation, the peak values are also considered acceptable in all cases.

ΔT [°C]	**Nominal**	**Optimistic**	**Average**	**Realistic**
Pipe 1	0.91	0.89	0.89	1.28
Pipe 2	0.86	0.89	1.13	1.57
Pipe 3	0.85	0.78	1.16	1.72

Table 6.5: Temperature increase of the water for each pipe and case of the previous ED loads.

$\sigma_{\max}$ [MPa]	**Nominal**	**Optimistic**	**Average**	**Realistic**
Pipe 1	101	101	101	117
Pipe 2	103	105	123	158
Pipe 3	97	100	122	158

Table 6.6: Peak Von Mises stress for each pipe and case of the previous ED loads. These are always located at the lower edge of the pipe.

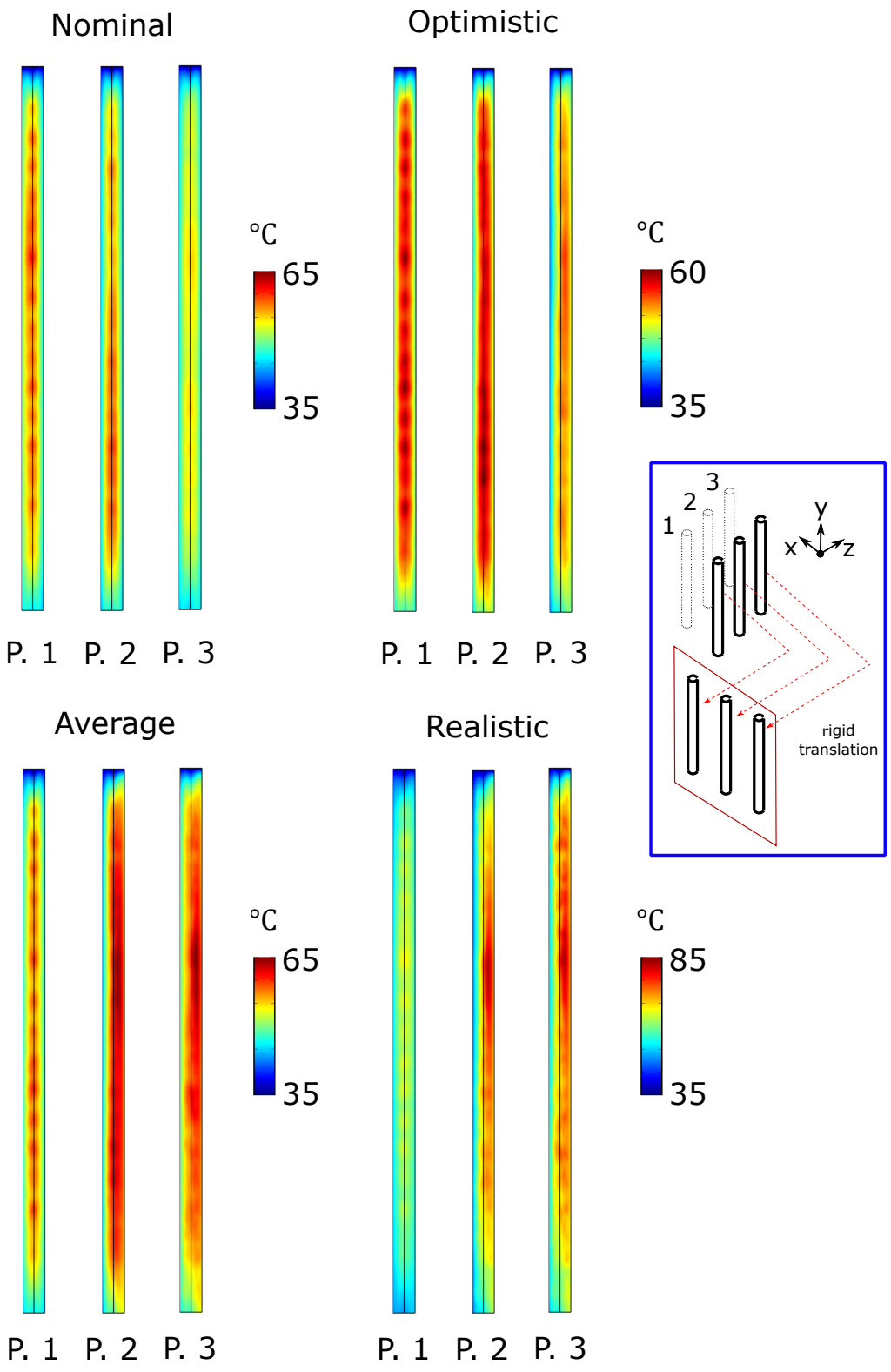

Figure 6.7: Temperature map of each ED pipe for the different cases considered. A little sketch illustrates how to interpret the plots.

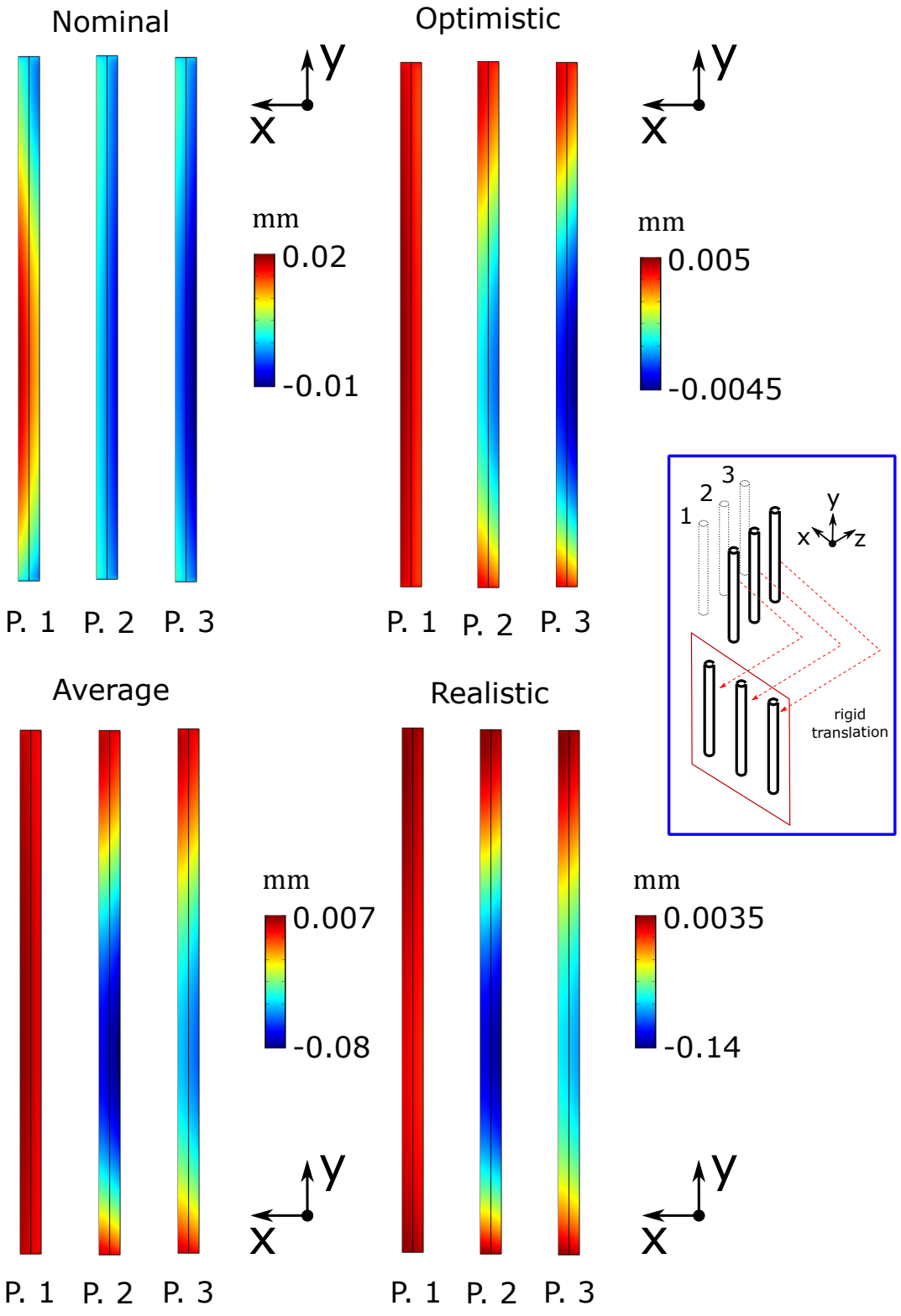

Figure 6.8: Transversal (in this case along the x coordinate) deformation plot for each ED pipe for the different cases considered. A little sketch illustrates how to interpret the plots.

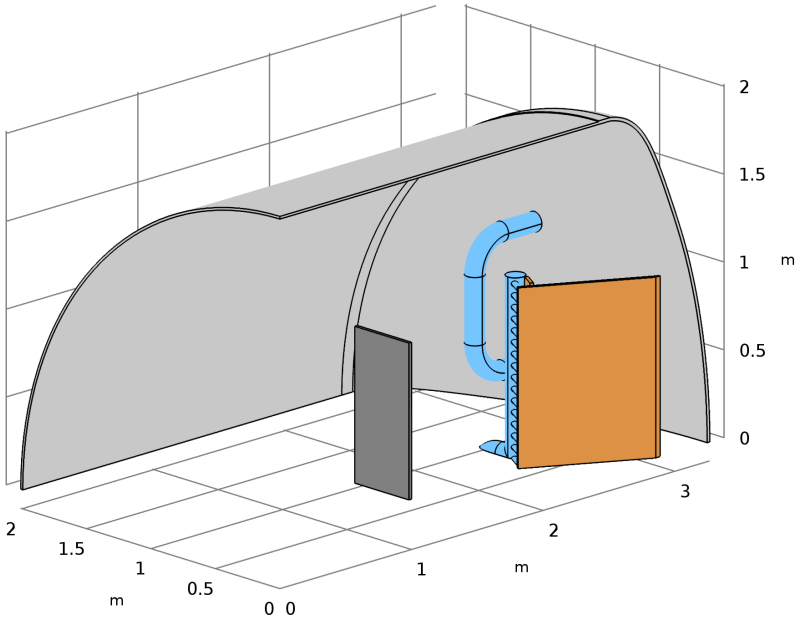

Figure 6.9: Geometry used for the extended particle tracing analysis. The pale blue pipes are the cooling manifolds, and in orange is the Beam Dump, with the possibility of including the presence of the STRIKE calorimeter (in black).

6.3 Full-power thermal investigation of the SPIDER vessel

During a full-power experiment, a large portion of the power accelerated consists of electrons with a large spread of transversal energy, translating into consistent heat loads on components that are not designed to sustain them for extended periods of time (e.g., the Vacuum Vessel walls). To obtain a temperature map of the Vacuum Vessel of SPIDER, the trajectory data of the "Realistic" case was used, but this time the domain has been extended to about 1/4 of the SPIDER source (Figure 6.9). The Beam Dump with its cooling manifolds are present, while the STRIKE calorimeter is supposed to be placed outside of beam range. The heat load maps obtained are then mirrored in the four quadrants and applied to a time-dependent thermal simulation. The material set for the Vessel is Inox steel (AISI 304, thermal conductivity 16.2 W m^{-1} K^{-1}); the system exchanges heat through natural convection (using an internal COMSOL model) and through radiation (supposing emissivity equal to 0.1). The internal radiative exchange has not been modelled, since it would require quite memory-intensive simulations to be considered; this keeps the temperature map on the conservative side anyway. The simulation has been set to run for the nominal 3600 s, and then another 3600 s with the beam switched off to check the cooling rate.

The simulations underlined how only electrons, both of stripped or co-extracted nature, are the only cause of heating of the vessel walls: the ED aptly performs its role by reducing the intensity of the power load from the electrons by an order of magnitude. Figure 6.10 shows the two contributions to the heat loads on the vessel, i.e., from stripping electrons and from co-extracted electrons, both in the case without and with the ED. It can be observed that the ED reduces the peak of power density from the stripping electrons by a factor of 3.3, and the one from the co-extracted electrons by a factor of 25. From Table 6.7, it can be seen that the ED reduces the total power load from the stripping electrons by a factor of 10.9, and the one from the co-extracted electrons by a factor of 27. The temperature of the front lid after 1 hour of continuous application is shown in Figure 6.11. It can be observed that it is not acceptable both in the case with and without ED, with the case without ED being significantly more critical. The corresponding maximum temperature value as a function of time in the two cases is plotted in Figure 16, where it can be observed that the curve with the ED is much lower (about 5 times) than the one without the ED.

	e^- type	**Power deposited [kW]**
No ED	Stripped	153
	Co-ext.	104
With ED	Stripped	14
	Co-ext.	3.8

Table 6.7: Power deposited on the Vacuum Vessel walls, with or without the Electron Dump.

6.3.1 Influence of the STRIKE calorimeter

Another possibility that has been proposed is to appropriately place the STRIKE calorimeter to shield the front lid from a good part of the stray electron load. In this configuration STRIKE is placed at about 1.295 m from the GG (maximum downstream position), and the two panels are 0.8 m apart from each other. This position of STRIKE is particularly suitable to protect the front lid from an excessive heat load because the STRIKE panels are located in front of the critical regions evidenced as hotspots in Figure 6.11. The new set of results is reported in Table 6.8 and Figures 6.13 to 6.15.

6.3.2 Possible cooling for the SPIDER Vacuum Vessel

In order to maintain a safe temperature, a cooling device must be present, either in or outside the Vessel. The simpler choice is to apply an external cooling coil near

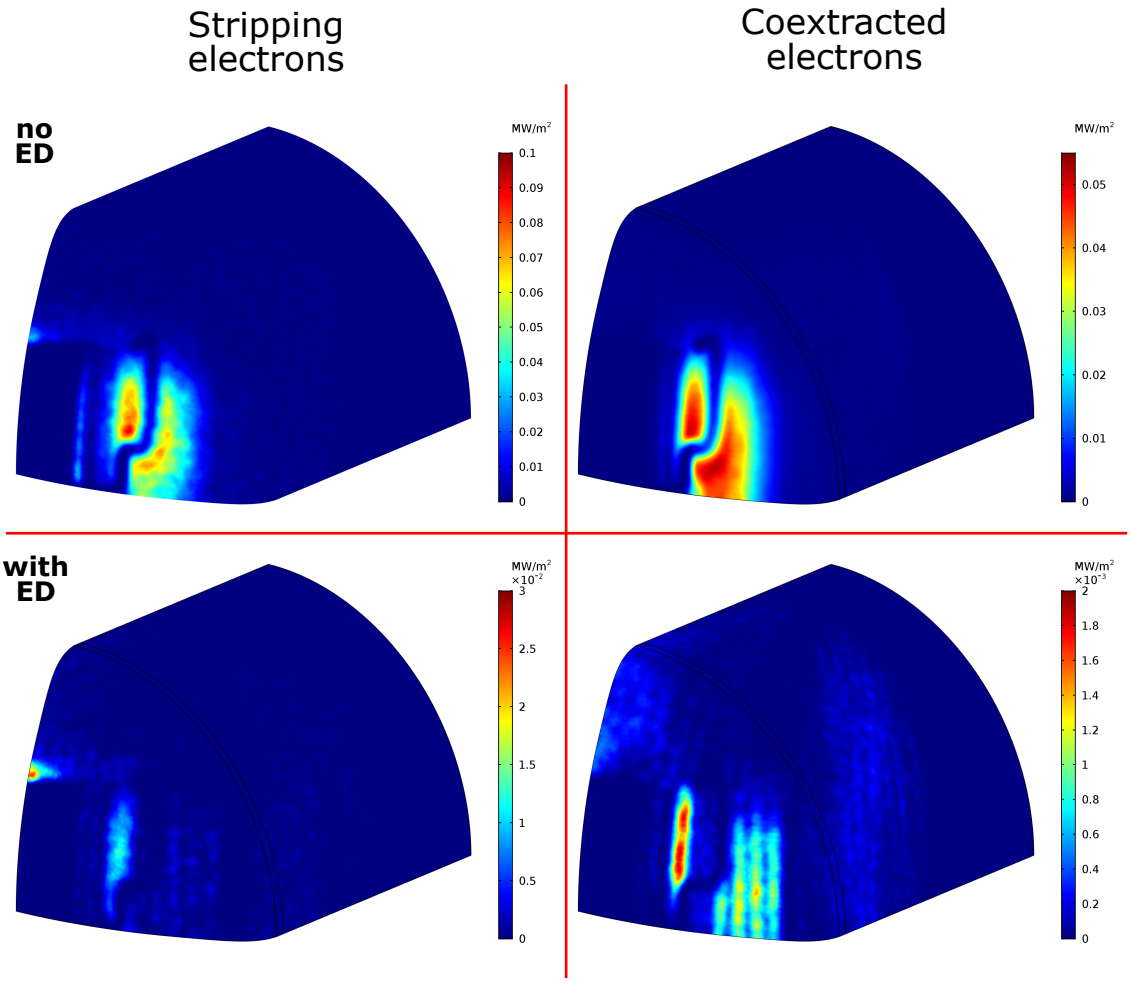

Figure 6.10: Heat load maps for both stripping and coextracted electrons, with and without ED.

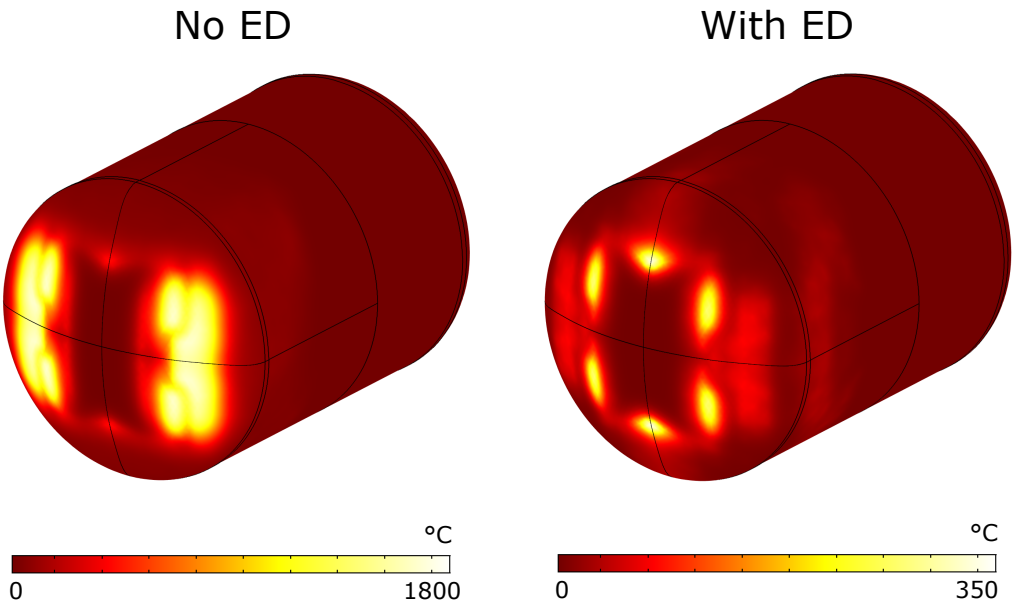

Figure 6.11: Temperature map for the two cases, at the end of the first 3600 s.

	e^- type	Power deposited [kW]
No ED	Stripped	55.0
	Co-ext.	35.4
With ED	Stripped	7.11
	Co-ext.	2.20

Table 6.8: Power deposited on the Vacuum Vessel walls, with or without the Electron Dump.

the locations of the hotspots, for which a tentative design has been designed. To check its effectiveness, a heat exchange simulation has been run once again; however, since a full CFD simulation for this complex geometry could prove quite difficult, a simplified forced convection model has been applied to the internal pipe surfaces, emulating the water behaviour. The heat load used is the one with STRIKE shielding and no ED; to simplify, only half of the vessel is present, and the back lid is cut off where the temperature is not different from 20 °C. The pipe is 20 mm of internal diameter, with a water speed of 1 m s^{-1} and a constant pipe temperature of 35 °C. The simulation has been run with two versions of the cooling coil, in either stationary or time-dependent runs. The time-dependent model run appears to behave badly at lower temperature, with sharp variations during the cooling part; this is probably due to the internal COMSOL model "switching" formulations based on temperature and power flow.

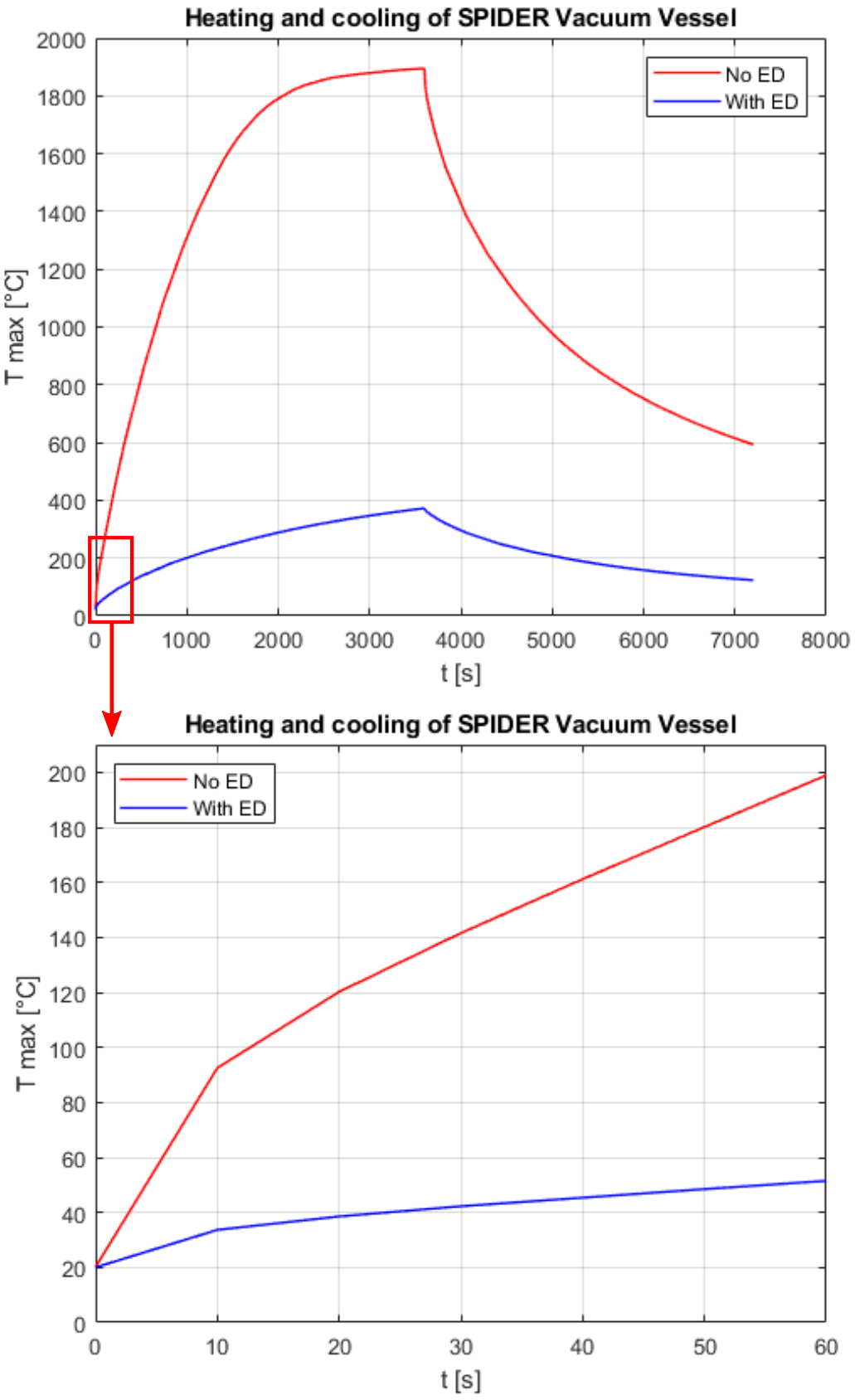

Figure 6.12: Linear plot of the maximum temperature inside the vessel during the operation, with and without the ED. A zoom on the first 60 s is also reported.

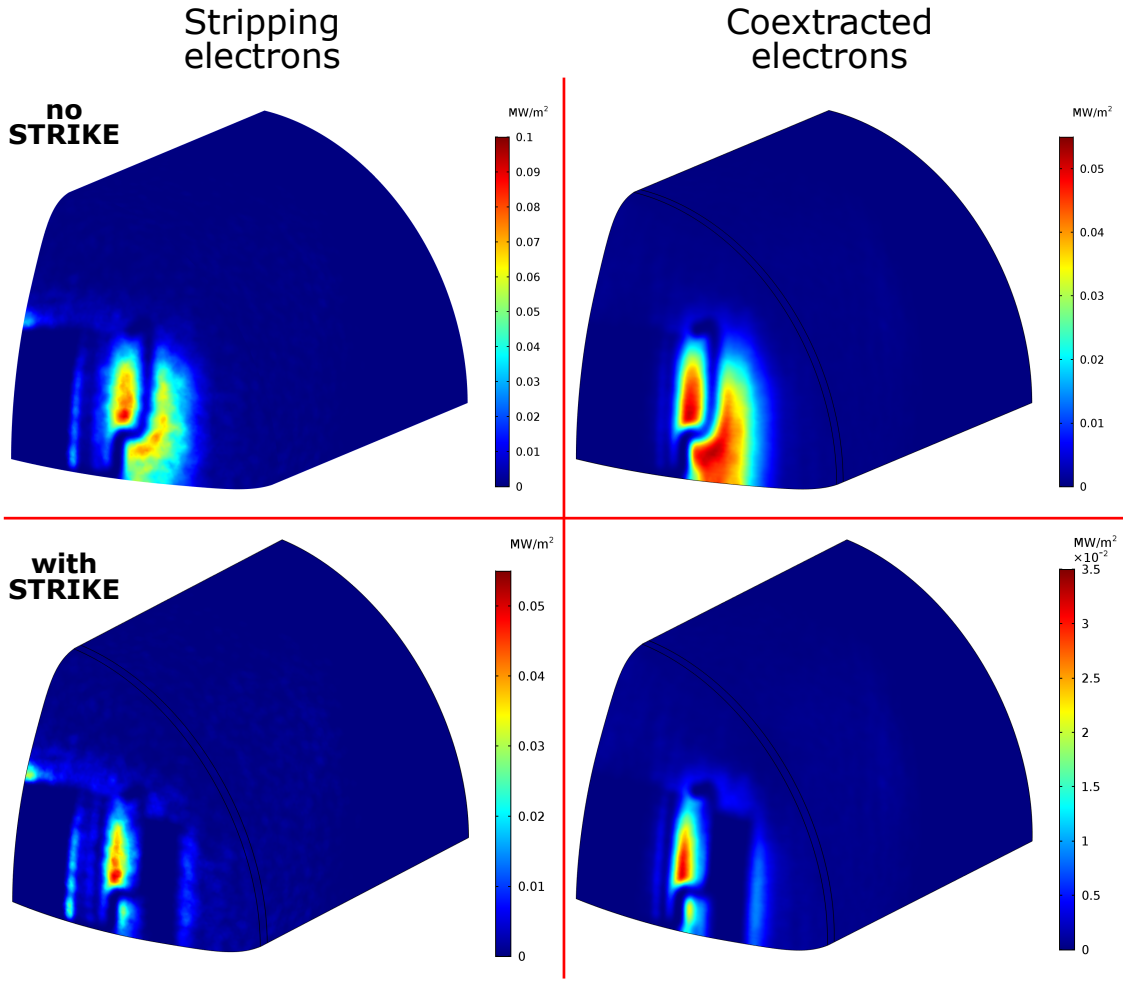

Figure 6.13: Heat load maps with the addition of the STRIKE calorimeter. The original loads are reported for comparison.

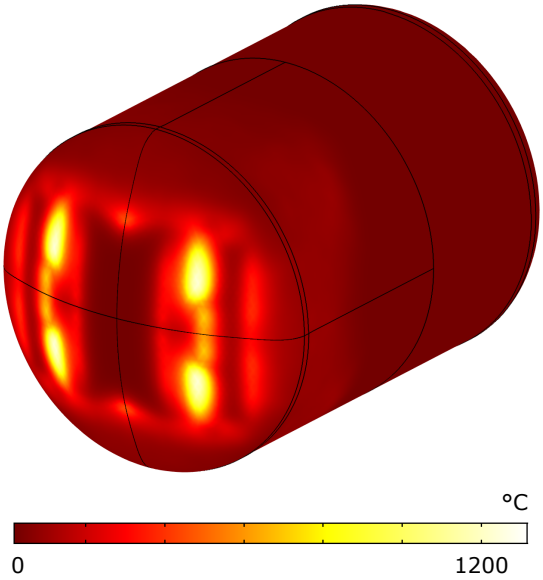

Figure 6.14: Temperature map resulting from the heat transfer simulation in the case with STRIKE. The outline of the calorimeter can be seen on either side of the vessel.

6.4 Extracted current sweep

Following these simulations, an interest was shown in determining in how long it takes for the vessel maximum temperature to reach a fixed value (in this case 100 °C) when changing the extracted current. Another request was made to better check the cooling phase and understand the timescales needed to have the vessel reach ambient temperature once again. For the first step, reducing the extracted current directly affects the macro-particles' emission frequency in a straightforward manner, in such a way that the original trajectory files can be kept but need to be properly scaled back in energy: the extraction voltage is scaled back with the current using the three-halves power Langmuir relation, while the ratio between the acceleration gap voltage and extraction voltage is kept constant. Considering J_n the nominal extracted ion current density and V_n the nominal acceleration voltage, these relations hold:

$$v_\% = j_\%^{2/3};\ j_\% = \frac{J}{J_\mathrm{n}};\ v_\% = \frac{V}{V_\mathrm{n}}. \tag{6.1}$$

This $v_\%$ coefficient can be used to scale back the particle energies and determine the new velocity components, taking care of using relativity-corrected formulas (since electrons may reach a considerable fraction of c_0). The cases considered are using 100% (as reference), 50%, 25% and 10% of the nominal extracted ion current density ($J_\mathrm{n} = 355$ A m^{-2}). A ratio of 1 is here always considered between the co-extracted electrons and the extracted ions.

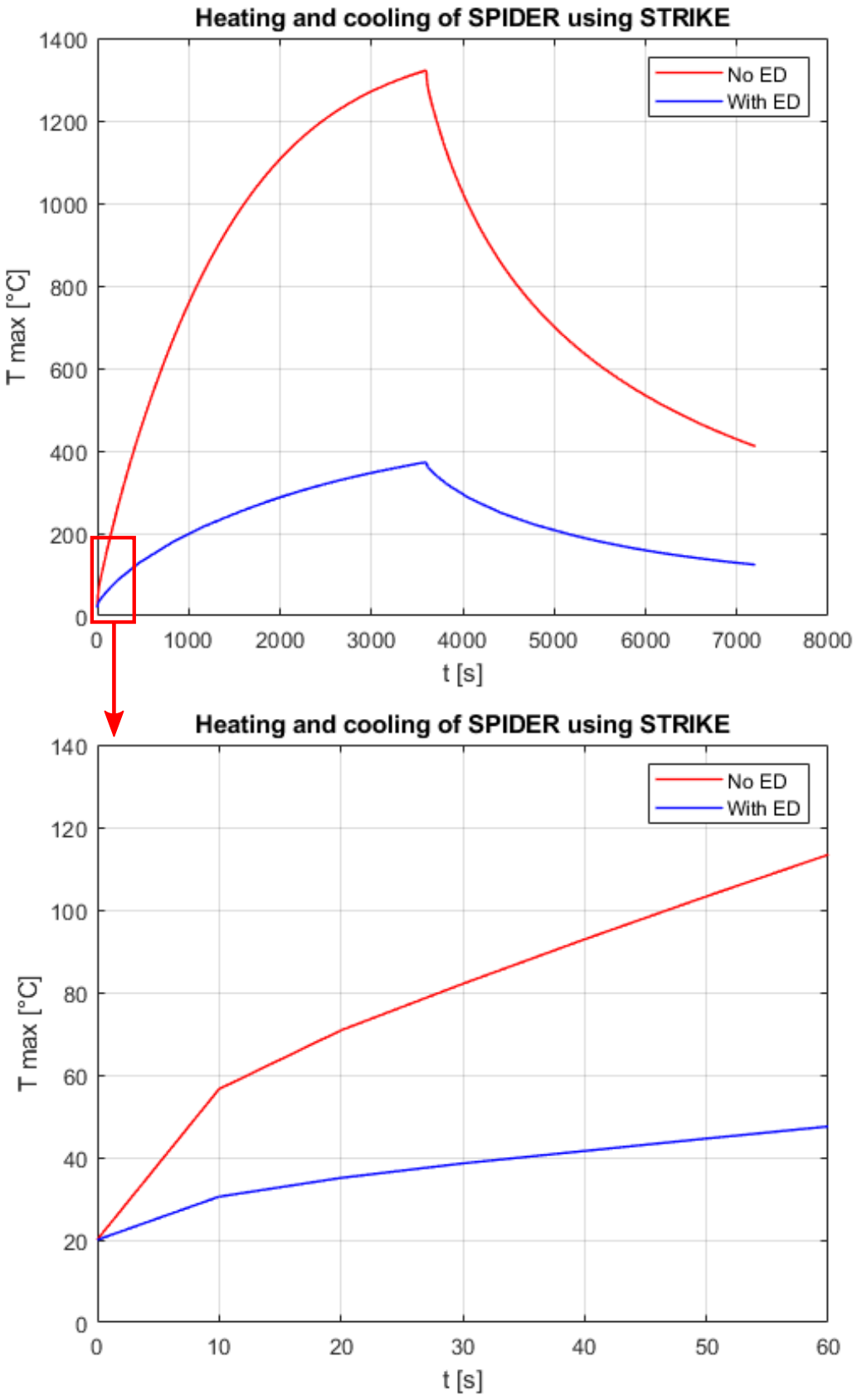

Figure 6.15: Linear plot of the maximum temperature inside the vessel with the addition of STRIKE in shielding position, with and without the ED. A zoom on the first 60 s is also reported.

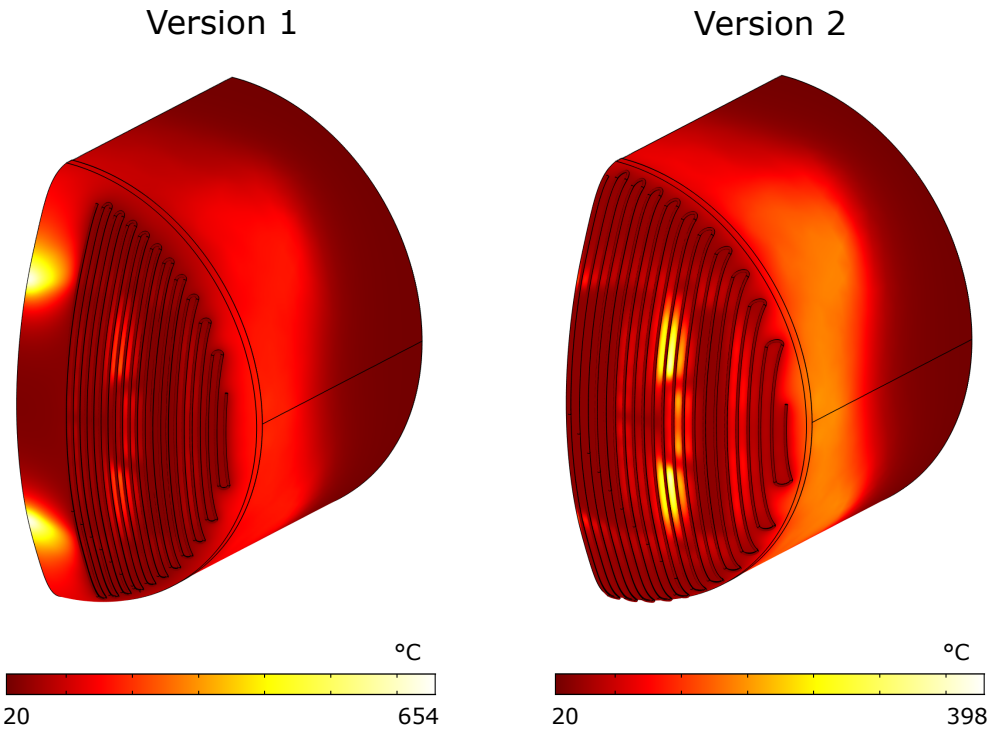

Figure 6.16: Temperature map of the vessel with tentative cooling coils, version 1 and 2.

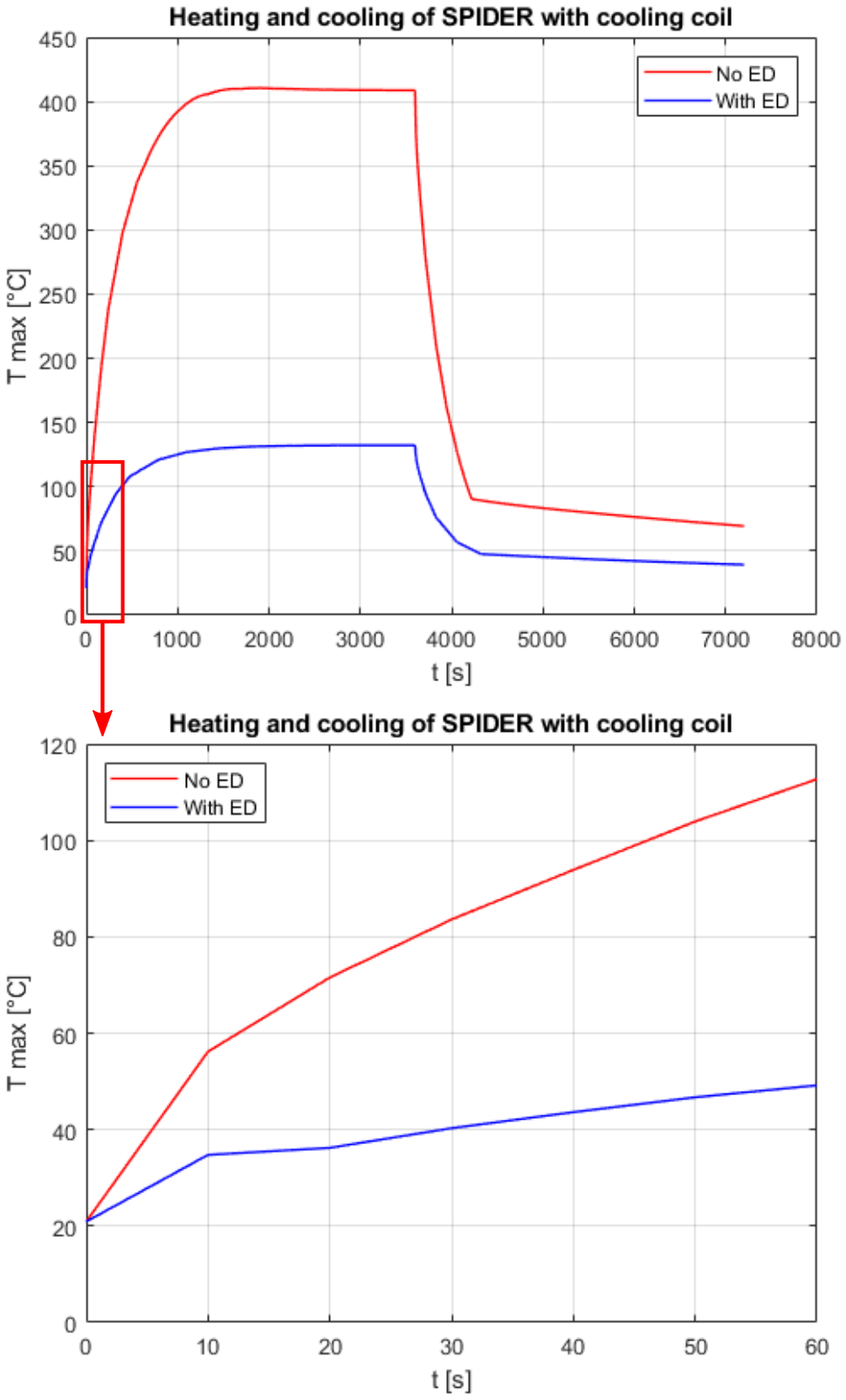

Figure 6.17: Linear plot of the maximum temperature inside the Vessel during the operation, with and without the ED, with the cooling coil of version 2 (see Figure 6.16). A zoom on the first 60 s is reported.

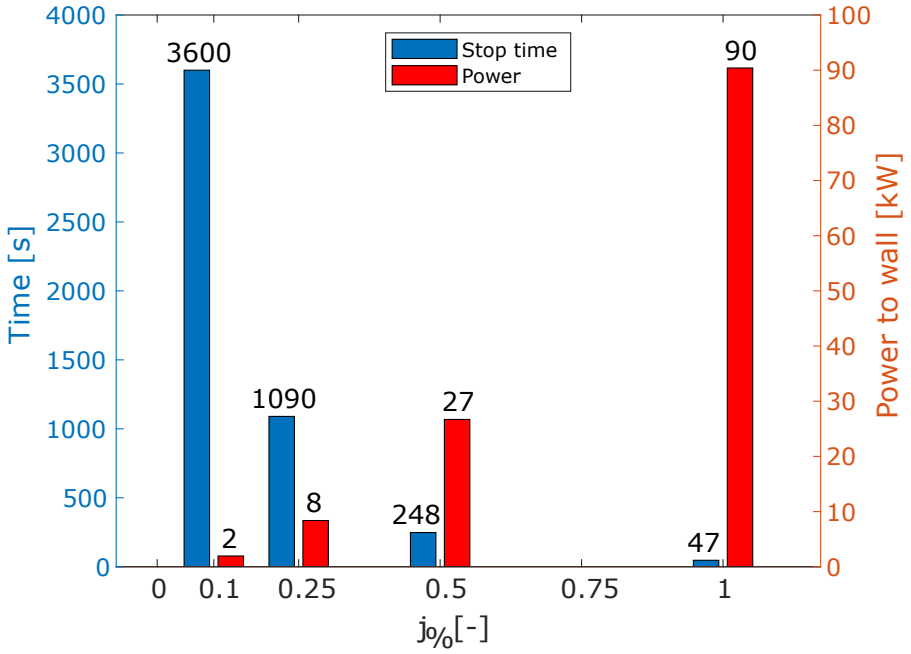

Figure 6.18: Bar plot reporting the result of the extracted current sweep simulation. On the left are reported the times needed to reach 100 °C (or end of simulation) while on the right are reported the wall power loads. The power to the wall here is given only by electrons, because ions are impinging on the beam dump.

The particles were launched in the SPIDER geometry with no ED and with STRIKE in shielding position shown in Figure 6.9. The subsequent thermal analysis was then launched imagining natural convection and radiation cooling (as in section 6.3.2) for $t = 3600$ s, with the addition of a termination condition $T_{\max} < 100$ °C. The results are reported in Figure 6.18. At the end of this simulation, the vessel was allowed to cool by turning the power loads off and following the maximum temperature evolution profile, for a time up to 3600 s. Since all the thermal simulations have a similar power distribution shape (but different intensity), it is the same for the temperature, and only one starting result can be considered. The convection heat transfer coefficient α_h was also swept from a typical value of 5 W m^{-2} K^{-1} up to 20, to appreciate its importance in determining the final maximum temperature (Figure 6.19). Heat transfer by radiation with an emissivity of $\epsilon = 0.1$ is still present. The simulation shows how even after an hour of time, the maximum temperature can range between 30 and 40 °C, even with a four times stronger convection. This is due to the very low thermal conductance of steel, which slows considerably the distribution of temperature toward the exterior.

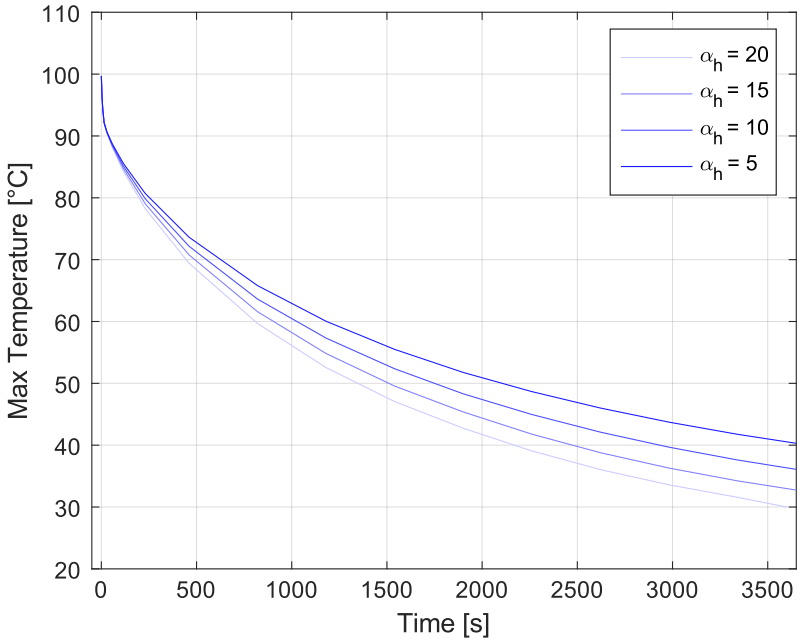

Figure 6.19: Maximum temperature profile inside the SPIDER vacuum vessel during the cooling phase, while sweeping the convection coefficient α_{h}.

6.4.1 Temperature profile evolution in a possible experimental setup

After finding out the timescales involved in reaching critical temperatures and in cooling to ambient temperature, the interest shifted in determining how the vessel would perform when subjected to a series of time-limited shots and cooling phases at various powers. A proposed time scheme is to reach the performance of ELISE, where 10 s shots are alternated to 180 s of pause. This can be simulated by turning the load on periodically in the previous model and counting how many shots can be performed before reaching a set maximum temperature. A fully time-dependent simulation can take quite some time to go through the periodical switching of the load up to the maximum temperature. The solver was set to run for the whole theoretical 8 hours of work in cycles of 190 s, and made to stop once reached the limit temperature. The convection coefficient in this model is left to internal COMSOL models for horizontal cylinders, in order to have it change with the temperature, while radiation is still present. The result is presented in Figure 6.20. Operation with this duty cycle is surprisingly effective in delaying reaching the critical temperature of 100 °C: in the case of half extracted current, the vessel could stay under about 90 °C for the whole day, while in the nominal case only 7–8 cycles would be possible. This "flattening" of the curve is mostly due to the increased ΔT between the interior and exterior that accelerates heat diffusion during the off-time.

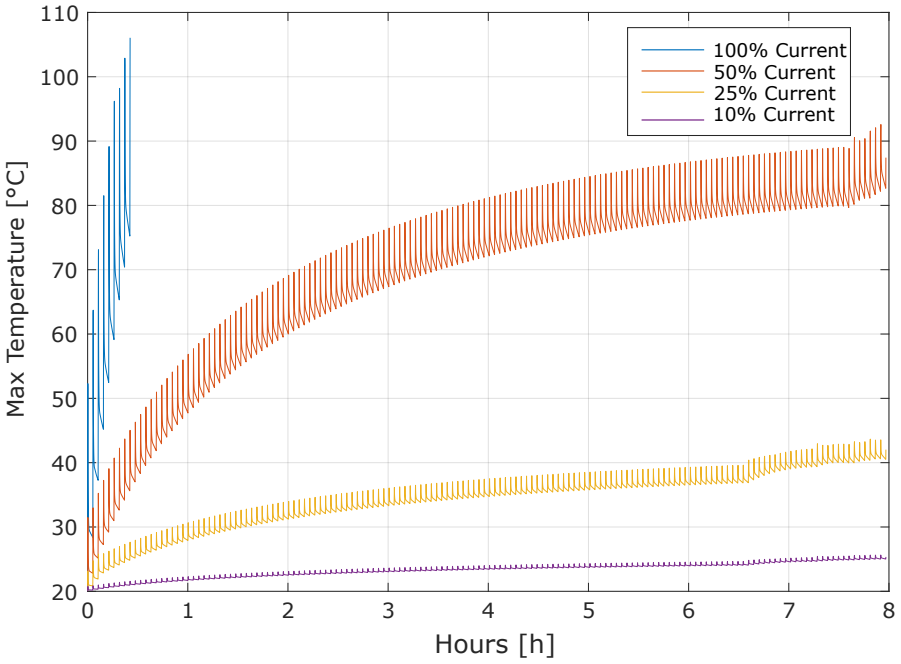

Figure 6.20: Results of thermal cycling at different extracted currents. The solver shows some issues when running for too long.

6.5 Conclusions

The main takeaway message from this set of simulations is the fact that the ED is very important in reducing the stray electron loads on the vacuum vessel (as per its design), but also quite impactful on the shape of the accelerated beams, altering the halo component observable from the diagnostic calorimeter: said impact would be even more pronounced as the source operates far from the nominal power, which is usually the case. Being the study of the halo component one of the next objectives of the SPIDER experimental campaign, altering it through the ED does not appear to be the best course of action in the near future. The issue of excessive electron heating can be brought under control by operating in short pulses, while continuously monitoring the temperature of the front lid.

Chapter 7

Conclusion

This thesis tries to collect and explain all of the choices and work done during this long conceptual design phase for DTT NBI. The project has come a long way now, starting from the bare requirements and slowly growing to include all of the needed subsystems, involving a larger and larger group of researchers.
Within this framework one of the main original contributions that stemmed from this Ph.D. regards the electrostatic accelerator, where beam optics requirements have been met through the use of the Hyperlens Grids concept, an additional set of grids with a lens-like profile able to guide effectively the multi-beamlet array of the NBI.
Following the desire to improve the performance of the injector, another important contribution has been the redesigning of the Beam Line Components following a more rigorous approach based on pre-established transmission losses and bigaussian beam approximations, denominated the beam-fitting design approach.
After noticing potential issues for the beam caused by the stray poloidal tokamak field, the Stray Field Shielding System has been added as an original design in order to suppress the deflecting effect on the charged beam.
All of these effects have then been considered all together to first estimate the resulting heat loads on the beamline and accelerator, key to design the necessary cooling systems.
Right now, DTT NBI is poised to be a trailblazer in a lot of fields, considering the novel concepts that have been introduced here for the first time, as well as adopting state of the art techniques such as copper printing and NEG pumps as first choice. So many things are new, that the inherent danger to the possibility of realization may very well be coming from the testing phase, manufacturing, or integration issues. To avoid this, great attention is being dedicated to each and every aspect of each system, giving priority in sharing information between research teams during meetings.
The DTT NBI design phase is also a great occasion to put together different codes and streamlining the simulation processes, learning precious methods and good-practice techniques in generating inputs and reading outputs.
As mentioned before, especially helpful in this aspect was the parallel work done at IPP Garching for DEMO NBI and its BDPN optimization. The whole experience

required a better description of the beam trajectories, aligning the model with existing inputs; also, since DEMO had no fixed geometry to follow, the beam-fitting concept was born there as an attempt to improve how channels are designed. Also, the optimization of the BDPN design and the direct comparison with a gas neutralizer counterpart are definitely going to be a factor in deciding the future usefulness of the BDPN within an NBI system.
Useful lessons were learned as well by working on the SPIDER experiment, as an example of how a problem-solving pipeline works with an already established device, and of what there is to pay attention to when tons of material are involved.
Many smaller things during the years also have helped in correcting various issues on the codes and in the designs, all contributing to the skill set that will be important when going forward.
The future overlook on DTT NBI is promising, since now the rough design and boundary conditions seems to have settled and many more people are going to work on ironing out possible issues; manufacturing tests of the copper components are ongoing, with additional test on different experiments planned as well.
For DEMO NBI the future is not as certain, since its prospected efficiency is still too low for a potentially steady-state reactor; still, the BDPN concept is going to be explored more in detail with a dedicated experiment at IPP Garching, to see if plasma confinement in this configuration is satisfactory and accurate to models.
The future may be uncertain, but moderate optimism is the key to success.

Chapter 8

Acknowledgements

Finally, the acknowledgements. These three years started strong, only to incur months after on one of the biggest obstacles that modern society had to weather, the pandemic.
During all this (and in general), my work was and is one of the few creative outlets that I have, and that I love pouring myself into. All of it was made possible by my supervisor Piero Agostinetti, which I thank deeply. This makes the third time we collaborated, each time aiming bigger.
Many thanks also to my supervisor Kristel Crombé, which gave me the occasion of pursuing this Ph.D. in the first place.
I am also thankful to Christian Hopf and Giuseppe Starnella at IPP Garching, for following and helping me during my stay in Germany: a great deal of the concepts described in the thesis are there thanks to them. Also, the Grad-Shafranov cup looks very cool on my desk!
Finally, many thanks to the professors Paolo Bettini and Piergiorgio Sonato, which showed the right direction to me and many others towards the world of fusion research.
These three years were very important to me to decide what to do next in life, and to see what is beautiful about research. I plan to stick around for a while!

Bibliography

[1] *BP Statistical Review of World Energy.* 71st Edition (2022).

[2] Kikuchi M., Lackner K., Tran M. Q. *Fusion Physics.* International Atomic Energy Agency, Vienna (2012).

[3] A. L. Kritcher, et al. *Design of inertial fusion implosions reaching the burning plasma regime.* Nat. Phys. 18, 251-258 (2022).

[4] H.P. Eubank, et al. *PLT neutral beam heating results.* IAEA Conference Proceedings (1978). DOI: 10.2172/6504076

[5] F. Wagner, et al. *Regime of Improved Confinement and High Beta in Neutral-Beam-Heated Divertor Discharges of the ASDEX Tokamak.* Phys. Rev. Lett. 49, 1408 (1982). DOI: 10.1103/PhysRevLett.49.1408

[6] M. Kuriyama, et al. *Operation of the negative-ion based NBI for JT-60U.* Fus. Eng. Des. 39-40 (1998) 115-121.

[7] L. Langmuir, K. R. Blodgett. *Currents limited by space charge between concentric spheres.* Phys. Rev. 24, 49 (1924).

[8] J. R. Coupland, et al. *A Study of the Ion Beam Intensity and Divergence Obtained from a Single Aperture Three Electrode Extraction System.* Rev. Sci. Inst. 44 (1973) 1258.

[9] J. R. Pierce. *Rectilinear Electron Flow in Beams.* Journal of Applied Physics 11, 548 (1940).

[10] F. Romanelli et al. *Fusion electricity - a roadmap to the realization of fusion energy (EFDA).* http://eurofusion.org/wpcms/wp-content/uploads/2013/01/JG12.356-web.pdf (2012)

[11] R. Albanese and F. Crisanti et al. *Divertor Tokamak Test facility Interim Design Report.* ENEA, ISBN: 978-88-8286-378-4 (2019).

[12] R. Ambrosino, et al. *DTT - Divertor Tokamak Test facility: A testbed for DEMO.* Fus. Eng. Des. 167 (2021) 112330.

[13] P. Agostinetti, et al. *Manufacturing and testing of grid prototypes for the ITER neutral beam injectors.* IEEE Trans. Plasma Sci. 42 (2014) 628.

[14] A. Kojima et al. *Progress in long-pulse production of powerful negative ion beams for JT-60SA and ITER.* Nucl. Fusion 55 (2015) 063006.

[15] Y. Takeiri et al. *High-power and long-pulse injection with negative-ion-based neutral beam injectors in the Large Helical Device.* Nucl. Fusion 46 (2006) S199-S210.

[16] B. Heinemann et al. *Latest achievements of the negative ion beam test facility ELISE.* Fusion Eng. Des., 136 (2018) 569.

[17] F. Siviero, et al. *Characterization of ZAO® sintered getter material for use in fusion applications.* Fus. Eng. Des. 146 (2019) 1729-1732. DOI: 10.1016/j.fusengdes.2019.03.026

[18] L. Murr et al. *Metal Fabrication by Additive Manufacturing Using Laser and Electron Beam Melting Technologies.* Journal of Materials Science and Technology -Shenyang- (2012).

[19] M. Schmidt et al. *Laser based additive manufacturing in industry and academia.* CIRP Annals, Volume 66, Issue 2 (2017), p. 561-583.

[20] D. Marcuzzi, et al. *Detail design of the beam source for the SPIDER experiment.* Fus. Eng. Des. 85 (2010) 10-12, pg. 1792-1797.

[21] D. Marcuzzi, et al. *Detail design of the beam source for the SPIDER experiment.* Rev. Sci. Instrum. 87, 02B309 (2016).

[22] Y. Ikeda, et al. *Recent R&D Activities of Negative Ion-Based Ion Source for JT-60SA.* IEEE Transactions On Plasma Science, Vol.36, No.4 (2008).

[23] R.S. Hemsworth, et al. *Overview of the design of the ITER heating neutral beam injectors.* New J. Phys. 19 (2017) 025005.

[24] G. Chitarin, et al. *Improvements of the magnetic field design for SPIDER and MITICA negative ion beam sources.* AIP Conference Proceedings 1655, 040008 (2015). DOI: 10.1063/1.4916450

[25] Molecular Flow User's Guide, pp. 62-78. COMSOL Multiphysics® v. 6.0. COMSOL AB, Stockholm, Sweden. 2021

[26] M. Hanada, et al. *Progress in development and design of the neutral beam injector for JT-60SA.* Fusion Engineering and Design 86 (2011) 835-838. DOI: 10.1016/j.fusengdes.2011.04.068.

[27] S. Goetz, et al. *Design of Ion Removal System and Magnetic Shielding for the ASDEX-Upgrade Neutral Injection Beam Line.* Fusion Technology 1988, Vol. 1, 615-619.

[28] M. Roccella, et al. *Analysis of active and passive magnetic field reduction systems (MFRS) of the ITER NBI.* Fusion Engineering and Design 82 (2007) 709-715. DOI: 10.1016/j.fusengdes.2007.07.049.

[29] G. Barrera, et al. *Magnetic analysis of the magnetic field reduction system of the ITER neutral beam injector.* Fusion Engineering and Design 96-97 (2015) 400-404. DOI: 10.1016/j.fusengdes.2015.02.054.

[30] M.Q. Tran, et al. *Status and future development of Heating and Current Drive for the EU DEMO.* Fusion Engineering and Design 180 (2022) DOI: j.fusengdes.2022.113159

[31] P. Sonato, et al. *Conceptual design of the DEMO neutral beam injectors: main developments and R&D achievements.* Nuclear Fusion 57 (2017) 056026.

[32] K. H. Berkner, *Plasma neutralizers for H^- or D^- beams.* Second International Symposium on the Production and Neutralization of Negative Ions and Beams, Upton, NY (1980).

[33] M. Hanada, M. Kashiwagi, T. Inoue, K. Watanabe, and T. Imai. *Experimental comparison between plasma and gas neutralization of high-energy negative ion beams.* Rev. Sci. Inst. 75 (2004) 1813-1815.

[34] E. Surrey, A. Holmes. *The beam driven plasma neutralizer.* AIP Conference Proceedings 1515, 532 (2013).

[35] I. Turner, A. Holmes. *Model for a beam driven plasma neutraliser based on ITER beam geometry.* Fusion Engineering and Design (2019).

[36] G. Starnella, C. Hopf, P. N. Maya. *On suitable experiments for demonstrating the feasibility of the beam-driven plasma neutraliser for neutral beam injectors for fusion reactors.* Nuclear Fusion (2022).

[37] L. Xueli, et al. *Updated assessment of NBI vacuum requirements.* Version 1.3 (2020), IDM ID: EFDA_D_2NY6UX.

[38] Barnett C. F. *Collisions of H, H_2, He, and Li atoms and ions with atoms and molecules.* Technical Report No. ORNL-6086, Oak Ridge National Laboratory (1990).

[39] P. Sonato, et al. *Conceptual design of the beam source for the DEMO Neutral Beam Injectors.* New J. Phys. 18 (2016) 125002.

[40] R. Hemsworth, et al. *Status of the ITER heating neutral beam system.* Nuclear Fusion 49 (2009) 045006.

[41] U. Fantz, et al. *Physical performance analysis and progress of the development of the negative ion RF source for the ITER NBI system.* Nuclear Fusion 49 (2009) 125007.

[42] P. Sonato, et al. *The ITER full size plasma source device design.* Fus. Eng. Des. 84 (2009) 269.

[43] P. Agostinetti, et al. *Physics and engineering design of the accelerator and electron dump for SPIDER.* Nuclear Fusion 51 (2011) 063004.

[44] P. Agostinetti, et al. *Detailed design optimization of the MITICA negative ion accelerator in view of the ITER NBI.* Nuclear Fusion 56 (2016) 016015.